Design of nanocatalysts supported on magnetic anocomposites containing silica, ceria and titania

Lucas Lucchiari Ribeiro Vono

Université Fédérale
Toulouse Midi-Pyrénées

THÈSE

En vue de l'obtention du

DOCTORAT DE L'UNIVERSITÉ DE TOULOUSE

Délivré par :

Université Toulouse 3 Paul Sabatier (UT3 Paul Sabatier)

Cotutelle internationale avec Institute of Chemistry of the University of São Paulo

---

Présentée et soutenue par :
Lucas Lucchiari Ribeiro Vono

le 18 de Mars de 2016

Titre :

Elaboration de catalyseurs supportés par dépôt de nanoparticules métalliques sur des composites magnétiques contenant de la silice, de l'oxyde de cérium et de l'oxyde de titane

---

École doctorale et discipline ou spécialité :
ED SDM : Chimie organométallique de coordination - CO 043

Unité de recherche :
Laboratoire de Chimie de Coordination - Centre National de la Recherche Scientifique

Directeur/trice(s) de Thèse :
Prof. Dr. Liane Marcia Rossi
Dr. Karine Philippot

Jury :

Liane Marcia Rossi, Professor, University of São Paulo
Karine Philippot, Directeur de recherche, Laboratoire de Chimie de Coordination - CNRS
Pedro Henrique Cury Camargo, Associated Professor, University of São Paulo, Examinateur
Robert Wojcieszak, Chargé de recherches, Unité de Catalyse et Chimie du Solide - CNRS, Examinateur
Mario Roberto Meneghetti, Professor, Federal University of Alagoas, Rapporteur
Benjamin Katryniok, Maître de Conférences, École Centrale de Lille, Rapporteur

LUCAS LUCCHIARI RIBEIRO VONO

Desenvolvimento de nanocatalisadores suportados em nanocompósitos magnéticos contendo sílica, céria e titânia

Design of nanocatalysts supported on magnetic nanocomposites containing silica, ceria and titania

Tese apresentada ao Instituto de Química da Universidade de São Paulo e à Université Toulouse III – Paul Sabatier para obtenção do título de Doutor em Ciências (Química)

Orientadora: Prof[a] Dar. Liane Marcia Rossi
Coorientadora: Dr[a] Karine Philippot

São Paulo
2015

UNIVERSIDADE DE SÃO PAULO
INSTITUTO DE QUÍMICA

"Desenvolvimento de nanocatalisadores suportados em nanocompósitos magnéticos contendo sílica, céria e titânia"

LUCAS LUCCHIARI RIBEIRO VONO

Tese de Doutorado submetida ao Instituto de Química da Universidade de São Paulo como parte dos requisitos necessários à obtenção do grau de Doutor em Ciências no Programa de Química.

Aprovado(a) por:

Profa. Dra. Liane Marcia Rossi
(Orientadora e Presidente)

Profa. Dra. Karine Nathalie Philippot
UPS - França

Prof. Dr. Pedro Henrique Cury Camargo
IQ - USP

Prof. Dr. Mario Roberto Meneghetti
UFA

Prof. Dr. Benjamin Katryniok
ECL - França

Prof. Dr. Robert Jan Wojcieszak
ECL - França

SÃO PAULO
18 de março de 2016

For Natália
You are the light of my life

For my mother and my uncle
You are not here, but you will always be with us

ACKNOWLEDGMENTS

To Prof. Dr. Liane M Rossi for her long time support and supervision of this thesis.

To Dr. Karine Philippot for all the support during my time in Toulouse and the co-supervision of this thesis.

To Prof. Dr. Jivaldo R. Matos for thermal analysis, Prof. Dr. Alcindo A. Dos Santos for gas chromatography, Prof. Dr. Renato F. Jardim for magnetic measurements, Prof. Dr. Marcia C. A. Fantini for X-ray Diffraction, Prof. Dr. Pedro K. Kiyohara for Transmission electron microscopy, Prof. Dr. Richard Landers for X-ray photoelectron spectroscopy and Prof Dr Renato F. Jardim for SQUID measurements.

To my wife who is the reason for finishing this text

To my aunt that provided a comfortable place to write and awesome food

To the colleagues in Brazil and in France that helped me in the lab

To the Brazilian Nanotechnology National Laboratory (LNNano) for the Transmission electron microscopy facilities (JEOL JEM 2100).

To the Brazilians agencies that gave financial support the Fundação de Amparo à Pesquisa do Estado de São Paulo (FAPESP), that provided a PhD fellowship in Brazil, and the Coordenação de Aperfeiçoamento de Pessoal de Nível Superior (CAPES), that provided a PhD fellowship connected to the CAPES-COFECUB (Comité Français d'Évaluation de la Coopération Universitaire et Scientifique avec le Brésil) project 695/10 during the time in France.

Je vois la vie en rose

La Vie en Rose
Edith Piath

RESUMO

Vono, L.L.R. *DESENVOLVIMENTO DE NANOCATALISADORES SUPORTADOS EM NANOCOMPÓSITOS MAGNÉTICOS CONTENDO SÍLICA, CÉRIA E TITÂNIA*. 2016. (205p). Tese de Doutorado – Programa de Pós-Graduação em Química. Instituto de Química, Universidade de São Paulo, São Paulo, Brasil e Université Toulouse III – Paul Sabatier, Toulouse, França.

A separação magnética tem recebido muita atenção como uma tecnologia robusta, altamente eficiente e rápida para recuperar catalisadores sólidos após uso em reações em fase líquida. Muitos estudos têm focado nas metodologias para a imobilização de espécies cataliticamente ativas, mas o desenvolvimento de suportes magnéticos tem se limitado a nanopartículas magnéticas revestidas com sílica, polímeros ou carbono. O desenvolvimento de nanocompósitos magnéticos com a incorporação de outros óxidos é muito desejável para ampliar a aplicação dessa tecnologia de separação em catálise. Nesse contexto, estudos da estabilidade térmica de magnetita revestida com sílica (Fe_3O_4@SiO_2) foram realizados para avaliar a possibilidade de calcina-la sem perder as propriedades magnéticas do suporte. Uma etapa de calcinação é necessária para a deposição de diferentes óxidos na superfície da sílica, tais como céria e titânia. O Fe_3O_4@SiO_2 calcinado preservou a morfologia *"core-shell"* e as propriedades magnéticas, porém apresentou um aumentou de seis vezes na área superficial. Novos suportes magnéticos foram desenvolvidos pela deposição de céria e titânia sobre magnetita previamente revestida com sílica. Nanocatalisadores magneticamente recuperáveis de Rh, Pd e Ru foram preparados. Os catalisadores foram utilizados na hidrogenação de ciclo-hexano, benzeno ou fenol e o principal objetivo dessa tese foi o estudo da influência de cada suporte na atividade catalítica. Os catalisadores foram preparados de duas formas diferentes: impregnação-redução e imobilização de nanopartículas (NPs) metálicas pré-formadas. As NPs coloidais foram preparadas pela redução de sais metálicos e, também, pela decomposição de complexos organometálicos. Catalisadores de ródio preparados pela impregnação de cloreto de ródio(III) e redução com H_2 mostraram alguns problemas de reprodutibilidade, que foram superados utilizando $NaBH_4$ ou hidrazina como agentes redutores. A preparação de catalisadores pela imobilização de NPs coloidais é uma alternativa interessante para obter catalisadores reprodutíveis e muito ativos. Nanopartículas de Pd, Rh e Ru foram preparadas a partir de organometálicos e imobilizadas em Fe_3O_4@SiO_2 calcinada, Fe_3O_4@SiO_2CeO_2 e Fe_3O_4@SiO_2TiO_2. A eliminação do agente estabilizante torna os catalisadores mais ativos durante os reusos. O catalisador de Rh sobre o suporte de céria foi o catalisador mais ativo na hidrogenação de ciclohexeno (TOF 125000 h^{-1}). O catalisador de Pd foi o catalisador mais seletivo para a hidrogenação de fenol em ciclo-hexanona, independente do suporte usado. A formação de ciclo-hexanol é favorecida pelo suporte de titânia e a hidrodesoxigenação para produzir ciclo-hexano ocorreu principalmente no suporte de sílica.

Palavras-chave: Catálise, suporte magnético, nanopartículas, sílica, céria, titânia, hidrogenação, paládio, ródio, rutênio e ouro.

ABSTRACT

Vono, L.L.R. *DESIGN OF NANOCATALYSTS SUPPORTED ON MAGNETIC NANOCOMPOSITES CONTAINING SILICA, CERIA AND TITANIA*. 2016. (205p) PhD Thesis – Graduate program in Chemistry. Instituto de Química, Universidade de São Paulo, São Paulo, Brazil and Université Toulouse III – Paul Sabatier, Toulouse, France.

Magnetic separation has received a lot of attention as a robust, highly efficient and rapid catalyst separation technology. Many studies have focused on developing methodologies for the immobilization of catalytic active species, but the development of magnetic supports has been mainly limited to silica, polymer or carbon-coated magnetic nanoparticles (NPs). The design of magnetic nanocomposites and the incorporation of other oxides are highly welcome to broaden the application of this separation technology in the field of catalysis. In this context, studies of the thermal stability of silica-coated magnetite ($Fe_3O_4@SiO_2$) were performed to evaluate the possibility of calcining it without losing the magnetic properties of the support. The calcination would permit the deposition of different oxides on the silica surface, such as ceria and titania. The calcined $Fe_3O_4@SiO_2$ material preserved the core-shell morphology and magnetic properties, but increased its surface area six times. New magnetic supports were developed by using post-coating process for the deposition of ceria and titania onto silica-coated magnetite. Magnetically recoverable Rh, Pd and Ru nanocatalysts were prepared. The catalysts were employed in hydrogenation of cyclohexene, benzene or phenol and the study of the influence of each support on the catalytic activity was a main objective of this thesis. The catalysts were prepared by two different approaches: the impregnation and the sol-immobilization of pre-formed metal NPs. The colloidal metal NPs were prepared by reduction of metal salts and also by decomposition of organometallic complexes. Rhodium catalysts prepared by impregnation of rhodium(III) chloride and reduction with H_2 showed some reproducibility issues that were surpassed by using $NaBH_4$ or hydrazine as reducing agents. The preparation of catalysts by the immobilization of colloidal NPs is an interesting alternative to obtain reproducible and very active catalysts. Nanoparticles of Pd, Rh and Ru were prepared by an organometallic approach and immobilized on calcined $Fe_3O_4@SiO_2$, $Fe_3O_4@SiO_2CeO_2$ and $Fe_3O_4@SiO_2TiO_2$. The elimination of the stabilizing agent leads to more active catalysts upon recycling. Rhodium catalysts supported on ceria support was the most active catalyst in the hydrogenation of cyclohexene (TOF 125,000 h^{-1}). Palladium catalysts were the most selective catalyst for the hydrogenation of phenol to cyclohexanone, no matter the support used. The formation of cyclohexanol is enhanced with titania and the hydrodeoxygenation to produce cyclohexane occurred mainly with silica.

Keywords: Catalysis, magnetic support, nanoparticles, silica, ceria, titania, hydrogenation, palladium, rhodium, ruthenium and gold.

RESUME

Vono, L.L.R. *ELABORATION DE CATALYSEURS SUPPORTES PAR DEPOT DE NANOPARTICULES METALLIQUES SUR DES COMPOSITES MAGNETIQUES CONTENANT DE LA SILICE, DE L'OXYDE DE CERIUM ET DE L'OXYDE DE TITANE*. 2016. (205p) Thèse de doctorat – Programme d'études supérieures en chimie. Instituto de Química, Universidade de São Paulo, São Paulo, Brésil et Université Toulouse III – Paul Sabatier, Toulouse, France.

Introduction

L'une des principales différences entre les catalyseurs homogènes et hétérogènes est la séparation du catalyseur des produits de réaction. En général, les catalyseurs hétérogènes sont assez facilement séparés, mais cela peut s'avérer parfois difficile en fonction de la granulométrie et de la densité du support de catalyseur et nécessiter le recours à des méthodes telles que filtration et centrifugation. De ce fait, la séparation magnétique a reçu beaucoup d'attention, offrant une technologie de séparation aisée, rapide et efficace du catalyseur solide. Par ailleurs, la séparation magnétique du catalyseur peut être effectuée sans le retirer du réacteur, évitant ainsi la perte de masse et l'oxydation due à l'exposition à l'air. La caractéristique essentielle pour un bon support magnétique est la propriété de superparamagnétisme. Le superparamagnétisme se caractérise par une aimantation à saturation élevée lors de l'application d'un champ magnétique et l'absence de magnétisation résiduelle lorsque le champ magnétique n'est plus appliqué. Des matériaux magnétiques massifs présentent une structure de multidomaines, mais lorsqu'ils sont préparés de façon à obtenir une taille de grains en dessous d'un diamètre critique, la formation d'un domaine unique est énergétiquement favorable. La magnétite (Fe_3O_4) est un matériau magnétique exploré pour plusieurs applications et est notamment très utilisés pour la séparation

magnétique de catalyseurs. Une caractéristique très importante pour un support de catalyseur est sa stabilité dans les conditions de réaction et l'encapsulation est l'une des stratégies pour atteindre cette caractéristique. De nombreuses études ont été focalisées sur l'immobilisation d'espèces actives catalytiques, mais le développement de supports magnétiques est souvent limité à des nanoparticules enrobées par du carbone, un polymère ou une silice. Par conséquent, l'élaboration de nanocomposites magnétiques incorporant d'autres oxydes que la silice apparait comme une voie intéressante pour élargir l'application de la technologie de séparation magnétique dans le domaine de la catalyse.

Préparation de supports magnétiques

Préparation et comportement thermique de particules de magnétite recouvertes de silice

Un nanocomposite constitué de particules de magnétite recouvertes de silice ($Fe_3O_4@SiO_2$) a été préparé par la méthode de micro-émulsion inverse, conduisant à des matériaux de haute qualité. L'influence de la durée de la réaction a été évaluée en prélevant des échantillons à différents temps de réaction typiquement: 1, 2, 6, 12, 24 et 48 h (figure 1a). Le matériau préparé en 6 h présente une taille de particules de 28,0 ± 2,0 nm (figure 1b).

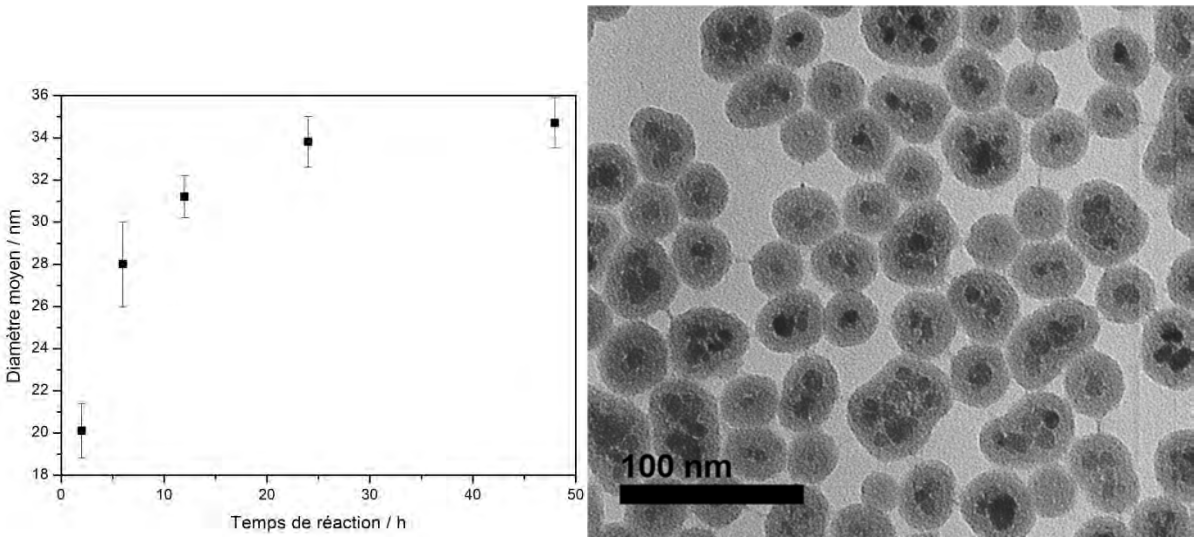

Figure 1. (a) L'influence de le temps de la réaction sur la taille des particules de $Fe_3O_4@SiO_2$ et (b) micrographie obtenue par MET.

Le comportement thermique a été évalué par thermogravimétrie (TG) et la calorimétrie à balayage différentiel (DSC). L'analyse par thermogravimétrie a montré que le résidu organique présent dans l'écorce de silice est principalement composé de tensioactif qui demeure après lavage (figure 2a). L'analyse par DSC a indiqué que l'écorce de silice protège les noyaux de magnétite contre l'oxydation (figure 2b). Après calcination sous air à 500 ° C pendant 2 h le matériau obtenu ($Fe_3O_4@SiO_2Cal$) a montré une morphologie et une taille de particules core-shell préservées. (figure 3) Les solides $Fe_3O_4@SiO_2$ et $Fe_3O_4@SiO_2Cal$ ont été caractérisés par diffraction des rayons X sur poudres et la comparaison des pics de diffraction de la magnétite montre qu'elle a été préservée.

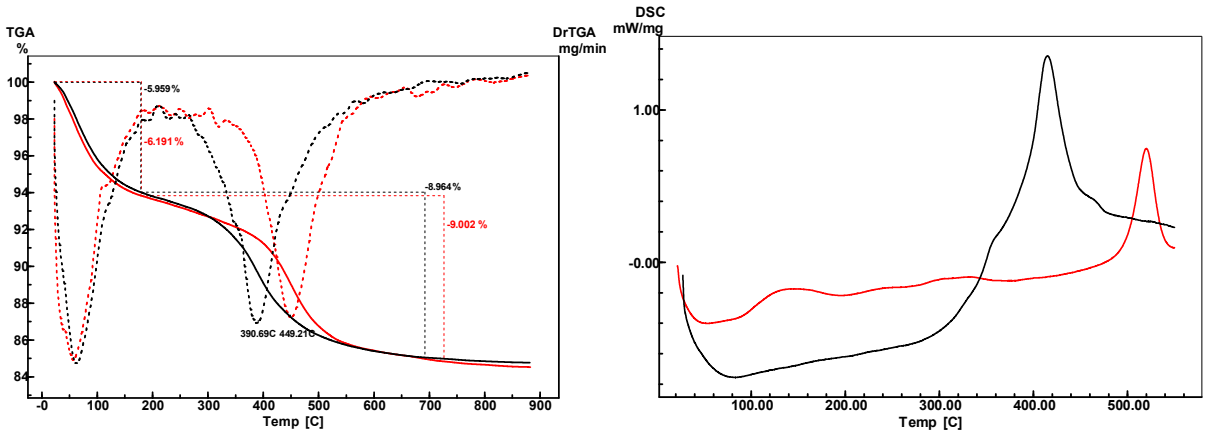

Figure 2. (a) TG (ligne solide) et DTG (ligne pointillés) obtenu avec l'énchantilion Fe_3O_4@SiO_2 sous l'air (noir) et azote (rouge). (b) DSC obtenues pour la magnétite pure (rouge) et de magnétite revêtues d'oxyde de silicium (noir).

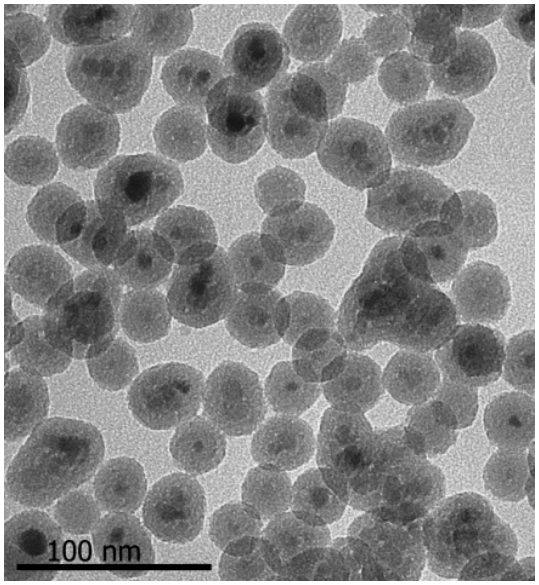

Figure 3. Micrographie obtenue par MET d'échantilion Fe_3O_4@SiO_2 aprés calcination.

Les mesures magnétiques ont montré que les deux matériaux sont superparamagnétiques et que l'aimantation à saturation est réduite à 13% après calcination (figure 4). La calcination a permis d'augmenter de 6 fois la surface spécifique. Ainsi, la calcination devrait permettre le dépôt de différents oxydes sur la surface de la silice, tels que l'oxyde de cérium et l'oxyde de titane.

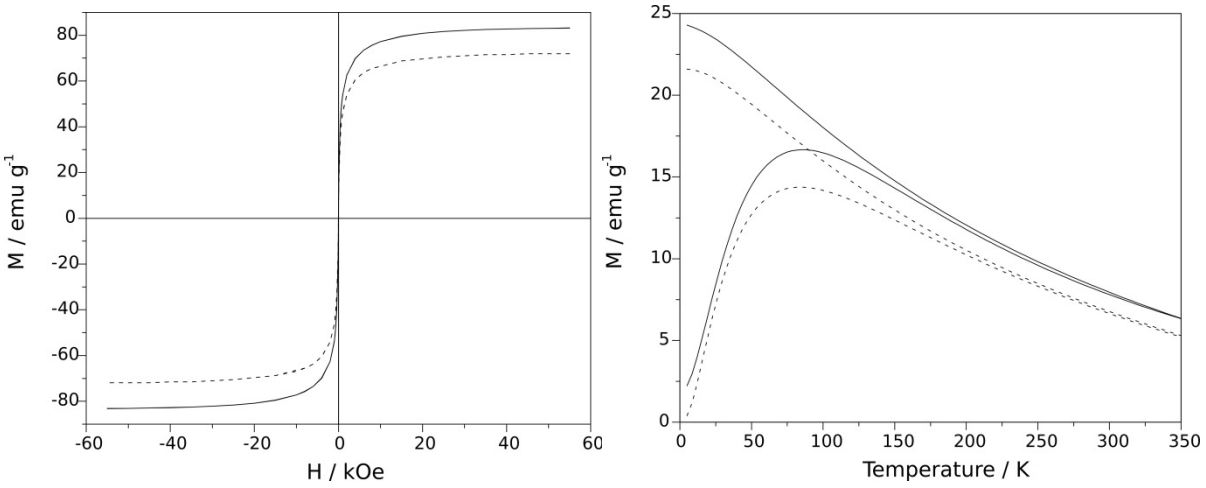

Figure 4. Mesures magnétiques de Fe_3O_4@SiO_2.

Post-revêtement avec d'oxyde de cérium ou d'oxyde de titane

Un processus de post-revêtement a été développé pour le dépôt d'oxyde de cérium et d'oxyde de titane sur Fe_3O_4@SiO_2. Malgré plusieurs tentatives, le dépôt de TiO_2 à la surface de Fe_3O_4@SiO_2 n'a pas pu être réalisé. Le dépôt de TiO_2 sur Fe_3O_4@SiO_2 a donc été effectué par modification d'une méthode décrite pour la préparation de composites « jaune d'œuf » conduisant au matériau Fe_3O_4@SiO_2TiO_2. Pour le dépôt de CeO_2 le solide Fe_3O_4@SiO_2 a été traité avec une solution de cérium (IV) et le sel solide a ensuite été séché pour obtenir Fe_3O_4@SiO_2CeO_2. Les solides Fe_3O_4@SiO_2TiO_2 et Fe_3O_4@SiO_2CeO_2 ainsi obtenus ont été calcinés sous air à 500 °C pendant 2 h. La caractérisation par microscopie électronique en transmission (MET) de l'échantillon Fe_3O_4@SiO_2TiO_2 (figure 5a) a montré que la morphologie cœur-coquille a été préservée et que le dépôt de TiO_2 a eu lieu principalement sous la forme de nanoparticules d'environ 5 nm. Le diffractogramme DRX enregistré pour Fe_3O_4@SiO_2TiO_2 n'a révélé que les pics de la magnétite, malgré la présence d'environ 8% en poids de TiO_2. Les clichés de microscopie électronique à haute résolution (MEHR) obtenus

pour les nanoparticules de TiO_2 ont montré une distance interplanaire de 3,71 Å correspondant au plan de Bragg (1 0 1) de la phase de titane anatase (figure 5b).

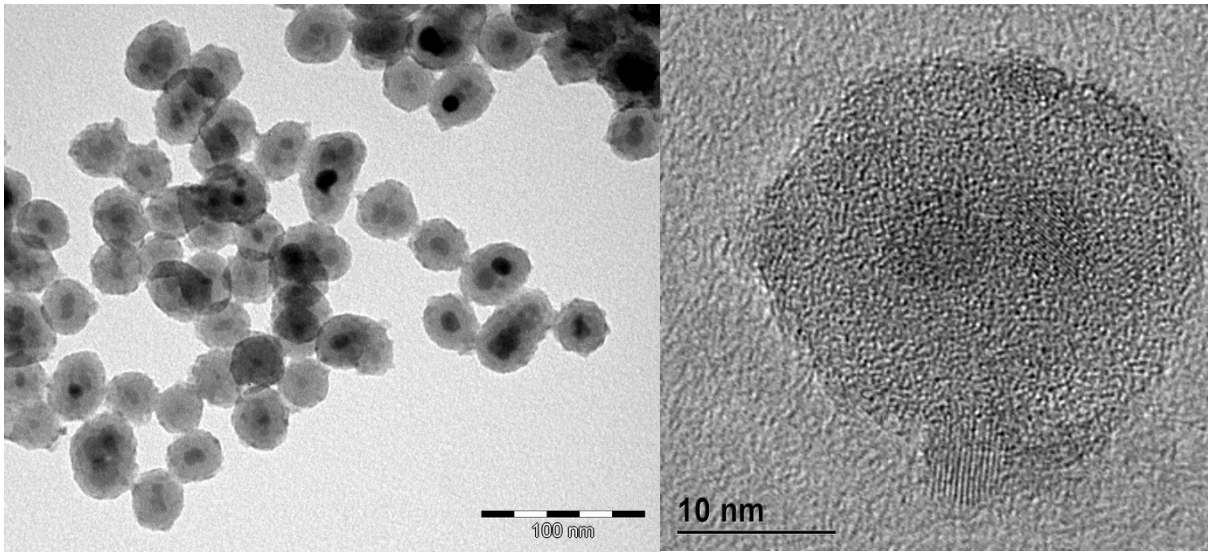

Figure 5. Micrographie de $Fe_3O_4@SiO_2TiO_2$ obtenu par (a) MET et (b) MEHR.

L'analyse MET de $Fe_3O_4@SiO_2CeO_2$ a montré le dépôt de nanoparticules de CeO_2 de 2,6 ± 0,4 nm à la surface du matériau initial (figure 6). Le diffractogramme DRX de $Fe_3O_4@SiO_2CeO_2$ a révélé la présence de pics correspondant à la magnétite d'une part et à l'oxyde de cérium (phase cubique) d'autre part. Sur les deux diffractogrammes un large pic lié à la silice amorphe est observé.

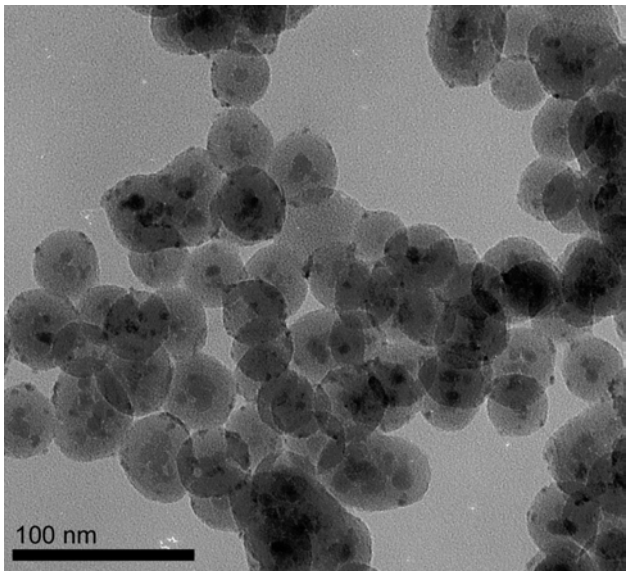

Figure 6. Micrographie obtenue par MET de $Fe_3O_4@SiO_2CeO_2$.

Les solides $Fe_3O_4@SiO_2$, $Fe_3O_4@SiO_2TiO_2$ et $Fe_3O_4@SiO_2CeO_2$ ont aussi été caractérisés par spectroscopie de photoélectrons X-ray. Les spectres XPS de tous les échantillons ont révélé la présence de pics de photoélectrons correspondant à C 1s, O 1s et Si 2p. Les pics de photoélectrons pour Ti 2p ont montré les composantes Ti^{4+} et Ti^{3+} mais augmentées de 0,7 eV, par rapport au TiO_2 massif. Les pics du Ce ont montré une augmentation de 2,1 eV, par rapport au CeO_2 massif. Le pic de photoélectrons O 1s montre deux composantes attribuées à SiO_2 massif et à des groupes Si-OH de surface. Par ailleurs, le dépôt d'oxyde de cérium et d'oxyde de titane augmente l'intensité de cette composante, ce qui peut être attribué à O résultant de CeO_2 et TiO_2.

Développement de catalyseurs magnétiquement récupérables

Catalyseurs de rhodium préparé avec trichlorure de rhodium (III)

Des nanocatalyseurs de rhodium (Rh) supportés ont été préparés par imprégnation d'un support $Fe_3O_4@SiO_2$ préalablement fonctionnalisé par des groupements amines ($Fe_3O_4@SiO_2NH_2$) avec une solution de trichlorure de rhodium(III). La réduction du Rh(III) en Rh(0) a été réalisée en utilisant le dihydrogène H_2, le borohydrure de sodium $NaBH_4$ ou l'hydrazine N_2H_4. Les catalyseurs préparés par réduction sous H_2 n'ont montré pas une bonne reproductibilité. La réduction par $NaBH_4$ a permis la préparation d'un catalyseur très actif dans l'hydrogénation du cyclohexène. Toutefois, il a été observé que l'activité de ce catalyseur est dépendante de la charge en métal (tableur 1), alors que les images MET ont révélé des nanoparticules de rhodium de tailles similaires. Les nanoparticules de Rh obtenues en utilisant l'hydrazine comme agent réducteur ont montré une taille de nanoparticules très proche de celle observée pour le catalyseur préparé avec $NaBH_4$. Cependant une différence majeure a été observée en ce qui concerne la dispersion des nanoparticules sur le support qui s'est avérée bien meilleure dans le cas du catalyseur préparé avec $NaBH_4$. L'activité catalytique en hydrogénation du cyclohexène obtenue pour le catalyseur préparé avec N_2H_4 (TOF = 48,700 h^{-1}) s'est révélée inférieure à celle du catalyseur issu de la réduction par $NaBH_4$. Par contre, le contraire a été observé pour l'hydrogénation du benzène: l'activité catalytique pour le catalyseur préparé par N_2H_4 (TOF = 1600 h^{-1}) est supérieure à celle déterminée pour le catalyseur obtenu avec $NaBH_4$ (TOF = 960 h^{-1}).

Tableur 1. L'activité des catalyseurs de Rh préparé pour imprégnation

Entrée	Rh (wt%)	Diamètre moyen (nm)	Temps (h)[a]	TOF (h^{-1})
1	0,1	2,8 ± 0,5	0,57	153190
2	0,5	2,2 ± 0,4	0,65	85440
3	1,0	3,1 ± 0,5	0,58	133300
4	1,5	2,8 ± 0,7	0,87	65469

[a] Cyclohexène (14,6 mmol), catalyseur (0,4 μmol de Rh), substrat/catalyseur = 35600, 75 ºC, 6 bar H_2. [b] Le temps de conversion complète (> 99 % conversion déterminé par CG). [c] Turnover frequency défini par mole de substrat consommé x mole de catalyseur introduit x temps de réaction (h) (obtenu à partir de la pente de la courbe d'hydrogénation dans la conversion < 20 %).

Un autre aspect de ce travail de thèse a consisté en la préparation de nanoparticules de rhodium stabilisées par le polyvinylalcool (PVA) pour obtenir des suspensions colloïdales de rhodium (Rh@PVA) (figure 7a). Pour ce faire, le trichlorure de rhodium(III) a été réduit par $NaBH_4$ en présence de PVA. La suspension colloïdale Rh@PVA ainsi obtenue s'est montrée très active pour l'hydrogénation du cyclohexène dans des conditions de catalyse biphasique, mais elle s'est avérée instable au cours du temps, la formation d'un précipité ayant été observée après la réaction. Les résultats de l'hydrogenation ont montré que la réaction était limitée par le transfert de masse. L'immobilisation de cette suspension colloïdale par imprégation sur le support $Fe_3O_4@SiO_2NH_2$ (figure 7b) a conduit à une meilleure stabilité du catalyseur et a permis plusieurs recyclages successifs pendant lesquels une augmentation drastique de l'activité catalytique a été observée.

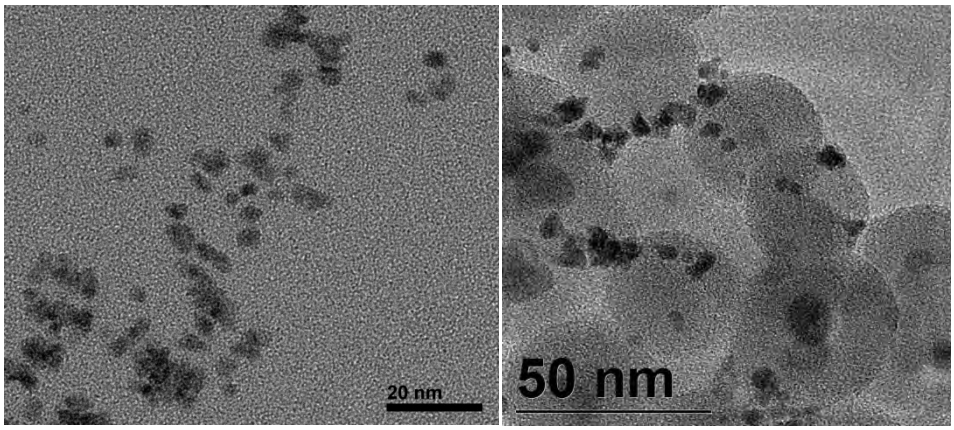

Figure 7. Micrographie obtenue par MET de (a) Rh@PVP NPs et de (b) $Fe_3O_4@SiO_2NH_2RhPVA$.

Catalyseurs de palladium préparé avec disodium tetrachloropalladate(II)

Des catalyseurs de palladium (Pd) supportés ont été préparés par imprégnation de différents supports ($Fe_3O_4@SiO_2$, $Fe_3O_4@SiO_2NH_2$, $Fe_3O_4@SiO_2CalNH_2$ et $Fe_3O_4@SiO_2Cal$) avec une solution de disodium tetrachloropalladate(II) suivie d'une étape de réduction par H_2. Les supports se sont avérés capables d'adsorber des ions Pd^{2+} sauf le support $Fe_3O_4@SiO_2Cal$. Le support sans fonctionnalisation ultérieure a montré une activité supérieure en hydrogénation du cyclohexène, mais au 5ème cycle catalytique, l'activité catalytique a été réduite à 63% de la valeur initiale (figure 8). Les catalyseurs obtenus avec les supports fonctionnalisés ont montré une activité catalytique similaire, mais l'activité de $Fe_3O_4@SiO_2NH_2Pd$ était plus constante. Cela pourrait être dû à la faible quantité de groupements amines sur ce support comparativement au système $Fe_3O_4@SiO_2CalNH_2$. Pour comparaison, des nanoparticules de Pd stabilisées par la polyvinylpyrrolidone (PVP) ont été préparées en chauffant au reflux une solution aqueuse de Na_2PdCl_4 en présence de PVP et d'éthanol, conduisant à une suspension colloïdale Pd@PVP-1 qui a pu être immobilisée sur

les mêmes supports. Toutefois, seuls les supports ayant des groupements amines en surface ont pu adsorber le métal. L'activité observée pour l'hydrogénation du cyclohexène en utilisant $Fe_3O_4@SiO_2CalNH_2$ comme support pour le Pd a été observée inférieure de 22% par rapport à celle du catalyseur préparé avec $Fe_3O_4@SiO_2NH_2$.

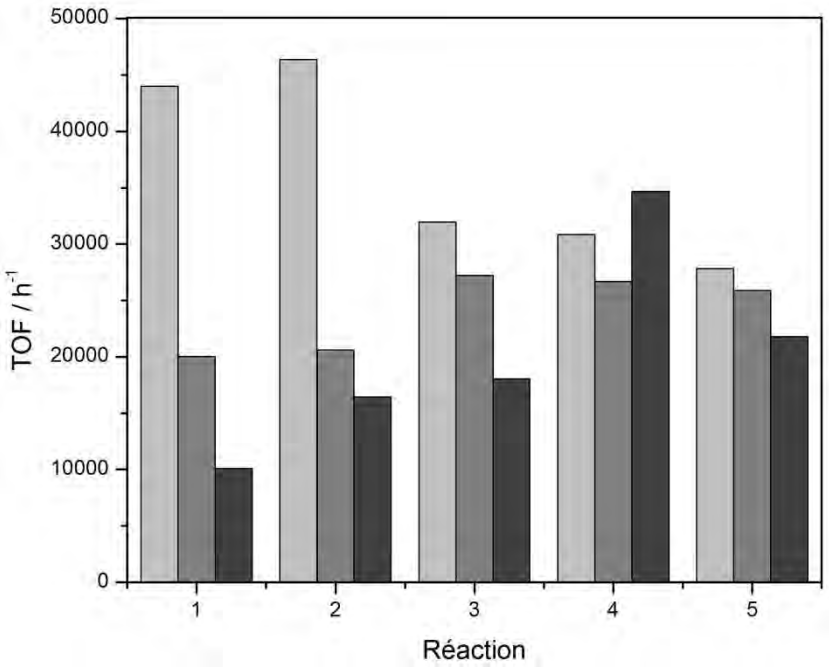

Figure 8. L'activité du $Fe_3O_4@SiO_2Pd$ (gris clair), $Fe_3O_4@SiO_2NH_2Pd$ (gris) et $Fe_3O_4@SiO_2CalNH_2Pd$ (gris foncé) dans l'hydrogénation du cyclohexène. Les conditions de réaction: 75 ºC, 6 bar H_2 et TON 10000.

Il résulte des résultats obtenus avec les catalyseurs préparés à partir de $Fe_3O_4@SiO_2$ que la préparation par imprégnation n'est pas triviale et que les caractéristiques du support peuvent avoir une forte influence sur l'activité du catalyseur.

Préparation de nanocatalyseurs à partir de précurseurs organométalliques

La préparation de nanoparticules métalliques à partir de précurseurs organométalliques est un procédé très prometteur du fait de l'obtention de surfaces métalliques très propres mis à part la coordination du ligand introduit comme stabilisant. Des suspensions colloïdales de Rh, Pd et Ru ont été stabilisées par la PVP. Elles ont été préparées en utilisant des précurseurs organométalliques $Rh(C_3H_5)_3$, Pd_2dba_3 ou Ru(COD)(COT) et la réduction avec H_2 réalisée en solution dans le THF. Les suspensions colloïdales ainsi obtenues sont constituées de petites nanoparticules métalliques bien dispersées dans la matrice polymère (figure 9) et leur immobilisation sur $Fe_3O_4@SiO_2Cal$, $Fe_3O_4@SiO_2TiO_2$ et $Fe_3O_4@SiO_2CeO_2$ a pu être effectuée directement à partir des suspensions dans le THF (figure 10).

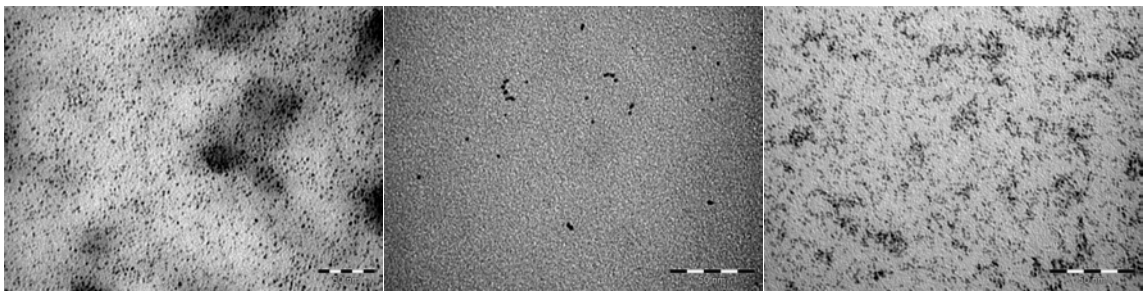

Figure 9. Micrographie obtenu par MET: (a) Rh@PVP, (b) Pd@PVP et (c) Ru@PVP.

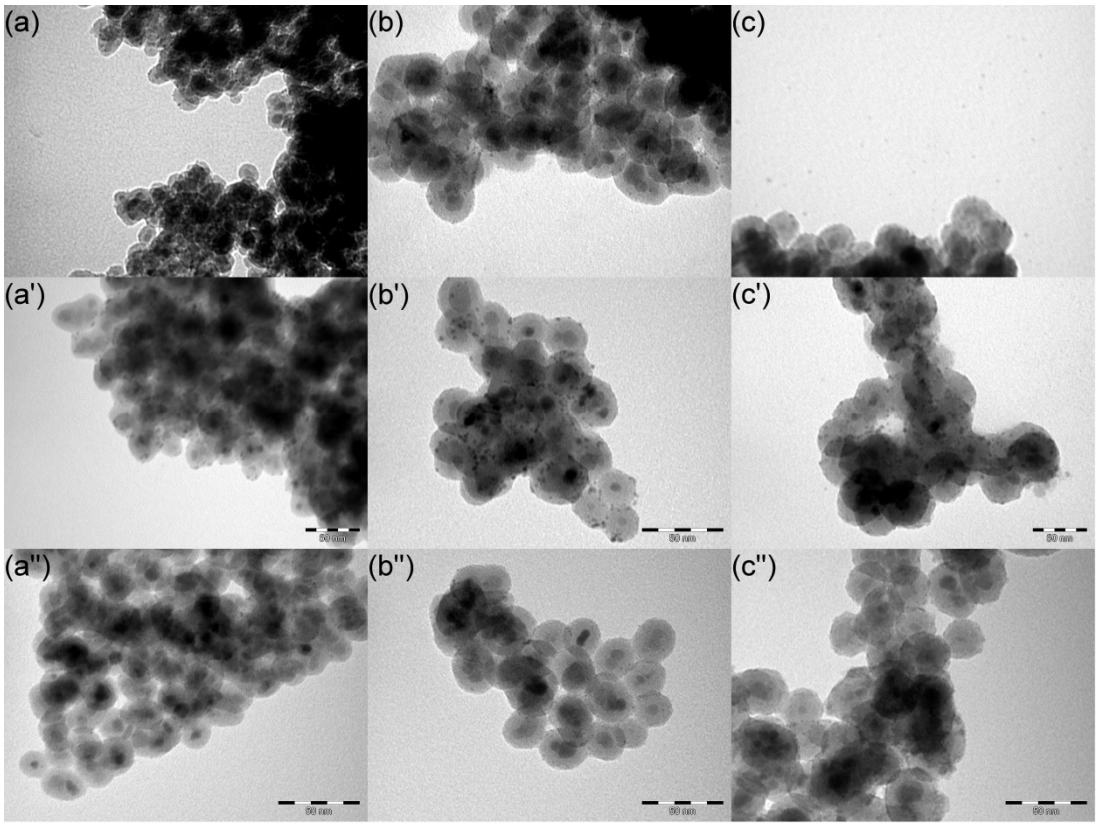

Figure 10. Micrographie obtenu par MET: (a) Rh@PVP, (b) Pd@PVP et (c) Ru@PVP NPs supporté sur (') $Fe_3O_4@SiO_2Cal$, (") $Fe_3O_4@SiO_2CeO_2$ et ("') $Fe_3O_4@SiO_2TiO_2$.

Les catalyseurs au Rh ainsi obtenus ont montré l'influence du support sur l'activité catalytique et l'utilisation du support $Fe_3O_4@SiO_2CeO_2$ a permis d'atteindre une activité catalytique plus élevée (TOF 125000 h^{-1}). Le catalyseur préparé avec l'oxyde de titane ($Fe_3O_4@SiO_2TiO_2$) a atteint une activité similaire, mais après plusieurs cycles catalytiques. Le catalyseur préparé avec la silice ($Fe_3O_4@SiO_2Cal$) a atteint une activité de 40% inférieure par rapport aux autres (figure 11). La température de conversion maximale pour l'hydrogénation en phase gazeuse du cyclohexène est en accord avec l'activité catalytique observée en phase liquide. Les catalyseurs de Pd ont montré un comportement différent et la meilleure combinaison avec de la silice pour l'hydrogénation en phase liquide, mais les températures pour l'hydrogénation en phase gazeuse a été la même pour tous les supports

(figure 12). La différence dans l'activité des catalyseurs Rh pourrait me connecté à PVP élimination.

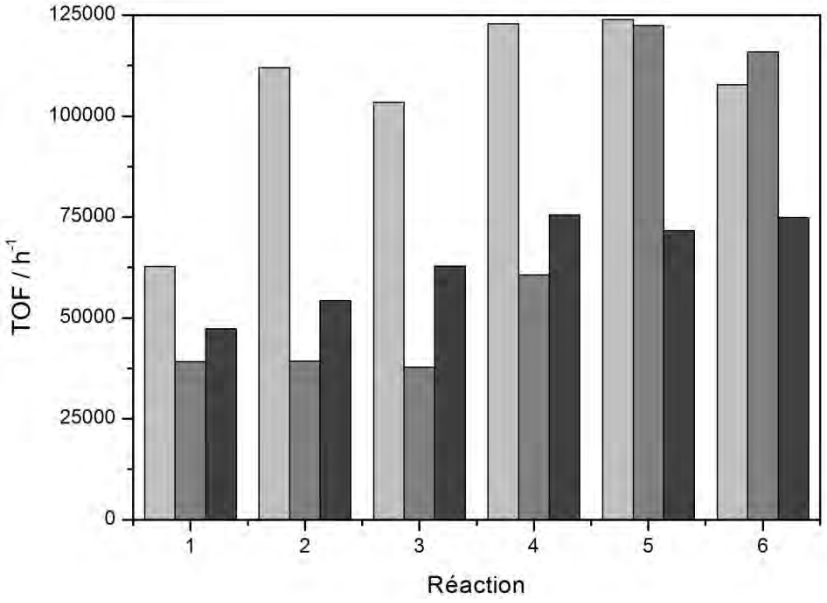

Figure 11. L'activité catalytique de Rh@PVP supporté sur Fe_3O_4@SiO_2CeO_2 (gris clair), Fe_3O_4@SiO_2TiO_2 (gris) et Fe_3O_4@SiO_2Cal (gris foncé) dans l'hydrogenation du cyclohexène. Les conditions de réaction: 6 bar H_2, 75 °C et TON = 35600.

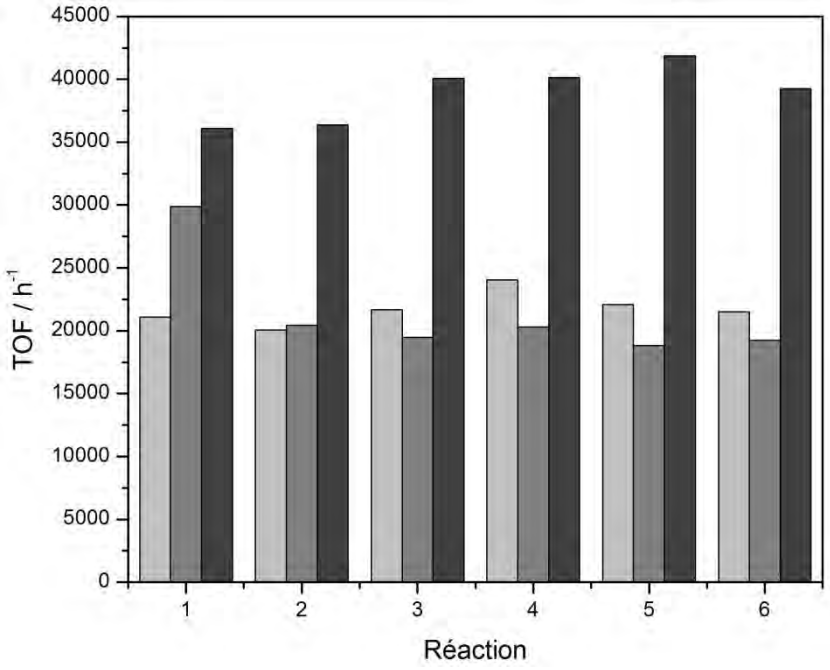

Figure 12. L'activité catalytique de Pd@PVP supporté sur Fe_3O_4@SiO_2CeO_2 (gris clair), Fe_3O_4@SiO_2TiO_2 (gris) et Fe_3O_4@SiO_2Cal (gris foncé) dans l'hydrogenation du cyclohexène. Les conditions de réaction: 6 bar H_2, 75 °C et TON = 10000.

Les catalyseurs préparés par immobilisation des nanoparticules obtenues par approche organométallique ont également été utilisés pour l'hydrogénation du phénol. L'utilisation de PVP comme agent stabilisant présente l'inconvénient de lixiviation dans des solvants polaires, comme les alcools et l'eau, c'est pourquoi l'hydrogénation du phénol a été menée en utilisant du n-hexane comme solvant. L'utilisation de n-hexane rend également inutile l'extraction des produits alors que c'est nécessaire avec l'eau. Les catalyseurs au palladium ont montré la plus grande sélectivité pour la formation de la cyclohexanone, indépendamment du support utilisé (tableur 2). Cependant, le support d'oxyde de titane a amélioré la conversion en cyclohexanol pour toutes les nanoparticules métalliques supportées (figure 13).

Tableur 2. L'hydrogenation du phénol en untilisant organométalliques NPs supporté.[a]

Entrée	**Catalyseur**	**Conv. (%)[b]**		**Selectivité (%)[b]**					
				Cyclohexanone		**Cyclohexanol**		**Cyclohexane**	
		2 h	**20 h**	**2 h**	**20 h**	**2 h**	**20 h**	**2 h**	**20 h**
1	Fe_3O_4@SiO_2CalPdPVP	94	100	90	82	6	12	4	6
2	Fe_3O_4@SiO_2CePdPVP	86	99	86	80	12	17	2	3
3	Fe_3O_4@SiO_2TiPdPVP	91	99	82	78	16	19	2	3
4	Fe_3O_4@SiO_2CalRhPVP	100	100	26	1	71	87	3	12
5	Fe_3O_4@SiO_2CeRhPVP	100	100	39	5	61	94	0	1
6	Fe_3O_4@SiO_2TiRhPVP	100	100	12	0	88	99	0	1
7	Fe_3O_4@SiO_2CalRuPVP	93	100	24	1	73	92	3	7
8	Fe_3O_4@SiO_2CeRuPVP	99	100	17	0	83	100	0	0
9	Fe_3O_4@SiO_2TiRuPVP	100	100	0	0	100	100	0	0

[a] Les conditions de réaction: phènol (75 μmol), solvant n-hexane (3 mL), catalyseur (36 mg, 3,7 μmol), et substrat/catalyseur = 20, 75 °C, 6 bar H_2. [b] Conversion et selectivité déterminé par CG.

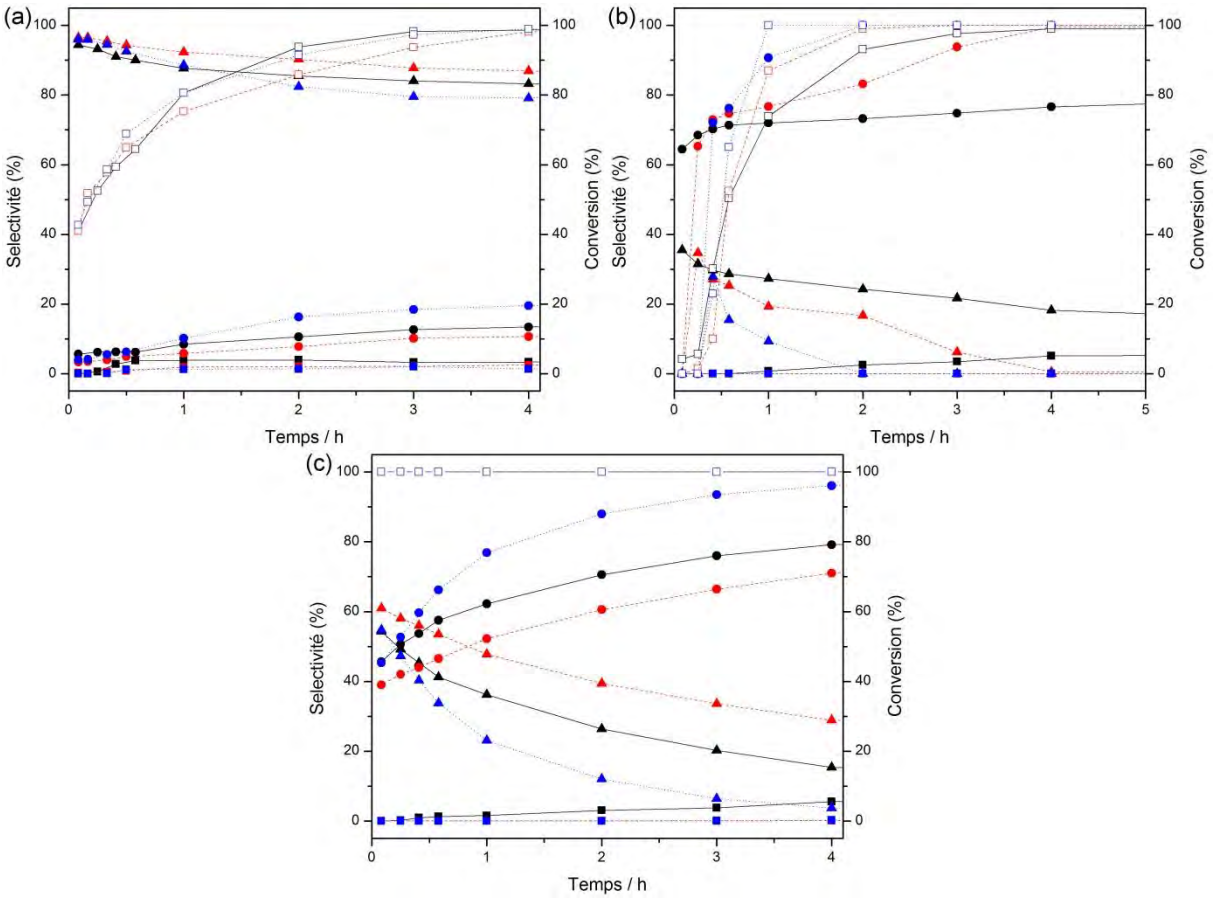

Figure 13. L'hydrogenation/hydrodesoxygénation du phenol en utilisant (a) Pd, (b) Ru et (c) Rh NPs supporté sur Fe_3O_4@SiO_2Cal (noir), Fe_3O_4@SiO_2Ce (rouge) et Fe_3O_4@SiO_2Ti (bleu). Conversion du phènol (carrés vides) et sélectivité pour cyclohexanol (cercles), cyclohexanone (triangles) et cyclohexane (carrés)

Une autre réaction qui peut se produire est l'hydrodéoxygénation conduisant à l'obtention de cyclohexane en tant que produit. La formation de cyclohexane a été observée principalement avec les supports de silice. Le catalyseur Fe_3O_4@SiO_2CalPdPVP, après un temps de réaction de 20 h, a montré une sélectivité en 12% en cyclohexane dans des conditions douces (75 °C et 6 bar H_2). Les catalyseurs au Rh ont montré une activité très élevée, ce qui a permis de réaliser la réaction avec un ratio substrat/catalyseur plus élevé (Figure 14). Toutefois, l'augmentation du ratio substrat/catalyseur a conduit à la modification de la sélectivité, tous les catalyseurs ayant montré une réduction de la sélectivité en cyclohexanol et la composition du cyclohexanol et de la cyclohexanone était d'environ 50%

pour chacun. La hydrodéoxygénation n'a pas été observée lorsque le rapport substrat/catalyseur a été augmenté.

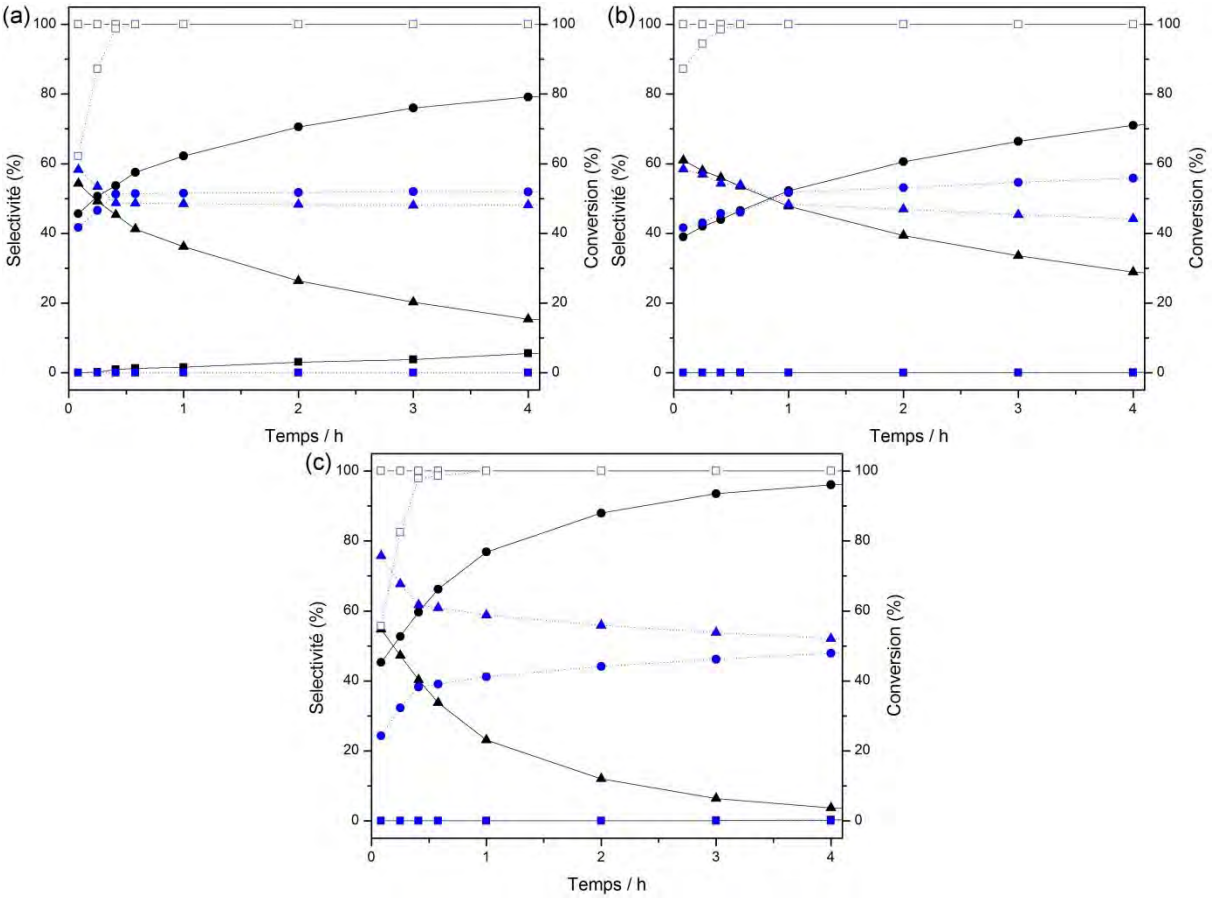

Figure 14. L'hydrogenation/hydrodesoxygénation du phenol en utilisant (a) Fe_3O_4@SiO_2CalRhPVP, (b) Fe_3O_4@SiO_2CeRhPVP et (c) Fe_3O_4@SiO_2TiRhPVP. TON = 20 (noir) et 200 (bleu). Conversion du phènol (carrés vides) and selectivité pour cyclohexanol (cercles), cyclohexanone (triangles) and cyclohexane (carrés).

Le catalyseur Fe_3O_4@SiO_2CalPdPVP a également été étudié pour l'hydrogénation du phénol sous 1 et 3 bar de H_2 à 55 ºC (figure 15). La formation de cyclohexène n'a pas été observée à des pressions inférieures à 6 bar de H_2. La conversion du phénol était également plus faible pour les pressions inférieures (16, 24 et 34% de 1, 3 et 6 bar H_2). Cependant, la pression n'a pas affecté la sélectivité de la formation du produit.

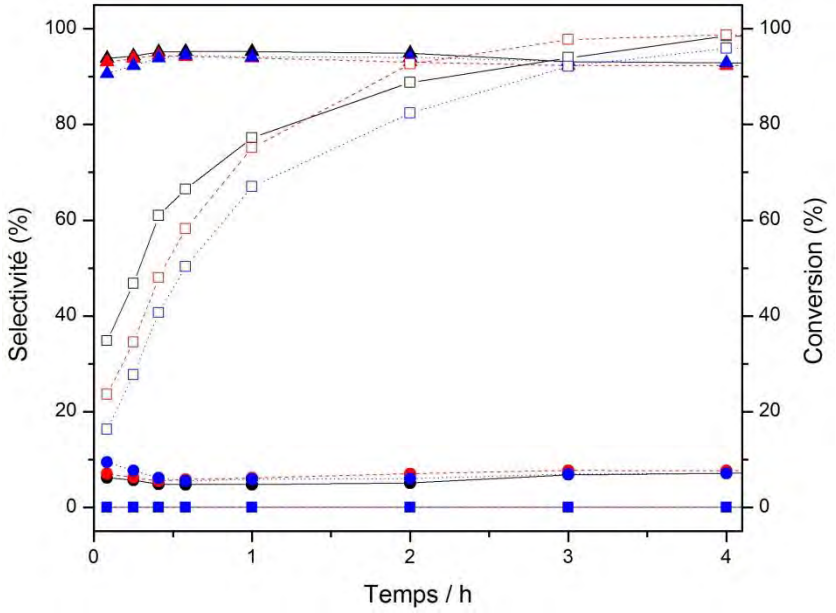

Figure 15. L'hydrogenation/hydrodesoxygénation du phenol en utilisant Fe_3O_4@SiO_2CalPdPVP. 6 (noir), 3 (rouge) et 1 bar de H_2 (bleu). Conversion du phènol (carrés vides) et selectivité pour cyclohexanol (cercles), cyclohexanone (triangles) et cyclohexanol (carrés).

Les catalyseurs de Pd ont été calcinés sous air à 300 °C pendant 2 h pour éliminer la PVP et évaluer l'hydrogénation du phénol en phase aqueuse (tableur 3). Le mélange réactionnel dans l'eau a montré 100 % de sélectivité en cyclohexanone. Seul le catalyseur avec de l'oxyde de cérium a conduit à 7 % de cyclohexane alors que celui avec de l'oxyde de titane a montré 100 % de conversion du phénol. Les catalyseurs au Pd calcinés ont montré une activité légèrement améliorée par rapport aux catalyseurs de Pd bruts. L'inconvénient de l'eau en tant que solvant est l'impossibilité de séparer magnétiquement les catalyseurs du fait de la plus grande affinité des supports avec l'eau.

Tableur 3. L'hydrogenation du phénol en untilisant Pd NPs supporté et calciné et l'eau or n-hexane comme solvant[a]

Entrée	Catalyseur	Conv. (%)[b]	Selectivité (%)[b]		
			cyclohexanone	cyclohexanol	cyclohexane
1	Fe_3O_4@SiO_2CalPdPVP[c]	79	100	0	0
2	Fe_3O_4@SiO_2CeO_2PdPVP[c]	70	93	0	7
3	Fe_3O_4@SiO_2TiO_2PdPVP[c]	100	100	0	0
4	Fe_3O_4@SiO_2CalPdPVP[d]	98	95	5	0
5	Fe_3O_4@SiO_2CeO_2PdPVP[d]	25	95	5	0
6	Fe_3O_4@SiO_2TiO_2PdPVP[d]	99	96	4	0

[a] Les conditions de réaction: phènol (75 µmol, in 3 mL [c] water ou [d] n-hexane), catalyseur (36 mg, 3,7 µmol) et substrat/catalyseur = 20, 75 °C, 6 bar H_2. [b] Conversion and selectivité déterminé par CG.

Mots clés: Catalyse, support magnétique, nanoparticule, silice, oxyde de cérium, oxyde de titane, hydrogénation, palladium, rhodium, ruthénium et or

LIST OF ABBREVIATIONS

APTES. (3-Aminopropyl)triethoxysilane
Au@PVP. Polyvinylpirrolidone stabilized gold nanoparticles
BE. Binding energy
BET. Brunauer-Emmett-Teller
COD. Crystallographic open database
DSC. Diferential scanning calorimetry
EDS. Energy-dispersive X-ray spectroscopy
FAAS. Flame atomic absorption spectroscopy
FC/ZFC. Field cooling/Zero field cooling
Fe_3O_4@SiO_2. Silica-coated magnetite
Fe_3O_4@SiO_2Pd. Palladium catalyst supported in Fe_3O_4@SiO_2
Fe_3O_4@SiO_2NH_2. Amino functionalized silica-coated magnetite
Fe_3O_4@SiO_2NH_2Pd. Palladium catalyst supported in Fe_3O_4@SiO_2NH_2
Fe_3O_4@SiO_2NH_2PdPVP-1. Pd@PVP-1 NPs supported in Fe_3O_4@SiO_2NH_2
Fe_3O_4@SiO_2NH_2RhPVA. Rh@PVA NPs supported in Fe_3O_4@SiO_2NH_2
Fe_3O_4@SiO_2Cal. Calcined silica-coated magnetite
Fe_3O_4@SiO_2CalPd. Palladium catalyst supported in Calcined silica-coated magnetite
Fe_3O_4@SiO_2CalNH_2. Amino functionalized calcined silica-coated magnetite
Fe_3O_4@SiO_2CalNH_2Pd. Palladium catalyst supported in Fe_3O_4@SiO_2CalNH_2
Fe_3O_4@SiO_2CalNH_2PdPVP-1. Pd@PVP-1 NPs supported in Fe_3O_4@SiO_2CalNH_2
Fe_3O_4@SiO_2CeO_2. Ceria deposited on silica-coated magnetite
Fe_3O_4@SiO_2TiO_2. Titania deposited on silica-coated magnetite
Fe_3O_4@SiO_2CalPdPVP. Pd@PVP NPs supported in Fe_3O_4@SiO_2Cal
Fe_3O_4@SiO_2CalRhPVP. Rh@PVP NPs supported in Fe_3O_4@SiO_2Cal
Fe_3O_4@SiO_2CalRuPVP. Ru@PVP NPs supported in Fe_3O_4@SiO_2Cal
Fe_3O_4@SiO_2CeO_2PdPVP. Pd@PVP NPs supported in Fe_3O_4@SiO_2CeO_2
Fe_3O_4@SiO_2CeO_2RhPVP. Rh@PVP NPs supported in Fe_3O_4@SiO_2CeO_2
Fe_3O_4@SiO_2CeO_2RuPVP. Ru@PVP NPs supported in Fe_3O_4@SiO_2CeO_2
Fe_3O_4@SiO_2TiO_2PdPVP. Pd@PVP NPs supported in Fe_3O_4@SiO_2TiO_2
Fe_3O_4@SiO_2TiO_2RhPVP. Rh@PVP NPs supported in Fe_3O_4@SiO_2TiO_2
Fe_3O_4@SiO_2TiO_2RuPVP. Ru@PVP NPs supported in Fe_3O_4@SiO_2TiO_2
FID. Flame ionization detector
FTIR. Fourrier transformed infrared spectroscopy
GC. Gas chromatography
ICDD. International Centre for Diffraction Data
ICP OES. Inductively coupled plasma optical emission spectroscopy
IF-USP. Instituto de Física da Universidade de São Paulo
IMP. Impregnation method for the preparation of supported metal nanoparticles
IQ-USP. Instituto de Química da Universidade de São Paulo
LCC-CNRS. Laboratoire de Chimie de Coordination du Centre National de la Recherche Scientifique

Pd@PVP. Polyvinylpirrolidone stabilized palladium nanoparticles
Pd@PVP-1. Polyvinylpirrolidone stabilized palladium nanoparticles prepared with Na_2PdCl_4
$Pd_2(dba)_3$. Tris(dibenzylideneacetone)dipalladium(0)
PVA. Polyvinyl alcohol
PVP. Polyvinylpirrolidone
Rh@PVA. Polyvinyl alcohol stabilized rhodium nanoparticles
Rh@PVP. Polyvinylpirrolidone stabilized rhodium nanoparticles
Ru(COD)(COT). (cyclo-octadiene)(cyclo-octatriene)ruthenium(0)
Ru@PVP. Polyvinylpirrolidone stabilized ruthenium nanoparticles
SI. Sol-immobilization method for the preparation of supported metal nanoparticles
SQUID. Superconducting quantum interference device
TEM/HRTEM. Transmission electron microscopy/High resolution transmission electron microscopy
TEO. Titanium(IV) 2-ethylhexyloxide
TEOA. Triethanolamine
TEOS. Tetraethoxysilane
TG/DTG. Thermogravimetry/derivative thermogravimetry
THF. Tetrahydrofuran
TOF. Turnover frequency
TON. Turnover number
TTIP. Titanium(IV) isopropoxide
XRD. X-ray diffraction

LIST OF FIGURES

LIST OF TABLES

INDEX

1. INTRODUCTION

1.1. Nanocatalysis

The transformation of raw materials into countless valuable chemical products involves catalytic processes in at least one step. Catalysis is not only a tool for the chemical industry, but is also considered as a key to solve environmental challenges, mainly related to energy production and consumption and to waste minimization or prevention.[1] Catalysis is one of the 12 principles of green chemistry[2] and can be directly related to the principles of atom economy, design for energy efficiency and derivatives reduction.

Traditionally, catalysis is divided in two major groups: homogeneous and heterogeneous catalysis. Homogeneous catalysis is defined by the presence of catalyst and substrate in the same phase and soluble molecular and ionic compounds are used as catalysts. On the other hand, heterogeneous catalysis is defined by the presence of catalyst and substrate in different phases. Typically in the heterogeneous catalysis, metals and metal oxides are used as catalysts. Due to the different phases, the separation of heterogeneous catalysts from the products is easier and more effective when compared to homogeneous catalysts. Homogeneous catalysts may require solvent addition, distillation and other time and energy consuming procedures. However, homogeneous catalysts are more selective and more active than heterogeneous catalysts. Even though, homogeneous catalysts are less interesting for industrial processes than heterogeneous catalyst due to the onerous separation, the increase in the regulation of trace amounts of catalytic moieties in commodity chemicals and pharmaceutical products, and the typical higher price.[3]

The effort to surpass the disadvantages of homogeneous catalysis and to integrate the advantages of heterogeneous catalysis brought the attention of the catalysis research to nanocatalysis. The term nanocatalysis adopted by the literature corresponds to application of nanoparticles as catalysts. For example, bulk gold does not show catalytic activity, but when reduced to nanoscale (less than 20 nm) gold nanoparticles act as a remarkable catalyst for diversified reactions.[4] A typical example of the gold nanoparticles catalytic activity is the CO oxidation demonstrated by Haruta.[5] The remarkable activity and selectivity of metal and metal oxide nanocatalysts are basically related to two effects: the size effect and the electronic effect.

The size effect is considered because there is a huge increase of surface area with the reduction of bulk metals to nanoscale. This means also that the amount of corner and edge atoms, with lower coordination number, are increased in the nanoscale. The metal atoms with low-coordination number in a solid metal structure are often responsible for the active sites of the catalyst.[6]

The electronic effect is mainly related to the surface stress. With the reduction of the bulk metal to nanoscale arises a surface stress that corroborates to an increase of broken bonds of surface atoms when compared to the bulk, resulting in an increase of surface energy that is not negligible. The surface stress also contributes to the decrease of the lattice parameter by inducing a pressure towards the center of the nanoparticle. Then, in many cases the equilibrium shape of a nanoparticle does not correspond to the equilibrium shape of the bulk material, and as consequence different facets are displayed in the nanoparticle. The outcome induced by the surface stress directly influences the electronic band structure: the valence band is reduced and its center of gravidity is shifted on the way to the Fermi level. These changes in electronic band structure affect directly the chemisorption of the substrate on the surface of the catalyst in a catalytic process, resulting in different activity and selectivity as

compared to the bulk catalyst.[7] Even though the size effect is related to the enhancement of surface area, the electronic effects are also connected with nanoparticle size, since the surface stress is proportional to the nanoparticle size and morphology. As a result, the variation of nanoparticle size and shape also affects their catalytic performance, which opens a huge possibility of studies in this area.[8]

1.1.1. Structure and size sensitive and insensitive reactions

The idea of size reduction in order to maximize the surface area to obtain more surface metallic atoms can suggest higher activity, once there is more metal able to interact with substrate. However, this is not always true. It is clear that we have a inumerous combination of catalyst, substrate and type of reaction, but those combinations will resume into three main groups: size-insensitive, negative and positive size-sensitive reactions.[9] These groups are characterized by the behavior of the turnover frequency (TOF, mol substrate converted per mol (normalized by surface atom) catalyst per time) as function of particle size. The size-insensitivity is characterized by the independence of TOF with nanoparticle size. The positive size-sensitivity is observed when the TOF increases with the decrease in nanoparticle size and the negative size-sensitivity observed when the TOF decreases.[9-10]

The size-sensitivity dependence is related to the particle surface characteristics, because the chemical properties of the substrate bond that needs to be activated will determined the characteristics of surface atom where the lowest activation energy can be achieved.[10] For the formation or dissociation of π-bond there is a step-edge atom dependence, which leads to negative size-sensitivity due to the reduction of this type of atom on particle surface with decrease in particle size.[9] On the other hand, reaction where the cleavage of σ C-

C bonds is limiting typically shows a positive size-sensitivity.[9] The hydrogenation of hydrocarbons is typically size-insensitive reactions.[10] On the same way of nanoparticle size, the nanoparticles structure can also play a role in the characteristic of size-sensitivity because some structures can result in the presence of more surface atom of certain type.[9-10]

1.2. Nanocatalyst

The efforts to develop nanocatalysts started from the initial observations made by different research groups concerning the advantages of using nanoparticles as catalysts:[11]

1) The possibility of the size and shape control of the nanoparticles by preparation conditions;
2) Colloidal metal nanoparticles can be dispersed in solution like homogeneous catalyst acting in mild conditions (temperature below the boiling point of the solvent);
3) Colloidal metal nanoparticles can be explored as photocatalysts;
4) Metal nanoparticles can be functionalized promoting different catalytic activity;
5) A huge variety of bimetallic and trimetallic nanoparticles with different composition can be studied;
6) Supported nanocatalysts can be used in gaseous phase reaction;
7) Colloidal and supported metal nanoparticles are commonly more active and selective than conventional industrial catalysts.

Nanoparticle catalysts have already been used successfully in hydrogenation, oxidation, C-C coupling, H_2 generation, hydrogenolysis, water splitting and photocatalysis reactions, among others. Also, nanocatalysts have been efficient for production of biofuels.

Their large applicability in increasingly explored green conditions turned nanocatalysts strong candidates to create new sustainable pathway for chemical processes.[3b]

Nanocatalysts can be used in their colloidal form or as supported nanoparticle catalysts. Usually colloidal nanoparticles are dispersed in a liquid phase and will have limited thermal stability. The liquid phase can be a homogeneous or a heterogeneous mixture with the substrate. Typically, the synthesis of colloidal nanoparticles requires a metal precursor, a reducing agent, a stabilizing agent and a solvent. The ability to disperse nanoparticles in the reaction media, the control of their size and shape can be tuned by choosing the stabilizing agent (polymer, surfactant, charged compounds, organic ligands, etc.), which makes the choice of this reactant extremely important to the design and performance of colloidal nanocatalysts.[12] The reducing agent can be replaced for some reactant or condition that destabilizes the metal precursor, for example, when the metal precursor is a zero valance organometallic compound.[13]

Generally, the colloidal nanoparticles are synthesized, purified and suspended in the reaction media. Depending on the reaction conditions, colloidal nanoparticles are easy deactivated by sintering, morphological changes and leaching.[14] Colloidal metal nanoparticles can also show some deactivation due to destabilization of the colloidal suspension.[15] Therefore, supported nanoparticles are more versatile when used as catalyst to a variety of reactions because of the easy recovery and enhanced stability. Supported nanoparticles can be successfully explored in a larger range of reaction conditions than colloidal nanoparticles, which can enlarge their applicability as catalyst.

1.2.1. Supported nanocatalysts

Catalysis by supported metal nanoparticles is somehow more complex because of the support, which can present some effects in the catalytic activity. These effects are linked to the interactions of the metal nanoparticles and the reactants with the support, which can direct the catalytic process to different ways of selectivity and activity. The most important effects of support and metal particle interaction are the reverse-spillover and the morphology and edges.[7]

Reverse-Spillover effect is known as the diffusion of molecular species from the metal surface to the support surface. The reverse-spillover is the most known phenomenon in heterogeneous catalysis and corresponds to the inverse of spillover: the diffusion of adsorbed molecular species from the support to the catalyst particles. This phenomenon provides a different way for chemisorption of reactants on the metal particle surface that can be energetically more favorable. The structures of the support surface and support defects are extremely important to reverse-spillover effect. In some cases, a step of the reaction can occur previously on support surface followed by diffusion of intermediaries to the metal nanoparticles. The addition of promoter on the support may also influence the reverse-spillover effect.[16]

The Morphology and Edges effect is more related to structure sensitive reactions, as for example, the reduction of NO by CO on Pd that occurs preferably over the plane (1 1 1) of Pd nanoparticles. The high bind energy of CO on Pd edges at low coverage is also an example of structure sensitivity. The supported nanoparticles have the disadvantage (or advantage) of having a part of its structure encapsulated by the support, not being available for catalysis. The resulting encapsulation of the metal nanoparticle by the support is defined as “Strong Metal-Support Interaction (SMSI)” and is used to explain the decreased chemisorption

capacity for CO and H_2 on supported metal particles on oxides after heating treatment.[17] The SMSI depends on the nature of the oxide support and also contributes for the decrease of sintering of nanoparticles, which is an advantage compared to colloidal nanoparticles. For example, Ag particles are more strongly attached on CeO_2 and Fe_3O_4 (1 1 1) surfaces than on MgO (1 0 0), which means that the undesired sintering of nanoparticles occurs easily on MgO (1 0 0).[18]

The dependence of the catalytic activity with the nanoparticle morphology and support structure requires the rigorous control of their size, shape and composition in order to ensure the reproducibility of their properties and also of the results for a given application. In that context, nanoparticles studies are of interest only if their synthesis is reproducible with a well-defined or tunable size and morphology. The variety of nanocatalysts presented in the literature seems wide, but the synthetic process is not simple. Both colloidal and supported nanoparticles are not the thermodynamically stable form of a metal aggregate. Thus, their synthesis has to be kinetically controlled, with the help of stabilizing agents. The synthesis of supported nanoparticles with a narrow size distribution and good dispersion is still a challenge in the field of nanocatalysis.

1.2.2. Synthesis of supported nanocatalysts

The preparation of supported metal nanoparticles can be achieved by physical, chemical or physicochemical approaches. In the physical approach, also known as the top-down-type method, the supported nanoparticles are prepared from bulk metal treatment in the presence of a support. The treatment of the bulk metal can be done with techniques that provide energies higher than the bond energy of metal as mechanical force, vaporization or

laser ablation, for example. The Physical Vapor Deposition, that includes sputtering deposition method, was originally developed for the production of thin films, but was later adapted for the deposition of metal nanoparticles on liquid (ionic liquids, silicon oil and vegetable oils) and solid substrates.[19] In the chemical approach, also known as bottom-up-type method, metal ions are reduced to metal atoms,[11] that aggregate to form metal nanoparticles. The aggregation occurs in two steps: nucleation and growth.[20] The physicochemical approach involves a combination of the physical and chemical approaches. A good example is the sonoelectrochemistry method that is a combination of sonochemistry (physical) and electrochemistry (chemical).

This thesis will focus exclusively in the preparation of supported metal nanoparticles by chemical approaches. There are innumerous chemical methods to prepare supported metal nanoparticles, among then the impregnation (IMP), sol-immobilization (SI), co-precipitation (CP), deposition-precipitation (DP), deposition-reduction (DR), microemulsion, photochemical, chemical vapor deposition (CVD) and electrochemical reduction (ER) can be highlighted.[21] Figure 1.1 shows a schematic illustration of the different methods mentioned for the preparation of supported metal nanoparticles.

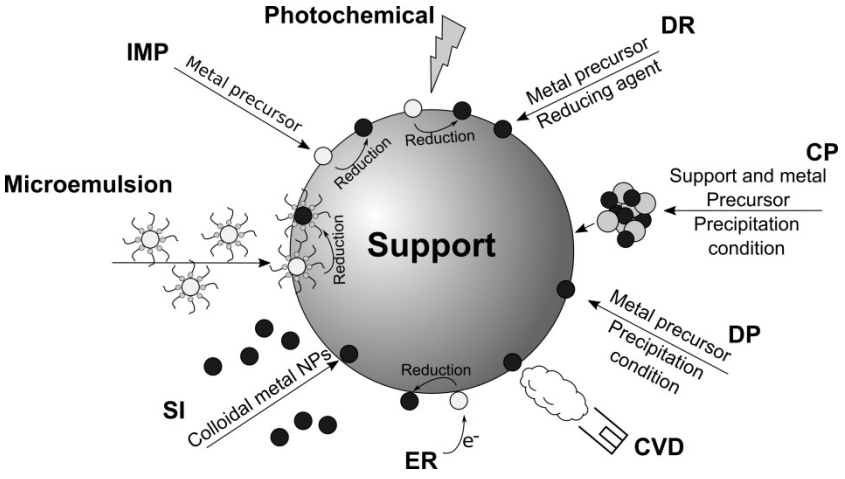

Figure 1.1. Illustration of different preparation methods of supported metal nanoparticles. Adapted from Okumura *et al.*[22].

The impregnation (IMP), also called incipient wetness impregnation or dry impregnation, is the most used synthetic approach to prepare supported nanocatalysts. It consists in the mixture of a metal precursor solution and the support, followed by the removal of the solvent with rotary evaporator or centrifugation.[21a] Then, the metal loaded solid is submitted to a reduction process which can be a reducing agent solution or thermal reduction. If previously to the metal reduction the solid was washed to remove the excess of metal, the metal loading will depend strongly on the affinity of the metal ion with the support. The improvement of this affinity can be done by the functionalization of the support surface with organic ligands that can be further removed by calcination. However, if the ligand is not removed, it can also have an influence the catalytic activity of the supported metal.[23]

In the co-precipitation (CP) method, the support and the metal ions precipitation occurs at the same time and is followed by reduction.[21a] As a result, it is possible to obtain metal nanoparticles immersed on the support matrix, and the catalytic activity will depend strongly on the support's porosity. In some cases, the metal ion can interfere on the polymerization or condensation reaction of the support formation. This influence can lead to a non-desirable material, which will hardly result in a good nanoparticle dispersion and narrow size distribution. An interesting modification of this method is the precipitation of the support in the presence of preformed metal nanoparticles.[24] In this way, the preparation of desired materials can be easily achieved, because the size and morphology of the metal nanoparticles were previously controlled in the colloidal synthesis.

The Deposition-precipitation (DP) method was first reported by Haruta *et al.*[25] It consists in preparation of a solution containing the solubilized metal precursor and the support precursor followed by slow precipitation of the support by pH adjustment and reduction of the metal precursor by subsequent calcination process. However, the precipitation-deposition

presents the same problems of size control and dispersion as found for the co-precipitation method.

The Deposition-Reduction (DR) method consists in the direct reduction/decomposition of the metal precursor over the support. This methodology was used for the reduction of metal complexes by the addition of $NaBH_4$ over the support in liquid phase.[26] A modification of this method consists in the decomposition of organometallic precursors by hydrogen over the support in liquid phase conditions.[27]

In the microemulsion method the metal precursor is solubilized in a homogeneous mixture of water, oil and surfactant. Then the solid support is impregnated with the microemulsion containing the metal ions similar to the impregnation approach.[28] Finally, the solid containing the metal ions is submitted to metal reduction step. The nanoparticles obtained by this methodology have demonstrated a good dispersion and good size and morphology control. The explanation can be given by the impregnation of the entire micelles of the microemulsion that confines determined amount of metal ions delimiting the nanoparticle growth. The affinity of the micelles by the support can be improved by increasing the hydrophobicity of the support.

The photochemical method is considered an environmentally friendly process because it minimizes the use of reactants. It consists in the photodecomposition of the metal precursor over the support to form supported metal nanoparticles.[29] However, this methodology requires photosensitivity metal precursors.

The Chemical Vapor Deposition (CVD) has shown to be a controlled and reproducible approach to promote well-dispersed metal nanocatalysts. The procedure is accomplished by the vaporization of metals and growth of the metal nanoparticles under high vacuum.[30]

The electrochemical reduction approach consists in the electrochemical deposition of metal nanoparticles on the support. Generally a solution containing the metal ions and the

support are kept under stirring during electrolysis, resulting in the formation of supported nanocatalysts.[21a] The presence of the stabilizing agent or/and a support is important to prevent metal deposition on electrode surface.

Considering all the advances in the preparation of colloidal metal nanoparticles and the multiple strategies and possibilities to achieve the highly desired size, shape and composition control (during the nanoparticles synthesis in liquid phase and by choosing the metal precursors, stabilizers and reducing process), the immobilization of pre-formed nanoparticles on solid supports has received attention as a versatile strategy to prepare supported catalysts.[12a] This approach, also called sol-immobilization (SI) method,[31] has been shown as a successful alternative to improve the dispersion, size and morphology control of supported nanoparticles. The properties of the colloidal nanoparticles, such as size and size distribution, are retained when the nanoparticles are immobilized on the support. The immobilization of colloidal nanoparticles occurs typically by the interaction of the support surface with metal surface or with the colloidal nanoparticle stabilizing agent. The affinity of the support for colloidal nanoparticles can be tuned by the support surface functionalization[23] or changing the characteristics of the nanoparticle stabilizing agent.

The aqueous phase reduction of metal salts by $NaBH_4$ in the presence of polyvinyl alcohol (PVA) has been very often used for the preparation of colloidal nanoparticles to achieve supported catalysts by SI method.[31] This very simple method provides metal particles suitable for catalytic application and is possible to remove the excess of PVA.[32] Another route to prepare colloidal metal nanoparticles for the SI method is the decomposition of organometallic complexes. Generally, olefinic complexes and other metal-organic complexes can be decomposed by reaction with of H_2 or CO leading to hydrogenation or decoordination of the ligands present in the coordination sphere of the metal. The decomposition of the organometallic complexes results in free metal (0) atoms that tend to aggregate to form the

metal bulk. However, if the decomposition is accomplished in presence of a stabilizing agent the aggregation is controlled and nanoparticles are formed.[33]

The organometallic approach is known as an advantageous methodology to the preparation of metal nanoparticles because it permits to obtain nanostructures with well-controlled size, dispersion, chemical composition and morphology. Despite disadvantages related to the laborious synthesis of the organometallic precursors and their sensitivity to air and moisture of some complexes, this method allows the preparation of nanomaterial of high quality and, in the case of catalysis, which may presents remarkable activity due to a cleaner surface state.[33-34]

1.2.3. Catalytic activity of supported nanocatalysts

The choice of the support is very important because the nanocatalyst activity, selectivity and metal dispersion can be modified due to the influence of the support. One of the most important steps for selecting a support is the chemical and thermal stability at the reaction conditions. The most commonly used supports are alumina, silica and carbon. However, carbon, graphene, titania, zinc oxide, zirconia, zeolites, magnesia and silicon carbide have particular properties that are explored in specific reactions mainly as multifunctional catalysts.[21a, 35] For example, TiO_2 has photocatalytic activity that allied to some metal nanoparticles as co-catalysts can result in a miniature photoelectrochemical cell and this combination acts as catalyst for photocatalytic water splitting.[36] Magnesia presents basic properties that can substitute the addition of base in reactions that needs basic media as for example, the oxidation of benzyl alcohol by gold supported on basic supports.[37]

The catalytic activity of supported nanocatalysts is explored in a huge variety of reactions and conditions, which makes impossible the description of every application described in the literature. Thus, the description below will focus on hydrogenation reactions using supported Pd, Rh and Ru nanoparticles, which are related to the results presented in this thesis. Hydrogenation reaction consists in the incorporation of molecular hydrogen to a molecule in the presence of a catalyst. Cyclization and isomerization that occur under H_2 conditions are also considered as hydrogenation reactions. This reaction is present in very important industrial process, as hydrogenation of fat oils, production of organic compounds, transformations of functional groups as for example the hydrogenation of nitro to amino groups. Particularly, stereoselective hydrogen addition is very important for the pharmaceutical industry. The selective reduction by H_2 is much explored for purification processes as the selective reduction of acetylene in the production of ethene. Other reduction methods as hydrogen transfer, metallic hydrides, hydrazine and electrolysis for example can be used as alternatives for the catalytic hydrogenation with hydrogen.[38]

The metal nanoparticles have shown to be much more active for hydrogenation reaction than single crystals.[39] The hydrogenation on metal surface occurs *via* chemisorption of the hydrogen and the substrate to be hydrogenated. The chemisorbed substrates have their bonds weakened allowing the incorporation of hydrogen to the substrate. So, it is important that the hydrogen atoms have easy diffusion on metal surface. Generally, the hydrogen is bonded weakly to metal subsurface, and these atoms are responsible to participate in the hydrogenation. Studies made with palladium showed that the subsurface hydrogen in metal nanoparticles is more accessible than those in single crystals, which can explain why nanocatalysts are more active than their bulk counterparts in hydrogenation reactions.[39]

The following subsections will give an overview of some examples reported in the literature for catalysis by supported Pd, Ru and Rh nanoparticles in hydrogenation reactions.

1.2.3.1. Supported Palladium nanocatalysts

Palladium is the most explored noble metal in catalysis due to its very broad application. The easy chemisorption of CO, O_2, H_2, and several functional groups makes Pd a very interesting choice for catalysis. However, Pd high activity for different reactions has the disadvantage to make Pd not very selective. The literature reports several Pd catalysts supported in different materials for hydrogenation reactions.

Silica is one of the most common inorganic supports used for Pd nanoparticles. Domínguez-Quintero *et al.*[40] reported high catalytic activity of Pd nanoparticles supported on silica in hydrogenation reactions. The authors demonstrated the preparation of 1.9 nm Pd nanoparticles by the decomposition of the organometallic palladium(II) bis-dibenzylidene acetone on commercial silica gel. The catalyst was very active in the hydrogenation of 1-hexene, cyclohexene, benzene, 2-hexanone, cyclohexanone and benzonitrile, reaching the highest hydrogenation rate of 38,250 $mol_{product}$ $mol^{-1}{}_{metal}$ h^{-1} for hydrogenation of 1-hexene at 25 ºC and 30 psi H_2.

The selective hydrogenation of 3,3-dimethylbutanoyl chloride (DMBC) to 3,3-dimethylbutyraldehyde (DMBA) was explored by Li *et al.*[41] with silica supported Pd nanoparticles. In this case, the catalyst was synthesized by the co-precipitation method, also called sol-gel methodology, using dinitrodiamminepalladium(II) and tetraethylorthosilicate (TEOS) as precursors for palladium and silica. The resulting material containing 3 wt% Pd was treated in two different conditions. The activation at 80 °C by bubbling H_2 in cyclohexane for 1 h showed the highest yield of DMBA. The catalyst was also activated in H_2 atmosphere at 80 °C, 160 °C or 200 °C for 4 h. The activation in H_2 atmosphere enhanced the catalyst activity, but resulted in the formation of non-desired 3,3-dimethylbutanol product. The catalyst could be used in up to seven consecutive runs keeping the conversion above 90%

without significant change in the surface area of the catalyst. The reaction conditions were 20 g DMBC, 2 g Pd catalyst (3wt% Pd), cyclohexane as solvent, 80 °C, H_2 bubbling (120 mL/min) and stirring at 1000 rpm.

One advantage for the application of silica as catalyst support is that the surface can be easily modified with organosilanes, resulting in grafted ligands on the silica surface. The functionalization of silica can improve the metal/nanoparticle impregnation/immobilization, alter the catalytic activity and selectivity and modulate the size during nanoparticle formation.[23]

Lim *et al.*[42] showed that Pd supported nanoparticles of 2-4 nm prepared by impregnation of palladium acetate on amine and 2-pyridinecarboxaldehyde functionalized silica supports were very active for hydrogenation of a large variety of olefins in aqueous media.

The catalyst separation can be enhanced by the presence of magnetic cores in the silica matrix. In the same way for bare silica particles, silica-coated magnetite can be easily functionalized using organosilanes. Thus, the silica coating of magnetite is an attractive approach for preparing magnetically recoverable catalysts. Our research group has studied the preparation of Pd supported nanocatalysts for hydrogenation in this type of support functionalized with thiol,[43] amine,[44] ethylenediamine[44] and terpyridine[27] ligands.

In a previous study, Pd nanoparticles of 3.0 nm over amine functionalized silica-coated magnetic support were prepared by impregnation method. The activity of this catalyst in hydrogenation of cyclohexene achieved a hydrogenation rate of 11538 $mol_{product}$ $mol^{-1}{}_{metal}$ h^{-1} at 2500 mol of substrate per mol catalyst, 75 °C and 6 atm of H_2. Even after 20 cycles of cyclohexene hydrogenation, leaching was not observed with this catalyst.[45]

Pd nanocatalyst of 6 nm supported on amine-functionalized silica-coated nanoparticles showed reaction rates of 5500 $mol_{product}$ $mol^{-1}{}_{metal}$ h^{-1} in the solventless hydrogenation of

cyclohexene at 75 °C and 6 atm H_2. The simple change of amine groups for ethylenediamine groups on the support surface resulted in nanoparticles of 1 nm with lower catalytic activity (800 $mol_{product}$ $mol^{-1}{}_{metal}$ h^{-1}).[44]

The Pd nanocatalyst synthesized by direct deposition method on magnetic support functionalized with terpyridine ligand was used successfully for the hydrogenation of β-myrcene with high selectivity for the formation of monohydrogenated compounds. The activity and selectivity of the catalyst on terpyridine functionalized support was largely increased when compared to similar nanocatalyst on amino-modified magnetic support or to Pd/C.[27]

Mesoporous silica has been extensively studied as support because of the encapsulation of the metal nanoparticles, which makes them stable. For example, Pd nanoparticles in mesoporous silica have been used in the hydrogenation of biomass-derived furfural to furfuryl alcohol. The Pd nanoparticles supported in mesoporous silica were synthesized by impregnation approach using palladium(II) nitrate as metal precursor and adjusting the metal loadings to 1, 3 and 5 wt%. A better homogeneous distribution of Pd nanoparticles was obtained for loadings lower than 5 wt% Pd. However, the catalyst containing 5 wt% Pd was the most active reaching a conversion of 75% with selectivity of 71%, under mild conditions.[46] Excellent activities in the hydrogenation of nitroaromatics[47] and alkynes[48] were observed for Pd nanoparticles supported on mesoporous silica MCM-41 prepared by co-precipitation method. Different mesoporous supports as mesocellular foam silica,[49] MMT-1[50] and SBA-15[51] were also explored as support for Pd nanocatalyst in hydrogenation reactions.

Micro and nanospheres complex structures of mesoporous support have gained attention to be used as support for Pd. Pd nanoparticles of 4.3 nm supported in amine functionalized structured mesoporous silica nanospheres were prepared by impregnation

method. This catalyst was active for hydrodechlorination of chlorophenols and presented activity for further hydrogenation of phenol, indicating his potential use as hydrogenation catalyst.[52] A hydrophobic core–hydrophilic shell structured mesoporous silica spheres was used successfully as support for Pd nanocatalyst. This catalyst was employed in the selective hydrogenation of phenol to cyclohexanone in aqueous phase reaching 98.5 % of conversion and 97.1 % of selectivity at 1 atm of H_2 and 80 ºC. The cyclohexanone is an important intermediate in the production of nylon 6 and nylon 66 in the chemical industry.[53]

Porous silica shell prepared over Pd nanoparticles is another type of catalyst found in the literature. However, the synthesis of this material is not simple, and involves different approaches based on controlled hydrolysis of silica precursor. The resulting material is present as Pd nanocatalyst type core-shell (for the coating of isolated metal nanoparticles) or embedded (for the coating of several metal nanoparticles). Silica-coated Pd nanoparticles showed interesting catalytic activity for hydrogenation CO_2[54] and 4-carboxybenzaldehyde.[55]

In the petrochemical industry the Pd/α-Al_2O_3 catalyst is one of the most important hydrogenation catalysts. This fact makes alumina support very interesting in the preparation of supported Pd NPs for hydrogenation. Zhang *et al.*[56] prepared Pd/α-Al_2O_3 by impregnation α-Al_2O_3 with colloidal Pd nanoparticles and obtained a catalyst more active than the conventional catalyst in the selective hydrogenation of acetylene in ethylene-rich stream. Boehmite-supported Pd nanoparticles achieved a reaction rate of 23520 $mol_{product}$ $mol^{-1}{}_{metal}$ h^{-1} with 99% of conversion for hydrogenation of allyl alcohol under mild condition (30 ºC, 1 MPa H_2).[57] Pd nanoparticles were prepared by thermal treatment of porous alumina spheres modified by hydrotalcite impregnated with Pd ions resulting in 4 nm nanoparticles. This catalysts was active in the hydrogenation of dimethyl terephthalate to dimethyl cyclohexane-1,4-dicarboxylate, an important polymer modifier.[58]

Carbon is one of the most common catalyst supports. Recently, Pinilla and co-workers[59] reported the preparation of carbon supported small spherical and homogeneously dispersed Pd nanoparticles by direct decomposition of tris(dibenzylideneacetone)dipalladium(0) over mesoporous carbon beads. The nanocatalyst was used for hydrogenation of anthracene achieving high conversions. The hydrogenated byproducts produced by cracking or ring-opening reactions were not observed. The carbon supports can also be modified by a doping process. N-doped carbons prepared by different approaches were used as supports of small-sized Pd nanoparticles for application as catalyst in the selective hydrogenation of phenol to cyclohexanone. The N-doped carbons were prepared using carbons with porous size of 3 or 5 nm and by gas thermal ammonolysis or heat treatment with melamine. The supports were impregnated with different loadings of Pd. The most active catalyst was the one with 1 wt% Pd comprised by the smallest Pd nanoparticles (1.2 nm) in the N-doped support (porous size of 3 nm) obtained by gas thermal ammonolysis. Moreover, this catalyst was reused five times without losing the activity.[60] Carbon nanotubes are also being employed as potential supports for nanocatalysts. Pd nanoparticles supported on carbon nanotubes were investigated in hydrogenation of polystyrene,[61] nitrobenzene,[62] biomass-derived levulinic acid[63] and alkenes.[64] N-doped carbon nanotubes obtained by gas thermal ammonolysis and O-doped carbon nanotubes obtained by vapor of HNO_3 treatment were investigated as support for Pd nanocatalyst in the hydrogenation of 1,5-cyclooctadiene in gas flow reaction at 50 ºC. The Pd nanoparticles in both supports present similar size (2.7 nm) but the N-doped carbon nanotubes resulted in better catalytic performance for the olefin hydrogenation. The exceptional catalytic activity observed for Pd nanoparticles supported on N-doped carbon nanotubes was attributed to the structural and electronic promoting effect of the support since the nitrogen species can be considered as both structural and electronic promoters. One example is the influence of the significant polarity changes by the nitrogen

that can influence the adsorption of reactant molecules in catalysis.[65] Literature also reports carbon-coated magnetic nanoparticles as catalysts supports. Baig and Varma[66] reported a magnetic carbon-supported Pd catalyst synthesized *via* co-precipitation of nanoferrites and carbon deposition by calcination using renewable cellulose as carbon source. The nanocatalyst was active for the hydrogenation of a variety of alkenes and aryl nitro compounds at 1 atm H_2 and room temperature, with total conversion in less than 1 h. Carbon-coated cobalt nanoparticles can also be used as Pd nanoparticles support for hydrogenation.[67]

Polymers are very interesting supports for nanocatalyst due to the presence of various functional groups and the formation of porous structure. Pd(II) complexes are known as catalyst for polymerization and the further reduction of Pd(II) can result in Pd nanoparticles encapsulated in the polymer structure. Pd nanoparticles supported on polymer were tested in hydrogenation of quinolines to tetrahydroquinolines that are important intermediates in chemical industry. The polymer supported Pd nanocatalyst was prepared by co-polymerization of the metal containing monomer palladium 2-(acetoacetoxy)ethyl methacrylate, with the suitable co-monomer ethyl methacrylate and the cross-linker ethylene glycol dimethacrylate. The Pd nanoparticles are formed under the conditions of hydrogenation of the quinolines (0.5 mol% of Pd, 10 atm H_2 and 80 °C in autoclave reactor). The 4 nm Pd nanocatalyst formed achieved 98 % conversion for six different quinolines and could be reused for at least nine times without losing activity and selectivity and without showing aggregation or leaching during the reuses.[68] Another example of Pd-catalyzed polymerization in the preparation of polymer supported nanoparticles was also used by Ishida *et al.*[69] In this case Pd nanoparticles encapsulated by microporous polymer were obtained by polymerization of 1,3,5-triethynylbenzene and 1,4-diiodobenzene in the presence of $Pd(PPh_3)_4$, followed by a thermal treatment with N_2 or H_2. The change of 1,4-diiodobenzene by similar biphenyl or hydroxyl containing aromatic groups also was investigated. The series of polymer supported

Pd nanoparticles presented 1.6-3.5 nm size and they were very active to hydrogenation of 4-nitrostyrene and hydrogenation of N-benzylideneaniline, reaching conversions of 99%. The preparation of Pd nanoparticles supported on polymer can also be made by simple immobilization method, as reported by Zhang and co-workers.[70] Pd nanoparticles were immobilized to the polymer Cr-MIL-101, with incorporation of HSO_3 in different amounts in the polymer structure. The catalyst was tested in hydrogenation of γ-valerolactone to ethylvalerate, although without good catalytic activity and a maximum conversion of 51% and selectivity of 26% at 200 ºC, 3 MPa H_2 and 10 h. On the other hand, the Pd nanocatalyst in Cr-MIL-101 without HSO_3 treatment was also explored in hydrogenation of 2,3,5-trimethylbenzoquinone to 2,3,5-trimethylhydroquinone (used for vitamin E production) with better activity than conventional Pd/C catalyst.[71]

Others catalyst supports for hydrogenation reaction have been explored less extensively but with promising results. Pd nanoparticles over magnetite and functionalized magnetite were investigated in nitrocompounds[72] and olefins[43] hydrogenation. Pd nanoparticles supported in functionalized zeolite were used for hydrogenation of styrene.[73] Graphene and graphene oxide supported Pd nanoparticles were used as catalysts in hydrogenation of olefins,[74] α, β-unsaturated ketones,[75] α,β-unsaturated carboxylic acids[76] and citral.[77] Magnesium oxide is not very often used as support for hydrogenation reaction because its basicity is more interesting for oxidation reactions. However, Pd nanoparticles supported on magnesium oxide were used for hydrogenation of quinolines, alkenes and biodiesel showing to be four times more active than commercial Pd/SiO_2 and Pd/Al_2O_3 catalysts in the hydrogenation of quinoline.[78] Finally, Pd nanoparticles on TiO_2 were active for hydrogenation of cinnamaldehyde.[79]

Some studies reported in the literature compare the catalytic activity of Pd nanoparticles in different supports for hydrogenation reactions. A huge variety of supports for

Pd nanoparticles were investigated by Kulagina and co-workers.[80] Pd NPs were prepared *via* reduction of Pd(II) ions over carbon, SiO_2, diatomites, WO_3, Ta_2O_5, Nb_2O_5, V_2O_5, TiO_2, CeO_2, ZrO_2, Ga_2O_3, In_2O_3, Cr_2O_3, Fe_2O_3, Al_2O_3, CaF_2, $BaSO_4$ and $Ca_3(PO_4)_2$. The possibility of changes in chemical surface of some supports during in situ reduction of Pd(II) was considered in this study. According to the authors the WO_3, V_2O_5, TiO_2, CeO_2, Nb_2O_5 and ZrO_2 supports could have shown chemical changes, but their surfaces were preserved, as observed by diffuse reflectance spectra after air exposure. However, during the catalytic hydrogenation conditions there is a high possibility of chemical surface changes that must be considered. The Pd nanocatalysts with this variety of supports were evaluated on catalytic hydrogenation of maleic acid, which showed to be a support-dependent process. The effect of the nature of oxide support was discussed in terms of the effective ionic potentials of the cations at the support surfaces. The authors could obtain a good relationship between the reaction rates and the effective ionic potentials of the cations in the hydrogenation of maleic acid. The Pd nanoparticles on oxide followed the rule of increasing reaction rates with the decreasing of oxidation number of the cations that belong to the support (decreasing their polarizability): $Ta_2O_5 < TiO_2 \approx SiO_2 < Al_2O_3$. The catalyst on Cr_2O_3, Fe_2O_3, Ga_2O and In_2O_3 were the less active ones, probably because the metal containing oxides have uncompleted external electron shells which raises their polarizability. Pd NPs supported on carbon was the most active catalyst.

Pd nanocatalysts supported on CeO_2, ZnO and TiO_2 were studied in the selective hydrogenation of butadiene. The supports were treated by calcination at 300 °C for 1 h under O_2 atmosphere or by removal of physisorbed water by vacuum at room temperature for 2 h. The Pd NPs were deposited on the support by organometallic chemical vapor deposition technique. The nanocatalysts were tested in selective hydrogenation of butadiene, a well-known structure-sensitive reaction. The calcined supports showed better selectivity to

butadiene. One explanation for this behavior is the structural evidences obtained for palladium nanoparticles that were more dispersed in the calcined supports. Moreover, the spectra of CO adsorbed on Pd NPs demonstrated a significant presence of exposed (111) faces for calcined TiO_2 and ZnO. The Pd (1 1 1) faces are reported to be very selective in butadiene hydrogenation.[81]

Colloidal Pd nanoparticles stabilized by PVP of 3-5 nm were immobilized on carbon, alumina, silica and calcium carbonate support for hydrogenation of 2-butyne-1,4-diol to 2-butene-1,4-diol at 50 ºC and 22 atm H_2. The Pd nanoparticles on carbon and $CaCO_3$ presented similar selectivity, but the carbon support was almost two times more active. Intermediate activity was obtained with the supports Al_2O_3 and SiO_2, but due to formation of side products, as butyraldehyde, butanol and acetals, the selectivity was poor. The comparison of prepared catalysts with conventional Pd catalysts supported in similar materials demonstrated that the nanocatalysts were around 10 times more active and more selective.[82]

Domínguez-Domínguez and co-workers[83] investigated γ-alumina, zeolite Beta, MCM-41, Al-MCM-41 with immobilized pre-synthesized 2.5 nm colloidal Pd nanoparticles. The catalysts were tested in the partial hydrogenation of phenylacetylene, although activity and selectivity were not considerably different with the different supports. However, all catalysts were considered highly active and selective under mild conditions (50 ºC and H_2 flow 30 mL/min). The catalysts with MCM-41 and Al-MCM-41 were also prepared by an alternative method. This method consisted in the synthesis of the supports by precipitation in the presence of Pd colloidal nanoparticles. The resulting MCM-41 and Al-MCM-41 catalysts were about 4 and 7 times more active than those prepared by Pd nanoparticles immobilization, and the selectivity was preserved. This result was interesting because the last method resulted in Pd NPs of diameter around 6.5 nm and a reduction of the catalytic activity could be

expected. This result is a demonstration of the importance of metal interaction with the support that may surpass the size effect.

1.2.3.2. Supported Rhodium nanocatalysts

Rhodium is an important metal in hydrogenation reactions because it displays high activity for hydrogenation of arenes. Supported Rh NPs for hydrogenation of arenes are found in the literature using a large variety of supports, such as silica,[84] nanozeolite,[85] mesoporous clay,[86] charcoal,[87] carbon nanotubes,[88] aluminum oxyhydroxide,[89] boehmite,[90] hydroxyapatite[91] and magnetic support.[92]

The catalytic performance of Rh nanocatalysts can be drastically affected by nanoparticle shape. Park and co-workers[87] prepared colloidal Rh of different shapes and immobilized them on charcoal. The resulting materials were tested as catalysts in the hydrogenation of arenes. The tetrahedral supported Rh NPs were almost 6 times more active than spherical ones, and 109 times more active than conventional Rh/C catalyst.

The influence of the support for Rh NPs was also explored. For example basic oxides MgO, CaO and SrO were tested as supports for Rh NPs. The supported nanocatalysts were prepared *via* impregnation of organometallic Rh complex in the support followed by reduction under 3.4 bar H_2 at 50 ºC in a glass reactor. The catalysts presented comparable Rh particle size, dispersion and surface area. For quinoline hydrogenation, the catalytic activity increased with the basicity: MgO < CaO < SrO. However, for hydrogenation of toluene, the authors did not observe any relationship with basicity. The explanation for the relationship observed for quinoline hydrogenation is that basic supports are able of promoting heterolytic hydrogen activation and an ionic hydrogenation mechanism. The ionic mechanism is related

to the strong N-H bonding created with the nitrogen atom of the substrate and the basic site of the support, which facilitates the hydrogenation of the aromatic ring. However, toluene does not interact with the support basic sites, thus the reaction is not influenced by the basicity of the support.[93]

The effect of the support grains size was also studied in hydrogenation by Rh NPs. Silicas of different grains size (80 and 120 μm) with similar porous volume and diameter were evaluated as support for 5 nm colloidal Rh NPs. The supported nanocatalysts were prepared *via* sol-immobilization method without calcination step and were used in the hydrogenation of different arenes. However, the authors did not report differences in catalytic activity for the different supports.[94]

The catalytic performances of silica or titania supported Rh nanoparticles were compared in arene hydrogenation. Hubert and co-workers[95] prepared Rh NPs supported in SiO_2 and TiO_2 by sol-immobilization of colloidal Rh NPs. Colloidal and supported Rh NPs were evaluated in the hydrogenation of toluene in water (solvent), 1 mol% Rh, 1 atm H_2 and room temperature. The catalytic activities followed the order: colloidal Rh NPs < Rh NPs on SiO_2 < Rh NPs on TiO_2 with reaction rate of 53, 163 and 222 $mol_{product}\ mol^{-1}{}_{metal}\ h^{-1}$, respectively. However, none explanation was given for the high activity of titania supported Rh nanoparticles. Generally, TiO_2 and SiO_2 do not differ in terms of support for hydrogenation since their polarizability is similar.[80]

1.2.3.3. Supported Ruthenium nanocatalysts

Ruthenium nanoparticles are active in several hydrogenation reactions. For example, Ru NPs supported in clays, as hectorite and montmorillonite, were active in the hydrogenation

of nitro compounds,[96] arenes[97] and selective hydrogenation of α,β-unsaturated ketones.[98] Carbon supports (porous carbon, carbon nanotubes and carbon nanofibers) were used successfully in the preparation of supported Ru NPs for hydrogenation of arenes,[99] nitro compounds,[100] cinnamaldehyde,[101] lactic acid[102] and oils.[103] Inorganic oxides like SiO_2,[104] MgO[105] and SnO_2[106] were investigated in the hydrogenation of arenes as support for Ru NPs. Finally, Ru NPs on magnetic support were active in selective hydrogenation of α,β-unsaturated ketones.[107]

The influence of support in hydrogenation reactions by Ru NPs was reported in the literature by some research groups. Cao and co-workers[108] prepared γ-alumina and carbon supported Ru NPs by impregnation of Ru(III) ions followed by thermal reduction. The catalysts were evaluated in hydrogenation of levulinic acid to γ-valerolactone. The carbon support showed higher activity than alumina. The authors suggested that the high activity observed for carbon supported Ru NPs is related to the stability of metallic Ru in carbon against oxidation. According to XPS data, the binding energy of Ru 3d 5/2 on carbon is closer to metallic Ru than on Al_2O_3. FTIR data also showed that the ratio Ru^0/Ru^{n+} is higher in carbon support than for Al_2O_3. The doping of the supports with potassium increased the catalytic activity for both supports and the activity of Ru NPs on K-doped Al_2O_3 support reached similar activity to K-doped carbon support. The Ru NP catalysts were five times more active than commercial Ru catalysts.

Liu and co-workers[109] used porous alumina microfibers as template for the preparation of Ru NPs embedded in mesoporous carbon microfiber. The deposition of carbon on alumina template containing Ru(III) was accomplished by chemical vapor deposition of carbon using benzene or pyridine as the carbon source. The Ru was reduced under catalyst preparation conditions. The catalytic activity of Ru NPs in mesoporous carbon microfiber was studied in hydrogenation of D-glucose. Commercial carbon nanotubes and carbon microfibers were

impregnated with Ru(III) and thermally reduced for comparison with the synthesized catalysts. The catalysts prepared in synthesized mesoporous carbon microfibers were more active due to the 1-D morphology that can facilitate the diffusion of reactants and products. Also, the hydrogen spillover is easier by the high metal-support interaction.

Rutile and anatase phase of TiO_2 were investigated as support for Ru NPs in hydrogenation of CO_2. Lin and co-workers[110] prepared the catalysts by impregnation of Ru(III) in TiO_2 followed of calcination and reduction in H_2 atmosphere. The supported Ru nanoparticles size was 4 nm in anatase-TiO_2 and 1.1 nm in rutile-TiO_2. Also in rutile-TiO_2 the nanoparticles were well-dispersed on the support. The Ru-O-Ti bond was characterized by EXAFS in rutile-TiO_2 supported Ru NPs, which suggest a strong metal-support interaction. As consequence, rutile-TiO_2 promotes a better metal dispersion and a higher thermal stability in hydrogenation of CO_2. The Ru NPs in anatase-TiO_2 were more active initially, because the nanoparticle size is more suitable for CO_2 hydrogenation. However, they are easily deactivated by thermal treatment.

Jahjah and co-workers[111] compared the activity of colloidal Ru NPs prepared with organometallic precursor immobilized in carbon nanotubes, SiO_2, Al_2O_3 and activated carbon. The catalysts were tested in the hydrogenation of styrene, acetophenone and p-methylanisole. The Ru NPs immobilized on activated carbon was the less active catalyst due to the high microporosity of the support, which result in more transfer mass limitations compared to the others supports. The intermediary activity observed for Al_2O_3 support was a result from the weak interaction of the colloidal nanoparticles, because Ru NPs were agglomerated after catalytic reaction. Carbon nanotubes and SiO_2 supports resulted in the highest activity, although the Ru NPs supported on SiO_2 deactivated after the first run in the hydrogenation of styrene and the Ru NPs in carbon nanotubes were active after 3 cycles. Under the reaction conditions, the nanoparticles could migrate inside the SiO_2 porous. On the other hand, the

metal nanoparticles are dispersed on the surface of carbon nanotubes, which can facilitate the contact with substrates.

1.2.3.4. Deactivation of supported nanocatalysts

The catalyst deactivation is an issue in Nanocatalysis, as it is in heterogeneous catalysis. The sintering of supported metal nanoparticles is one of the main mechanisms for the loss of catalytic activity, because of the particle migration and coalescence or Ostwald ripening.[112] The nanoparticle growth can occur by detachment and migration of metal atoms from one nanoparticle to another *via* the support surface or gas phase. This process is called as Ostwald ripening and results in a solid containing a mixture of different nanoparticles sizes and shapes. Also, the nanoparticle growth during the sintering can occur by migration of an entire nanoparticle by diffusion on the support surface followed by collision and coalescence. In the case of nanoalloys, the sintering can also result in composition change.[113]

Temperature is one of the main factors responsible for sintering because the melting point is a size-dependent physical property and metal nanoparticles, typically, present a lower melting point compared to bulk metal.[7] The sintering process is also affected by changes in the nanoparticle surface energy. The nanoparticle surface energy can be modified by atmosphere, stabilizing agents, support surface functionalization, addition of promoters, among several other factors.[113] The metal dispersion on the support can also contribute to the sintering process. Nanocatalysts strongly attached to the support, metal nanoparticles encapsulated in core-shell, yolk-shell, core-sheath or mesoporous structures are ways to avoid sintering.[113] However, the encapsulation of the nanoparticles in the support is difficult and can drastically decrease the catalytic activity of the metal nanoparticles. The reduction of catalytic

activity can be a result of the blockage of active sites by the support and also because the substrate diffusion will be limited by the shell porosity. In any way, the encapsulation of nanoparticles is recommended for the preparation of catalysts that will be used under extreme reaction conditions.[114]

The deactivation of supported nanocatalysts can also occurs *via* poisoning, fouling and volatization of active components, similar to common heterogeneous catalysts.[115] After sintering, the second common reason for nanocatalyst deactivation is the poisoning that consists in strong binding of molecular species on the catalyst active sites or due to carbon deposition on metal surface.

1.3. Magnetically recoverable and recyclable nanocatalysts

As mentioned before, heterogeneous catalysts as well as supported metal nanoparticle catalysts have the advantage of easy separation compared to homogeneous catalysts. However, even heterogeneous catalysts can sometimes still be harsh to separate from the products depending on the granulometry and density of the catalyst support. Separation processes that involve centrifugation, filtration, decantation and distillation are time or energy consuming. On the other hand, magnetic separation allows fast removal of catalysts from crude samples avoiding mass loss and catalyst oxidation since separation process occurs without removing the catalyst from the reaction flask. The catalyst recycling can be easily performed by washing it directly in the reaction flask and by adding new portions of the substrate. In comparison with traditional separation, the magnetic separation is much more simple and can be more efficient.[116] In this context, magnetic supports are intensively explored as supports for molecular catalysts[117] and nanocatalysts.[118]

Magnetite (Fe_3O_4) under the form of nanoparticles is being employed in several applications as magnetic resonance image contrast,[119] enzyme immobilization,[120] cell separation,[121] drug delivery[122] and catalysts support[43] due to its low toxicity and superparamagnetic behavior.[123] The superparamagnetism is a size-dependent property that is characterized by elevated saturation magnetization in the presence of a magnetic field and absence of residual magnetization when ceased the magnetic field.[124] Bulk magnetic materials present a multidominium structure, but when the material is reduced below a critical diameter the formation of single domain nanoparticles is energetically favorable. The absence of residual magnetization of superparamagnetic materials is a consequence of the easy magnetic reorientation at temperatures higher than blocking temperature (Tb). Tb is the temperature where the thermal energy is higher than the barrier energy, which allows the magnetic reorientation. At temperature lower than Tb the material will be in a blocked condition and showing residual magnetization, but above Tb it can be separated (high magnetization in the presence of an applied magnetic field) and easily redispersed (no residual magnetization) after removal of magnetic field. The absence of residual magnetization of superparamagnetic supports allows the catalyst to be dispersed in reaction media without support aggregation. This characteristic is indispensable for catalyst separation and reuse.[125] Figure 1.2 shows an example of magnetic separation of silica-coated magnetite.

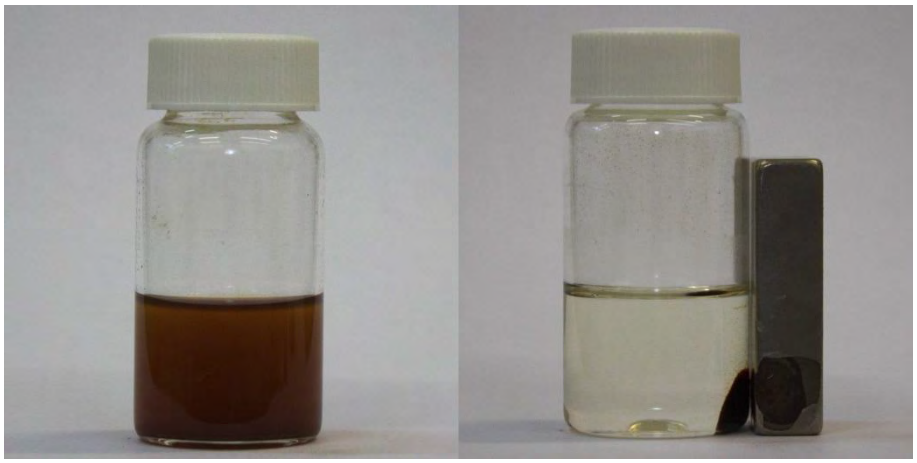

Figure 1.2. Magnetic separation of silica-coated magnetite

Support stability under reaction conditions is a very important characteristic to preserve the magnetic properties for an efficient magnetic separation. The encapsulation of magnetic nanoparticles with a protective coating is an interesting strategy to produce more stable materials. Besides improving the support stability, the coating also facilitates the catalyst preparation by offering a surface that can be easily modified with organic compounds or contains high surface area with a mesoporous material, for example, silica.[125] Silica[126] and carbon[127] are so far the most explored coating for magnetic nanoparticles. The silica coating is the most versatile because it is easy performed, very resistant to organic solvents, provides an easy functionalization, is chemically and thermally stable under typical reaction conditions.[126] The most known methods to coat iron oxide with a protective shell of silica is by Stöber method,[128] microemulsion,[129] reverse microemulsion,[130] aerosyl pyrolysis,[131] and arc-discharge method.[132] All these methods present advantages and disadvantages, for example Stöber method is simple and low cost, but it can easily result in pear-necklace structures instead of single particles.[133] The aerosyl pyrolysis method can produce large amounts of materials and arc-discharge method results in high purity materials, but both methods require sophisticated equipment. The disadvantage of microemulsion and reverse microemulsion methods is the higher cost compared to Stöber method. However, the formation of micelles

permits the confinement of the particles and the control of silica growth[134] and high quality materials can be prepared.[92]

The carbon coating is resistant in acid and basic conditions, but the coating requires more sophisticated methods. The most explored synthesis for magnetic nanoparticles encapsulated in carbon was accomplished *via* template,[135] chemical vapor deposition (CVD),[136] and hydrothermal/solvothermal method.[137]

The coating of iron oxides with other oxides that are relevant for application as catalysts supports is limited to few examples. Álvarez *et al.*[138] reported a method for preparation of titania-coated magnetite. The method consists in the treatment of an aqueous suspension of magnetite with isopropyl alcohol and titanium(IV) isopropoxide, which result in a poorly controlled morphology that was enhanced when a previous silica-coating was performed. The preparation of "peapod" like structures were reported by Ye *et al.*[139] through the deposition of titania over silica-coated magnetite. The control of addition of tetrabutyltitanate resulted in the preparation of well-controlled material with spherical to 'peapod' like morphology. The precipitation of $Ti(SO_4)_2$ in the presence of magnetic NPs resulted in the direct coating of magnetite with titania.[140] The urea used as precipitation agent allows the slow release of ammonia and the hydrolysis and condensation rate of TiO_2 precursor is controlled. The titania-coating was also reported in an ultrasonic bath at 90 ºC for 1.5 h using a mixture of ethanol/water and titanium butoxide in the presence of magnetic particles, although the material obtained showed a very large size (bigger than 100 nm).[141] Liu *et al.*[142] demonstrated the titania-coating of silica-coated magnetite using glacial acetic acid to promote the hydrolysis of titanium butoxide, which resulted in particles with a layer of titania (8-10 nm). The direct coating of magnetite with alumina was reported by Sun *et al.* by the suspension of magnetite powder in an ethanolic solution of aluminum propoxide and the drop wise addition of water/ethanol mixture. However, the authors showed a scanning electron

microscopy that does not clarify the quality of the alumina-coating control.[143] Some studies have demonstrated that it is possible to obtain metal nanoparticles encapsulated by others oxides than silica; even in a core-shell structure, but the conditions of the synthesis does not allow the isolation of sufficient material to make viable their use as catalyst support.[24, 144]

1.4. Justification

The main goal of this thesis is to contribute for the preparation of magnetically recoverable catalysts that are more resistant to reaction media. The type of magnetic support available are mainly based on bare magnetic nanoparticles (e.g. magnetite and other ferrites), silica-coated or carbon-coated magnetic nanoparticles. There is a lack of magnetic supports containing titania, ceria or other oxides prepared with good morphological control that are very welcome for application in the field of catalysis. In this thesis, we explored strategies for the coating of iron oxide with titania and ceria and their influence in the catalytic activity of supported metal nanoparticles.

As described in section 1.2.2, there are several methods to prepare supported metal nanoparticles and here we selected the IMP and SI methods for the preparation of controllable and reproducible catalysts. The preparation of supported metal NPs is very important for the study of the support influence in the catalytic activity. Initially we explored the preparation of Rh catalysts by IMP method using different reducing agents (H_2, $NaBH_4$ and N_2H_4) and by SI method. The IMP method was also employed in the preparation of Pd catalysts using silica-coated magnetite before and after thermal treatment and their amino-functionalized counterparts.

The direct influence of silica-coated magnetite containing ceria or titania in the catalytic activity of Rh, Pd and Ru NPs was explored in the hydrogenation of cyclohexene (Rh and Pd) and in the hydrogenation of phenol (Rh, Pd and Ru). The Rh, Pd and Ru catalysts were prepared using an organometallic approach in order to obtain well-controlled and reproducible NPs and the catalysts were prepared by SI method. It is very important to note that there are several examples of support influence studies in the literature where supported metal NPs are prepared by different methods. The differences between the supported metal NPs can be more important than the support effect in the catalytic performance. Thus, the use of well-controlled and reproducible NPs is the most important requirement to a support effect study.

2. OBJECTIVES

2.1. General

The general objective of this thesis is the development of magnetic nanocomposites containing silica, ceria and titania for the preparation of magnetically recoverable supported metal nanoparticles catalysts for hydrogenation reactions.

2.2. Specifics

The specific objectives of this thesis are:

- Preparation of silica-coated magnetite using a reverse microemulsion method and the study of its thermal behavior;
- Deposition of cerium and titanium oxides on silica-coated magnetite;
- Characterization of the physical and chemical properties of the magnetic nanocomposites;
- Preparation of catalysts based on the impregnation of rhodium(III) chloride and disodium tetrachloropalladate(II) on magnetic supports;
- Preparation of catalysts based on the sol-immobilization of colloidal suspensions of rhodium and palladium nanoparticles on magnetic supports;

- Preparation of colloidal rhodium, palladium and ruthenium nanoparticles using an organometallic approach and immobilization of the colloidal nanoparticles on magnetic supports;
- Evaluation of the catalytic activity of the obtained magnetic nanomaterials in hydrogenation reactions using cyclohexene, benzene or phenol as substrates.

3. MATERIALSAND METHODS

3.1. Materials

3.1.1. Reagents

Iron(III) chloride hexahydrate, cyclohexane, oleic acid, IGEPAL CO-520, tetraethylortosilicate (TEOS), (3-aminopropyl)triethoxysilane (APTES), Brij-30, titanium(IV) isopropoxide (TTIP), ammonium cerium(IV) nitrate, rhodium(III) chloride hydrate, allylmagnesium chloride 2M in THF, tetrahydrothiophene, sodium borohydride, polyvinylpyrrolidone (PVP) (K30, Mw 40000), polyvinylalcohol (PVA) (80% hydrolyzed, Mw 10000), hydrazine, cyclohexene (without stabilizer), phenol, n-hexane, titanium(IV) 2-ethylhexyloxide (TEO), triethanolamine (TEOA), 1-butanol, 1-heptanol, 1-dodecanol, tetrahydrofuran (THF) (without stabilizer), dichloromethane and pentane were purchased from Sigma-Aldrich. Iron (II) chloride tetrahydarate, gold(III) chloride hydrate, benzyl alcohol and Tris(dibenzylideneacetone)dipalladium(0) ($Pd_2(dba)_3$) were purchased from Alfa Aesar and used as received. Palladium(II) chloride was purchased from Alfa Aesar and the solubilization in water was performed by addition of 2 eq. NaCl. (cyclo-octadiene)(cyclo-octatriene)ruthenium(0)(Ru(COD)(COT)) was purchased from Nanomeps and stored in glove box. Hydrochloric acid (35%), ammonia solution (26-28%) and isopropyl alcohol were purchased from J.T. Baker. Acetone, methanol, ethanol and toluene were purchased from Synth. The solvents were used as received, otherwise it is specified in the experimental part.

3.1.2. Equipments

The main instruments used are listed below:

Gas chromatographer GC-2010 equipped with a FID detector (Shimadzu, Japan) and capillary columns Rtx-wax or Rtx-5 both with 30 m length and I.D. 0.25 mm (Restek, United States) from the Prof. Dr. Liane M Rossi and Prof. Dr. Alcindo A. dos Santos (IQ-USP, Brazil) and HP 5890 equipped with the same Rtx-wax column from Dr Karine Philippot (LCC-CNRS, Toulouse).

Fourier transform infrared spectrometer GX 2000 (Perkin Elmer, United States) from LCC-CNRS, Toulouse.

Thermobalance TG-51 and Differential Scanning Calorimeter DSC-50 (Shimadzu, Japan) from Prof. Dr. Jivaldo R Matos, IQ-USP, Brazil.

Transmission electron microscope JEM 2100 (JEOL, United States) from LNNano, Brazil and from IQ-USP, Brazil; JEM 1011 (JEOL, United States) from TEMSCAN, Toulouse; Philips CM200 from Prof. Dr. Pedro K. Kiyohara (IF-USP, Brazil).

Flame atomic absorption spectrometer AA-6300 (Shimadzu, Japan) from Prof. Dr. Liane M Rossi IQ-USP, Brazil.

Inductively coupled plasma optical emission spectrometer Arcos (Spectro, Germany) from Analysis Center at IQ-USP, Brazil.

X-ray diffractometer Ultima + (Rigaku, Japan) from Prof. Dr. Márcia C. A. Fantini (IF-USP, Brasil).

Glove box UNIlab (MBRAUM, Germany) from Dr. Karine Philippot (LCC-CNRS, Toulouse).

Integrated Microreactor-MS system equipped with a CATLAB-PCS Module and a QIC-20 MS Module (Hiden Analytical, UK) from Prof. Dr. Liane M. Rossi (IQ-USP, Brazil).

Hydrogen monitoring system was assembled using homemade stainless steel vessels, pressure transmitter 510 (Huba Control, Germany), data logger FieldLogger (Novus, Brazil) and the control software FieldChart (Novus, Brazil) from Prof. Dr. Liane M. Rossi (IQ-USP, Brazil).

SQUID magnetometer XL-200 (Quantum Design, United States) from Prof. Renato F. Jardim (IF-USP, Brazil).

Spherical analyzer HA-100 (VSW, UK) from Prof. Dr. Richard Landers (IF-USP) for X-ray photoelectron analysis.

3.2. Methods

3.2.1. Synthesis of silica-coated magnetite supports

The synthesis of magnetite and their stabilization with oleic acid was prepared as described previously.[43, 145] Typically, a mixture of an aqueous solutions of Iron(III) chloride hexahydrate (10 mL, 1.0 mol L^{-1}) and Iron(II) chloride tetrahydrate (2.5 mL, 2.0 mol L^{-1} in hydrochloric acid 2.0 mol L^{-1}) was added to a solution of ammonia (250 mL, 0.7 mol L^{-1}) under N_2 atmosphere and mechanical stirring (10000 rpm, Ultra-Turrax T-18 Homogenizer, IKA Works). The mixture was kept under stirring and under inert atmosphere for 30 min. The obtained material was separated with a magnet and washed 3 times with portions of 250 mL of deionized water. The stabilization of the magnetite nanoparticles in cyclohexane was performed by the addition of oleic acid.[43, 146] This procedure consist in the dispersion of the as prepared magnetite nanoparticles in 250 mL deionized water followed by the drop-wise addition of oleic acid (7 mmol, 2 mL diluted in 10 mL acetone) under mechanical stirring

(10000 rpm, Ultra-Turrax T-18 Homogenizer, IKA Works). The obtained solid was magnetically separated and washed 3 times with portions of 25 mL acetone. After the washing procedure the material was dispersed in 50 mL cyclohexane and centrifuged at 2000 rpm for 30 min (Eppendorf 5804 centrifuge). The supernatant solution was collected and, typically, contained 20 to 25 mg L^{-1} of oleic acid stabilized magnetite nanoparticles in cyclohexane.

Silica coating was performed by means of a reverse microemulsion.[147] Initially, 700 mL cyclohexane and 44.6 g IGEPAL CO-520 were added in a round bottom flask. This mixture was stirred mechanically until total dispersion of the surfactant. Then, 200 mg of oleic acid stabilized magnetite (20 mL of the previously prepared suspension diluted to 10 mg mL^{-1}) and 9.44 mL ammonia solution (21 mmol) were added. The solution was vigorously stirred until total solubilization of the ammonia solution. Finally, 7.7 mL TEOS (2 mmol) was added and the mixture kept under mechanical stirring for the desired time, typically 6 h. The silica-coated magnetite was recovered from the solution by the addition of 300 mL methanol. The suspension in methanol was centrifuged (6500 rpm for 20 min) and washed two times with 300 mL portions of ethanol. The obtained material was dried under air at 90 ºC in an oven. This procedure, typically, results in around 1.5 g of silica-coated magnetite (Fe_3O_4@SiO_2). In order to remove any organic matter still present in the silica shell, the Fe_3O_4@SiO_2 material was calcined under static air atmosphere at 500 ºC for 2 h (heating rate of 20 ºC min^{-1}). The calcined sample was denoted as Fe_3O_4@SiO_2Cal.

3.2.1.1. Functionalization of silica surface with amine groups

The silica-coated magnetite solids (Fe_3O_4@SiO_2 and Fe_3O_4@SiO_2Cal) were functionalized with amine groups using (3-aminopropyl)triethoxysilane (APTES). Typically,

300 mg solid were added to 45 mL dry toluene under N_2 atmosphere and magnetic stirring. After the solid was well-dispersed, 450 µL APTES were added and the mixture kept under magnetic stirring for 2 h. The obtained material was magnetically separated and washed with 45 mL toluene and, then, washed two times with portions of 45 mL acetone. The solid $Fe_3O_4@SiO_2NH_2$ was dried under air at 100 ºC for 20 h in an oven.

3.2.1.2. Quantification of amine groups

The quantification of amine groups grafted on the surface of $Fe_3O_4@SiO_2$ and $Fe_3O_4@SiO_2Cal$ was determined by a colorimetric method of ninhydrin.[148] The reaction of the ninhydrin probe with primary amines is selective and results in a purple solution that can be quantified by UV-Vis spectroscopy. Typically, 50 mg of functionalized solid was mixed with 1 mL ninhydrin solution (5 wt% in ethanol) and 5 mL phosphate buffer solution (pH = 6.4). The mixture was maintained under magnetic stirring and boiling water bath for 1 h. The magnetic solid was magnetically separated and washed with portions of deionized water (70 ºC). The obtained solution volume was adjusted to 100 mL and the absorbance at 565 nm obtained by UV-Vis spectroscopy. The calibration curve was prepared using APTES.

3.2.2. Deposition of metallic oxides in silica-coated magnetite

3.2.2.1. Deposition of titanium oxide

The deposition of titania on the $Fe_3O_4@SiO_2$ composite was performed by a modification of the method described by Güttel *et al.*[149] for the preparation of gold yolk-shell material.[149] Initially, 200 mg $Fe_3O_4@SiO_2$ were dispersed in Brij-30 in ethanol (0.4 mmol L^{-1}, in 30 mL ethanol). To ensure the dispersion of the solid, the mixture was stirred for 20 h. Then, 90 μL of titanium(IV) isopropoxide (TTIP) solution (80 % in 1-butanol) were added under magnetic stirring. After 20 h, the solid was magnetically separated and washed with 3 portions of 15 mL ethanol. The obtained material was calcined under static air atmosphere at 500 ºC for 2 h. The resulting material was denoted as $Fe_3O_4@SiO_2TiO_2$.

3.2.2.2. Deposition of cerium oxide

The deposition of ceria on the $Fe_3O_4@SiO_2$ composite was performed by the impregnation of the solid with ammonium cerium(IV) nitrate. Typically, 100 mg $Fe_3O_4@SiO_2$ were dispersed in 4 mL ethanol under magnetic stirring. After 2 h, 8 mg of ammonium cerium(IV) nitrate were added and the mixture kept under magnetic stirring for another 20 h. The impregnated solid was recovered by evaporation of the solvent under low pressure. The obtained solid was collected and calcined under static air atmosphere at 500 ºC for 2 h. The resulting material was denoted as $Fe_3O_4@SiO_2CeO_2$.

3.2.3. Synthesis of metal precursors

3.2.3.1. Synthesis of Tris(allyl)Rhodium(III) complex

The tris(allyl)rhodium(III) complex was prepared following a modification of a previously reported method.[150] Initially, 1.5 g of $RhCl_3.xH_2O$ was added to a Schlenk flask and the atmosphere was changed to Ar using a vacuum/Ar line. The rhodium salt was solubilized in 140 mL THF (dry and without stabilizer), that was transferred from a Schlenk flask under Ar through a cannula. The addition of 36 mL allylmagnesium chloride solution (2 mol L^{-1} in THF) was made under vigorous magnetic stirring and a cold bath (ethanol with liquid N_2). The reaction mixture was kept under magnetic stirring for 20 h. The solution color changed to yellow and the THF was slowly removed under vacuum. In order to enhance the extraction of the product, the solid was removed from the Schlenk wall using a spatula under a constant flow of argon. The product was extracted by the addition of small portions of dry pentane under argon atmosphere. The suspension was transferred by cannula to a celite column. The pentane was removed under vacuum and the product transferred to sublimation apparatus inside a glove box (MBRAUN, Germany. Water and O_2 lower than 1 ppm). The sublimation was done under vacuum and 50 ºC. The purified $Rh(C_3H_5)_3$ was stored at -3 ºC in a freezer inside the glove box. The obtained mass of $Rh(C_3H_5)_3$ was around 700 mg.

3.2.3.2. Synthesis of Chloro(tetrahydrothiophene)gold(I)

The chloro(tetrahydrothiophene)gold(I) complex was prepared following a previously reported method.[151] Initially, 1 g of $HAuCl_4.3H_2O$ was transferred to a Schlenk flask inside

the glove box (MBRAUN, Germany. Water and O_2 lower than 1 ppm). Under a positive flow of argon, 8.2 mL of ethanol absolute (degassed by freezing pump) and 1.6 mL distilled water (degassed by bubbling with argon for 20 min) were added by syringe under stirring. Then 0.47 mL tetrahydrothiophene were added drop-wise resulting in the precipitation of a yellow solid, which turns white with the addition of more tetrahydrothiophene. After 30 minutes under stirring, the obtained solid was transferred to a porous glass filter using a cannula, under argon atmosphere, and washed with ethanol. The product was removed from the filter with dichloromethane and the solution recovered in a Schlenk flask. The dichloromethane was removed under reduced pressure. Yield: 624 mg AuCl(THT).

3.2.4. Synthesis of metal nanoparticles

3.2.4.1. Synthesis of palladium nanoparticles by reduction of metal salts

Polyvinylpyrrolidone-stabilized palladium nanoparticles (Pd@PVP-1) were prepared by reduction of Pd^{2+} ions following a literature reported method.[152] Typically, 15 mL disodium tetrachloropalladate(II)aqueous solution (2 mmol L^{-1}), 21 mL deionized water, 14 mL ethanol and 33.5 mg of PVP were added in a round bottom flask under magnetic stirring and kept for 2 h under reflux. The obtained solution was concentrated in a rotary evaporator to final volume of 10 mL and the colloidal Pd nanoparticles were used without further purification.

3.2.4.2. Synthesis of rhodium nanoparticles by reduction of metal salts

Polyvinyl alcohol-stabilized rhodium nanoparticles (Rh@PVA) were prepared in aqueous solution using $NaBH_4$ as reducing agent, following a modification of the method reported by Lopez-Sanchez *et al.* for the preparation of Au@PVA NPs.[32] Typically, an aqueous solution of rhodium(III) chloride hydrate (80mL, 0.8 mmol L^{-1}) was mixed with 13.5 mL of an aqueous PVA solution (1 wt%) under magnetic stirring. Then, a fresh prepared $NaBH_4$ aqueous solution (3 mL, 0.1 mol L^{-1}) was drop wise added under vigorous magnetic stirring. The magnetic stirring was maintained for 30 min and the obtained colloidal metal nanoparticles were used without further purification.

3.2.4.3. Synthesis of ruthenium, palladium and rhodium nanoparticles by decomposition of organometallic complexes

The preparation of Rh, Ru and Pd@PVP NPs were performed by the decomposition of the corresponding organometallic complexes in the presence of H_2 and PVP in THF solution. All metal nanoparticles were prepared by a modification of a previously reported method.[153]

Inside a glove box (MBRAUN, Germany. Water and O_2lower than 1 ppm), 42 mg Ru(COD)(COT), 30 mg $Rh(C_3H_5)_3$ or 61 mg $Pd_2(dba)_3$ were added to a 300 mL Fischer-Porter glass reactor. Under a positive flow of argon, 30 mL of THF (dry and purified) were transferred by syringe to a Schlenk flask containing 136 mg PVP under magnetic stirring. After the solubilization, the PVP solution in THF was transferred by cannula to the Fischer-Porter glass reactor containing the metal precursor without stirring and under a cold bath (ethanol and liquid N_2). Then, the reactor was pressurized with 3 bar H_2 and the stirring was

initiated. The cold bath was removed and the reactor kept under static pressure and magnetic stirring for 24 h. The THF was removed under reduced pressure and the material was washed with two portions of hexane. The resulting solid was dried under vacuum and stored in a glove box.

3.2.4.4. Synthesis of gold nanoparticles

The Au@PVP NPs were prepared following two different methods. The first method was reported by de Caro *et al.*[154] and consists in the decomposition of a gold(I) complex in the presence of H_2. The second method was reported by Tsunoyama *et al.*[155] and consists in the reduction of gold(III) chloride by $NaBH_4$.

Method 1: Inside the glove box (MBRAUN, Germany. Water and O_2 lower than 1 ppm), 43 mg AuCl(THT) were added to a Fischer-Porter reactor. Under a positive flow of argon, 30 mL of THF (dry and purified) were added to a Schlenk flask containing 136 mg PVP. After the solubilization, the PVP solution in THF was transferred by cannula to the Fischer-Porter reactor containing the Au(I) precursor without stirring and under a cold bath (ethanol and liquid N_2). Then the reactor was pressurized with 3 bar of H_2 and at the same time the stirring was initiated. The mixture was kept under room temperature for 24 h. The volume of THF was reduced under vacuum to 4 – 5 mL, and then the material was washed with two portions of hexane and dried under vacuum.

Method 2: Initially, 20 mg $HAuCl_4.3H_2O$ and 555 mg of PVP were solubilized in 50 mL deionized water under an ice bath. Then, an aqueous solution of $NaBH_4$ (5 mL, 100 mmol L^{-1}) was fast added. After stirring for 30 min, the resulting brown solution was transferred to a dialysis bag. The solution was left for 48 h in dialysis against deionized water.

3.2.5. Catalysts preparation by impregnation method

3.2.5.1. Rhodium catalysts

Rhodium catalysts were prepared by the impregnation of $Fe_3O_4@SiO_2NH_2$ support with $RhCl_3.xH_2O$ aqueous solution followed by three different methodologies for the reduction of the Rh^{3+} ions on the support surface. Basically, three different reducing agents were employed (H_2, $NaBH_4$ and N_2H_4). The reduction under H_2 was made following the procedure previously reported by Jacinto *et al.*[92] Typically, 50 mg $Fe_3O_4@SiO_2NH_2$ was dispersed in 10 mL aqueous rhodium(III) chloride solution (0.21 g mL^{-1}) under magnetic stirring. The solution was kept under magnetic stirring for 2 h. The solid was magnetically recovered and washed with two portions of 4 mL acetone. The catalysts were dried under air at 90 ºC for 3 h. The reduction of the Rh^{3+} by H_2 occurred *in situ* during the first catalytic hydrogenation cycle (see item 3.3.7). The reduction with $NaBH_4$ or N_2H_4 was performed by the addition of 2.5 mol $NaBH_4$ or 10 mol N_2H_4 per mol of Rh. Typically, 50 mg of the support freshly impregnated with Rh^{3+} ions dispersed in deionized water (volume adjusted to final solution of 4 mL) and 1 mL of a freshly prepared $NaBH_4$ aqueous solution (0.7 mg, $1.8x10^{-2}$ mmol) or neat N_2H_4 (2µL, $7.3x10^{-2}$ mmol) were mixed under stirring. After 2 h under stirring at room temperature, the solid was magnetically recovered and washed with two portions of 2 mL deionized water and one portion of 2 mL acetone. The solids were dried under air for 20 h. The catalysts were expected to obtain nominal 1.5 wt% metal, but the actual metal content was determined by FAAS.

3.2.5.2. Palladium catalysts

Palladium catalysts were prepared by the impregnation of the support with Na_2PdCl_4 aqueous solution. In a 20 mL scintillation flask were added 4 mL of Na_2PdCl_4 aqueous solution (0.5 mg Pd) and 50 mg of different supports: $Fe_3O_4@SiO_2$, $Fe_3O_4@SiO_2NH_2$, $Fe_3O_4@SiO_2Cal$, and $Fe_3O_4@SiO_2CalNH_2$. The solution was kept under magnetic stirring for 2 h. The solid was magnetically recovered and washed with two portions of 2 mL deionized water and one portion of 2 mL acetone. The solids were dried under air for 20 h. The reduction of the Pd^{2+} by H_2 occurred *in situ* during the first catalytic hydrogenation cycle (see item 3.3.7) The catalysts were expected to obtain nominal 1.0 wt% metal, but the actual metal content was determined by FAAS.

3.2.6. Catalyst preparation by immobilization of preformed metal nanoparticles

3.2.6.1. Immobilization of preformed metal nanoparticles prepared with salt precursors

Rhodium catalysts were prepared by the dispersion of 30 mg of $Fe_3O_4@SiO_2$ or $Fe_3O_4@SiO_2NH_2$ in 18 mL colloidal suspension Rh@PVA NPs (0.5 mg Rh). The mixture was kept under stirring for 2 h. Then, the solid was magnetically separated and washed with two portions of 2 mL deionized water and one portion of acetone. The solid was dried under air at 100 ºC for 20 h. The actual metal content was determined by FAAS.

Palladium catalysts were prepared by the dispersion of 50 mg of magnetic support (Fe_3O_4@SiO_2, Fe_3O_4@SiO_2NH_2, Fe_3O_4@SiO_2Cal, and Fe_3O_4@SiO_2CalNH_2) in 4 mL colloidal aqueous suspension of Pd@PVP-1 NPs (0.5 mg Pd). The mixture was kept under stirring for 2 h. Then, the solid was magnetically separated and washed with two portions of 2 mL deionized water and one portion of acetone. The solid was dried under air at 100ºC for 12 h. The actual metal content was determined by FAAS.

3.2.6.2. Immobilization of preformed metal nanoparticles prepared with organometallic precursors

The metal nanoparticles were immobilized on the magnetic supports by the dispersion of the magnetic solid in THF containing the desired amount of metal nanoparticles to obtain catalysts with nominal 1.5 wt% metal. Typically, 200 mg of magnetic support (Fe_3O_4@SiO_2Cal, Fe_3O_4@SiO_2CeO_2 and Fe_3O_4@SiO_2TiO_2) and 40 mg of metal nanoparticles were dispersed in 80 mL of dried THF (without stabilizer). The mixture was kept under stirring for 48 h. Then, the solid was magnetically separated and washed two times with portions of 40 mL THF. The solid was dried in vacuum. The actual metal content was determined by FAAS.

3.2.7. Catalytic reactions

3.2.7.1. Hydrogenation of cyclohexene and benzene in liquid phase

The hydrogenation of cyclohexene was performed in a 100 mL Fischer-Porter glass reactor at constant H_2 pressure. The reactor containing the catalyst powder or solution and the substrate was pressurized with 2 bar H_2 and purged 3 times. The reactor was placed in an oil bath and the temperature controlled by a magnetic heating plate (IKA works, H7 CMAG with ETS-D5 temperature controller). The typical catalytic conditions were substrate to catalyst molar ratio of 35600 for cyclohexene and 500 for benzene, constant pressure of 6 bar H_2 and 75 ºC. Additional reactions were performed with different conditions (details are provided in table footnotes). The consumption of H_2 was monitored in a reservoir connected to the reactor through a pressure regulator. The catalytic activity was expressed in terms of turnover frequency (TOF) as the amount in mol of substrate converted by mol of metal per hour at initial reaction times (conversion < 20%). The reaction total time was determined by the end of H_2 consumption. The H_2 monitoring system and the TOF calculation are described in section 3.3.7. The conversion of substrate was confirmed by gas chromatography. The GC settings are described in the section 3.3.5.

3.2.7.2. Hydrogenation of cyclohexene in gas phase

The hydrogenation of cyclohexene in gas phase was performed on an Integrated Microreactor-MS system equipped with a CATLAB-PCS Module and a QIC-20 MS Module (Hiden Analytical, UK). Typically, 15-25 mg catalyst powder were placed in a quartz tube

(length: 20 cm, width: 5 mm) with a quartz wool bed. The Ar flow was diverted to a saturator at 21 ºC filled with cyclohexene and then passed through the reactor. Flow reactant mixture containing 2:4 vol% cyclohexene:H_2 and Ar balance was passed through the reactor with a total flow rate of 50 mL min^{-1} and heated at 10 °C/min from 50 to 500 ºC. The reactions performed with O_2 followed the same conditions, but with the substitution of H_2 for O_2. Analysis of the products was carried out by on-line mass spectrometry (Hiden Analytical, UK). For the on-line analysis of the gas mixture, the mass spectrometer was operated in continuous mass scanning mode (1 scan/min.) which allows for a simultaneous monitoring of the ion current corresponding to a mass range of 75 to 90 amu for the reactants and all possible reaction products.

3.2.7.3. Hydrogenation of phenol in liquid phase

The hydrogenation of phenol was performed in a 100 mL Fischer-Porter glass reactor at constant H_2 pressure following the same procedure described for the hydrogenation of cyclohexene and benzene (Section 3.2.7.1). The phenol was solubilized previously in hexane or water (0.025 mol L^{-1}) and 3 mL of the phenol solution were added into the reactor together with 36 mg (1.25 mmol) of catalyst. The typical catalytic conditions were substrate to catalyst molar ratio of 20, constant pressure of 6 bar H_2 and 75 ºC. Additional reactions were performed with different conditions (details are provided in table footnotes). Samples were collected after 5, 15, 25 and 35 min and after 1, 2, 3, 4 and 20 h. The conversion of phenol and the products selectivity were determined by GC using biphenyl as internal standard. The GC settings are described in the section 3.3.5.

3.2.7.4. Oxidation of Benzyl alcohol

The oxidation of benzyl alcohol was performed in a 100-mL Fischer-Porter glass reactor at constant O_2 pressure. The reactor was loaded with 4 mg catalyst (Ru@PVP (4μmol), Pd@PVP (4 μmol) or Rh@PVP (4 μmol)) or 62 mg catalyst (Au@PVP, 4 μmol). The Ru, Rh and Pd@PVP nanoparticle powders were manipulated inside a glove box (MBRAUN, Germany. Water and O_2 lower than 1 ppm) and the Au@PVP nanoparticle powder was manipulated in air. Under positive flow of argon, 2 mL of benzyl alcohol (20 mmol) was added to the reactor. After the dispersion of the catalyst under magnetic stirring, the solution was divided in two 100-mL Fischer-Porter reactors (for the 2 h and 24 h reaction). The reactors were pressurized with 3 bar O_2 and heated to 100 or 150 °C for the desired time. The typical conditions applied were substrate to catalyst molar ratio of 5000 without the use of base. Conversion of benzyl alcohol and selectivity of products in the catalytic reactions were determined by GC using mesitylene as internal standard. Before injection, the samples were filtrated in celite column to remove the catalyst. The GC settings are described in the section 3.3.5.

3.3. Analysis techniques

3.3.1. X-ray diffraction

X-ray diffraction (XRD) technique consists in the irradiation of a solid sample with a parallel X-ray beam at variable angles. Due to the small wavelength (0.5 to 2.5 Å) the X-ray beam penetrates the sample and is scattered by atoms from the crystalline array (with spacing

at the order of the X-ray wavelength), which generate constructive or destructive interactions. A constructive interaction will take place when the incidence angle results in an X-ray beam 2 penetrating nλ more than X-ray beam 1, where n is an integer number and λ the X-ray wavelength (figure 3.1).

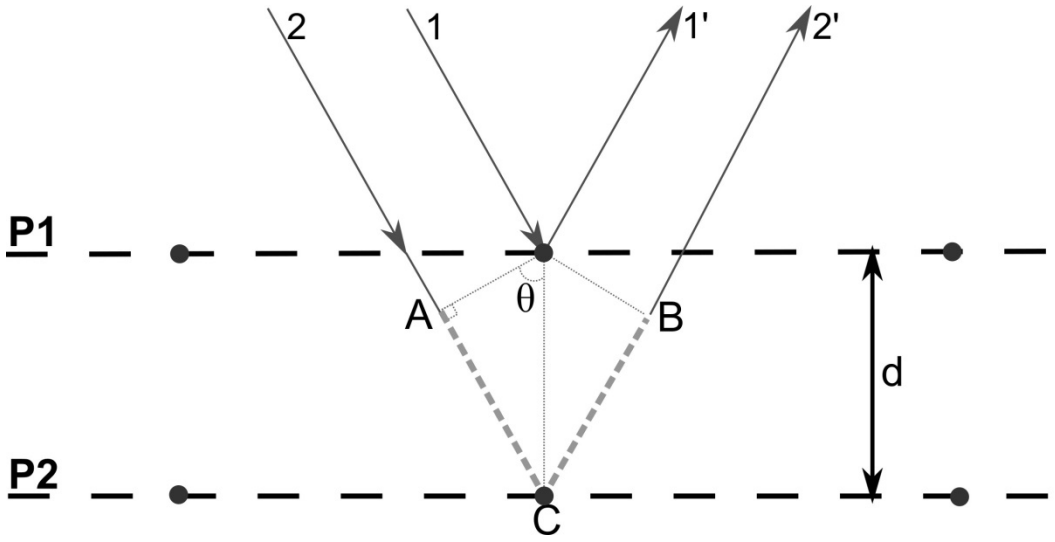

Figure 3.1. Constructive reflection of an X-ray beam.

From the figure 3.1 we see that, by definition, $\sin\theta = AC/d$ and, once, $2AC = n\lambda$, then the Bragg's law was deduced as $n\lambda = 2d\sin\theta$. The value d depends on the material, because it is one of the atoms distances in the crystalline array (of atoms, ions, etc.). In this way, the angles where a constructive interaction will take place are characteristic for each material. The X-ray diffraction patterns can be found in databases, for example Crystallographic Open Database (COD) or the International Center for Diffraction Data (ICDD).

The XRD analysis where performed in an X-ray diffratometer Ultima + (Rigaku, Japan) with Cu $K\alpha_1$ X-ray source (40kV, 20mA), 15 s per point, 15 rpm and angular step of 0.02º.

3.3.2. Transmission electron microscopy

The transmission electron microscopy (TEM) technique consists in the formation of an image by an electron beam that was transmitted through a sample. The transmission electron microscope is composed basically by an electron gun, a condenser lens, an objective lens and projective lenses. The electron gun is responsible for the electron beam generation and acceleration. The condenser lens will control the electron beam and the objective lens adjusts the image formation. The projective lenses are responsible for the magnification. The TEM microscope principle is represented in the figure 3.2.

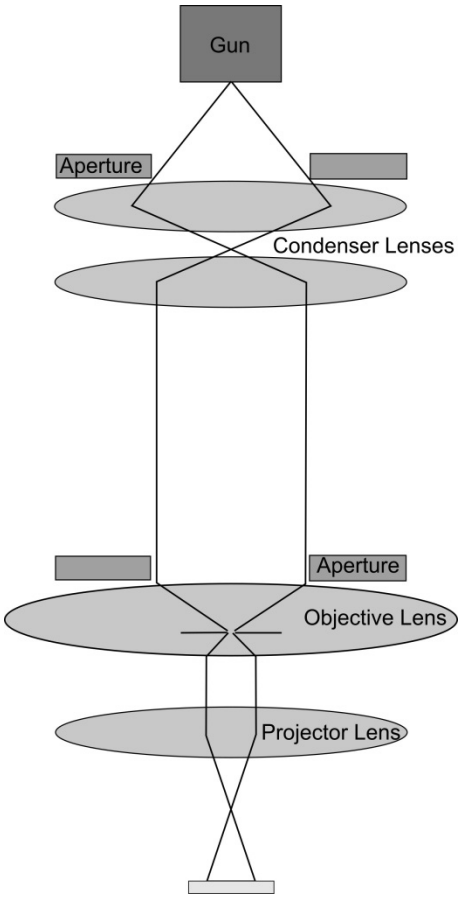

Figure 3.2. Illustration of a transmission electron microscope

One of the most important steps for TEM analysis is the sample preparation. Typically, the sample is placed on a copper grid coated with a polymer and a carbon layer. Normally, the sample is suspended in a solvent and a drop is allowed to dry over the grid. However, there are innumerous manners to deposit the sample on the copper grid.

The sample medium size can be determined by measuring of the dimensions of a large number of objects using appropriate image software. This measurement is made by the calibration of the image pixel size in relation to a known distance (scale bar). Here the particles sizes were determined using the ImageJ software, then converted into a frequency counting size distribution histogram using Origin software and fitted using a Gaussian function to obtain the average size and the size distribution value (full width at half maximum (FWHM) from a Gaussian fit).

The materials were characterized using a Philips CM200 (Prof. Pedro Kiyohara, IF-USP), JEOL JEM-2100 (LNNano, Brazil) or a JEOL JEM-1100 (TEMSCAN, France). The samples were prepared by the deposition of 4μL of a suspension in isopropyl alcohol or THF containing the nanomaterial sample in a copper grid coated with Formvar and carbon (TedPella, United States). The samples were dried under air and placed in a vacuum chamber before analysis.

3.3.3. Thermogravimetry Analysis and Differential Scanning Calorimetry

The Thermogravimetry analysis (TG) consists in the measurement of the mass sample variation in function of time or temperature. Typically, the sample is placed in an inert crucible and the system mass monitored during a temperature program. This temperature

program can be a heating ramp or an isotherm and analysis can be made under inert, reductive or oxidative dynamic atmospheres. The Differential Scanning Calorimetry (DSC) consists in the measurement of the heat flow of a sample in comparison with a standard. The DSC shows the occurrence of endothermic or exothermic process that the sample suffers as a function of temperature. Some of these processes are glass transition, phase transition, decomposition and others.

The TG curves were obtained in a thermobalance TGA-51 (Shimadzu, Japan) using dynamic atmosphere of air or N_2 (50 mL min^{-1}), heating rate of 10 ºC and sample mass between 12 and 20 mg. The DSC curves were obtained using a DSC-50 (Shimadzu, Japan) with dynamic atmosphere of N_2 (50 mL min^{-1}), heating rate of 10 ºC min^{-1} and sample mas around 3 mg.

3.3.4. Inductively Coupled Plasma Optical Emission Spectroscopy and Flame Atomic Absorption Spectroscopy

Inductively coupled plasma optical emission spectroscopy (ICP OES) and flame atomic absorption spectroscopy (FAAS) are techniques employed in the quantification of elements present in a sample. These techniques have a lot of common steps, but their detection is based in opposite phenomenon. ICP OES analyses light emitted and FAAS light absorbed. In both cases the sample is usually treated to obtain only ionic species of the desired analytes. The obtained solution is aspirated and nebulized to facilitate the atomization by argon plasma (ICP OES) or acetylene/air flame (FAAS). ICP OES can be considered a multi elemental technique and FAAS analyzes only one element at a time. FAAS can read only one element because the light source is a hollow cathode lamp of the element under analysis. In

ICP OES, there is an optical system normally composed of an echelle monochromator that separate the emitted light before it reaches the detector. In this way, the element being detected is dependent of the configuration of the optical system and, thus, the capability to read more elements in sequence.

All the ICP OES analysis was made in the Analytical Center at the Institute of Chemistry (IQ USP) using a Spectro Arcos Spectrometer (Spectro, Germany). FAAS analysis was performed using a Shimadzu AA-6300 Atomic Absorption Spectrophotometer (Shimadzu, Japan) equipped with Photron or Hamamatsu hollow cathode lamps.

3.3.5. Gas Chromatography

The gas chromatography (GC) is based in the interaction of a sample with a stationary phase located inside a capillary column and the detection of the separated components by a detector. There are a lot of different detectors and one of the most common is the flame ionization detector (FID). FID detects the presence of a molecule by the formation of charged species in a hydrogen flame by the variation of the flame potential. This charged species are created when one component from the sample reaches the detector. Typically, FID is less sensitive for molecules with low molecular weight and with oxygen atoms. GC can be easily used for quantitative analysis by the introduction of an internal standard. The internal standard is very important due to the different response factor of different analytes and also because the injection can lead to different amount of sample introduced in the capillary column. The internal standard is used to give a relative response factor and, then, through a calibration curve recover the sample quantitative composition.

The hydrogenation of cyclohexene or benzene products were analyzed in a Shimadzu GC-2010 equipped with an auto-injector Shimadzu AOC-21 (Shimadzu, Japan) and an Rtx-Wax capillary column (30 m, I.D. 0.25 mm, Restek, United States). The detector and injector temperature was 150 ºC and the temperature program was 40 ºC for 5 min and heating to 150 ºC at 5 ºC min^{-1} holding this temperature for 5 min. The samples were diluted in cyclopentane and there was no need for an internal standard because the response factor of benzene, cyclohexene and cyclohexane are similar.

The hydrogenation/hydrodesoxygenation of phenol product analysis was performed in the same equipment with an Rtx5 capillary column (30 m, I.D. 0.25 mm, Restek, United States). The injector and detector temperature was 200 ºC and the temperature program was 40 ºC for 5 min, then heating to 135 ºC at 5 ºC min^{-1} and 150 ºC at 20 ºC min^{-1} holding this temperature for 5 min. The samples were prepared in n-hexane and biphenyl was added as an internal standard (12.5 mmol L^{-1} at the sample). The phenol conversion and product selectivity were calculated using biphenyl as internal standard.

The oxidation of benzyl alcohol products were analyzed in a HP 5890 (HP, United States) with an Rtx-Wax capillary column (30 m, I.D. 0.25 mm, Restek, United States).The injector and detector temperature was 200 ºC and the temperature program was 60 ºC for 5 min, then heating to 200 ºC at 20 ºC min^{-1} holding this temperature for 15 min. The samples were prepared in cyclohexane and mesitylene was added as internal standard (100 mmol L^{-1}).

The identification of the products by gas chromatography was done by their characteristic retention time in the developed method. The retention times were determined by the injection of a sample containing the desired analyte. The response factors were obtained with a calibration curve with standard reactants and products. The calibration curve gives the relationship between the concentration of standards and the respective ratio of their peak area corrected by the internal standard area. The correction of the analyte signal area is performed

because the amount of sample that enters the capillary column can be different for several reasons. The internal standard is an inert compound that is present in all samples in a known concentration. The peak area is linearly proportional to the product amount enabling the calculation of conversion and selectivity based on the area of the peaks obtained in the chromatogram. The conversion and selectivity was calculates as below:

$$\%Conversion = \frac{[reactant]_{initial} - [reactant]_{final}}{[reactant]_{initial}}$$

$$\%Selectivity = \frac{[product]_{desired}}{\sum products}$$

An external standard was added to avoid variations in the quantification of the products due to deviations in sample preparation and injection volume.

3.3.6. Magnetic measurements

The principle of a Superconducting Quantum Interference Device (SQUID) is the Josephson effect and the quantization of a magnetic flow in a closed circuit. The Josephson effect is characterized by the superconducting condition of a system of two superconductors connected by a thin insulating barrier (Josephson junction). In the SQUID magnetometer there are two Josephson junctions. A current will be equally divided in the absence of an external magnetic field. The application of an external magnetic field results in a screening current that generates a magnetic field that cancels the external field. When the current in the Josephson junctions exceeds a critical current, the junction change to a normal state and the potential can be detected. The value of critical current of the magnetometer is a function of the applied

magnetic field. In this way, the measurement of critical current allows the determination of the magnetic flux that goes through the dispositive.

The magnetic measurements were performed in a SQUID magnetometer XL-200 (Quantum Design, United States). The measurements of MxH were collected at 300 K from 50 to - 50 kOe and the FC/ZFC curves collected with a magnetic field of 50 Oe and from 5 to 350 K.

3.3.7. Hydrogen monitoring system

The hydrogenation reactions and the hydrogenation/hydrodeoxygenation of phenol were performed in a 100 mL Fischer-Porter glass reactor. The reactor was connected to a H_2 high pressure reservoir (stainless steel vessel equipped with a pressure transmitter 510 (Huba Control, Germany) by a pressure regulator, so the reactions were performed at constant H_2 pressure (constant supply of hydrogen as the reaction proceeds). The temperature was controlled using an oil bath and a heating plate with a temperature controller and the reaction was magnetically stirred. The hydrogenation system was depicted in figure 3.3.

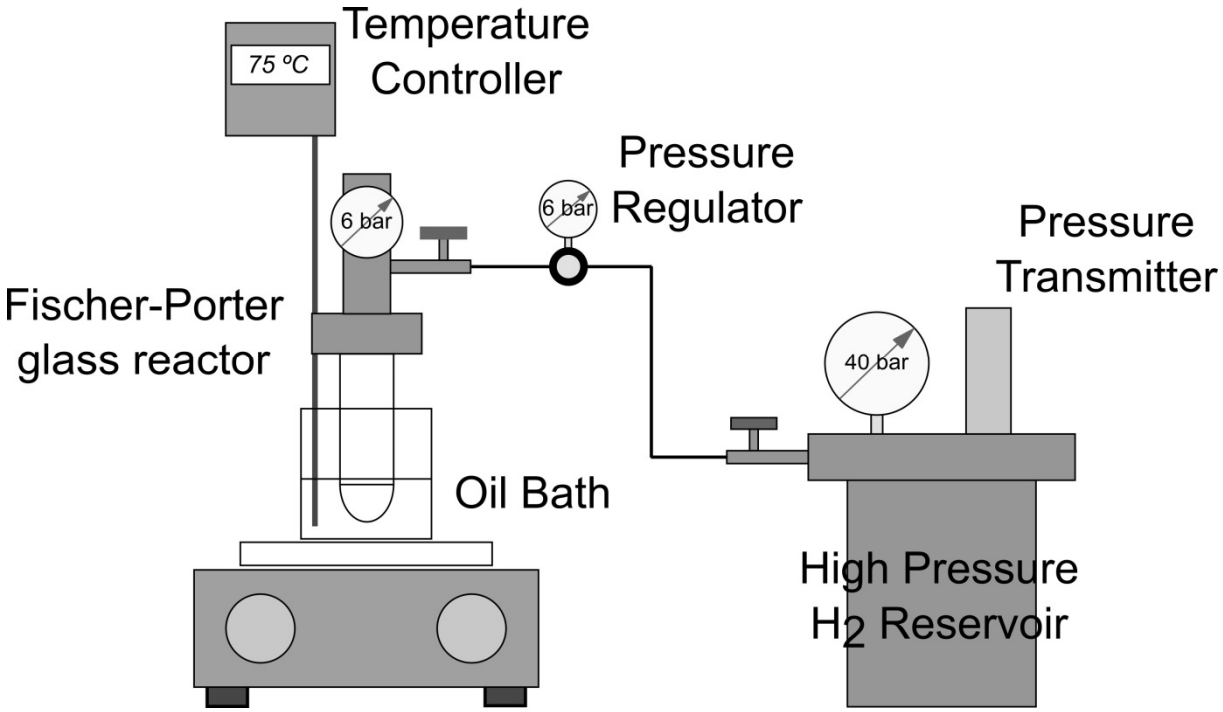

Figure 3.3. Scheme of the hydrogenation system

The pressure transmitter signal is converted (Novus Field Logger, Novus, Brazil) and the pressure of the H_2 reservoir as a function of time is recorded in a computer using the Field Chart Software (Novus, Brazil). When the reaction is no longer consuming H_2 in the monitoring system, the reactor is closed and allowed to cool to room temperature. Independently of the initial pressure at the H_2 reservoir, the consumption of hydrogen (drop in the reservoir pressure, ΔP) will be the same for a certain amount of double bonds being hydrogenated. This is true because the reservoir volume is constant and the temperature at the reservoir does not change during the reaction time (room temperature). This value of ΔP can be converted in number of mols of hydrogen consumed and consequently number of mols of double bonds hydrogenated. However, ΔP values are used as an indication if the reaction reached or not total conversion when the hydrogen consumption stopped and the true conversion is always determined by GC analysis. It is quite common that all the cyclohexene and benzene hydrogenations are able to reach total conversion.

The catalytic activity can be expressed in many different ways; e.g., the turnover number (TON), which is defined as the number of mols of substrate converted per mol (or mass or sites) of catalyst and the turnover frequency (TOF), which is defined as the number of mols of substrate converted per mol (or mass or sites) of catalyst per unit of time. We will present the TON and TOF in mol of catalysts (total mol of metal).[156] Considering that all catalysts are metal nanoparticles, the number of surface sites is difficult to determine using chemisorption techniques (CO, H_2) usually employed in heterogeneous catalysis and these techniques were not used here to avoid any misinterpretation of the results.

For these reactions that reach full conversion of the substrates, the TON is equal to substrate to catalysts molar ratio used in the reaction, otherwise it can be calculated using the reaction conversion obtained. The turnover frequency (TOF) can be determined by converting the H_2 consumption as a function of time curve into a substrate consumption (or conversion) versus time curve, which can then be converted into a TON versus time curve by multiplying each conversion data by the substrate to catalyst molar ratio value used in a particular reaction. The TOF is obtained by the linear fitting of the curve of TON against time (the linear portion of the curve which is typically obtained from initial conversion until ca. 20% conversion) (figure 3.4). The module of the angular coefficient will be the TOF, given in h^{-1}.

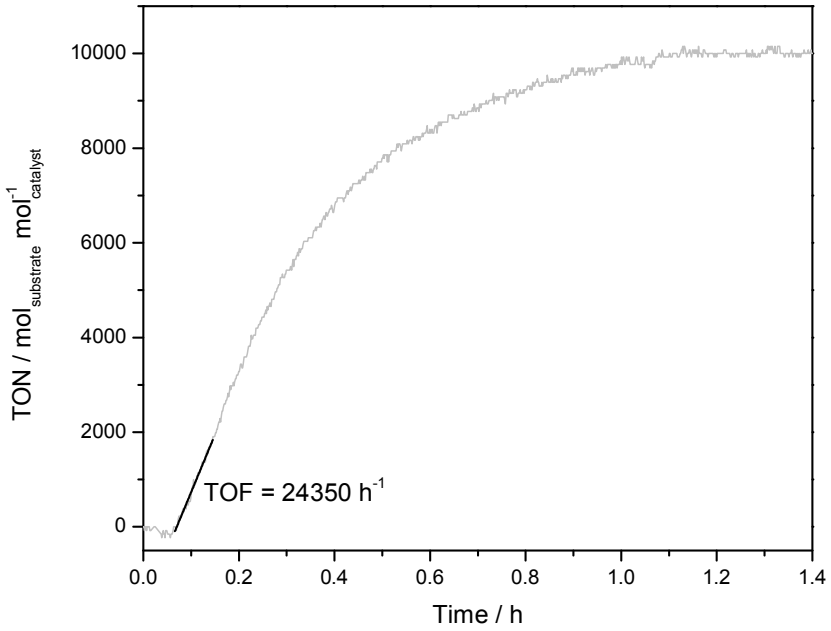

Figure 3.4. Example of the determination of TOF value

3.3.8. X-ray photoelectron spectroscopy (XPS)

The X-ray photoelectron spectroscopy is a technique that permits the determination of the chemical and electronic state and the elemental composition of a sample. Basically, the XPS consists in the irradiation with soft X-ray (ex. Al Kα 1,486 eV) of a sample under high (~10^{-8} mbar) or ultra-high vacuum (< 10^{-9} mbar) and the detection of emitted photoelectrons. The sample electrons will be excited by the X-ray and the ones with lower energy will be emitted as photoelectrons. The XPS is considered a surface analysis because electrons emitted from the sample internal part are reabsorbed, but the photoelectrons emitted from the surface can reach the detector. The XPS detector determines the kinetic energy and the amount of emitted photoelectrons. The detector has a hemi-spherical shape and the application of an electric field allows the selection of electrons with specific kinetic energies. The binding energy is determined by the subtraction of the X-ray energy from the kinetic energy of the

photoelectron. It is worth to mention that there is a work function that needs to be subtracted from the photoelectron kinetic energy, which is dependent on the spectrometer and the material. The obtained spectra can be deconvoluted in order to characterize the element species present in the sample, once the biding energies are characteristic of the element and its electronic and chemical states.

The XPS analysis were performed at high vacuum ($<5x10^{-8}$ mbar) using a hemispherical analyzer HA100 (VSW, United States) operating in FAT mode (Fixed analyzer transmission). The samples were fixed in a stainless steel support using a double-side tape.

4. RESULTS AND DISCUSSION

4.1. Development of magnetic supports

Magnetic nanoparticles have received a lot of attention as support for catalysts because of the great advantage in catalyst separation and recycle. However, the pure magnetic nanoparticles are very sensitive to oxidation, agglomeration and exhibit chemical reactivity, which are undesirable characteristics for catalysts supports. Then the encapsulation of the magnetic nanoparticles in inorganic component becomes a way to enhance the magnetic nanoparticles stability and increase their application field as catalyst supports. Silica is an important material for magnetic nanoparticle coating because it maintains the magnetic properties and promotes an equilibrium against the magnetic forces that lead to NPs agglomeration.[116, 126] Moreover, the grafting of specific ligands on silica surface is easily accomplished due to the presence of the silanol groups, which is an important characteristic in the preparation of supported molecular catalysts.[157] Nanoparticulated silica also have received a lot of attention as support due to its high surface area, rigid framework and excellent thermal and mechanical stability.[158]

Considering the importance of silica coating, here we investigated in more detail the silica-coated magnetite nanoparticle support reported elsewhere[92] in terms of synthesis, purification treatments and thermal stability. Furthermore, the silica-coated magnetic support surface was modified with functional groups and post-coated with TiO_2 and CeO_2 oxides in order to broaden the scope of magnetic supports for application in catalysis. Once silica is considered an inert support[126] in a huge variety of reactions, it is interesting to explore

magnetic supports containing surface that can promote changes in the catalytic behavior of metal nanocatalysts and by this way enhance the catalytic properties towards multifunctional catalysts.

4.1.1. Preparation and thermal behavior of silica-coated magnetite

Silica-coated magnetite was prepared using a microemulsion method adapted from the literature[147] and first published by Rossi's group in 2008.[92] This magnetic material has been routinely synthesized in our research group and used as catalyst support for the preparation of magnetically recoverable catalysts.[116] However, the evaluation of its thermal stability as well as how the silica shell formation occurs as a function of reaction time was never studied in our group. There were two main motivations for this study. The first was to control the size of the silica shell and, then, prepare a catalyst support containing less silica (more magnetite per mass of material means fast separation during magnetic separation), which would allow a post-coating process with other oxides without losing magnetic separation properties. The second motivation was to determine the thermal stability of the silica-coated magnetite (and uncoated) to understand what kind of thermal treatment can be applied to these materials without changing or losing the magnetic properties. The thermal treatment is an important step during a post-coating process with other oxides (ceria, titania, etc.). Another effect of calcination can be the enhancement of the surface area by removing the surfactants adsorbed at the silica shell.

The first step was the optimization of the reaction time. The coating of magnetite was typically prepared in 16 h reaction time. In order to follow the evolution of silica shell thickness in function of the reaction time, samples were collected from the same

microemulsion in 1, 2, 6, 12, 24 and 48 h. The same washing procedure was performed for all samples and their morphology and size were analyzed by TEM. Figure 4.1 displays the TEM micrographs and corresponding size distribution histograms. Figure 4.2 displays an analysis of the silica shell growth as a function of reaction time.

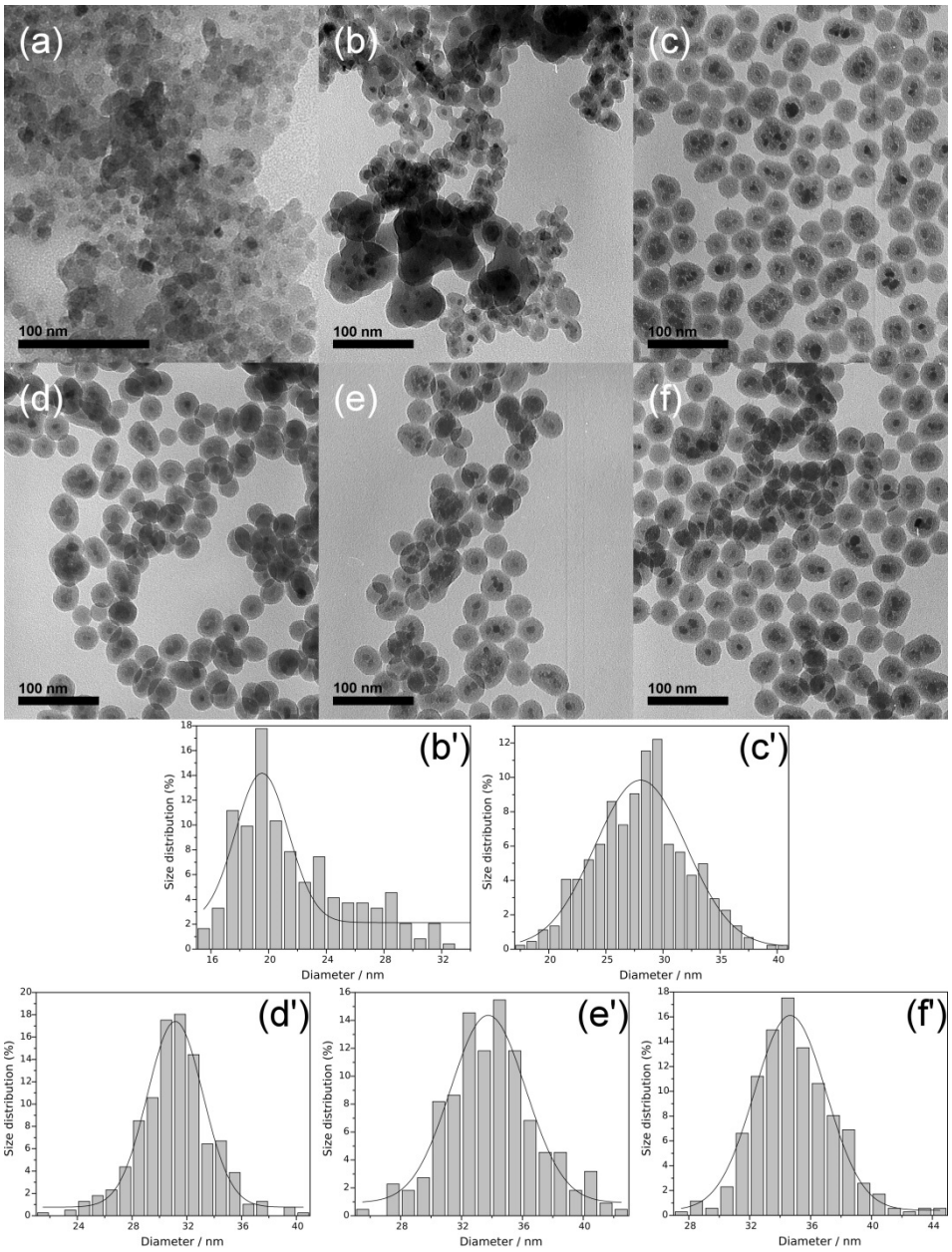

Figure 4.1. Micrographs obtained by TEM of the silica-coated magnetite prepared with reaction time of (a) 1h, (b) 2 h – 20.1 ± 1.3 nm, (c) 6 h – 28.0 ± 2.0 nm, (d) 12 h – 31.2 ± 1.0 nm, (e) 24 h – 33.8 ± 1.2 nm and (f) 48 h – 34.7 ± 1.2 nm. The corresponding size distribution histograms fitted to Gaussian function are shown in (').

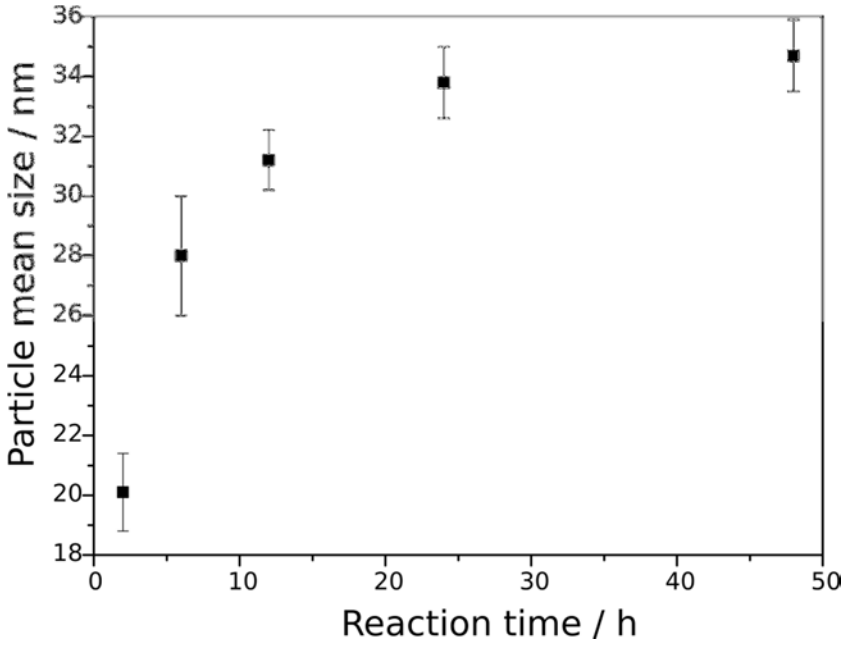

Figure 4.2. Silica-coated magnetite particle size as a function of reaction time.

The sample collected after 1 h showed a high aggregation level and we were not able to estimate the particle size (not included in figure 4.2). Similarly, the aggregation level in the sample collected after 2 h is also high; however, we were able to estimate an average particle size, despite the material's pearl-necklace structure. The aggregation observed for these samples are due to the high concentration of unreacted TEOS in the alcoholic phase, which promotes the material aggregation during the separation and washing procedures. The separation of the material from the microemulsion is a critical step to obtain a high quality material and this has been discussed in the literature. Wang *et al.*[159] reported the comparison of different methods to separate and wash silica-coated Ag NPs prepared by a similar reverse microemulsion. The authors demonstrated that the sedimentation washing procedure resulted in aggregation and washing by Soxhlet extraction caused dissolution of the silica shell. However, ethanol (the solvent used in washing by Soxhlet extraction) is not expected to cause silica corrosion. The authors indicated that the washing procedure by Soxhlet extraction was the better procedure, although by our experience and observation the centrifugation procedure

shows excellent results. The material obtained after 6 h of reaction is comprised of well-defined spherical core-shell magnetite-silica nanostructures with a final size of 28.0 ± 2.0 nm. The silica shell slightly grows after longer reaction times and reached 34.7 ± 1.2 nm after 48 h of reaction (figure 4.2).

Further experiments were performed using the material prepared with a reaction time of 6 h. This time is enough to obtain a material with a silica shell of ca. 10 nm and the formation of silica spheres without magnetic cores is negligible. Also, the amount of TEOS remaining in the reaction media does not promote aggregation during the separation and washing procedures. This material will be denoted as $Fe_3O_4@SiO_2$.

The thermal behavior of the silica-coated magnetite was evaluated by TG/DTG and DSC. Figure 4.3 shows the TG/DTG result for $Fe_3O_4@SiO_2$ under dynamic atmosphere of air and N_2. There are two main mass loss processes that sum ca. 15 % of mass loss. The first one represents a loss of ca. 6 % and is related to loss of water adsorbed in the silica shell. The second step is related to the loss of organic matter of ca. 9 %. As expected, the second mass loss process occurs at a higher temperature for heating under N_2 atmosphere when compared to air atmosphere. The figure 4.4 presents the TG/DTG analysis obtained for authentic samples of IGEPAL CO-520 and oleic acid. Comparing the temperatures for the decomposition of the surfactant and oleic acid with the second mass loss process in the silica-coated magnetite nanoparticles, it is clear that the organic material being decomposed from $Fe_3O_4@SiO_2$ corresponds to the residual surfactant, which was not completely eliminated during the washing process.

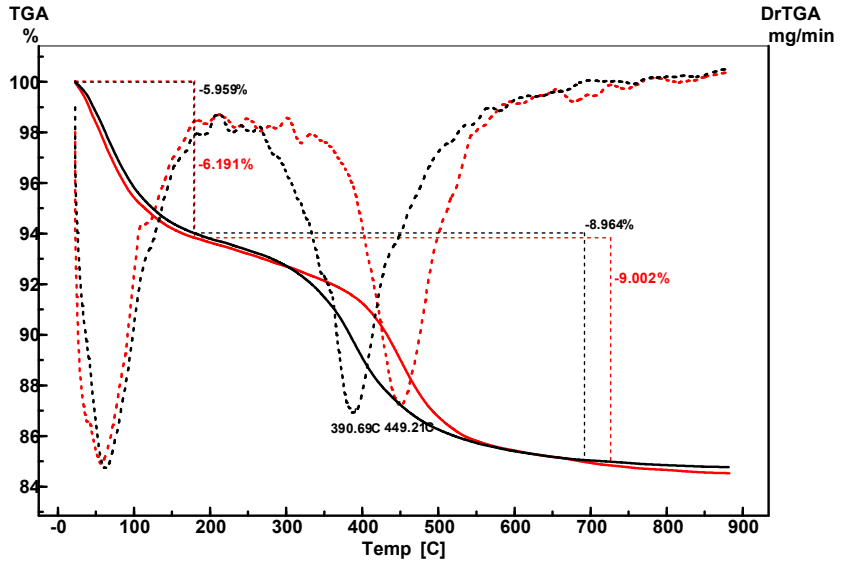

Figure 4.3. TG (solid) and DTG (dashed) obtained with the Fe_3O_4@SiO_2 at a heating rate of 10 ºC min-1 and dynamics atmosphere of air (black) and nitrogen (red).

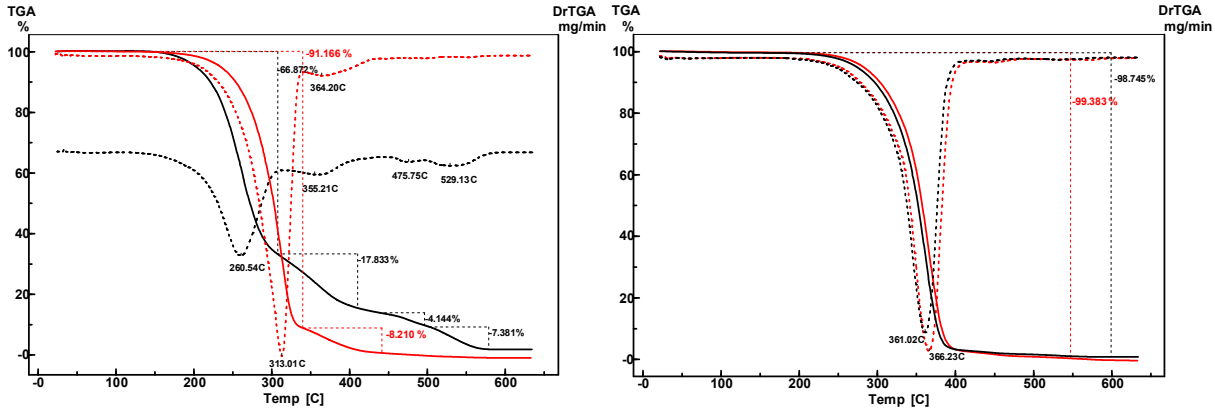

Figure 4.4. TG curves (solid) and DTG (dashed) obtained with (a) oleic acid and (b) IGEPAL CO-520 at a heating rate of 10 ºC min^{-1} and dynamic atmosphere of air (black) and of nitrogen (red).

Figure 4.5 displays DSC curves of bare magnetite nanoparticles (Fe_3O_4 prepared by co-precipitation) and silica-coated magnetite nanoparticles. The DSC analysis of the magnetite exhibits a peak after 500 ºC that can be assigned to an oxidation process, most probably its conversion into maghemite (Fe_2O_3). In fact, the material obtained after calcination at 500 ºC for 2 h has dramatically changed magnetic properties, possessing a very poor magnetic response when compared to the original magnetite sample. The material is

capable to align in the magnetic field, but is not pulled by the magnet. In the DSC curve for Fe_3O_4@SiO_2, the process at ca. 400 ºC that was assigned to the surfactant decomposition was observed, but the process attributed to the magnetite oxidation is not present. These results suggest that the silica layer protects the magnetite core against oxidation.

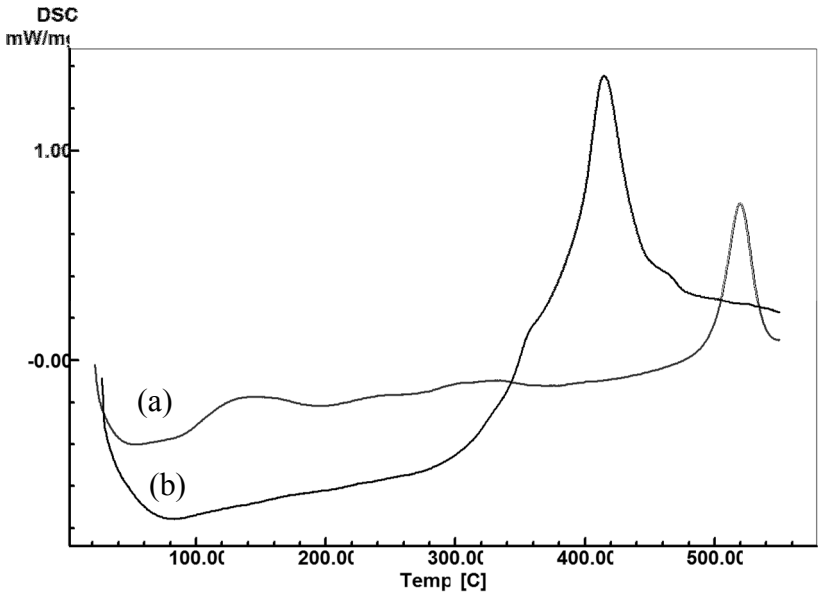

Figure 4.5. DSC curves obtained for (a) pure magnetite and (b) silica-coated magnetite.

The surface area of the silica-coated magnetite before and after calcination was evaluated by BET analysis. The as prepared solid has a surface area measured as 18 m^2 g^{-1} and the solid after calcination resulted in a surface area of 111 m^2 g^{-1}. Thus, the calcination procedure was able to increase the surface area by a factor of approximated 6 times. The material characterization by TG/DTG and BET suggests that the solid may have changed its morphology, once mass is being lost and surface area is increasing after calcination. In order to evaluate morphological modification, the material after calcination was analyzed by TEM. Figure 4.6 presents the silica-coated magnetite NPs after calcination. The core-shell morphology and the size of the silica nanospheres were preserved. The morphology and size is quite similar to the as prepared sample shown in figure 4.1b. The average size for the

calcined material was determined as 28.1 ± 1.2 nm. The difference in size is negligible and indicates that the change in surface area does not come from morphology changes, but from the removal of organic matter present in the pores and surface of the silica shell.

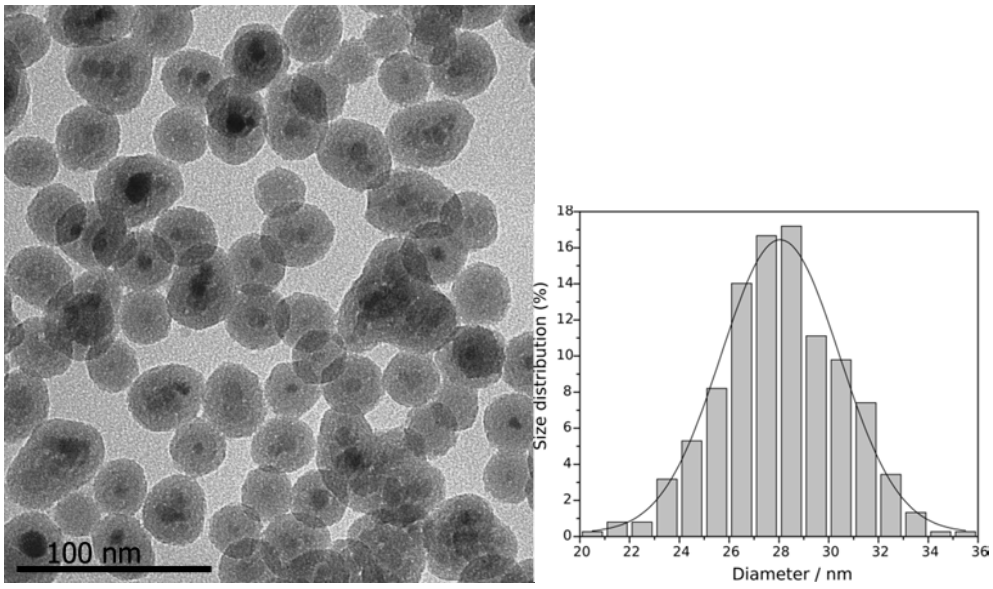

Figure 4.6. Micrograph obtained by TEM of Fe_3O_4@SiO_2 after calcination and the correspondent size distribution histogram fitted to a Gaussian function

The crystallinity and the phase purity of the as prepared and calcined materials were further characterized by XRD (figure 4.7). The XRD patterns of both samples are similar with respect to peak positions and relative intensity, which indicates that the thermal treatment did not induce any modification in the magnetic core crystal phase. The XRD analysis of Fe_3O_4@SiO_2 and Fe_3O_4@SiO_2Cal revealed an amorphous phase of silica and the diffraction peaks at 30.02°, 35.40°, 43.45°, 53.75°, 57.25° and 62.95° corresponding to the indexed planes of cubic crystals of Fe_3O_4 (220), (311), (400), (422), (511) and (440), according to the crystallographic data (ICSD# 084098). The fact that the XRD are similar can indicate that the material did not undergo oxidation, but the characterization of magnetite and maghemite is

not trivial by XRD, because their diffraction patterns are quite similar. Thus, the XRD analysis was inconclusive regarding the oxidation of the magnetite core.

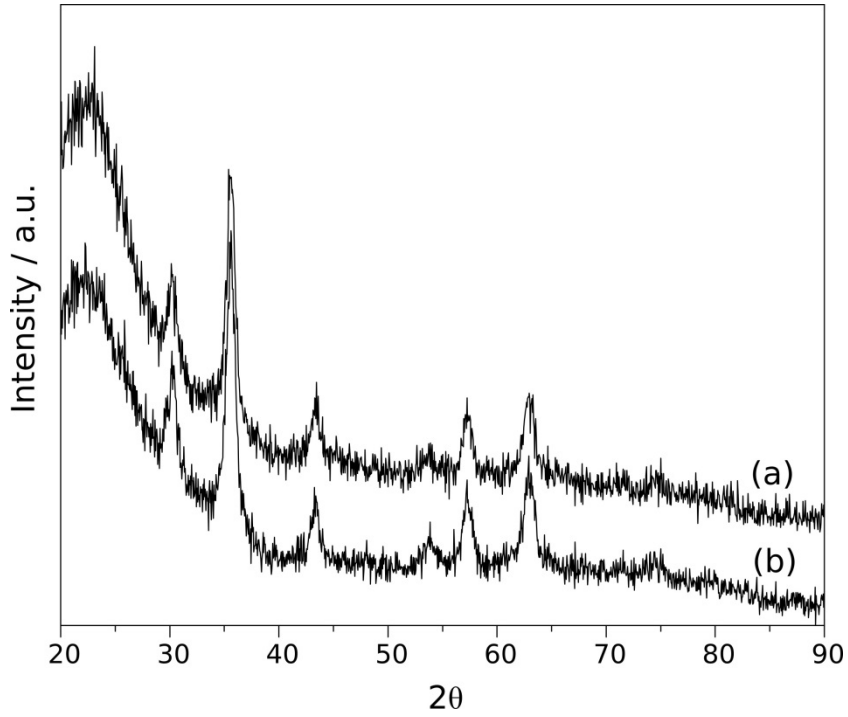

Figure 4.7. XRD diffraction pattern for silica-coated magnetite (a) before and (b) after calcination.

To fully characterize the influence of the calcination in the material's properties is necessary to evaluate its magnetic properties. The magnetization *M* as a function of the applied magnetic field, *M*(*H*), and cycles of zero field cooled (ZFC) and field cooled (FC), measured under *H* = 50 Oe and in a large range of temperature, were performed to evaluate the magnetic properties of the silica-coated magnetite nanoparticles before and after calcination. The *M*(*H*) curves taken at 300 K showed no hysteresis for both samples, with negligible coercive field and remanence (figure 4.8). This indicates that the magnetic cores are in the superparamagnetic state at room temperature before and after the thermal treatment. The magnetic properties are given in function of mass and once the calcination provoke an elimination of the organic matter it results in different proportion of non-magnetic and

magnetic material in the sample. This means that if the comparison is limited to the sample mass and magnetic response the sample before calcination will have less influence of the magnetic material than the sample after calcination. To correct this discrepancy and, then, be able to compare the two samples, the contents of iron in both samples were quantified by ICP OES. The quantification analysis resulted in 5.8% of iron in the sample before calcination and 9.1 % in the sample after calcination. The mass reduction observed in the TG is in agreement with the variation observed by ICP OES. This comparison demonstrates that the calcination procedure is enough to promote the total removal of the organic matter present in the silica shell, because any failure in the removal of organic matter would lead to a difference between the techniques. Correcting the magnetization values by the amount of magnetite in the material before and after calcination we notice that the thermal treatment caused only a slightly reduction of the saturation magnetization (*Ms*) from 83 to 72 emu g^{-1}. So, the calcination procedure provoked a reduction of ca. 13 % in the *Ms* value. The as prepared material shows a saturation magnetization around 10 - 17 % lower than bulk magnetite (92 - 100 emu g^{-1}).[160]

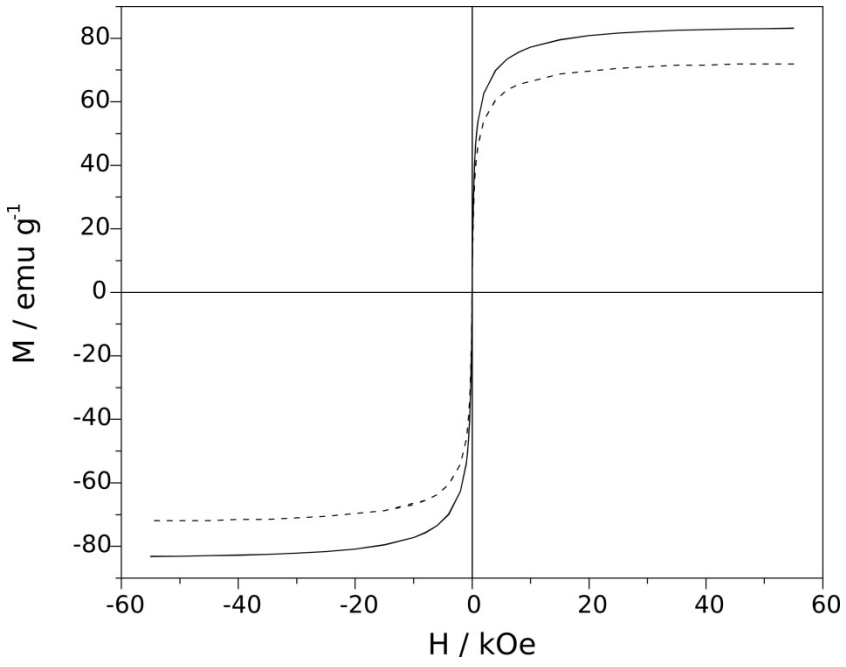

Figure 4.8. Magnetization curves for the materials Fe_3O_4@SiO_2 (solid) and Fe_3O_4@SiO_2Cal (dashed).

The reduction of the *Ms* value is a strong evidence of partial oxidation of the magnetite core. Although, the oxidation is the most likely reason for reduction of *Ms* there are other characteristics that need to be taken into account. In bulk magnetite, there are a very few atoms on the surface (surface area to volume ratio very low), so the material will have a large contribution of the bulk atoms for the magnetic response and only a small contribution of the surface atoms. The surface is not perfect and most likely presents an amorphous phase and in the case of magnetite there is oxygen deficiency in the surface. So, the crystalline phase is very important for the magnetic response and the disadvantage of decreasing particles size is the increase of surface area to volume ratio. In this sense, making magnetite nanoparticles very small can have an undesired effect of reducing the magnetic response.[161] A strategy to increase the magnetic response of very small magnetite particles is the coordination of organic acids to their surface. The acid coordination reduces the oxygen vacancies on the surface and, then, can increase the magnetic responsive volume of the particle.[161] Thus, the reduction of the magnetic response after calcination can be either related to the removal of the coordinated oleic acid by the thermal treatment or the partial oxidation of magnetite.

The cycles of zero field cooled (ZFC) and field cooled (FC) for the silica-coated magnetite nanoparticles before and after calcination (figure 4.9) revealed that the blocking temperature did not change after calcination. This is an indication that the calcination did not provoke magnetite oxidation, change in particle size or in the dipolar interactions between particles. It is worth to note that despite the small decrease in the magnetic response of the calcined material this material is capable of being magnetically separated in the presence of a neodymium magnet (4000 G) used in the separation process (catalytic studies).

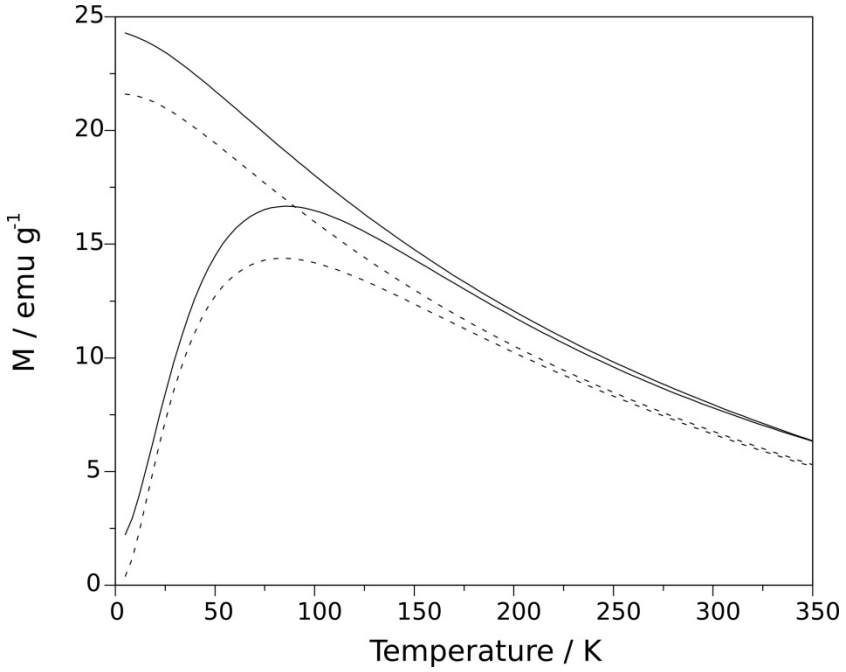

Figure 4.9. ZFC and FC curves for Fe_3O_4@SiO_2 (solid) and Fe_3O_4@SiO_2Cal (dashed) obtained under magnetic field of 50Oe.

The functionalization of the silica support with amine groups is largely employed as a strategy for the preparation of supported catalysts,[125] thus the effect of calcination (and increased surface area) on the functionalization of the silica-coated magnetite nanoparticles was evaluated. A typical functionalization using APTES was performed using the as prepared and calcined solids. The quantification resulted in 0.17 and 1 mmol NH_2 g^{-1} in the as prepared and calcined solid materials, respectively. This difference in the extension of the functionalization is directly related to the enhanced surface area of the calcined solid. This result is also an indication that the calcination procedure is not removing silanol groups from the silica surface, because a lower presence of silanol groups on the silica surface should lead to a lower functionalization extension.[162] In fact, the higher functionalization (~6 times) is comparable to the increase of six times of surface area of the calcined solid. It is also possible that some ethoxides groups are remaining in the silica after the coating and the calcination can

remove then. The removal of these groups should lead to the formation of silanol groups and, so, enhance the functionalization extension.

A summary of the all measured properties of silica-coated magnetite nanoparticles (prepared in a microemulsion for 6 h) before and after calcination is given in table 4.1

Table 4.1. Summary of silica-coated magnetite properties obtained by different techniques.

Entry	Measurement	$Fe_3O_4@SiO_2$	$Fe_3O_4@SiO_2Cal$
1	TEM	28.0 ± 2.0 nm	28.1 ± 1.2 nm
2	BET	18 $m^2 g^{-1}$	111 $m^2 g^{-1}$
3	Fe content	5.8 %	9.1 %
4	Saturation magnetization	83 emu g^{-1}	72 emu g^{-1}
5	NH_2	0.17 mmol g^{-1}	1 mmol g^{-1}

The reason why the silica layer is providing an extra protection to the magnetic cores is not totally understood, but it can be the result of different effects. The most reasonable one is the lack of accessibility of oxygen to the magnetic cores, owing to the high silica density at the inner shell. Another explanation can be the formation of Fe-O-Si bonds at the surface of the magnetite particles during the silica coating that can be more stable than Fe-OH against oxidation. In fact, the formation of this kind of bonds is reported in the literature as necessary for the transfer of magnetite particle from the organic solvent to the aqueous reverse micelle interior and promotion of silica coating. Vogt *et al.* demonstrated by FTIR the exchange of oleic acid for partial hydrolyzed TEOS on magnetic nanoparticles surface.[134]

X-ray photoelectron spectroscopy was used to determine the chemical state of the elements in the $Fe_3O_4@SiO_2$ support after calcination. The spectra of the O 1s, Si 2p and C 1s core levels have been collected and shown in figure 4.10 and the binding energy (BE) are summarized in table 4.2. The O 1s XPS spectrum depicted in figure 4.10 shows the presence

of two oxygen components at BE 530.3 and 533.0 eV. The peak at BE of 533.0 eV is to bulk SiO_2.[163]The peak at BE of 530.3 eV can be attributed to surface hydroxyl groups, but this peak is very often present in several oxides.[164] In addition to this, the peak corresponding to C 1s core-level was registered at 284.55 eV (C–C/C–H).[165] The presence of carbon is an indication that either the calcination procedure did not remove all the carbon from the silica shell/magnetic material or it is due to adventitious carbon contamination.

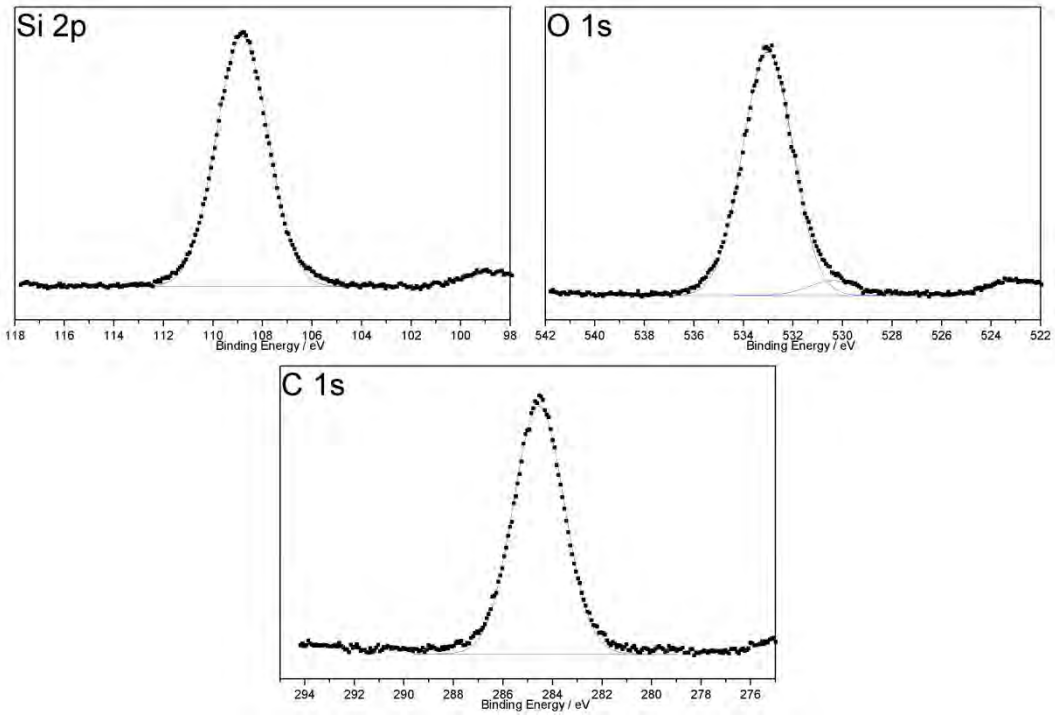

Figure 4.10. XPS spectra of O 1s, Si 2p and C 1s core-level obtained with Fe_3O_4@SiO_2

Table 4.2. Binding energies of O 1s, Si 2p and C 1s core levels observed in XPS analysis of Fe_3O_4@SiO_2

Entry	Element	Binding Energy / eV
1	C	284.55
2	O	530.34
3		533.02
4	Si	108.82

The studies about the thermal stability of silica-coated magnetite and their properties after calcination revealed that the coating with silica preserved the magnetic properties of the magnetic cores, even though the magnetic properties of pure magnetite are severely changed upon heating. The possibility of preserving the magnetic properties upon calcination at 500°C is a very important behavior that, in principle, expands the preparation of coated magnetite with other metal oxides than silica. Typically, a calcination step is involved in the preparation of oxides such as titania, alumina, ceria, etc. In the next sections, we will describe the preparation of magnetite coated with other oxides, i.e., ceria and titania.

4.1.2. Preparation of titania-coated magnetite: post-coating process

The initial goal was the deposition of titania directly on the magnetite surface. Thus the first attempt was the substitution of TEOS for titanium(IV) isopropoxide (TTIP) in the reverse microemulsion method. However, the addition of TTIP in the reaction medium resulted in the almost instantaneously formation of a white precipitate as the result of a fast hydrolysis. The major challenge is to control the hydrolysis rates that is higher for titanium alkoxides compared to their silicon counterparts. This higher rate of hydrolysis of TTIP is an intrinsic property of the molecule. For silicon alkoxides the Si-O-R bond has a covalent character, however, for titanium, this character is more ionic. In order to avoid the fast hydrolysis of TTIP and be able to prepare a titania-coated magnetite some modification were made on the reverse microemulsion method. The first attempt was the substitution of ammonia solution for water, but this substitution delayed the precipitation only in few seconds. In fact, only 30 seconds after the TTIP addition the solution started to become turbid and after few minutes the precipitation was observed. The precipitate was formed in two

steps. The initial solution was only turbid and then started to precipitate. Thus, it is very reasonable to consider new experiments using less TTIP. The TTIP addition was varied from 1 to 50 % of the initial amount and water was used instead of ammonia solution. However, even with only 1% of TTIP precipitation was observed. The precipitation was also observed for a microemulsion prepared in the absence of magnetite nanoparticles, which suggests that the precipitation of the microemulsion with TTIP was not caused by any interaction with the magnetite nanoparticles.

The role of ammonia used in the microemulsion for the preparation of silica-coated magnetite is to accelerate the hydrolysis rate of TEOS, but it also acts as a growth controller. This happens because the surface of oxides has a formal negative charge, which would attract the ammonium cations. The presence of ammonium cations hinders the surface growth, due to an electrostatic repulsion. Consequently, the substitution of ammonia solution for water reduces the hydrolysis rate, but might have a detrimental effect of removing the ammonium growth control. Thus, ammonia solution was used for a new series of experiments with various amounts of TTIP (from 1 to 50 %). However, the same behavior was observed.

With the aim to reduce the hydrolysis rate and avoid the microemulsion precipitation, we used a titania precursor with a lower hydrolysis rate than TTIP thanks to higher steric hindrance namely titanium(IV) 2-ethylhexyloxide (TEO). However, this substitution led to only a small difference on the precipitation time. The TEO started to precipitate after a longer time when compared to TTIP, but still was not able to control the growth of a shell of titania on magnetite.

In the literature, Kwon *et al.*[166] described the coating of gold nanoparticles with titania using TTIP. The authors used triethanolamine to reduce the hydrolysis rate of TTIP. The reduction of the hydrolysis rate was attributed to the formation of a complex between the triethanolamine and TTIP. We first noticed that a solution of triethanolamine and TTIP

prepared in isopropyl alcohol can be diluted in water without causing precipitation. Thus, this solution was added to the reverse microemulsion (without the addition of magnetite). The microemulsion become turbid just after the addition of the triethanolamine/TTIP solution, but the solution remained stable (without precipitation) for 30 min. The morphology of the material prepared using triethanolamine/TTIP solution was investigated by TEM. The micrograph presented in figure 4.11 showed particles with spherical morphology, but without control on the particle size.

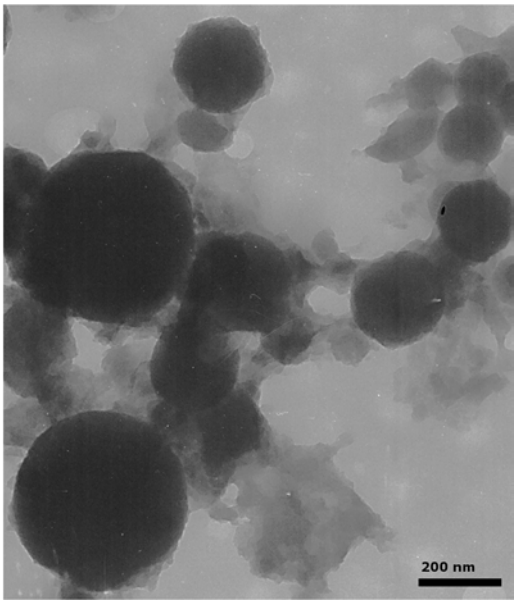

Figure 4.11. TEM micrograph of titania spheres prepared using the complex triethanolamine/TTIP.

Again, the substitution of ammonia solution by water did not result in any particular advantage to avoid precipitation. The utilization of isopropyl alcohol as solvent for TTIP/triethanolamine solution is also a point of concern to the microemulsion stability, because alcohols are typically used to precipitate reverse microemulsions. We next tested the addition of several alcohols to the reverse microemulsion, but the amount of alcohols added did not cause phase segregation. The alcohols added were methanol, isopropyl alcohol, 1-butanol, 1-heptanol and 1-dodecanol and none of them affected visually the stability of the

microemulsion. Similarly, the addition of a solution of triethanolamine did not cause a visual effect on the stability of the microemulsion. However, the direct mixture of TTIP and triethanolamine resulted in the hydrolysis of TTIP and precipitation. These observations suggest that the hydrolysis rate is still a problem for the titania coating following this methodology.

A further search in the literature showed that the coating of magnetite with titania is not trivial and most of the studies report materials with poor morphology control.[138, 167] In fact, some materials referred as core-shell nanomaterials are, in fact, comprised of random mixture of TiO_2 and magnetite. However, the results reported by Alvarez *et al.*[138] showed that the presence of a first coating with a silica layer can improve the morphology of titania deposition, when it is added through a post-coating step. Among the many post-coating methodologies reported in the literature, the one used to prepare a "yolk shell" like nanostructures called our attention and was selected for further studies. Güttel *et al.*[149] described the preparation of Au NPs encapsulated in hollow TiO_2 spheres ("yolk shell"). We thus adapted the methodology described above for the post-coating of Fe_3O_4@SiO_2 with titania. Figure 4.12 shows the micrograph obtained by TEM/HRTEM for the Fe_3O_4@SiO_2TiO_2 material obtained after calcination at 500 ºC. The material exhibits a morphology comprised of silica spheres (ca. 25-30 nm) that contain magnetic nanoparticles in the core (ca. 10 nm) and additional TiO_2 nanoparticles of about 5 nm decorating the silica shell (figure 4.12a) can be observed. EDS analysis of the small nanoparticles at the solid surface (dashed region in figure 4.12b) revealed Si and Ti atoms (figure 4.12c) and analysis of the whole nanostructure revealed the presence of Fe, Ti and Si atoms (figure 4.12d). The absence of Fe signal when the surface of the particle was analyzed is an indication that the crystalline particle in the surface is not magnetite. On the other hand the presence of Ti

demonstrates that the particle at the surface is TiO_2. The amount of TiO_2 in the Fe_3O_4@SiO_2TiO_2 is around 8 wt% (nominal).

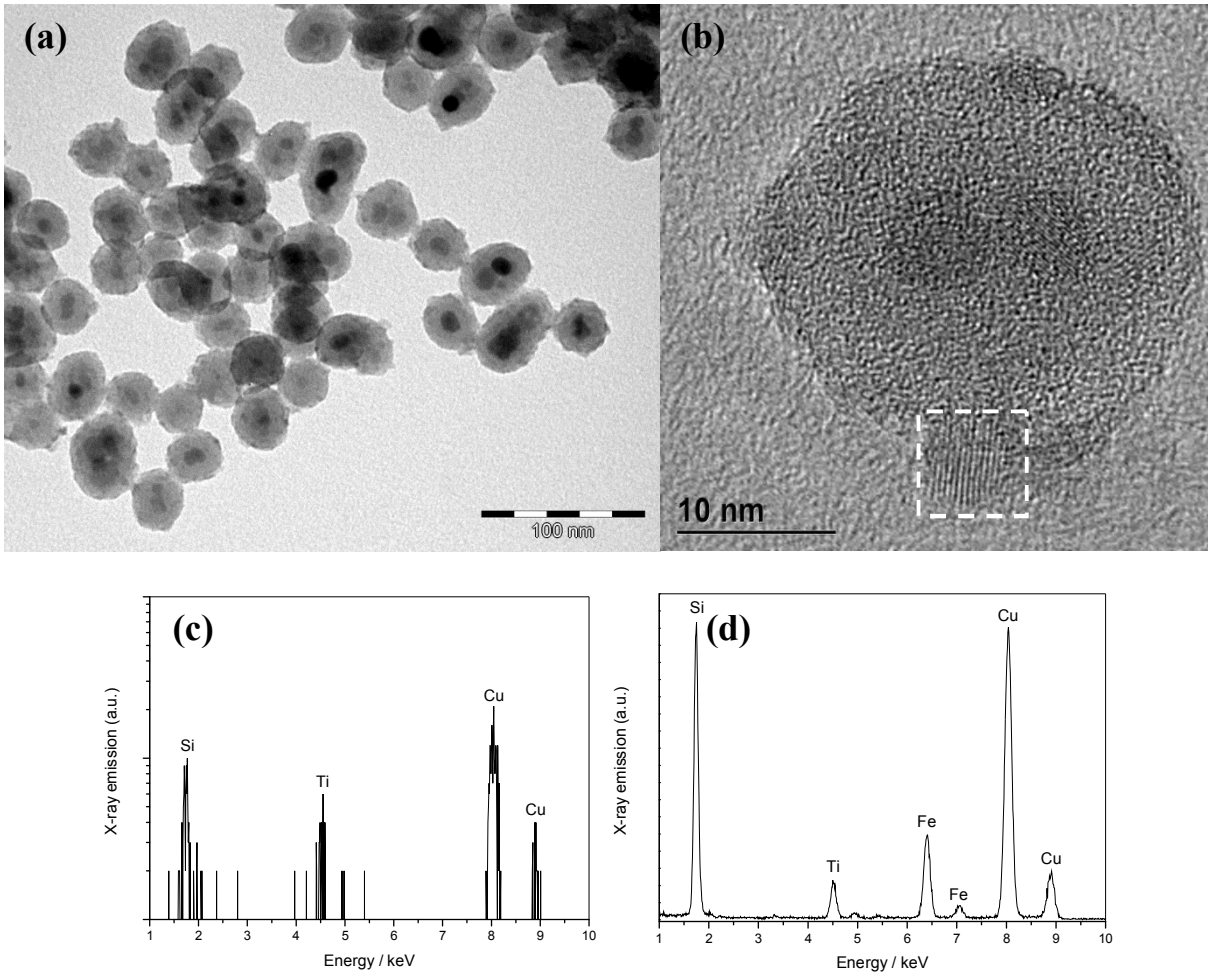

Figure 4.12. Characterization of Fe_3O_4@SiO_2TiO_2: micrograph obtained by (a) TEM and by (b) HRTEM and Energy dispersive X-ray spectroscopy (EDS) analysis of the (c) particle surface and (d) whole particle.

The TEM analysis revealed that the deposition of titania occurs as a mixture of nanoparticles and shell coating. Although, the XRD analysis of Fe_3O_4@SiO_2TiO_2 revealed the diffraction peaks of Fe_3O_4, but it does not contain any characteristic diffraction peaks expected for titania anatase or rutile phases (figure 4.13). However, HRTEM analysis of the small particles on the silica surface corroborates the presence of TiO_2 nanoparticles with an

interplanar distance of 3.71Å. This interplanar distance corresponds to the (1 0 1) Bragg plane of anatase phase of TiO_2.[168]

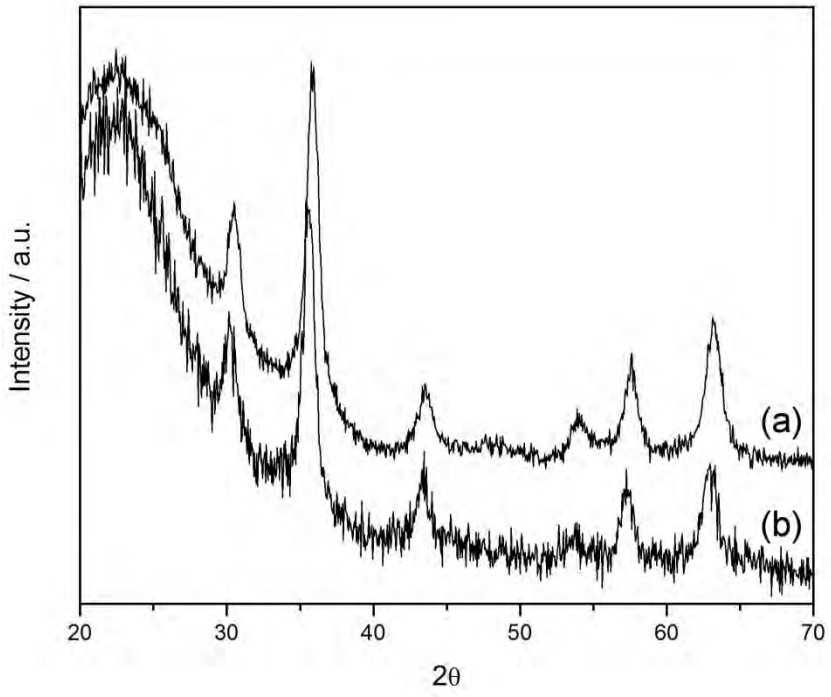

Figure 4.13. XRD pattern for $Fe_3O_4@SiO_2TiO_2$ (a) and $Fe_3O_4@SiO_2$ (b).

X-ray photoelectron spectroscopy was used to determine the chemical state of the elements in the $Fe_3O_4@SiO_2TiO_2$. The C 1s, O 1s, Si 2p and Ti 2p photoelectron peaks were detected in the XPS measurements and figure 4.14 shows the spectra and table 4.3 summarizes the BE.

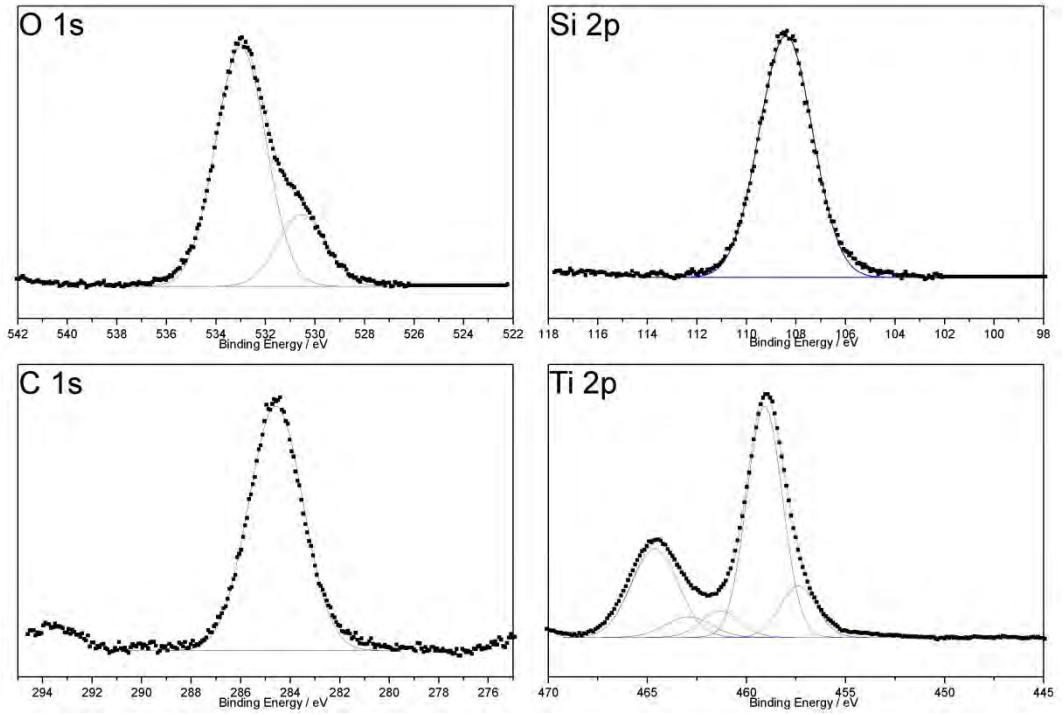

Figure 4.14. XPS spectra of O 1s, Si 2p, C 1s and Ti 2p core-level obtained with $Fe_3O_4@SiO_2TiO_2$

Table 4.3. Binding energies of O 1s, Si 2p, C 1s and Ti 2p core levels observed in XPS analysis of $Fe_3O_4@SiO_2TiO_2$

Entry	Element	Binding Energy / eV
1	C	284.55
2	O	530.53
3		533.00
4	Si	108.41
5	Ti	464.63
6		462.93
7		461.30
8		459.09
9		457.40

As for $Fe_3O_4@SiO_2$, the O 1s spectra showed two oxygen components. But, the oxygen component at BE 530.5 eV can been assigned to TiO_2.[163-164] The oxygen arising from

TiO_2 appears around 530 eV, which is the same energy as surface hydroxyl groups, and could lead to some errors if quantitative measurements are required. However, the intensity of the oxygen component at BE 530 eV increases after the post-coating process used for the deposition of titania (figure 4.14), which allows a qualitative analysis of the deposition of titania on silica. Moreover, the BE of $Fe_3O_4@SiO_2TiO_2$ increased about 0.7 eV with respect to the BE of pure titania at 529.8 eV,[169] which may be assigned to a decrease of basicity of surface oxygen ions, which arises from the enhancement of their coordinative unsaturation as a consequence of the very small titania particle size.

The XPS spectrum of the Si 2p core level of $Fe_3O_4@SiO_2TiO_2$ support exhibits one component at BE 108.4 eV. This BE is very close to the observed for $Fe_3O_4@SiO_2$ indicating that the silica shell was preserved. Figure 4.14 shows the Ti 2p XPS spectrum, which consists of a doublet. At the lower binding energy region, the peak is assigned to Ti 2p3/2 whereas the higher energy region is owing to the binding energy at the atomic orbital of Ti 2p1/2. Each one was fitted into two components for Ti^{4+} and Ti^{3+}species. The two Ti^{4+} peaks were observed at 464.6 and 459.1 eV, which agreed with Ti^{4+} in pure anatase TiO_2 form.[170] The two Ti^{3+} peaks are observed at 457.57 and 462.93 eV is very similar to reported values.[163] The peak separation of 5.54 eV for Ti^{4+} and 5.36 eV for Ti^{3+}between the Ti 2p1/2 and Ti 2p3/2 signals excellently agreed with the reported values in the literature.[163] The peak at BE 461.30 eV is related to the emission of the X-ray source. Again a peak corresponding to C 1s core level was registered at BE 284.9 eV (C–C/C–H) and is assigned to carbon contamination.[165]

The deposition of titania was performed using titanium(IV) isopropoxide, but the XPS analysis demonstrated the presence of Ti^{3+}. The composition percentage of Ti^{4+} and Ti^{3+} determined by the area of the respective peaks is 82 and 18 %, respectively. The presence of Ti^{3+} is very interesting and might be a consequence of the experimental conditions. The silica-coated magnetite is an insulator, so the X-ray irradiation generates a positive charge that is

compensated by an electron beam. The electron beam might be the reason for the reduction of Ti^{4+} to Ti^{3+}.

4.1.3. Preparation of ceria-coated magnetite: post coating process

Ceria deposition on $Fe_3O_4@SiO_2$ was performed using a post-coating step, as previously described for $Fe_3O_4@SiO_2TiO_2$. Based on the results with titania and also due to the lack of examples in the literature about coating of magnetite with ceria, we did not put too much effort to try to coat magnetite directly with a shell of ceria. The deposition of ceria particles on $Fe_3O_4@SiO_2$ was achieved by an impregnation step followed by calcination. $Fe_3O_4@SiO_2$ was treated with ammonium cerium nitrated in ethanol under stirring at room temperature for 20 h. The solid obtained after centrifugation and drying was calcined at 500 ºC for 2 h. The material obtained was characterized by TEM (figure 4.15a). The EDS analysis shows the presence of cerium on the silica surface. The material exhibits a morphology comprised of silica spheres (ca. 25-30 nm) that contains magnetic nanoparticles in the core (ca. 10 nm) and additional CeO_2 nanoparticles of about 2.6 ± 0.4 nm decorating the silica shell (figure 4.15b). The amount of deposited CeO_2 is around 2 wt% (nominal).

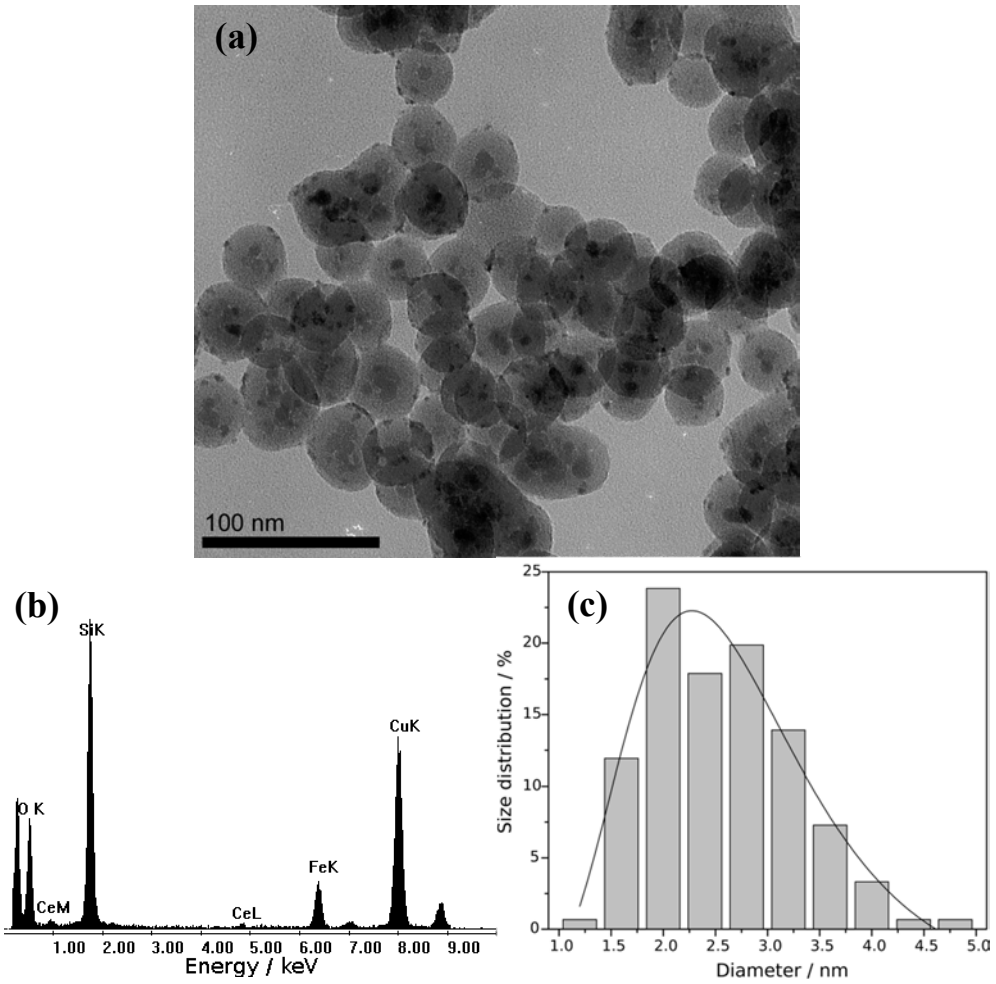

Figure 4.15. Characterization of Fe_3O_4@SiO_2CeO_2: (a) micrograph obtained by TEM, (b) Energy dispersive X-ray spectroscopy (EDS) analysis and (c) Lognormal adjusted size distribution histogram.

The XRD analysis of Fe_3O_4@SiO_2CeO_2 revealed the diffraction peaks of Fe_3O_4, an amorphous phase of silica, and the diffraction peaks of ceria with face centered cubic phase characterized by the Bragg diffractions at 2θ of 28º (111), 33º (200) and 47º (220) (figure 4.16). The peak attribution was made by the comparison with the crystallographic file JCPDS#810792. The broad diffraction peaks result from the small ceria nanoparticle size.

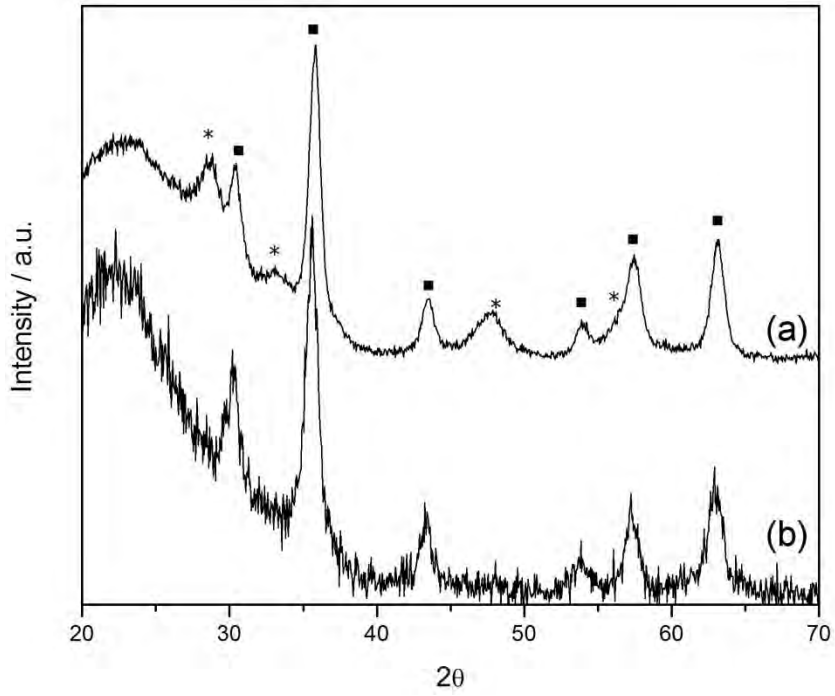

Figure 4.16. XRD pattern of (a) Fe_3O_4@SiO_2CeO_2 and (b) Fe_3O_4@SiO_2. The peaks attributed to magnetite are indicated with ■ and to ceria with *.

X-ray photoelectron spectroscopy was used to determine the chemical state of the elements in the Fe_3O_4@SiO_2CeO_2 supports. The Ce 3d photoelectron peaks were present in the Fe_3O_4@SiO_2CeO_2 sample and, as described before, the C 1s, O 1s and Si 2p photoelectron peaks were also detected. The spectra of the O 1s, Si 2p and Ce 3d core levels have been collected and shown in figure 4.17 and the BE are summarized in table 4.4.

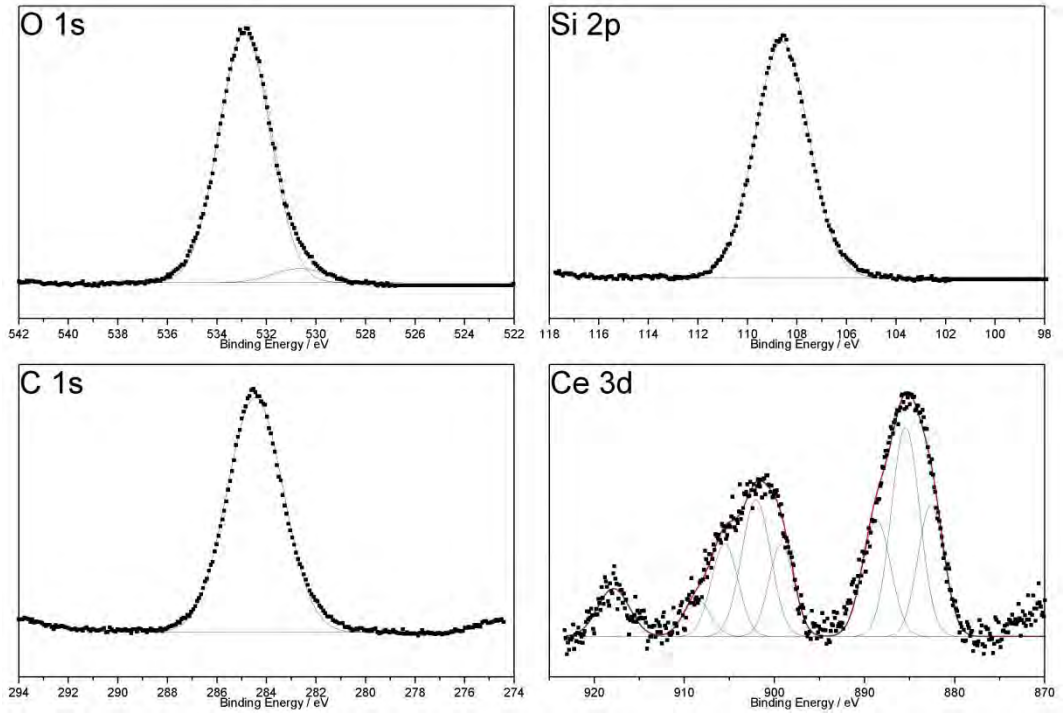

Figure 4.17. XPS spectra of O 1s, Si 2p, C 1s and Ce 3d core-level obtained with Fe_3O_4@SiO_2CeO_2

Table 4.4. Binding energies of O 1s, Si 2p, C 1s and Ce 3d core levels observed in XPS analysis of Fe_3O_4@SiO_2CeO_2

Entry	Element	Binding Energy / eV	Ce 3d attribution
1	C	284.45	
2	O	530.68	
3		532.88	
4	Si	108.61	
5	Ce	917.87	u'''
6		909.21	u''
7		906.30	u'
8		903.26	u
9		900.03	v'''
10		888.44	v''
11		885.33	v'
12		882.63	v

The O 1s XPS spectrum of $Fe_3O_4@SiO_2CeO_2$ shows two oxygen components; however, as described for $Fe_3O_4@SiO_2TiO_2$ the oxygen component at BE 530.7 eV can also been assigned to CeO_2.[164, 171] The intensity of the oxygen component at BE 530 eV also increases after the ceria post-coating process (figure 4.17), which, as mentioned for TiO_2, indicates a qualitative characterization of ceria deposition on silica. Again as for TiO_2, the BE of $Fe_3O_4@SiO_2CeO_2$ increased about 2.1 eV with respect to the BE of pure ceria at 528.6 eV,[171-172] which may be assigned to a decrease of basicity of surface oxygen ions due to small ceria NPs. Figure 4.17 shows the XPS spectra of the Si 2p core level of $Fe_3O_4@SiO_2CeO_2$ supports which exhibits one component at BE 108.6 eV. Figure 4.17 shows the XPS spectrum of the Ce 3d core level of the $Fe_3O_4@SiO_2CeO_2$ support. The spectra was fitted into 8 components in accordance with Burroughs *et al.*, where the components u, u", u"' and v, v", v"' are attributed to Ce^{4+} 3d. Also, the components v' and u' are attributed to Ce^{3+} 3d.[173] The components v_0 and u_0 were not observed due to the low concentration of Ce in the sample that results in low signal to noise ratio.[174] The components u, u", u"' and v, v", v"' were observed at BE 903.26, 909.21, 917.87, 882.63, 888.44 and 900.03 eV, respectively. The components u' and v' were observed at BE 906.30 and 885.33 eV, respectively. Thus, the Ce 3d core level spectrum demonstrates the presence of 69 and 31 % of Ce^{4+} and Ce^{3+}. In addition to this, peaks corresponding to C 1s core-level were registered for all used catalysts at 284.9 eV (C–C/C–H).[165]

The deposition of ceria was performed using ammonium cerium(IV) nitrate, but the XPS analysis demonstrated the presence of Ce^{3+}. As observed for TiO_2 deposition, the presence of Ce^{3+} might be a consequence of the experimental conditions related to the charge compensation.

4.2. Development of magnetically recoverable metal nanoparticle catalysts

Different methods were employed to obtain magnetically recoverable metal nanoparticle catalysts using the magnetic supports developed in the first part of this Thesis. Initially, the results obtained for Rh and Pd nanoparticle catalysts prepared using metal salts, $RhCl_3.xH_2O$ or Na_2PdCl_4, will be presented and discussed. These catalysts were prepared by an IMP method and by the SI method with preformed metal nanoparticles prepared using metal salts and the support $Fe_3O_4@SiO_2$. Later, the discussion will focus on Rh, Pd and Ru nanoparticle catalysts prepared by the SI method with metal nanoparticles prepared using organometallic precursors and the supports $Fe_3O_4@SiO_2$, $Fe_3O_4@SiO_2TiO_2$ and $Fe_3O_4@SiO_2CeO_2$. The last discussion will involve the difficulties to prepare Au nanoparticles through the decomposition of Chloro(tetrahydrothiophene)gold(I) and the preparation of Rh@PVA using a modification of the organometallic approach.

4.2.1. Rhodium catalysts prepared using $RhCl_3.xH_2O$

4.2.1.1. Rhodium catalysts prepared by the impregnation method

The first attempt to prepare a magnetically recoverable Rh catalyst followed a methodology developed in our research group.[92] The methodology is a modification of the well-known IMP method used in the preparation of heterogeneous catalysts. The main difference was the functionalization of the catalyst support before the impregnation with the

metal precursors. The functionalization of the support with amino groups improved the impregnation of $Fe_3O_4@SiO_2$ with metal salts (high metal loading) and avoided metal leaching during the catalytic reactions.[175] Another difference was the reduction of the metal precursor, which was performed *in situ* during the hydrogenation of an olefin model molecule, cyclohexene, with H_2.[92] The modified IMP method was compared with the impregnation of preformed Rh NPs (obtained in collaboration with the group of Prof. Dr. Alain Roucoux (Rennes, France) into $Fe_3O_4@SiO_2$. The catalytic studies on the hydrogenation of cyclohexene revealed that the catalyst prepared by impregnation of preformed Rh nanoparticles is very active even with low metal loading (< 0.1 wt%). However, a catalyst prepared by the modified IMP method with 0.1 wt% of Rh on $Fe_3O_4@SiO_2NH_2$ was not as active. In fact, some difficulties were found to prepare this catalyst. The first preparation of this catalyst, following the previously reported procedure,[92] but with 0.1 wt% metal resulted in an inactive catalyst for the hydrogenation of cyclohexene. So, the preparation of a catalyst was repeated with a metal loading of 1.5 wt%, as previously reported. However, the material remained inactive. The impregnation and washing procedure was considered the problematic step, so different washing procedures were investigated. The solid after metal impregnation was washed with portions of water, ethanol and acetone or only with acetone. The most reproducible washing method to obtain an active catalyst was acetone washing only; however, inconsistencies in the catalytic activity were observed from batch to batch. The catalysts containing 0.1 and 1.5 wt% Rh were used for the hydrogenation of cyclohexene and the results are summarized in table 4.5.

Table 4.5. Catalytic activity of supported Rh catalysts reduced by H_2 in the hydrogenation of cyclohexene.[a]

Entry	Rh (wt%)	Cycle	Time (h)[b]	TOF (h^{-1})[c]
1	0.1	1	22	3360
2		2	65	Inactive
3	1.5	1	2	75000

[a] Reaction conditions: Cyclohexene (14.6 mmol), catalyst (0.4 μmol of Rh), substrate/catalyst=35600, 75ºC, 6 bar H_2. [b] Time interval required for each cycle reaction completion estimated by H_2 consumption curves (> 99 % conversion as determined by GC). [c] Turnover frequency expressed as moles of the substrate transformed per moles of catalyst per hour (calculated by the slope of the hydrogenation curve at <20 % conversion).

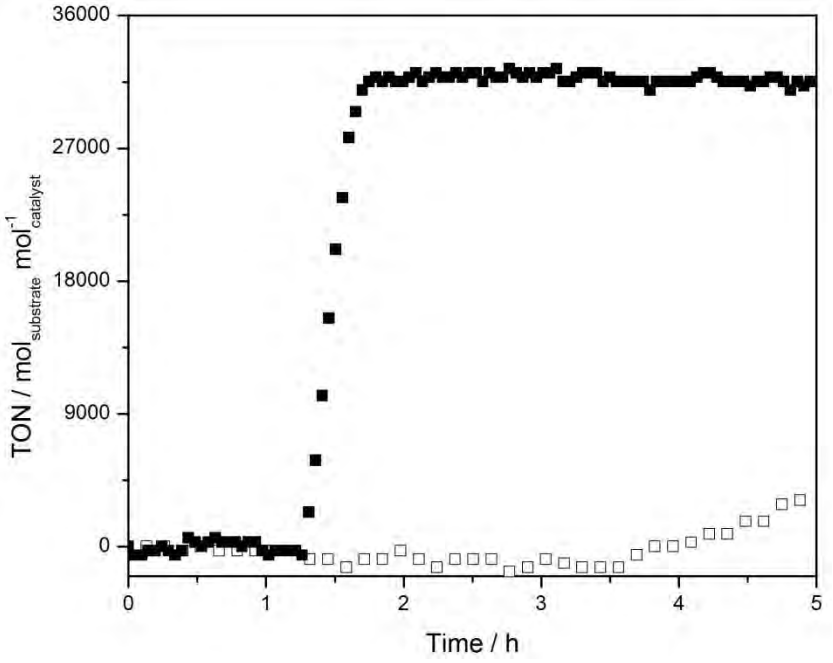

Figure 4.18. Hydrogenation of cyclohexene by Rh catalysts containing 0.1 (empty squares) and 1.5 (squares) wt% Rh supported on Fe_3O_4@SiO_2NH_2 and reduced by H_2. Reaction conditions: 6 bar H_2, 75 ºC and substrate/catalyst = 35600.

The catalytic activity of the catalyst containing 0.1 wt% Rh was 6 times lower than the catalyst containing 1.5 wt% Rh, and 70 times lower than the catalyst containing 0.1 wt% Rh prepared using preformed metal nanoparticles.[176] Moreover, this catalyst was inactive when tested for a second reaction cycle. These results demonstrate that despite the simplicity, the preparation of the catalyst by IMP (*in situ* reduction with H_2) is not trivial. Rh NPs were not

observed during TEM analysis of the 0.1 wt% Rh catalyst. This can be an indication of the presence of very small nanoparticles, which resulted in the very low consumption of H_2 observed in figure 4.18, after 3.5 h of reaction. A plausible explanation for this can be a strong metal-support interaction that affects the metal reduction process. The catalyst prepared with 1.5 wt% Rh contains Rh nanoparticles of 3-5 nm decorating the silica surface,[92] but it took more than one hour to the catalyst become active. The period of time without any noticeable consumption of hydrogen is denoted as activation time and corresponds to the time necessary for metal reduction under hydrogen, or restructuring into the active metal form.

Considering that the reduction of the metal precursor with H_2 was not efficient, we decided to try a different reducing agent and have chosen $NaBH_4$. Various catalysts containing 0.1, 0.5, 1.0 and 1.5 wt% of Rh were prepared. They were more active than the catalysts reduced by H_2 and the results are summarized in table 4.6 and figure 4.19. All catalysts exhibited an activation time without consumption of H_2, but as the Rh^{3+} was previously reduced by $NaBH_4$, this time necessary to form the active catalyst was much faster, ca. 15 min. The size of the Rh nanoparticles in each catalyst was determined after analysis of the micrographs obtained by TEM/HRTEM (figure 4.20).

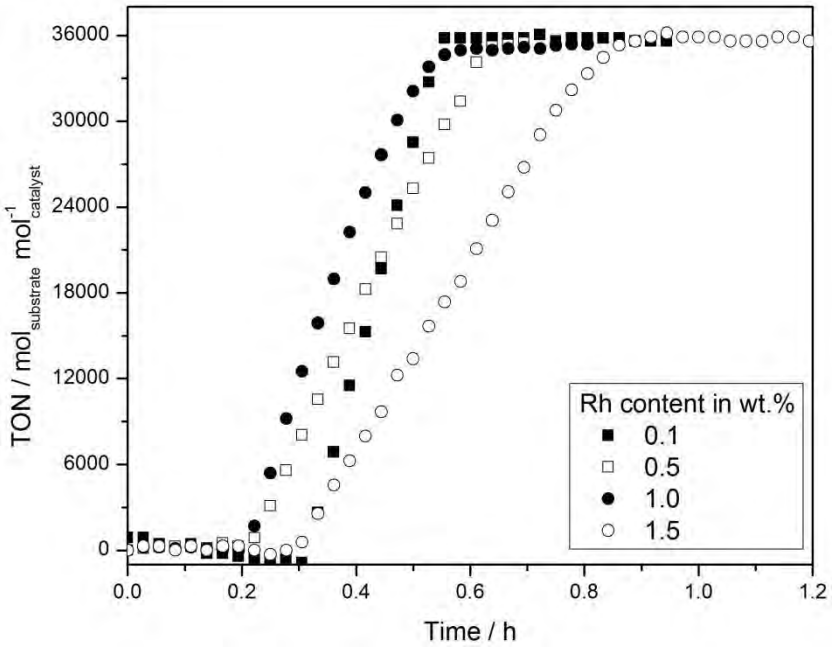

Figure 4.19. Hydrogenation of cyclohexene by Rh containing catalysts (0.1 to 1.5 wt% Rh) supported in Fe_3O_4@SiO_2NH_2 and reduced by $NaBH_4$. Reaction conditions: 6 bar H_2, 75 ºC and substrate/catalyst molar ratio = 35600. Metal content: 0.1 (squares), 0.5 (empty squares), 1.0 (circle) and 1.5 % (circle).

Table 4.6. Catalytic activity of supported Rh catalysts reduced by $NaBH_4$ in the hydrogenation of cyclohexene and Rh NPs size.

Entry	Rh (wt%)	Mean diameter (nm)	Time (h)[a]	TOF (h^{-1})
1	0.1	2.8 ± 0.5	0.57	153,190
2	0.5	2.2 ± 0.4	0.65	85,440
3	1.0	3.1 ± 0.5	0.58	133,300
4	1.5	2.8 ± 0.7	0.87	65,469

[a] Reaction conditions: Cyclohexene (14.6 mmol), catalyst (0.4 μmol of Rh), substrate/catalyst=35600, 75ºC, 6 bar H_2.[b] Time interval required for reaction completion estimated by H_2 consumption curves (> 99 % conversion as determined by GC). [c] Turnover frequency expressed as moles of the substrate transformed per moles of catalyst per hour (calculated by the slope of the hydrogenation curve at <20 % conversion).

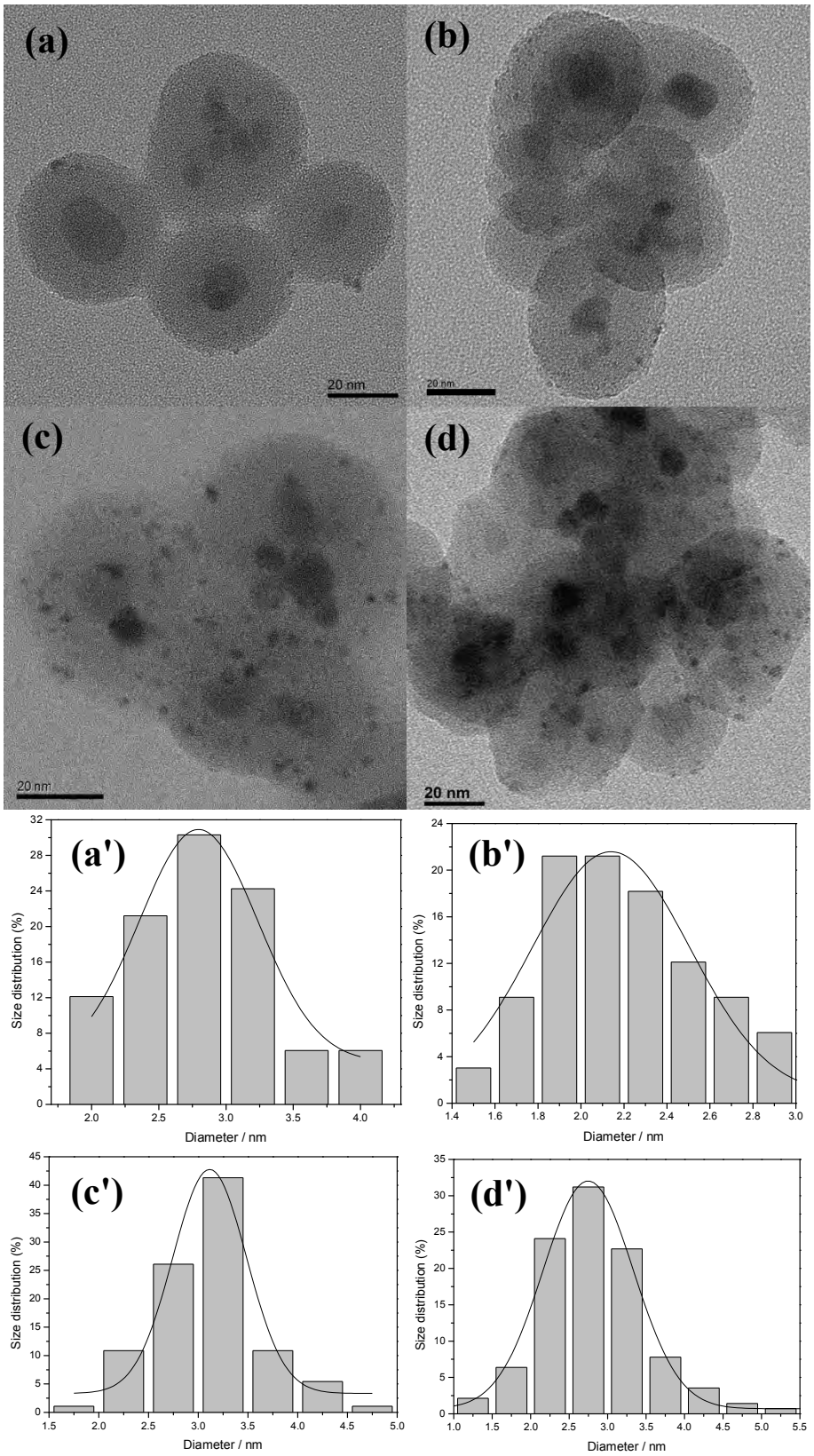

Figure 4.20. TEM micrographs of supported Rh catalysts reduced by $NaBH_4$: (a) 0.1; (b) 0.5; (c)1.0 and (d) 1.5 wt% Rh. The corresponding size distribution histograms fitted to Gaussian function are shown in (a'), (b'), (c') and (d').

All the catalysts have very similar mean sizes ranging from 2.2 to 3.1 nm, which are technically the same considering the size distribution range. The catalysts with different metal loadings presented different catalytic activity, but the difference can not be attributed to variation in the NP size. The catalysts with 0.1 wt% Rh was the most active, reaching TOF of 150,000 h^{-1}, which is comparable with the catalyst with 0.1 wt% Rh prepared by SI method reported elsewhere.[176] This result suggest that H_2 is a very mild reducing agent for this system (IMP with 0.1 wt% Rh), but $NaBH_4$ is more efficient allowing the preparation of very active catalysts. For higher metal loading the reduction with H_2 was as efficient as with $NaBH_4$. The Rh catalysts (1.5 wt% Rh) reduced by H_2 and $NaBH_4$ exhibited similar catalytic activity (table 4.5 entry 3 and 4.6 entry 4). It is also interesting to observe that the NPs size is not a function of the metal loading, at least in the concentration range studied. Some agglomeration or sintering of individual support particles can be observed in the TEM micrographs of the catalysts when compared with the micrographs of the support. This change in the support structure can be caused by an increase in the pH of the solution during the reduction with $NaBH_4$. Although, the agglomeration observed did not affect the magnetic separation capability of the materials.

The catalyst containing 1.5 wt% Rh was selected for further studies and was employed in the hydrogenation of benzene, which was used as a model substrate for aromatic hydrogenation. The hydrogenation curves are displayed in figure 4.21 and catalytic results are summarized in table 4.7.

Table 4.7. Catalytic activity of supported Rh catalyst (1.5 wt%) reduced by $NaBH_4$ in the hydrogenation of benzene.[a]

Entry	Cycle	Time (h)[b]	TOF (h^{-1})[c]
1	1	1	850
2	2	1.15	770
3	3	0.88	960

[a] Reaction conditions: Benzene (2.2 mmol), catalyst (4.5 μmol of Rh), substrate/catalyst = 500, 75ºC, 6 bar H_2, 1 mL n-hexane. [b] Time interval required for reaction completion estimated by H_2 consumption curves (> 99 % conversion as determined by GC). [c] Turnover frequency expressed as moles of the substrate transformed per moles of catalyst per hour (calculated by the slope of the hydrogenation curve at < 20 % conversion)

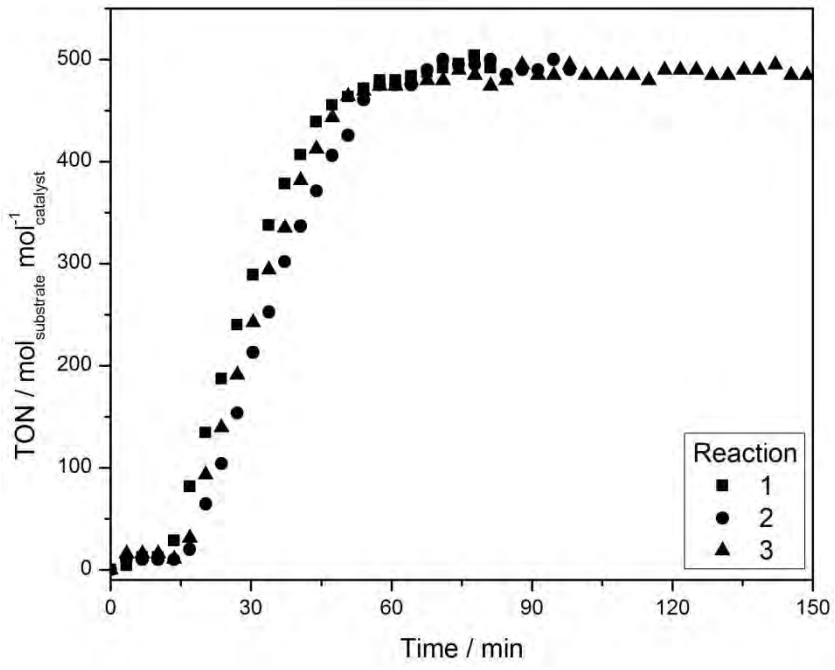

Figure 4.21. Hydrogenation of benzene by Rh containing catalysts (1.5 wt% Rh) supported on Fe_3O_4@SiO_2NH_2 and reduced by $NaBH_4$. Reaction conditions: 6 bar H_2, 75 ºC and substrate/catalyst molar ratio = 500.

The results obtained with the Rh catalyst reduced with $NaBH_4$ were very interesting; however the $NaBH_4$ can leave some contamination on the metal surface. Thus, we decided to study the effect of using hydrazine as reducing agent in the catalyst preparation, trying to prepare a catalyst with a cleaner surface. The reduction with hydrazine was conducted in water, following the same procedure as for $NaBH_4$, to prepare a catalyst containing 1.5 wt%

Rh. The hydrogenation curves are displayed in figure 4.22 and the catalytic performance for the catalyst reduced by hydrazine in the hydrogenation of cyclohexene and benzene are summarized in table 4.8. The catalyst reduced using hydrazine resulted in a lower activity for the hydrogenation of cyclohexene, when compared with the catalysts (1.5 wt% Rh) reduced with H_2 and $NaBH_4$, but this catalyst was more active in the hydrogenation of benzene than the catalyst prepared using $NaBH_4$. The best result reported before was a TOF of 1000 h^{-1} for the hydrogenation of benzene using the catalyst reduced by H_2.[92]

Table 4.8. Catalytic activity of supported Rh catalyst (1.5 wt%) reduced by hydrazine.[a]

Entry	Substrate	Cycle	Time (h)[b]	TOF (h^{-1})[c]
1	Cyclohexene	1	3.8	21,300
2		2	1.6	48,700
3	Benzene	1	1.45	740
4		2	0.8	1,500
5		3	0.55	1,280
6		4	0.7	1,600

[a] Reaction conditions: Cyclohexene (14.6 mmol) or Benzene (2.2 mmol), catalyst (0.4 μmol and 4.5 μmol of Rh, respectively), substrate/catalyst = 35600 (cyclohexene) and 500 (benzene), 75ºC, 6 bar H_2 and 1 mL n-hexane (benzene). [b] Time interval required for reaction completion estimated by H_2 consumption curves (> 99 % conversion as determined by GC). [c] Turnover frequency expressed as moles of the substrate transformed per moles of catalyst per hour (calculated by the slope of the hydrogenation curve at < 20 % conversion)

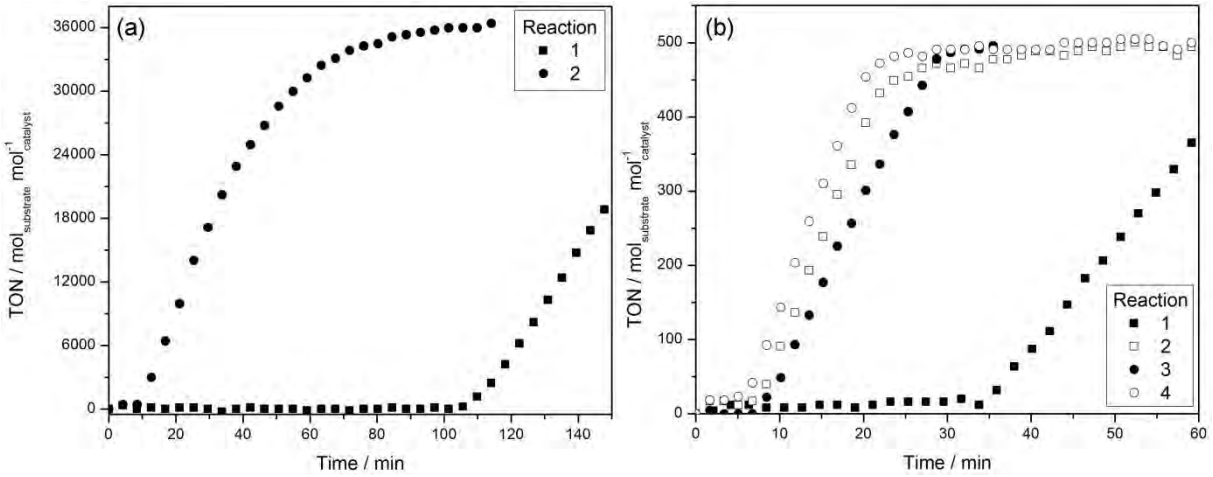

Figure 4.22. Hydrogenation of (a) cyclohexene and (b) benzene by Rh containing catalysts (1.5 wt% Rh) supported on Fe_3O_4@SiO_2NH_2 and reduced by N_2H_4. Reaction conditions: 6 bar H_2, 75 ºC and substrate/catalyst molar ratio= 35600 (cyclohexene) and 500 (benzene).

The size of the Rh nanoparticles in the 1.5wt% Rh catalyst reduced by hydrazine was 2.6 ± 0.6 nm, determined with the micrograph obtained by TEM and its corresponding size distribution histogram (figure 4.23). However, considering the NPs size distribution for metal reduction with hydrazine and $NaBH_4$ (2.8 ± 0.7 nm, shown in figure 4.20d), there was no significant difference in size.

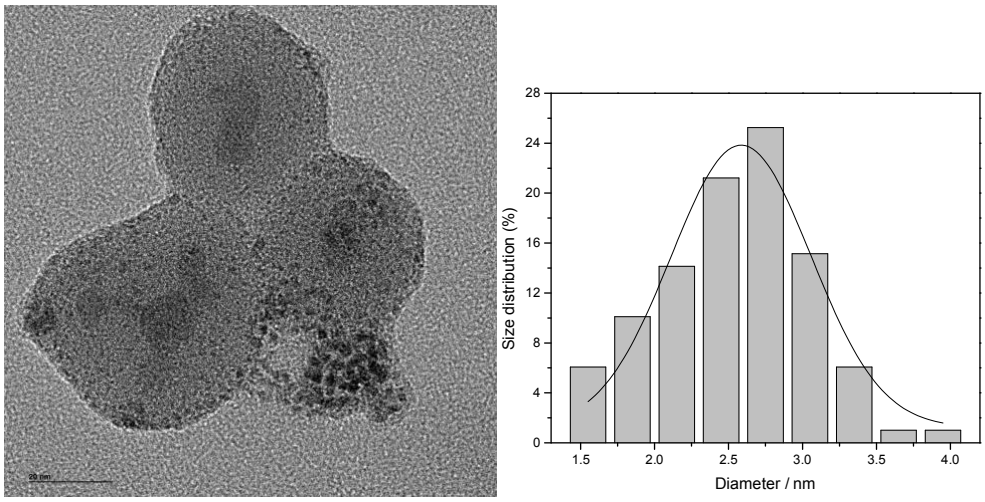

Figure 4.23. TEM micrograph of supported Rh catalyst (1.5 wt.%) reduced by hydrazine and the correspondent size distribution histogram fitted to a Gaussian function.

The only difference between the catalysts prepared with $NaBH_4$ and hydrazine was the dispersion of the Rh NPs on the support. The micrograph displayed in figure 4.23 shows that the Rh NPs in catalyst reduced by $NaBH_4$ are more evenly distributed over the solid surface than the Rh NPs in the catalyst reduced by hydrazine. Different interaction between the aromatic ring and the Rh surface can be the reason to the activities differences. Thus, Raman Spectroscopy was used in an attempt to characterize the interaction between the benzene ring and the Rh NPs in each catalyst, but no difference was observed that could explain why the catalyst reduced by hydrazine was more active for benzene hydrogenation than the catalyst reduced by $NaBH_4$. The fact that two similar catalysts display so different catalytic behaviors is very intriguing. Both catalysts were prepared using the support prepared in the same synthesis and the $RhCl_3.xH_2O$ from the same flask. So, the only difference in their synthesis was the reducing agent. Considering that each reducing agent will lead to different species adsorbed at the catalyst surface, the difference could be explained by different NPs surface state. In principle, the $NaBH_4$ would be more problematic in terms of contamination of the metal surface than hydrazine, which should have a cleaner oxidation in the perspective of surface contamination. Moreover, the behavior of the catalyst reduced with hydrazine is more similar to the behavior of the catalysts reduced with H_2 (cleaner surfaces). In this way, the reason for the different catalytic behavior should be related to the metal surface contamination, although the true reason could not be disclosed without analysis of the catalyst surface.

4.2.1.2. Rhodium catalysts prepared by the sol-immobilization method

The desire to obtain supported Rh catalysts very active and, on the same way, having a higher control on the metal characteristic (size and composition) led us to follow a current trend in the literature on the preparation of supported metal nanoparticles; i.e., to explore the immobilization of pre-formed metal nanoparticles on the support, which is also referred as sol-immobilization technique.[31] The choice of the stabilizing agent was a point of concern for the preparation of metal nanoparticles for their application in the field of catalysts. In this way, a methodology reported for the preparation of Au@PVA NPs was adapted to prepare Rh@PVA NPs.[32] There are several methods and stabilizing agents to produce Rh NPs, but this method was selected due to the simplicity of working in aqueous solution and the promising results that were being achieved by members of our research group with AuPd@PVA.[177] Moreover, the application of PVA as a stabilizer for Rh NPs was already reported in the literature and resulted in catalytically active nanoparticles.[178]

The synthesis of Rh@PVA NPs was performed in water and the metal salt precursor was reduced by $NaBH_4$ in the presence of excess of polyvinyl alcohol. The size of the Rh nanoparticles was 4.3 ± 1.3 nm, obtained after analysis of the micrograph obtained by TEM and its corresponding size distribution histogram (figure 4.24). The sample contains nanoparticles of mostly spherical morphology; however, the control on the nanoparticle shape was quite poor and other morphologies, such as triangular or cubic shapes were also observed. Despite the morphological issues, the colloidal suspension is very stable and could be stored for several months without visible precipitation. In any case, all reactions and impregnations were performed using a freshly prepared colloidal solution. As mentioned before, the choice of the stabilizing agent is always a compromise between size or shape control and surface properties (how strong, how much and where the stabilizing binds to the metal surface?),

which will reflect directly in the catalytic activity. A general rule says that a strong coordinating stabilizer can control better the particle size and shape, but also block the catalyst surface. Thus, a desirable stabilizing agent is one binding strongly enough to protect the metal NPs and weakly enough to not became a catalyst inhibitor.[179]

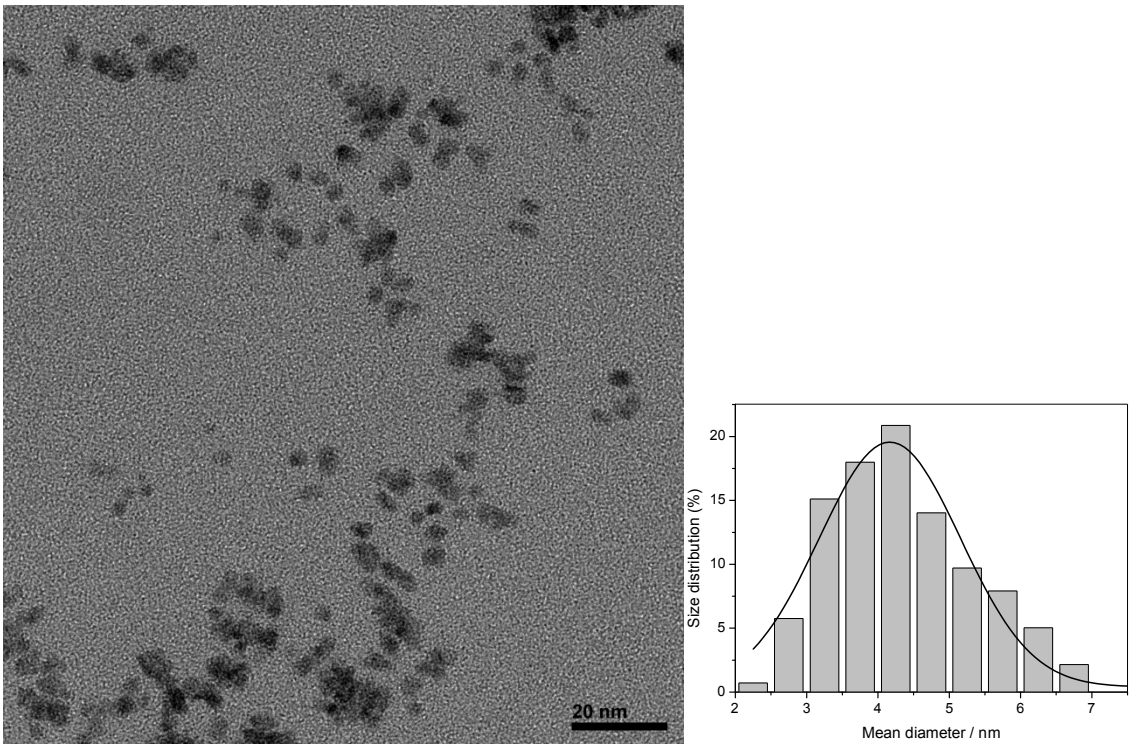

Figure 4.24. Micrograph obtained by TEM of Rh@PVA NPs and the correspondent size distribution histogram fitted to a Gaussian function.

Initially, the Rh@PVA aqueous colloidal suspension was used in biphasic hydrogenation of cyclohexene; the catalyst is present in the aqueous phase and the reactant and product form an immiscible organic phase. The catalytic reaction occurs at the interface and may be delayed by phase transfer limitations. Under these conditions, we studied the effect of temperature and of the substrate to catalyst molar ratio on the hydrogenation of cyclohexene. Table 4.9 entries 1-4 and figure 4.25 show the activity of Rh@PVA colloidal suspension in the hydrogenation of cyclohexene at different temperatures and at a fixed

catalyst to substrate molar ratio of 35600. The temperature had small effect in the catalyst activity. The only exception is the reaction at 100 ºC that resulted in a TOF around 1.6 times higher than the others, although the pressure increased a little at this temperature. This result demonstrates that the reaction is being limited by mass transfer and at the range of 25 to 75 ºC the temperature is not critical. We have tried to study the reaction at 125 and 150 ºC, but at temperatures higher than 100 ºC the pressure at the glass reactor started to increase a lot and the reaction was stopped for safety reasons. It is worth to note that the colloidal suspension precipitated after the reaction at all temperatures investigated and the catalyst could not be reused.

Table 4.9. Catalytic activity of colloidal suspension of Rh@PVA in the hydrogenation of cyclohexene.[a]

Entry	Temperature (ºC)	TON	Time (h)[b]	TOF (h^{-1})[c]
1	25	35,600	1.6	27,250
2	50	35,600	2.0	29,880
3	75	35,600	1.7	30,960
4	100	35,600	1.8	47,470
5	75	71,200	1.8	55,670
6	75	142,400	2	103,990
7	75	284,800	3.6	120,650
8	75	569,600	7.4	162,680

[a] Reaction conditions: Cyclohexene (14.6 mmol), catalyst (0.052-0.4 μmol of Rh), substrate/catalyst = 35600-569600 (cyclohexene), 75ºC, 6 bar H_2. [b] Time interval required for reaction completion estimated by H_2 consumption curves (> 99 % conversion as determined by GC). [c] Turnover frequency expressed as moles of the substrate transformed per moles of catalyst per hour (calculated by the slope of the hydrogenation curve at <20 % conversion)

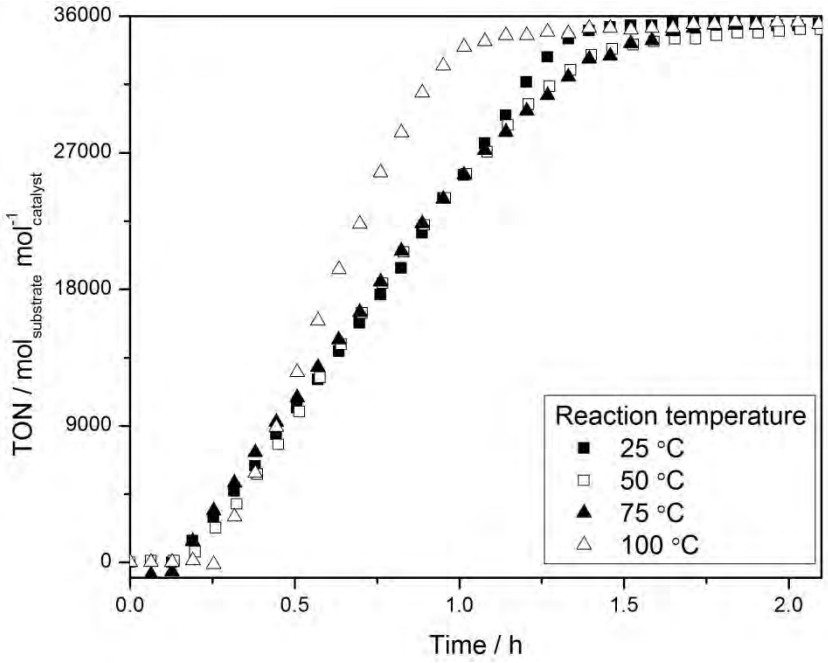

Figure 4.25. Hydrogenation of cyclohexene by aqueous colloidal Rh@PVA NPs at different temperatures.

Reaction conditions: 6 bar H_2, 25-100 ºC and substrate/catalyst molar ratio = 35600.

These Rh@PVA nanoparticles were also used to study the response in the catalyst activity due to variations in the substrate to catalyst molar ratio. In order to keep the conditions as close as possible for all reactions, the volume of aqueous colloidal solution and amount of substrate were kept constant and the reactions were performed at 75 ºC and 6 bar H_2. The Rh@PVA colloidal solution was diluted until the desired substrate to catalyst molar ratio value was achieved (for a given amount of substrate and using the same volume of water in all reactions). Table 4.9 and figure 4.26 show that the TOF increases with the increase of substrate to catalyst molar ratio or the TON (considering that all reactions reached 100% conversion). It is very interesting that even with a TON as higher as 569600 the activity was still increasing. This behavior is an indication that the system is really limited by mass transfer. During the reactions with different TON the catalyst colloidal suspension was still precipitating at the end of the reaction and could not be reused.

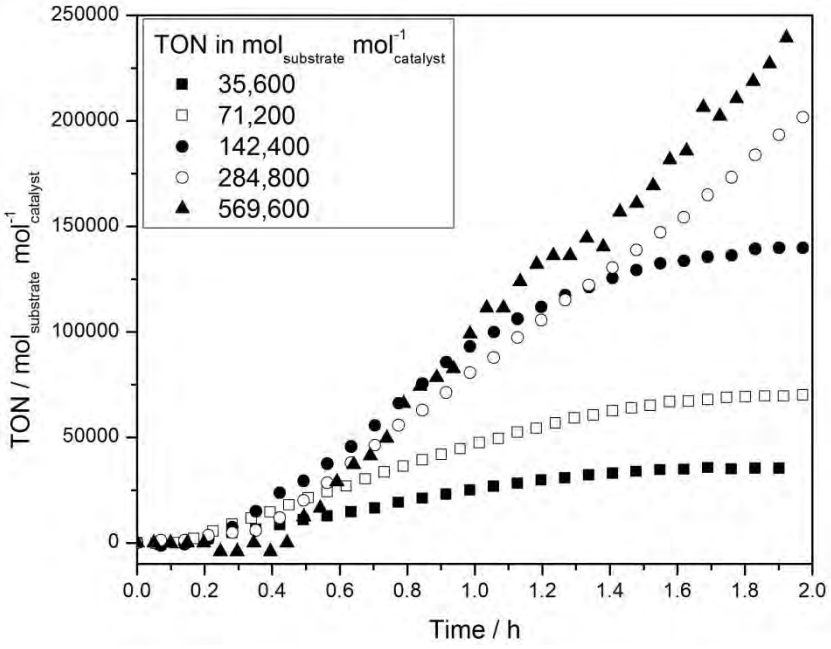

Figure 4.26. Catalytic activity of Rh@PVA in the hydrogenation of cyclohexene in function of substrate/catalyst ratio. Reaction conditions: 6 bar H_2, 75 ºC and substrate/catalyst ratio = 35600-569600.

The mass transfer limitation due to the aqueous-organic biphasic system and the catalyst precipitation during reaction are the major drawback of the utilization of Rh@PVA NPs colloidal solution in the hydrogenation of cyclohexene. However, these problems can be circumventeded by the immobilization of Rh@PVA NPs on a solid support, which in principle will improve the thermal stability, help to remove excess PVA during the washing steps and promote an intimate contact between the catalyst and substrate (the solid will disperse in the liquid phase). The magnetic solid Fe_3O_4@SiO_2 was used for the immobilization of Rh@PVA NPs; however, the support surface was first functionalized with amino groups using (3-aminopropyl)triethoxysilane, since Fe_3O_4@SiO_2 was not capable to adsorb the metal NPs from an aqueous solution probably due to low metal-support interaction was very low. The metal-support interaction was improved after functionalization with amine group. The difference was easily visualized by the different color of the supernatant of the impregnation solution, which was clear in the case of amino-functionalized support and dark

in the case of bare support. Therefore, the catalyst was prepared by the immobilization of Rh@PVA NPs on the amine functionalized solid (Fe_3O_4@SiO_2NH_2). The desired amount of Fe_3O_4@SiO_2NH_2 powder was added to an aqueous colloidal suspension of Rh@PVA NPs. The suspension was stirred at room temperature for 2 h. After washing and drying, the quantification of Rh by FAAS confirmed the presence of 1.0 wt% Rh on the solid.

The Fe_3O_4@SiO_2NH_2RhPVA (1 wt% Rh) catalyst was used for successive hydrogenations of cyclohexene and benzene and the results are summarized in table 4.10 and the hydrogenation curves in figure 4.27. The immobilization of the Rh@PVA on a solid magnetic support allowed the catalyst to be recycled and the catalyst was reused for consecutive hydrogenation reactions. The catalyst could be recycled five times without deactivation for the hydrogenation of cyclohexene. In the case of benzene hydrogenation, a decrease of 50% in the TOF could be seen in the 4^{th} recycle, but this decrease of activity was not caused by metal leaching (none metal was detected in the solution by ICP OES). Once metal leaching in not the reason for activity loss, the next concern is the morphology stability. During catalysis the metal NPs can suffer sintering which can result in less catalytic sites available for catalysis. The catalyst was characterized by TEM before and after benzene hydrogenation (figure 4.28). The catalyst morphology was preserved and the particle size before (4.3 ± 1.3 nm) and after catalysis (4.1 ± 1.0 nm) are similar, which indicates that no morphological changes occurred under reaction conditions. It is worth to mention that the Rh NPs sizes are the same in the colloidal solution (figure 4.24) and after immobilization in the solid support.

Table 4.10. Catalytic activity of Fe_3O_4@SiO_2NH_2RhPVA catalyst.[a]

Entry	Substrate	Cycle	Time (h)[b]	TOF (h^{-1})[c]
1	Cyclohexene	1	0.38	135,500
2		2	0.32	195,800
3		3	0.5	173,800
4		4	0.67	139,600
5		5	0.7	142,900
6	Benzene	1	1.4	1,700
7		2	1.5	1,180
8		3	3	830
9		4	2.8	700

[a] Reaction conditions: Cyclohexene (14.6 mmol) or Benzene (4.5 mmol), catalyst (0.4μmol and 4.5 μmol of Rh, respectively), substrate/catalyst = 35600 (cyclohexene) and 1000 (benzene), 75 ºC, 6 bar H_2 and 1 mL n-hexane (benzene). [b] Time interval required for reaction completion estimated by H_2 consumption curves (> 99 % conversion as determined by GC). [c] Turnover frequency expressed as moles of the substrate transformed per moles of catalyst per hour (calculated by the slope of the hydrogenation curve at < 20 % conversion)

The catalytic activity of Fe_3O_4@SiO_2NH_2RhPVA increased by 437 % compared to the catalytic activity of the colloidal Rh@PVA NPs solution. This can be attributed to the reduction of the mass transfer limitation. However, a further increase of 40 % at the second reaction suggests that the interaction polymer-metal might have changed or, even, a removal of the polymer. The immobilized Rh@PVA NPs showed the highest TOF value (195,800 h^{-1}, table 4.10 entry 2) for the hydrogenation of cyclohexene, considering all prepared Rh catalysts. Thus, demonstrating that even with the deleterious effect of the presence of large amount of stabilizer the preparation of preformed metal NPs is a very interesting route to prepare highly active catalysts.

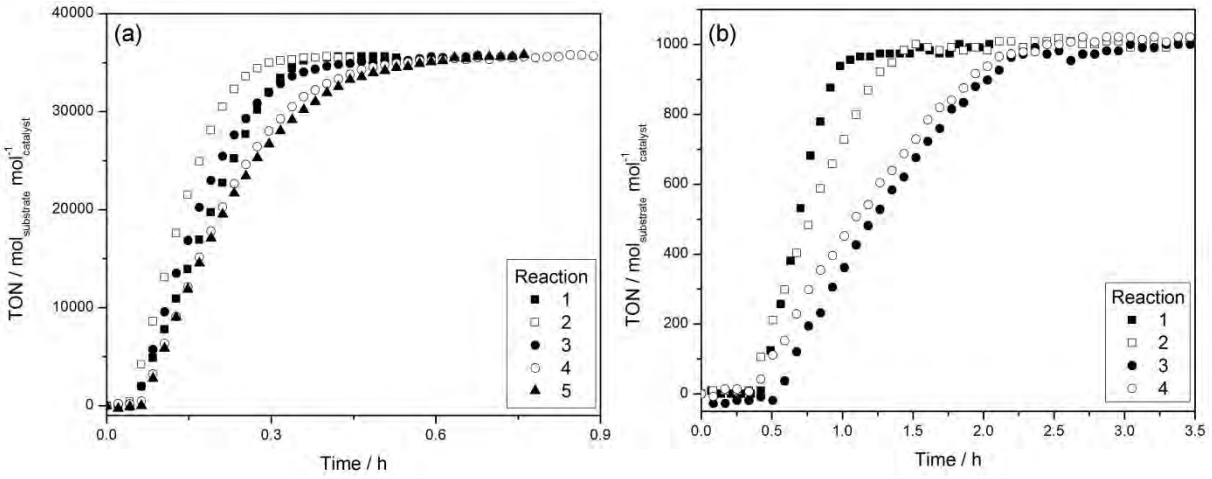

Figure 4.27. Hydrogenation of (a) cyclohexene and (b) benzene by Rh@PVA supported in Fe_3O_4@SiO_2NH_2 (1.5 wt%). Reaction conditions: 6 bar H_2, 75 ºC and substrate/catalyst molar ratio = 35600 (cyclohexene) and 1000 (benzene).

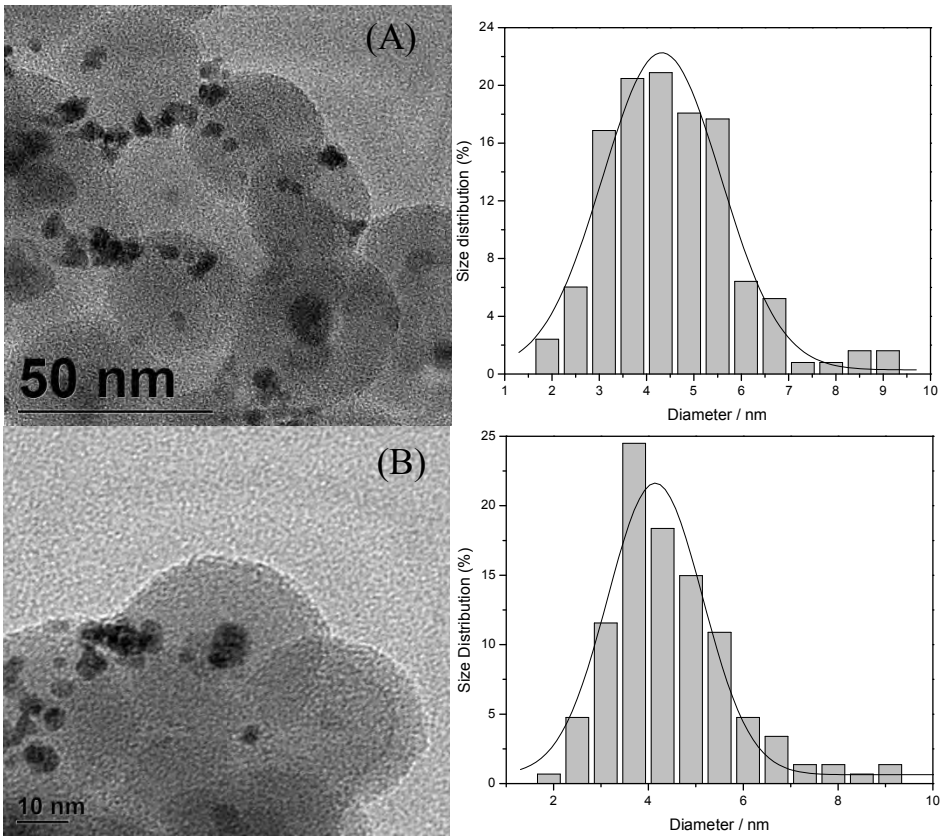

Figure 4.28. Micrograph obtained by TEM of Fe_3O_4@SiO_2NH_2RhPVA (A) as prepared and (B) after benzene hydrogenation cycle 4 and the correspondent size distribution histogram fitted to a Gaussian function.

4.2.2. Catalysts prepared with Na_2PdCl_4

4.2.2.1. Palladium catalysts prepared by the impregnation method

Palladium catalysts were prepared using Na_2PdCl_4 as precursor following the methodology used with $RhCl_3.xH_2O$. According to previous results in our research group, the synthesis of Pd catalysts does not show the same inconsistences observed in the preparation of Rh catalysts.

Initially, the supports $Fe_3O_4@SiO_2$, $Fe_3O_4@SiO_2Cal$, $Fe_3O_4@SiO_2NH_2$ and $Fe_3O_4@SiO_2CalNH_2$ were treated with an aqueous solution of Na_2PdCl_4 to obtain catalysts containing 1.0 wt% Pd. The catalysts were washed with deionized water and with acetone and dried in oven. The metal loading in each solid was determined by FAAS and the results are summarized in table 4.11. The amount of Pd in the different supports was found very close to the nominal value, except for $Fe_3O_4@SiO_2Cal$ (calcined and not functionalized) support, which was not able of adsorbing the Pd ions.

Table 4.11. Quantification of Pd in the magnetic supports by FAAS

Entry	Sample	Pd (wt%)
1	$Fe_3O_4@SiO_2Pd$	1.01 %
2	$Fe_3O_4@SiO_2CalPd$	0.06 % *
3	$Fe_3O_4@SiO_2NH_2Pd$	1.05 %
4	$Fe_3O_4@SiO_2CalNH_2Pd$	1.00 %

* Below the quantification limit.

The fact that the $Fe_3O_4@SiO_2Cal$ was not adsorbing the Pd^{2+} ions from the impregnation solution is an indication that the organic material present in the silica shell is

responsible for the metal uptake (in the case of $Fe_3O_4@SiO_2$, residual surfactant used in the microemulsion may be present). As reported before, the amino-functionalized solids were very efficient in the impregnation process, because the amine groups are able to improve the metal adsorption in a process called ligand-assisted preparation method.[44] The non-functionalized solid adsorbed the Pd^{2+} ions; however, the functionalization is very important to prevent the metal leaching during catalytic cycles.

The Pd catalysts were tested in the hydrogenation of cyclohexene at 75 ºC, 6 bar H_2 and a substrate to catalyst molar ratio of 10000. The results obtained after four successive reaction cycles are summarized in figure 4.29 and table 4.12. Figure 4.30 shows the hydrogenation curves obtained.

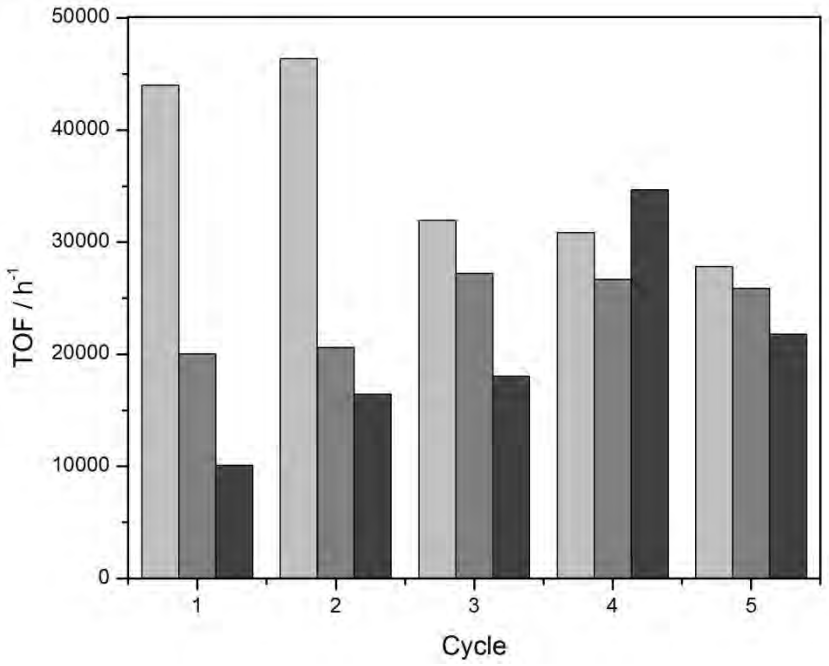

Figure 4.29. Activity of $Fe_3O_4@SiO_2Pd$ (light grey), $Fe_3O_4@SiO_2NH_2Pd$ (grey) and $Fe_3O_4@SiO_2CalNH_2Pd$ (dark grey) in the hydrogenation of cyclohexene. Reaction conditions: 75 ºC, 6 bar H_2 and TON 10,000.

Table 4.12. Catalytic activity of Pd catalyst prepared by IMP in the hydrogenation of cyclohexene.[a]

Entry	Catalyst	Cycle	Time (h)[b]	TOF (h^{-1})[c]
1		1	0.27	44,000
2		2	0.26	46,400
3	Fe_3O_4@SiO_2Pd	3	0.36	32,000
4		4	0.47	30,900
5		5	0.51	27,800
6		1	0.66	20,000
7		2	0.57	20,600
8	Fe_3O_4@SiO_2NH_2Pd	3	0.55	27,250
9		4	0.55	26,700
10		5	0.55	25,900
11		1	1.32	10,100
12		2	0.98	16,500
13	Fe_3O_4@SiO_2CalNH_2Pd	3	0.78	18,100
14		4	0.55	34,700
15		5	0.78	21,800

[a] Reaction conditions: Cyclohexene (14.6 mmol), catalyst (1.5 μmol of Pd), substrate/catalyst = 10000, 75 ºC, 6 bar H_2. [b] Time interval required for reaction completion estimated by H_2 consumption curves (> 99 % conversion as determined by GC). [c] Turnover frequency expressed as moles of the substrate transformed per moles of catalyst per hour (calculated by the slope of the hydrogenation curve at < 20 % conversion)

It is important to notice that the as prepared catalyst is comprised of Pd^{2+} and that the formation of the real active specie (Pd^0) occurs *in situ* during the first hydrogenation reaction. Thus, the catalysts have a longer activation time at the first reaction, when compared with the second reaction, where the Pd NPs was already formed. The amino-functionalized supports exhibited a longer activation time (without consumption of H_2, figure 4.30 b and c) than the non-functionalized solid (figure 4.30 a). This behavior suggests that the reduction of Pd^{2+} to Pd^0 is more difficult in the presence of coordinating groups grafted on the support surface, leading to longer activation time.

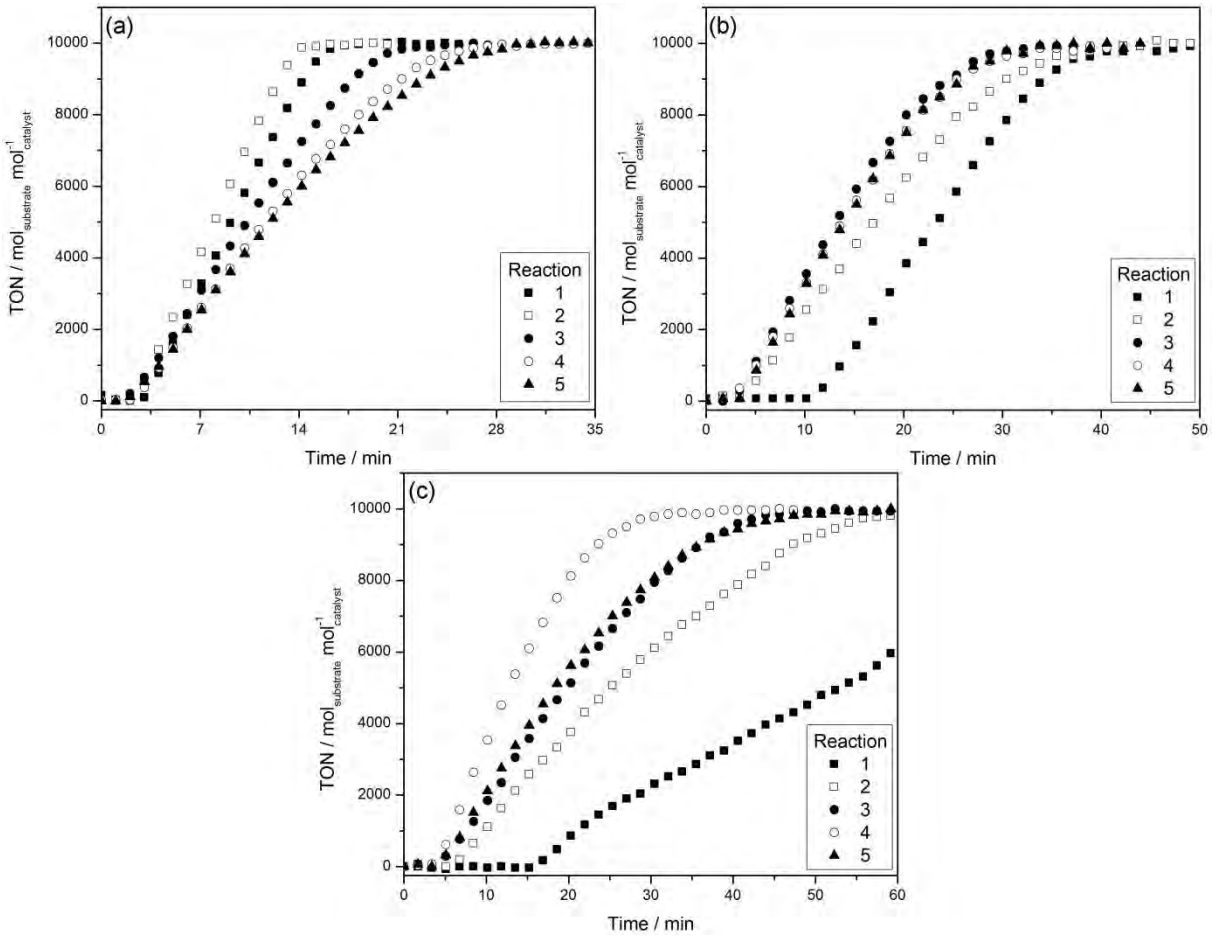

Figure 4.30. Hydrogenation of cyclohexene by Pd containing catalysts (1.0 wt% pd) supported in (a) $Fe_3O_4@SiO_2$, (b) $Fe_3O_4@SiO_2NH_2$ and (c) $Fe_3O_4@SiO_2CalNH_2$. Reaction conditions: 6 bar H_2, 75 ºC and substrate/catalyst molar ratio = 10000.

The catalyst with higher activity was the $Fe_3O_4@SiO_2Pd$, but at the 5th cycle its activity dropped to 63 % of the initial activity. This reduction of activity was observed before for a similar catalyst[44] and was attributed to the metal leaching or to coalescence due to a weak interaction metal-support. On the other hand, the catalyst $Fe_3O_4@SiO_2NH_2Pd$ showed a constant, but lower activity than $Fe_3O_4@SiO_2Pd$. The lower activity is attributed to an inhibition effect of the functional groups grafted in the silica surface and is observed also for the $Fe_3O_4@SiO_2CalNH_2Pd$. Despite the lower activity, the advantages of the functionalization are the catalytic activity retention in successive reaction cycles and the prevention of metal

leaching. The increasing of the Fe_3O_4@SiO_2CalNH_2Pd activity can be explained either by changes in NPs size (restructuring under reaction conditions) or to an effect of decreasing the amount of functional groups on support surface that are interacting with the metal nanoparticles. In order to compare the effect of the amount of ligand groups and at the same time eliminate the contribution of metal NPs size (and composition) on the catalytic activity, the same supports were treated with an aqueous colloidal suspension of Pd NPs (see results and discussion at 4.2.2.2).

4.2.2.2. Palladium catalysts prepared by the sol-immobilization method

The SI method using Pd@PVP-1 NPs provides the preparation of catalysts with metal nanoparticles of similar size and surface properties. The catalytic activity will be only affected by the support and the functional groups grafted on the support, so any difference in the measured TOF will be a consequence of the support characteristics. The supports Fe_3O_4@SiO_2, Fe_3O_4@SiO_2Cal, Fe_3O_4@SiO_2NH_2 and Fe_3O_4@SiO_2CalNH_2 were treated with a colloidal Pd@PVP-1 NPs solution to obtain catalysts containing 1.0 wt% Pd. The catalysts were washed with deionized water and acetone and dried in oven. The metal loading in each solid was determined by FAAS and the results show that only the functionalized supports were able to adsorb the Pd@PVP-1 NPs. The Fe_3O_4@SiO_2NH_2PdPVP and Fe_3O_4@SiO_2CalNH_2PdPVP catalysts contain 1.0 wt% of Pd, but the Fe_3O_4@SiO_2 and Fe_3O_4@SiO_2Cal supports were recovered with undetectable amounts of Pd. Due to the absence of Pd, the supports Fe_3O_4@SiO_2 and Fe_3O_4@SiO_2Cal were not employed in catalytic tests. The functionalized solids adsorbed Pd@PVP-1 NPs due to presence of NH_2 groups grafted on their surface. In the case of preformed NPs the adsorption by the support is directly

related to a stronger interaction of the support (or NH_2 groups) with the metal compared to the existing interaction of the metal nanoparticle with solvent through the stabilizing ligand (in this case, PVP). In this way, the absence of ligands on the support surface resulted in a weaker interaction with the metal when compared to the existing interaction with the solvent, but a stronger interaction occurred in the presence of NH_2 due to the coordinating properties of the amine groups. This has also being referred in the literature as a coordination capture method, due to the coordinating properties of the ligands grafted on the support.[23]

The Pd catalysts prepared by SI method were employed in the hydrogenation of cyclohexene at 75 ºC, 6 bar H_2 and a substrate to catalyst molar ratio of 10,000 and the results are summarized in figure 4.31 and table 4.13. Once the metal NPs are the same in both catalysts (prepared in the same synthesis batch) the difference in the activity observed is related to a support effect or maybe the amount of functional groups grafted on the support surface. The amount of -NH_2 grafted on the calcined support is six times the amount found in the as prepared support and the catalytic activity of Fe_3O_4@SiO_2CalNH_2PdPVP is 22 % lower than the catalytic activity of Fe_3O_4@SiO_2NH_2PdPVP. These results suggest that the increase in the amount of NH_2 groups grafted on the support has a detrimental effect on the catalytic activity. These results showed that despite the method to prepare metal NPs the characteristics of the support are essential for the quality of the catalyst prepared. The presence of functional groups is quite important for the preparation of catalysts, since they allow the preparation of durable and leaching-free catalysts. The drawback of the functionalization is the reduction of catalytic activity. The amount of functional groups can also result in a catalyst with unpredictable behavior, as demonstrated by Fe_3O_4@SiO_2CalNH_2Pd.

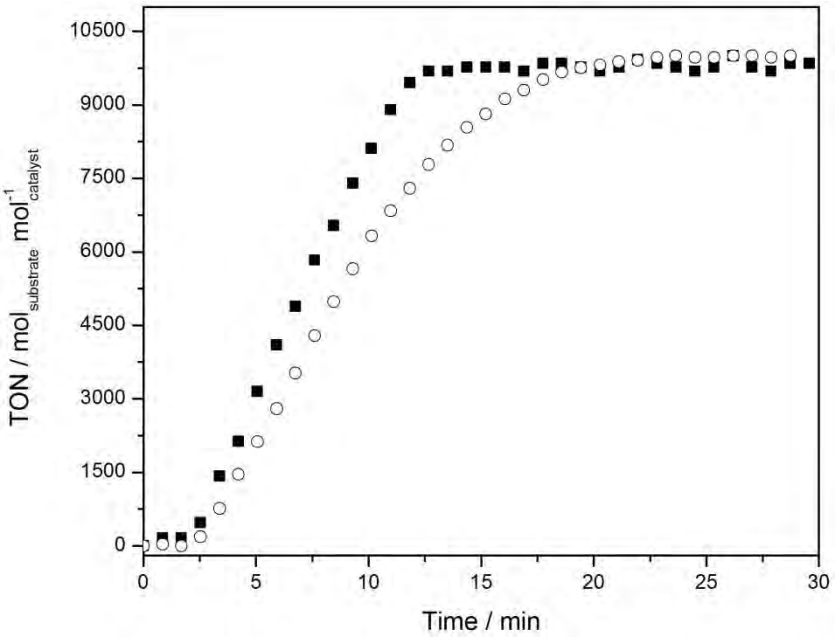

Figure 4.31. Hydrogenation of cyclohexene by colloidal Pd@PVP-1 (1.0 wt% Rh) supported in $Fe_3O_4@SiO_2$, $Fe_3O_4@SiO_2NH_2$ (squares) and $Fe_3O_4@SiO_2CalNH_2$ (circles). Reaction conditions: 6 bar H_2, 75 ºC and substrate/catalyst molar ratio = 10000.

Table 4.13. Catalytic activity of Pd catalyst prepared by SI of Pd@PVP-1 in the hydrogenation of cyclohexene.[a]

Entry	Catalyst	Time (h)[b]	TOF (h^{-1})[c]
1	$Fe_3O_4@SiO_2NH_2PdPVP-1$	0.25	57,200
2	$Fe_3O_4@SiO_2CalNH_2PdPVP-1$	0.4	44,300

[a] Reaction conditions: Cyclohexene (14.6 mmol), catalyst (1.5 μmol of Pd), substrate/catalyst = 10000, 75 ºC, 6 bar H_2. [b] Time interval required for reaction completion estimated by H_2 consumption curves (> 99 % conversion as determined by GC). [c] Turnover frequency expressed as moles of the substrate transformed per moles of catalyst per hour (calculated by the slope of the hydrogenation curve at < 20 % conversion)

4.3. Development of magnetically recoverable metal nanoparticle catalysts through decomposition of organometallic complexes

All the results and reactions performed so far showed that even with methodologies that are well established, the preparation of catalysts comprised of supported metal NPs is not trivial. For example, the studies dedicated to Rh catalysts prepared using $RhCl_3.xH_2O$ demonstrated that the washing procedure is very critical and can lead to an inactive catalyst or to a very active one. Also, the reducing agent showed to be able to affect the catalytic properties of metal NPs and has to be carefully selected. The studies with Pd catalysts demonstrated that the amount of functional groups on the solid affect the metal-support interaction and, consequently, the catalyst activity. The problems observed in the preparation of Rh catalyst by the IMP method could be minimized when preformed metal NPs where employed in the catalyst preparation by the SI method. Indeed, the use of preformed Rh@PVA NPs resulted in a reproducible Rh catalyst, which was very active in the hydrogenation of cyclohexene and benzene, but the morphological control was limited.

The different supports prepared by the deposition of ceria or titania on silica-coated magnetite were used for the preparation of magnetically recoverable catalyst. However, in order to study the influence of the support (silica, ceria and titania) on the catalytic properties, it is very important to minimize the differences in the catalyst preparation method and mainly in the metal NPs properties (size, composition and surface species). It is not uncommon to find in the literature studies where the comparison between supports uses different methods to prepare the supported metal NPs. In this way, the reported differences can be due to a difference in the preparation method rather than due to the support, as we demonstrated so far.

In order to avoid that the differences observed in catalytic performance results from differences in the preparation of the metal NPs, we prepared a series of catalysts supported on silica, ceria and titania magnetic composites using preformed metal NPs. However, a higher control over the NPs morphology, size and composition is desired. Thus, the organometallic approach developed in the group of Dr Karine Philippot at Laboratoire de Chimie de Coordination/CNRS has been chosen for the preparation of metal NPs. The next step is the immobilization of preformed metal NPs into magnetic supports. The magnetic supports selected for the immobilization was Fe_3O_4@SiO_2Cal, Fe_3O_4@SiO_2CeO_2 and Fe_3O_4@SiO_2TiO_2. The metals selected were rhodium, palladium and ruthenium.

4.3.1. Synthesis of Rh, Pd and Ru NPs stabilized with PVP

Rh, Pd and Ru NPs were synthesized by the decomposition of organometallic precursors in the presence of H_2 and polyvinylpyrrolidone (PVP) as the stabilizer agent, following a methodology developed at the Laboratoire de Chimie de Coordination/CNRS, Toulouse.[153]

The organometallic compounds used in this study were $Rh(C_3H_5)_3$, Ru(COD)(COT) and Pd_2dba_3 (figure 4.32). The metal NPs were synthesized under controlled atmosphere using Schlenk techniques, in order to preserve the reactants and products from humidity and air contact before immobilization on the supports. The organometallic complex $Rh(C_3H_5)_3$ was synthesized and Pd_2dba_3 and Ru(COD)(COT) were purchased from Alfa Aesar and from NanoMeps, respectively. The $Rh(C_3H_5)_3$ was synthesized by the reaction of allylmagnesium chloride with rhodium(III) chloride in dry and degassed THF. The obtained product was

purified by filtration on a celite column, THF was removed by vacuum and the organometallic compound obtained was finally purified by sublimation.

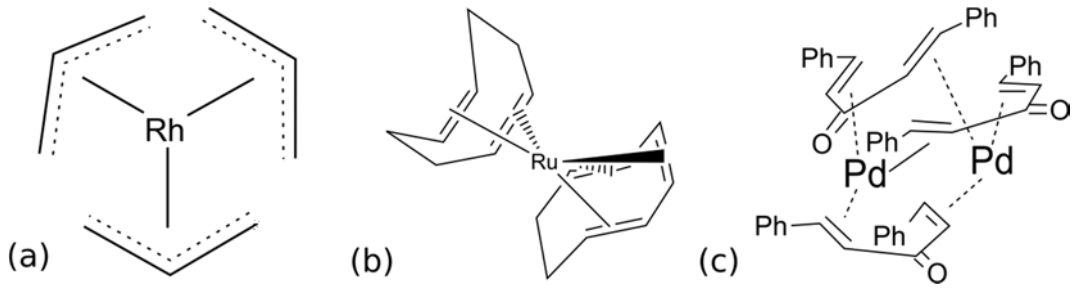

Figure 4.32. Structure of the organometallic compounds used: (a) $Rh(C_3H_5)_3$, (b) Ru(COD)(COT) and (c) Pd_2dba_3

Rh, Pd and Ru stabilized with PVP NPs were prepared using the same methodology and keeping the same molar proportion between metal and PVP. The three organometallic compounds are olefinic compounds and their treatment under hydrogen leads to the reduction of the olefinic ligands and formation of the NPs. The metal NPs obtained present a high morphological and size control. The medium NPs size measured from TEM micrographs were 1.9 ± 0.3, 2.0 ± 0.4 and 1.3 ± 0.3 nm for Rh@PVP, Pd@PVP and Ru@PVP, respectively (figure 4.33). These results demonstrate the versatility of the methodology and a wide range of metal NPs can be easily prepared.

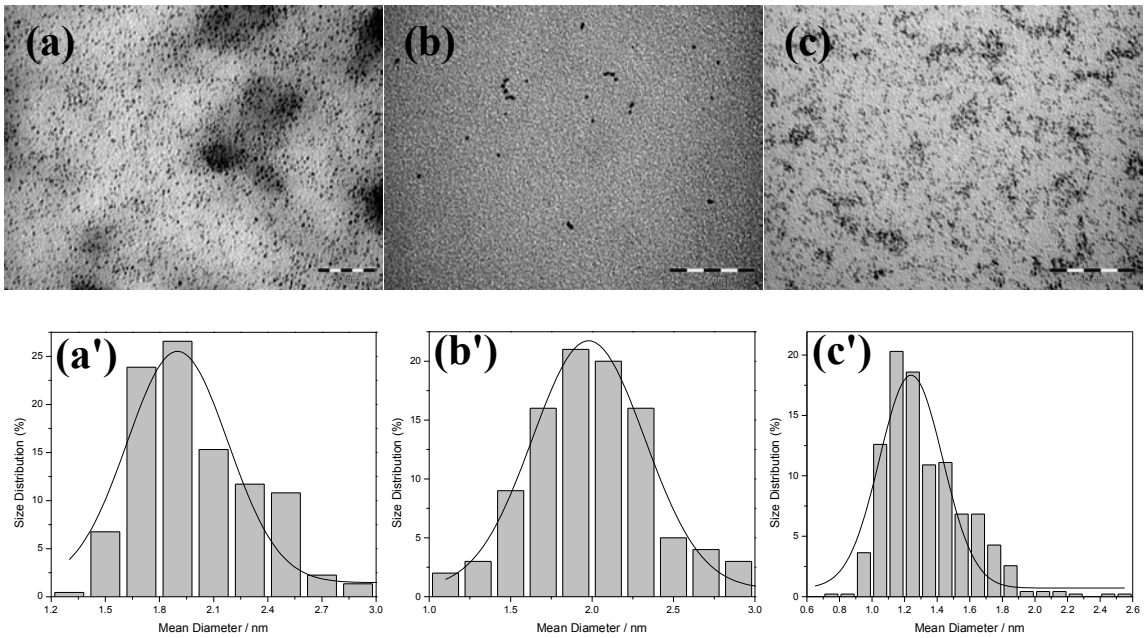

Figure 4.33. Micrograph obtained by TEM of (a) Rh@PVP, (b) Pd@PVP and (c) Ru@PVP. The corresponding size distribution histograms fitted to Gaussian function are shown in (a'), (b') and (c'). Scale bar = 50 nm.

4.3.2. Rh, Ru and Pd catalysts prepared by the sol-immobilization method

Rh@PVP, Pd@PVP and Ru@PVP NPs synthesized by the decomposition of organometallic precursor were immobilized on the supports Fe_3O_4@SiO_2Cal, Fe_3O_4@SiO_2CeO_2 and Fe_3O_4@SiO_2TiO_2. The supports were not functionalized because in this case the interaction between the metal and the support would be affected by the functional groups. The influence of the different oxides would be hindered by the influence of amine groups.

It is important to note that differently from the previously results, the immobilization of the metal NPs on non-functionalized solid was efficiently achieved using THF colloidal solutions of preformed NPs. This can be explained by a stronger interaction between the metal

NPs and support than the solvation of PVP in THF. However, the dispersion of these catalysts in water or alcohol results in the leaching of the metal due to higher solvation of PVP in water or alcohol. Consequently, non-polar solvents are preferred for the catalytic studies to avoid metal leaching.

TEM analysis of the catalysts revealed the immobilization of metal NPs on the supports (figure 4.34). We have shown before that the size of the metal NPs (Rh@PVA) is not altered during the catalyst preparation by SI method. In the particular case of figure 4.34, the size of Rh, Pd and Ru NPs was determined in figure 4.33. It was difficult to determine their size after immobilization because they are very small (1.3 – 2.0 nm).

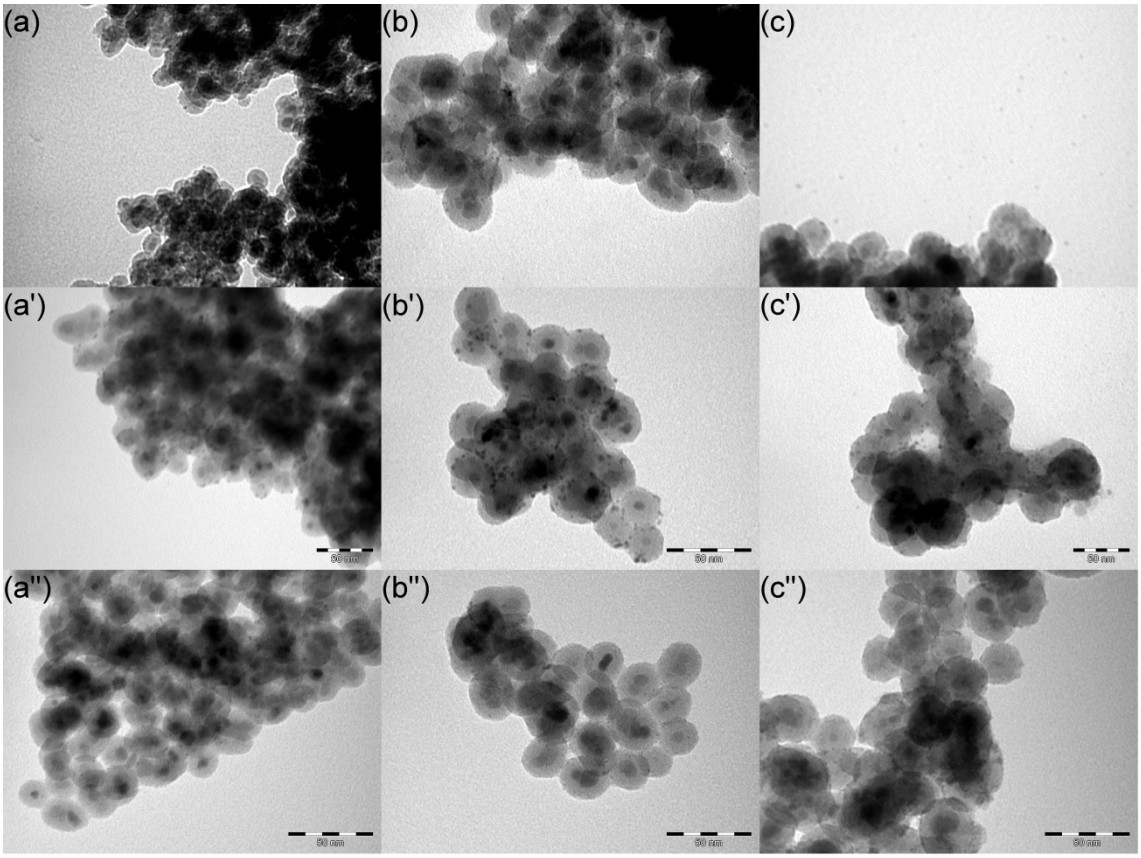

Figure 4.34. TEM micrographs of (a) Rh@PVP, (b) Pd@PVP and (c) Ru@PVP NPs supported on Fe_3O_4@SiO_2Cal, (') Fe_3O_4@SiO_2CeO_2 and (") Fe_3O_4@SiO_2TiO_2. Scale bar = 50 nm.

4.3.3. Catalytic reactions

The prepared catalysts were employed in different reactions, such as: Benzyl alcohol oxidation, hydrogenation of cyclohexene and phenol hydrogenation.

4.3.3.1. Hydrogenation of cyclohexene

The Rh and Pd catalysts were employed in the hydrogenation and dehydrogenation of cyclohexene in liquid phase or gas phase. The immobilization of the metal nanoparticles on magnetic supports allowed the catalyst to be easily recovered by magnetic separation in liquid phase reactions and their recycle for successive hydrogenation batches. The catalysts could be recycled six times without losing activity for the hydrogenation of cyclohexene. All the reactions were reached 100 % conversion (GC). The hydrogenation of cyclohexene was carried out applying the same conditions as for the catalysts prepared by reduction of metal salts and the results are reported in table 4.14 and recycling studies in figure 4.35 and 4.36.

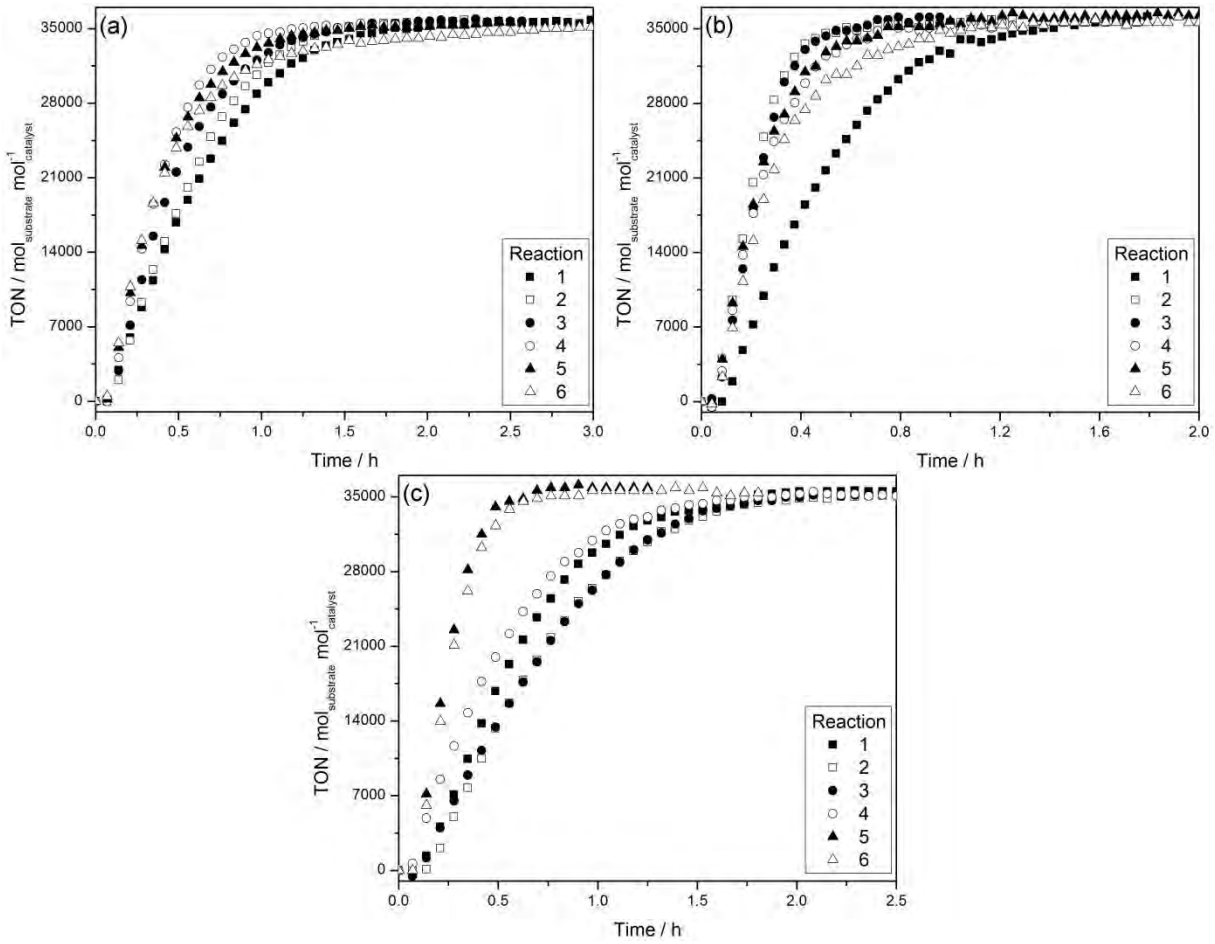

Figure 4.35. Catalytic hydrogenation of cyclohexene using Rh@PVP supported NPs on (a) Fe_3O_4@SiO_2Cal, (b) Fe_3O_4@SiO_2CeO_2 and (c) Fe_3O_4@SiO_2TiO_2. Reaction conditions: 6 bar H_2 and 75 °C and substrate/catalyst molar ratio = 35600.

The activation times observed for the Rh catalysts prepared by SI method using Rh@PVP prepared with organometallic approach were very short. These activation times indicate a very clean metallic surface, despite the presence of PVP. Thus, the PVP stabilizer appears to not interfere with the hydrogen chemisorption at the metal surface and olefin adsorption. Moreover, the expected steric hindrance of the PVP polymer remaining at the metal nanoparticle surface is not playing an important role in this system for the hydrogenation of cyclohexene.

Table 4.14. Influence of the support on the catalytic activity of immobilized Rh@PVP NPs prepared by organometallic approach in the hydrogenation of cyclohexene.[a]

Entry	Catalyst	Cycle	Time (h)[b]	TOF (h^{-1})[c]
1	Fe_3O_4@SiO_2CalRhPVP	1	2.4	47,400
2		2	2.0	54,250
3		3	1.9	63,000
4		4	1.8	75,550
5		5	2.0	71,600
6		6	3.0	74,900
7	Fe_3O_4@SiO_2CeO_2RhPVP	1	1.6	62,700
8		2	1.0	112,100
9		3	0.9	103,440
10		4	0.8	122,900
11		5	1.0	124,000
12		6	1.1	107,800
13	Fe_3O_4@SiO_2TiO_2RhPVP	1	2.1	39,250
14		2	1.9	39,300
15		3	2.3	36,700
16		4	2.0	60,650
17		5	0.8	122,470
18		6	0.8	116,000

[a] Reaction conditions: Cyclohexene (14.6 mmol), catalyst (0.4 μmol of Rh), substrate/catalyst = 35600, 75 ºC, 6 bar H_2. [b] Time interval required for reaction completion estimated by H_2 consumption curves (> 99 % conversion as determined by GC). [c] Turnover frequency expressed as moles of the substrate transformed per moles of catalyst per hour (calculated by the slope of the hydrogenation curve at < 20 % conversion)

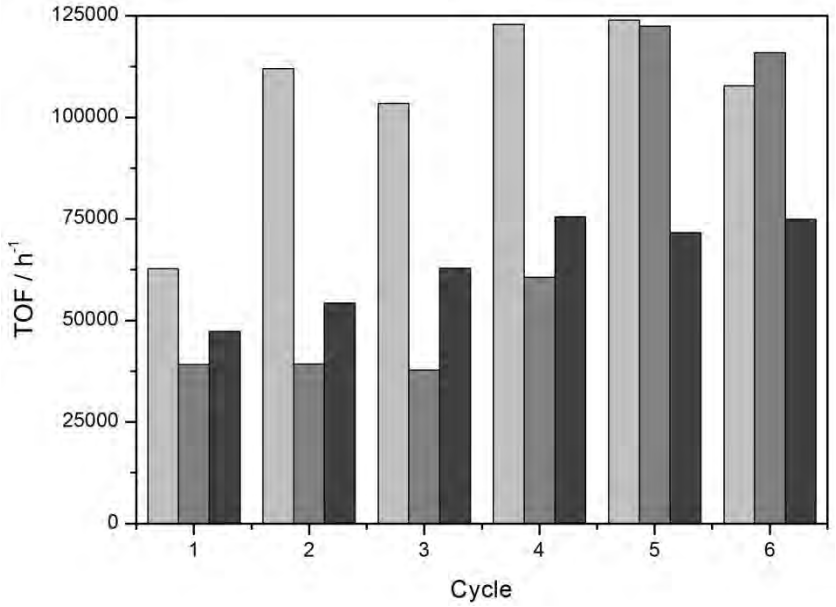

Figure 4.36. Catalytic activity in the hydrogenation of cyclohexene of Rh@PVP supported NPs in Fe_3O_4@SiO_2CeO_2 (light gray), Fe_3O_4@SiO_2TiO_2 (gray) and Fe_3O_4@SiO_2Cal (dark gray). Reaction conditions: 6 bar H_2 and 75 °C and TON of 35600.

The catalytic activity, expressed in TOF (calculated at initial rates), obtained with Fe_3O_4@SiO_2CalRhPVP, Fe_3O_4@SiO_2CeO_2RhPVP and Fe_3O_4@SiO_2TiO_2RhPVP catalysts in the first hydrogenation cycle of cyclohexene was quite close, but some differences were observed in the recycling experiments. The ceria supported catalysts Fe_3O_4@SiO_2CeO_2RhPVP showed an increase of about 50 % in the catalytic activity from the first reaction to the second reaction and was constant during the next recycles, reaching TOF of 125,000 h^{-1}. The titania supported catalyst Fe_3O_4@SiO_2TiO_2RhPVP showed a catalytic activity increase after the 5^{th} recycle and reached the same activity as the Fe_3O_4@SiO_2CeO_2RhPVP catalyst. The silica supported catalyst Fe_3O_4@SiO_2CalRhPVP presented a less intense increase of activity than the other catalysts upon recycling and reached a TOF of around 75,000 h^{-1}. These results suggest that the post-coating of the magnetic silica material with ceria and titania led to improvement of the Rh NP catalyst activity.

The catalytic activity of Fe_3O_4@SiO_2CalPdPVP, Fe_3O_4@SiO_2CeO_2PdPVP and Fe_3O_4@SiO_2TiO_2PdPVP in the first hydrogenation of cyclohexene and in the recycling experiments did not follow the same trend as observed for Rh catalysts. In the case of Pd, the best combination was Pd@PVP and silica support. The results are shown in table 4.15 and recycling studies in figure 4.37 and 4.38. The activation times observed for the Pd catalysts prepared by SI method using Pd@PVP prepared with organometallic approach were very short. As observed for Rh@PVP catalysts, these activation times indicate a very clean metallic surface, despite the presence of PVP.

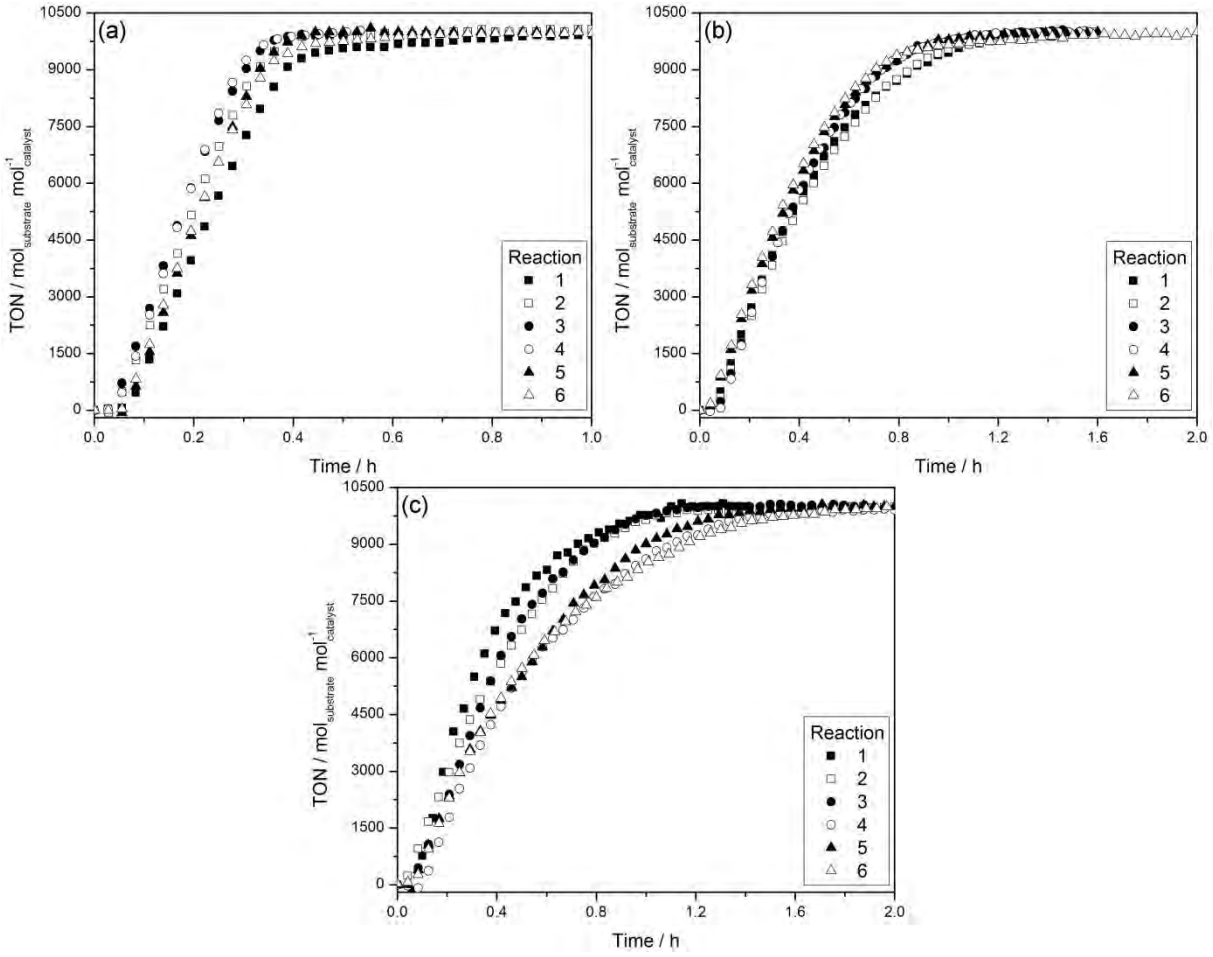

Figure 4.37. Catalytic hydrogenation of cyclohexene using Pd@PVP supported NPs (a) Fe_3O_4@SiO_2Cal, (b) Fe_3O_4@SiO_2CeO_2 and (c) Fe_3O_4@SiO_2TiO_2. Reaction conditions: 6 bar H_2, 75 °C and substrate/catalyst molar ratio = 10,000.

Table 4.15. Influence of the support on the catalytic activity of immobilized Pd@PVP NPs prepared by organometallic approach in the hydrogenation of cyclohexene.[a]

Entry	Catalyst	Cycle	Time (h)[b]	TOF (h^{-1})[c]
1	Fe_3O_4@SiO_2CalO_2PdPVP	1	1.2	36,100
2		2	0.6	36,360
3		3	0.43	40,080
4		4	0.45	40,160
5		5	0.45	41,880
6		6	0.7	39,260
7	Fe_3O_4@$SiO_2$$CeO_2$PdPVP	1	1.3	21,100
8		2	1.3	20,060
9		3	1.16	21,700
10		4	1.16	24,060
11		5	1.3	22,080
12		6	1.5	21,500
13	Fe_3O_4@$SiO_2$$TiO_2$PdPVP	1	1.12	29,900
14		2	1.3	20,400
15		3	1.3	19,500
16		4	1.9	20,300
17		5	1.7	18,800
18		6	2.0	19,200

[a] Reaction conditions: Cyclohexene (14.6 mmol), catalyst (1.46 μmol of Pd), substrate/catalyst = 10000, 75 ºC, 6 bar H_2. [b] Time interval required for reaction completion estimated by H_2 consumption curves (> 99 % conversion as determined by GC). [c] Turnover frequency expressed as moles of the substrate transformed per moles of catalyst per hour (calculated by the slope of the hydrogenation curve at < 20 % conversion)

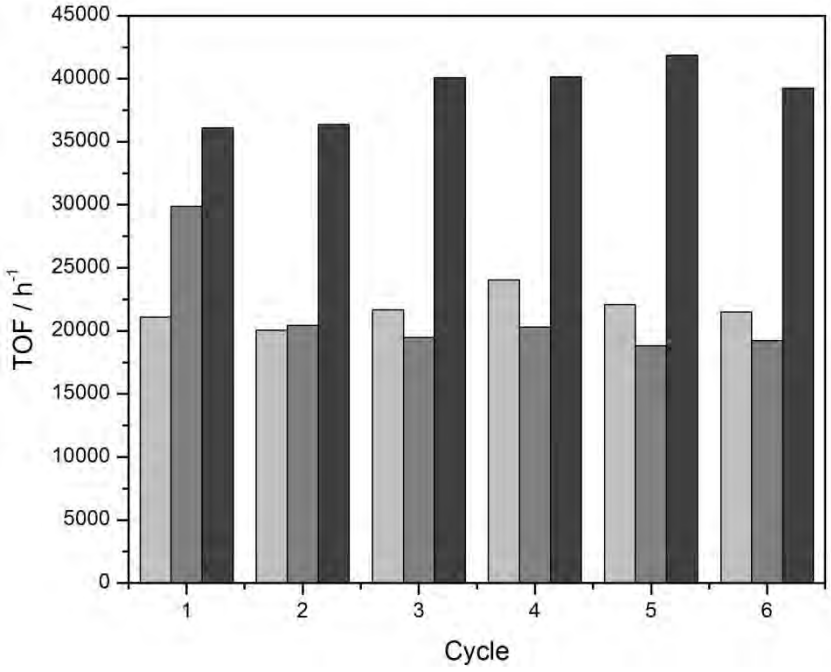

Figure 4.38. Catalytic activity in the hydrogenation of cyclohexene of Pd@PVP supported NPs in Fe_3O_4@SiO_2CeO_2 (light gray), Fe_3O_4@SiO_2TiO_2 (gray) and Fe_3O_4@SiO_2Cal (dark gray). Reaction conditions: 6 bar H_2, 75 °C and TON of 10,000.

It is very interesting to observe differences in the catalyst activity due to a support effect in a simple structure-insensitive reaction such as hydrogenation of cyclohexene. The support was not expected to have an influence in this reaction, because cyclohexene and H_2 expected to absorb on the metal surface and not on the support. Considering that all catalysts are prepared with metal NPs of the same size, the difference in activity may be related to the interactions of the metal NPs with the support. Strong interactions with the support can promote energy surface changes which can result in easy removal of PVP from metal NPs surface during the washing steps after the immobilization process,[23] while affecting the chemisorption of the reactants. TiO_2 and CeO_2 also can have their oxidation state changed under reducing conditions in presence of Pd, increasing their polarizability, and as consequence decreasing the Pd catalytic activity has been reported.[80] This was a very

interesting observation and gas phase hydrogenation of cyclohexene was performed to study this effect.

The hydrogenation of cyclohexene was carried out in gas phase using a flow reactor (CATLAB, Hiden Analytical). 15 mg of catalyst powder was placed in a quartz tube reactor (length: 20 cm, width: 5 mm). A flow reactant mixture containing 4 vol% H_2 and 2 vol% cyclohexene balanced with argon was passed through the reactor with a total flow rate of 100 mL min^{-1} and heated at 10 °C/min from 50 to 500 °C. Both hydrogenation and dehydrogenation products, cyclohexane and benzene, were observed in the temperature range from 50 to 350 °C. Figure 4.39 shows the reaction profile mass response for cyclohexane (m/z= 84) and benzene (m/z= 78) as a function of temperature. Previous studies on Pt/SiO_2 demonstrated that cyclohexene and benzene are not formed with thermodynamic selectivity.[180] The hydrogenation of cyclohexene at low temperature is thermodynamically preferred, while dehydrogenation dominates at high temperature, and the switch between preferential hydrogenation and dehydrogenation occurs over a very narrow temperature range. Reaction temperatures of 127 °C favor hydrogenation ($Kh/Kd = 10^7$), while 327 °C favors dehydrogenation ($Kh/Kd = 10^{-2}$).[181] There are few studies on the selectivity of cyclohexene conversion in excess hydrogen over experimental conditions where the formation of both cyclohexane and benzene is thermodynamically permissible[181] because most experimental studies have focused on conditions where only hydrogenation occurs (low temperature) or conditions where only dehydrogenation occurs (high temperature).[182]

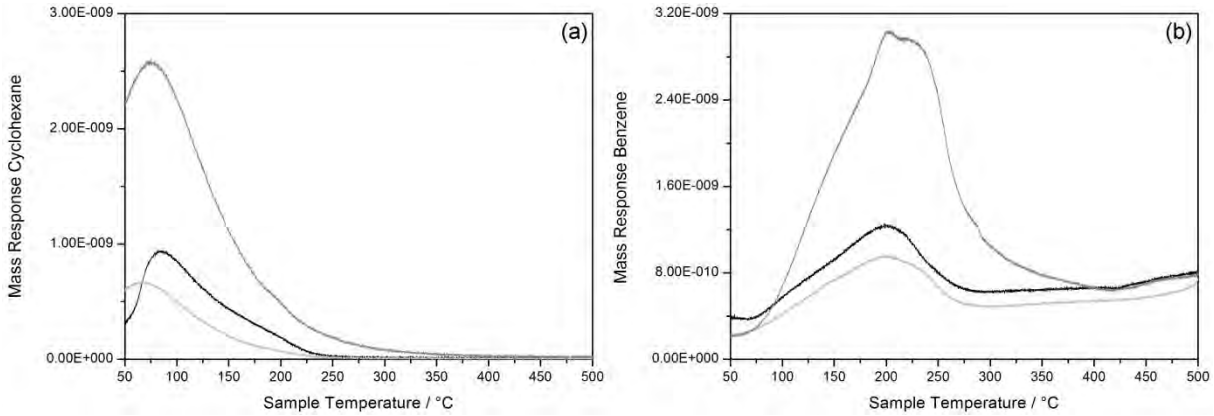

Figure 4.39. Gas composition by mass spectrometry of hydrogenation of cyclohexene in gas phase by Fe_3O_4@SiO_2CalRhPVP (black), Fe_3O_4@SiO_2CeO_2RhPVP (light gray) and Fe_3O_4@SiO_2TiO_2RhPVP (dark gray). Mass response of (a) cyclohexane (m/z = 84) and (b) benzene (m/z = 78).

Here, the conversion of cyclohexene in the presence of excess H_2 (H_2/cyclohexene ratio = 2:1) is characterized by three regimes: hydrogenation of cyclohexene to cyclohexane at low temperature (T < 100°C), an intermediate temperature range in which both hydrogenation and dehydrogenation occur; and a high temperature regime in which the dehydrogenation of cyclohexene dominates (T > 200°C). The temperatures where the Rh catalysts showed maximum hydrogenation activity are 65, 75 and 85 ºC for Fe_3O_4@SiO_2CeO_2RhPVP, Fe_3O_4@SiO_2TiO_2RhPVP and Fe_3O_4@SiO_2CalRhPVP, respectively. At this temperature range, cyclohexane is the main product. However, at higher temperatures, the reaction main product is benzene, due to the dehydrogenation of cyclohexene. This reaction occurs at a similar temperature range for all catalysts.

Supported catalysts possess oxide-metal interfaces that are absent from the extended single crystal surface. The nature of this oxide-metal interface is unknown but significant evidence exists suggesting that it is highly active and capable of altering reaction selectivity.[183] Reducible oxides, such as TiO_2 are well known for metal-support interactions with metal nanoparticles possibly providing sites of high Lewis acidity. In this way, Escobar *et al.* reported a positive effect on cyclohexane dehydrogenation activity of nickel supported

on Al_2O_3 by the addition of titania, since the resulting mixed oxide at Al/Ti 1/25 ratio promoted a better dispersion of Ni. However, dehydrogenating activity was suppressed on equimolar Al/Ti, that the authors attributed to be geometrical and electronic in nature.[184]

The catalytic conversion of cyclohexene to benzene, which is the rate determining step in cyclohexane to benzene conversion reaction - an important petroleum refining and reforming processes,[185] has also been studied under oxidative conditions in the presence of O_2, instead of H_2. The oxidative dehydrogenation can overcome a thermodynamic limitation of dehydrogenation of cyclohexane and coking issues, which can cause catalyst deactivation.[186] The dehydrogenation was attempted in the presence of O_2, keeping the same catalytic conditions, but replacing H_2 by O_2 (fresh catalysts were used). In these conditions, Fe_3O_4@SiO_2CalRhPVP was the only active rhodium catalyst. The temperature where the reaction starts (275 ºC) is higher than in the presence of H_2, but the conversion occurs from this temperature until the higher measured temperature.

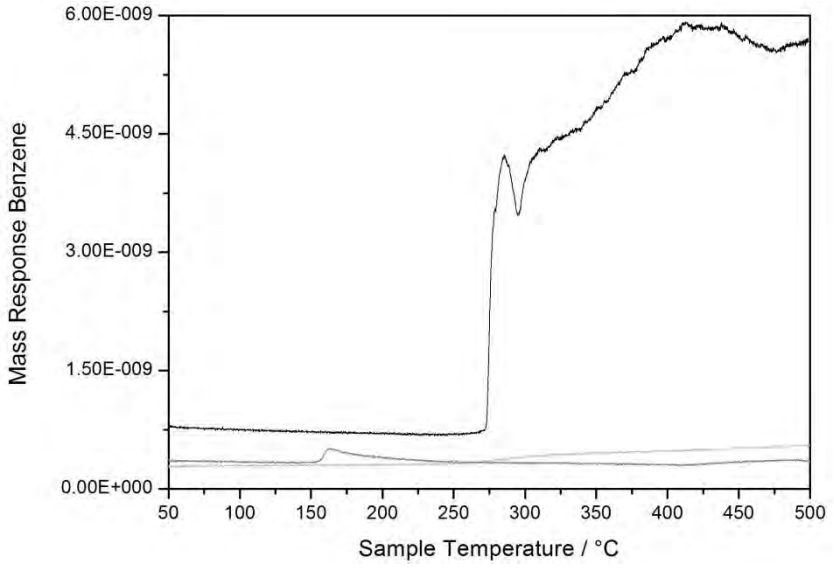

Figure 4.40. Gas composition obtained by mass spectrometry during dehydrogenation of cyclohexene in gas phase by Fe_3O_4@SiO_2CalRhPVP (black), Fe_3O_4@SiO_2CeO_2RhPVP (light gray) and Fe_3O_4@SiO_2TiO_2RhPVP (dark gray). Mass response of benzene (m/z = 78).

On the same way, Palladium catalysts supported on Fe_3O_4@SiO_2Cal, Fe_3O_4@SiO_2CeO_2 and Fe_3O_4@SiO_2TiO_2 were also employed in the gas phase hydrogenation of cyclohexene. Figure 4.41 shows the formation of cyclohexane and benzene as a function of temperature. The temperature range where the main selectivity is cyclohexane is similar as for Rh catalysts, but the temperature where the maximum conversion is achieved is around 70 ºC for all Pd catalysts. This result indicates that Pd catalytic activity on cyclohexene hydrogenation is not suffering support influence, which is in agreement with the very different results observed for Pd and Rh catalysts in the liquid phase hydrogenation of cyclohexene (figure 4.38 and 4.36).

The benzene formation temperature for maximum conversion with Pd catalysts supported on Fe_3O_4@SiO_2Cal, Fe_3O_4@SiO_2CeO_2 and Fe_3O_4@SiO_2TiO_2 is 248, 238 and 242 ºC, respectively. The Pd catalysts show maximum conversion at temperatures around 40 ºC higher than Rh catalysts.

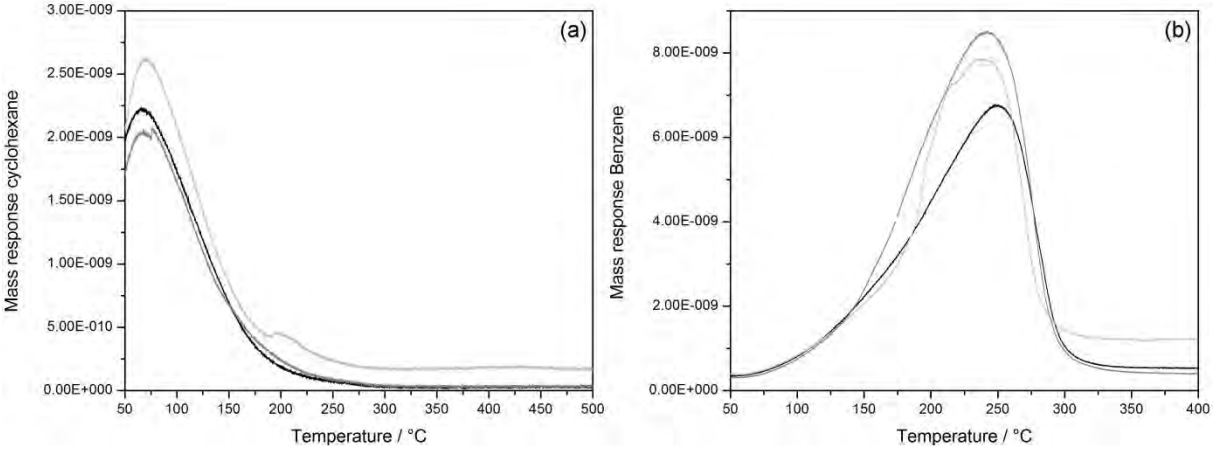

Figure 4.41. Gas composition by mass spectrometry of hydrogenation of cyclohexene in gas phase by Fe_3O_4@SiO_2CalPdPVP (black), Fe_3O_4@SiO_2CeO_2PdPVP (light gray) and Fe_3O_4@SiO_2TiO_2PdPVP (dark gray). Mass response of (a) cyclohexane (m/z = 84) and (b) benzene (m/z = 78).

The liquid phase hydrogenation of cyclohexene showed support influence for the Rh catalysts, where ceria and titania supports resulted in higher catalytic activity. On gas phase hydrogenation, the same behavior was observed for Rh catalysts, but Pd catalysts showed the same temperature for the maximum conversion to cyclohexane. This is an indication that the palladium nanoparticles are not being affected by the support in this specific reaction.

Supported Rh@PVP catalysts presented different PVP elimination profile during preliminary studies with CO oxidation. The elimination of PVP can be observed by an intense peak in CO_2 mass response just before the catalysts achieve the maximum conversion. This CO_2 peak can be observed for Fe_3O_4@SiO_2CalRhPVP at 150 ºC and for Fe_3O_4@SiO_2TiO_2RhPVP at 140 ºC. On the other side, the Fe_3O_4@SiO_2CeO_2RhPVP showed a very different behavior. The conversion was oscillating before PVP elimination and occurred in a much higher temperature (175 ºC) (figure 4.42b). We have little information about this behavior, but it clearly demonstrates a different interaction of PVP, metal and support, which should be the reason for the higher activity in the hydrogenation of cyclohexene observed for Fe_3O_4@SiO_2CeO_2RhPVP. The peak was attributed to the PVP elimination due to its absence in a second reaction using the catalyst Fe_3O_4@SiO_2TiO_2RhPVP, although the temperature where the reaction reaches maximum conversion shifted to 155 ºC. This increase is an indication of oxidation and/or aggregation of the Rh NPs.

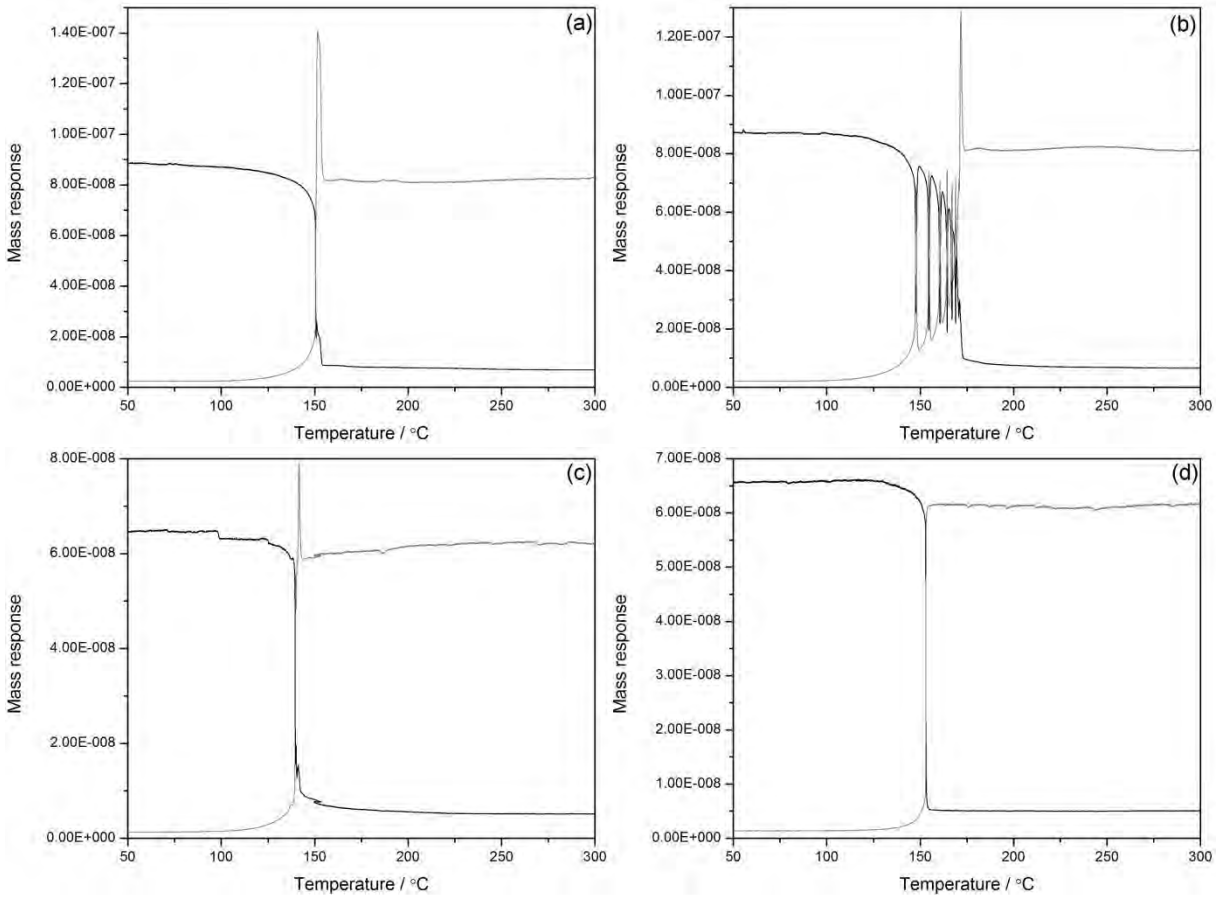

Figure 4.42. Conversion of CO (black) to CO_2 (gray) by (a) Fe_3O_4@SiO_2CalRhPVP, (b) Fe_3O_4@SiO_2CeO_2RhPVP, (c) Fe_3O_4@SiO_2TiO_2RhPVP and (d) reuse of the Fe_3O_4@SiO_2TiO_2RhPVP catalyst.

4.3.3.2. Hydrogenation of phenol

The hydrogenation of phenol is a reaction of interest to evaluate the influence of the nature of supports on the activity and selectivity of supported metal NPs. In this reaction the support can influence the product selectivity due to the adsorption of phenol on the support's surface. Literature data report that the adsorption of phenol at acidic sites occurs in a co-planar orientation and at basic sites in a non-planar orientation (figure 4.43). As a consequence, the supports with acidic sites tend to enhance the formation of cyclohexanol and

basic sites the formation of cyclohexanone.[187] Figure 4.43 shows the adsorption of phenol by basic sites and acidic sites and the favored product formation.

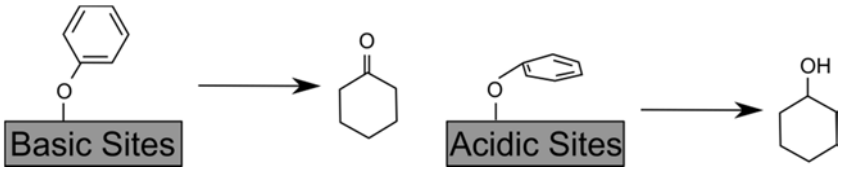

Figure 4.43. Phenol adsorption by basic and acidic sites and enhanced product selectivity. Adapted from Cheng *et al.*[187]

The hydrogenation of phenol was performed following the standard conditions for liquid phase catalysis using Fisher Porter glass reactor (75 ºC and 6 bar H_2) employed so far, except for a substrate-to-catalyst molar ratio of 20, which is much lower than the in cyclohexene hydrogenation. The H_2 monitoring system used to follow the cyclohexene hydrogenation (Experimental section – 3.3.7) is not sensitive enough to detect pressure drop in the conditions used, due to the small amount of substrate and consequently, small consumption of H_2. A reaction with this substrate-to-catalyst molar ratio and a detectable H_2 consumption would require an impractical amount of solution and catalyst for the used reactors. In any case, this reaction is not trivial to be monitored by H_2 consumption, because successive reactions that consume H_2 can occur (figure 4.44). Thus, differently from the previous hydrogenation reactions, the phenol hydrogenation was not be monitored by the H_2 monitoring system. The phenol conversion was followed by GC analysis of samples taken in time intervals from the reactor. In this way, the reactor was cooled down and depressurized to take each sample, a procedure that can affect the reaction course. In order to avoid a high influence during this time, all samples were taken following the same procedure and the time between cooling, sample collection and reinitialization of the reaction were as close as possible for all samples.

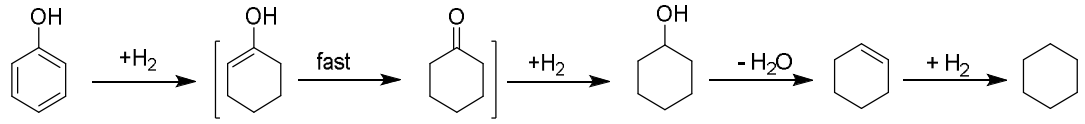

Figure 4.44. Hydrogenation and hydrodeoxygenation of phenol reaction and side reactions.

Table 4.16 shows the comparison of conversion and selectivity obtained with the different metals and supports in the hydrogenation of phenol for samples analyzed after 2 and 20 h. The catalysts used in this reaction were the Rh@PVP, Ru@PVP and Pd@PVP supported on the solids Fe_3O_4@SiO_2Cal, Fe_3O_4@SiO_2CeO_2 and Fe_3O_4@SiO_2TiO_2.

Table 4.16. Hydrogenation of phenol using supported metal NPs obtained by organometallic approach.[a]

Entry	Catalyst	Conv. (%)[b]		Selectivity (%)[b]					
				Cyclohexanone		Cyclohexanol		Cyclohexane	
		2 h	20 h	2 h	20 h	2 h	20 h	2 h	20 h
1	Blank	0	0	0	0	0	0	0	0
2	Phenol solution	0	0	0	0	0	0	0	0
3	Pd/C	99	100	47	39	52	61	0	0
4	Fe_3O_4@SiO_2CalPdPVP	94	100	90	82	6	12	4	6
5	Fe_3O_4@SiO_2CeO_2PdPVP	86	99	86	80	12	17	2	3
6	Fe_3O_4@SiO_2TiO_2PdPVP	91	99	82	78	16	19	2	3
7	Fe_3O_4@SiO_2CalRhPVP	100	100	26	1	71	87	3	12
8	Fe_3O_4@SiO_2CeO_2RhPVP	100	100	39	5	61	94	0	1
9	Fe_3O_4@SiO_2TiO_2RhPVP	100	100	12	0	88	99	0	1
10	Fe_3O_4@SiO_2CalRuPVP	93	100	24	1	73	92	3	7
11	Fe_3O_4@SiO_2CeO_2RuPVP	99	100	17	0	83	100	0	0
12	Fe_3O_4@SiO_2TiO_2RuPVP	100	100	0	0	100	100	0	0

[a] Reactions conditions: phenol (75 μmol), solvent n-hexane (3 mL), catalyst (36 mg, 3.7 μmol), and substrate/catalyst = 20, 75°C, 6 bar H_2. [b] Conversion and selectivity determined by GC.

Initially, the hydrogenation of phenol was performed with the commercially available catalyst Pd/C (3 wt%, Sigma-Aldrich, Co). Despite being very active in the hydrogenation of phenol (100 % conversion), this Pd/C catalyst was not selective, thus producing a mixture of cyclohexanone and cyclohexanol (Table 4.16, entry 3). Blank experiments were also performed, giving no conversion (Table 4.16, entry 1 and 2). Figure 4.45 shows the conversion and selectivity as a function of time obtained with the catalysts Fe_3O_4@SiO_2CalPdPVP, Fe_3O_4@SiO_2CeO_2PdPVP and Fe_3O_4@SiO_2TiO_2PdPVP. Independently of the support the Pd catalysts are selective to cyclohexanone formation. They display small differences in the selective during time, but all catalysts show the same tendency. The results obtained after 20 h are presented in the table 4.16 (entries 4 to 6) and show that the titania was the less selective catalyst, but the difference to ceria in cyclohexanone selectivity is only 2 %. In this way, we can conclude that the selectivity is not being modified by support influence. The biggest difference was observed for the silica support that shows conversion to cyclohexane, the product of hydrodeoxygenation of phenol, but the selectivity was 4 % after 2 h and only 6 % even after 20 h (table 4.16, entry 4). The other supports reached a selectivity of 3 % after 20 h to cyclohexene (table 4.16, entries 5 and 6).

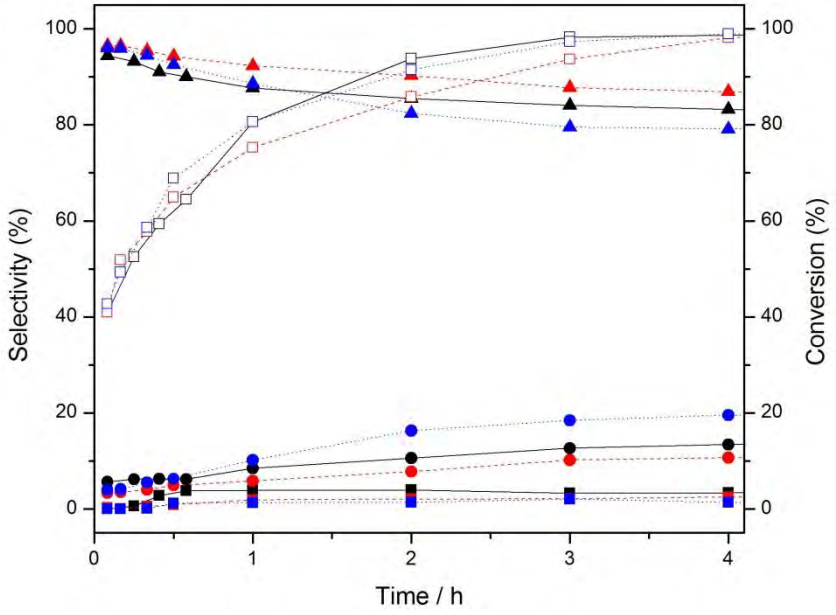

Figure 4.45. Phenol hydrogenation/hydrodeoxygenation using Fe_3O_4@SiO_2CalPdPVP (black), Fe_3O_4@SiO_2CeO_2PdPVP (red) and Fe_3O_4@SiO_2TiO_2PdPVP (blue). Conversion of phenol (empty squares) and selectivity to cyclohexanol (circles), cyclohexanone (triangles) and cyclohexane (squares)

Similar studies were performed with Ru catalysts prepared by the immobilization of Ru@PVP NPs on different supports (Fe_3O_4@SiO_2CalRuPVP, Fe_3O_4@SiO_2CeO_2RuPVP and Fe_3O_4@SiO_2TiO_2RuPVP catalysts). The curves of selectivity and conversion of phenol as a function of reaction time are presented in the figure 4.46. The reactions conditions were the same as for Pd catalysts and the GC analysis were performed in the same way. Differently from Pd, the Ru catalysts were more selective to cyclohexanol and in the case of ceria and titania supports, the selectivity to cyclohexanol reached 100 % in 4 h. At initial reaction times, the Ru catalysts showed low conversion compared to Pd, but after 30 min the conversion increased very fast with time. This might be an indication that the Ru is partially oxidized, which would be expected since the immobilization was performed under air and the catalysts were not kept under argon before catalysis. The catalyst supported on ceria and titania reached 100 % phenol conversion faster than silica supported catalyst. The samples analyzed after 1 h reaction showed quite different conversion values. The catalysts containing titania reached

100 % conversion, but the conversion with catalysts with only silica was around 80 %. Besides the hydrogenation products, cyclohexanone and cyclohexanol, the product of hydrodeoxygenation of phenol, cyclohexane, was observed for the silica supported catalyst and the selectivity reached 7 % after 20 h (Table 4.16, entry 10). Cyclohexane was not present in the samples collected when ceria and titania supports were used.

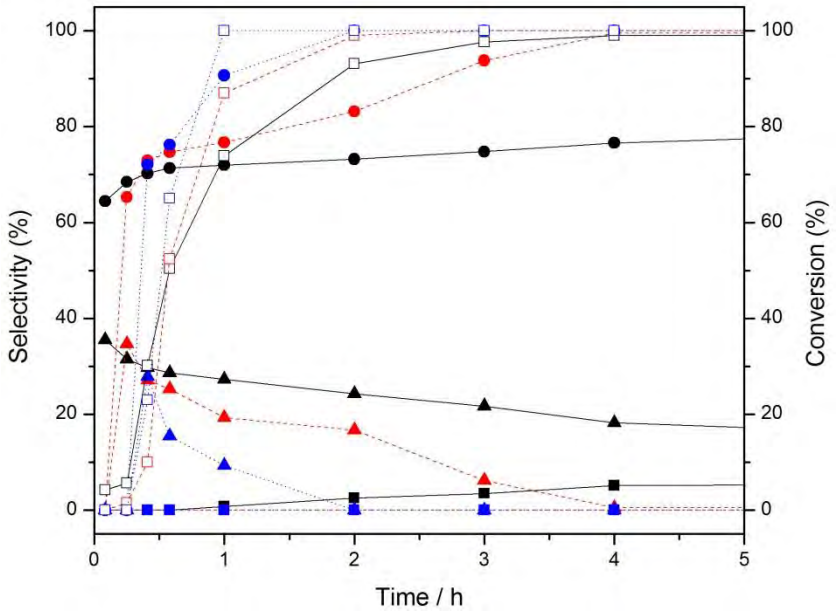

Figure 4.46. Phenol hydrogenation/hydrodeoxygenation using Fe_3O_4@SiO_2CalRuPVP (black), Fe_3O_4@SiO_2CeO_2RuPVP (red) and Fe_3O_4@SiO_2TiO_2RuPVP (blue). Conversion of phenol (empty squares) and selectivity to cyclohexanol (circles), cyclohexanone (triangles) and cyclohexane (squares)

The Rh catalysts prepared by the immobilization of Rh@PVP NPs on different supports (Fe_3O_4@SiO_2CalRhPVP, Fe_3O_4@SiO_2CeO_2RhPVP and Fe_3O_4@SiO_2TiO_2RhPVP catalysts) were also more selective to cyclohexanol as demonstrated in figure 4.47. However, Rh showed total conversion of phenol even for samples collected after 5 min. This result characterizes the Rh catalysts as the most active for phenol hydrogenation. The major differences are the conversion rates of cyclohexanone to cyclohexanol. Titania support reached 96 % selectivity to cyclohexanol after 4 h. As observed with Ru catalysts, only the Rh

catalyst supported on silica was active in the hydrodeoxygenation of phenol with formation of cyclohexane. After 20 h, the selectivity to cyclohexane was 12 %.

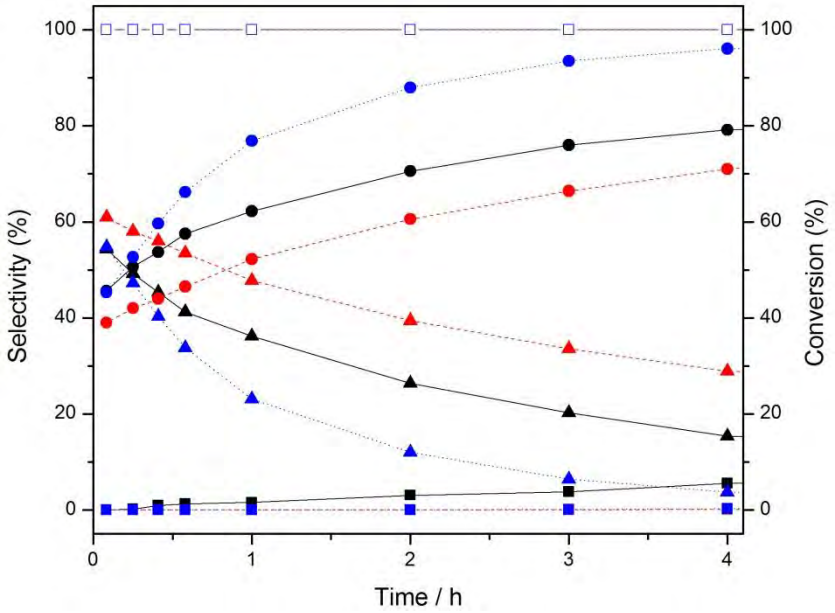

Figure 4.47. Phenol hydrogenation/hydrodeoxygenation using Fe_3O_4@SiO_2CalRhPVP (black), Fe_3O_4@SiO_2CeO_2RhPVP (red) and Fe_3O_4@SiO_2TiO_2RhPVP (blue). Conversion of phenol (empty squares) and selectivity to cyclohexanol (circles), cyclohexanone (triangles) and cyclohexane (squares)

In order to better study the selectivity of the Rh catalysts, the substrate-to-catalyst molar ratio was increased to 200. The curves of conversion and selectivity as a function of reaction time under these new conditions are shown in the figure 4.48. The conversion of phenol for all catalysts was slower when using a higher substrate-to-catalyst molar ratio, as expected. However, the selectivity changed, which resulted in different compositions as the reaction proceeds. All catalysts showed the tendency to an equal selectivity to cyclohexanone and cyclohexanol (table 4.17 and figure 4.48). The Fe_3O_4@SiO_2TiO_2RhPVP with substrate/catalyst ratio of 200 was the only Rh catalyst to show after 2 h a slightly higher selectivity to cyclohexanone. This is an indication that the catalyst supported on titania was more affected by the changes in catalytic conditions.

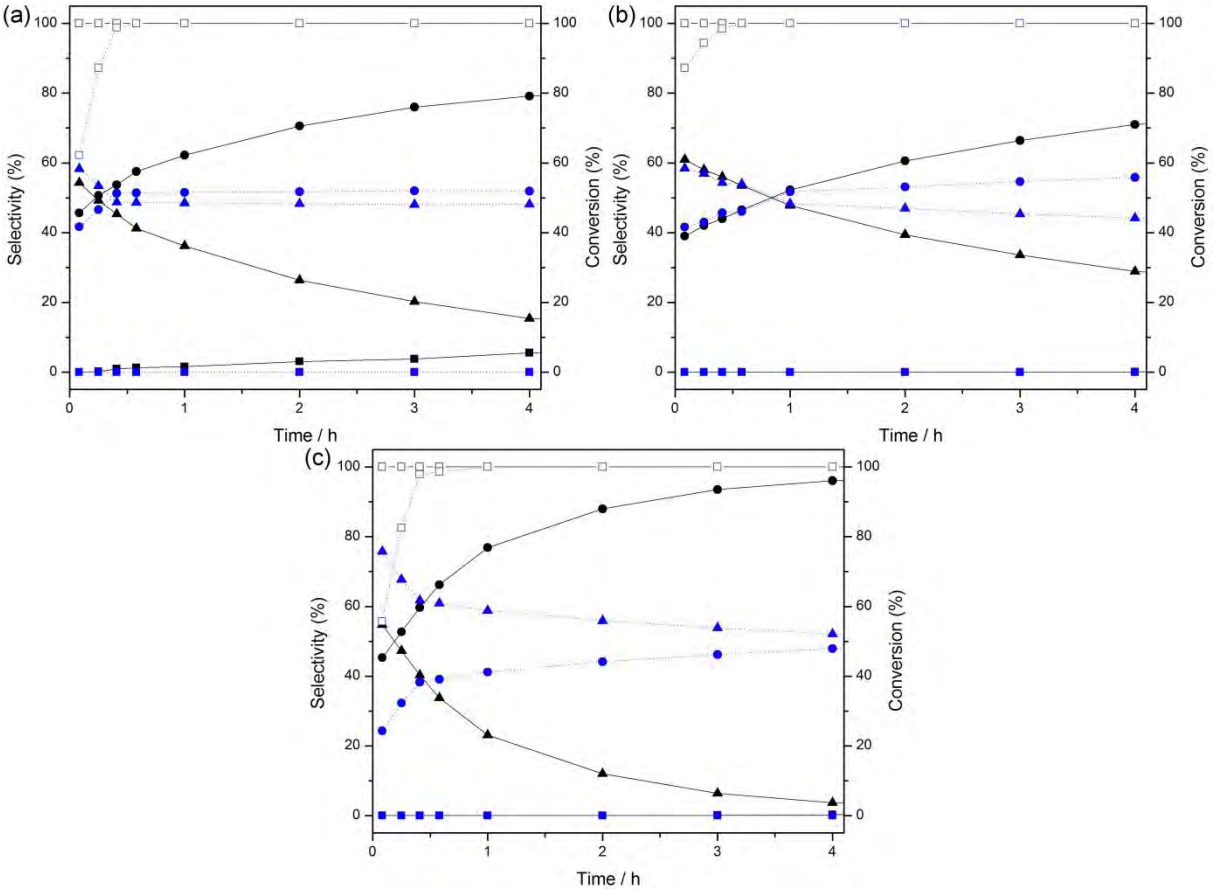

Figure 4.48. Phenol hydrogenation/hydrodeoxygenation using Fe_3O_4@SiO_2CalRhPVP (a), Fe_3O_4@SiO_2CeO_2RhPVP (b) and Fe_3O_4@SiO_2TiO_2RhPVP (c) with substrate/catalyst molar ratio = 20 (black) and 200 (blue). Conversion of phenol (empty squares) and selectivity to cyclohexanol (circles), cyclohexanone (triangles) and cyclohexane (squares).

Table 4.17. Hydrogenation of phenol using supported Rh NPs obtained by organometallic approach.[a]

Entry	Catalyst	Conv. (%)[b]		Selectivity (%)[b]					
				Cyclohexanone		Cyclohexanol		Cyclohexane	
		2 h	20h	2 h	20h	2 h	20h	2 h	20h
1	Fe_3O_4@SiO_2CalRhPVP	100	100	52	53	48	47	0	0
2	Fe_3O_4@SiO_2CeO_2RhPVP	100	100	53	60	47	39	0	0
3	Fe_3O_4@SiO_2TiO_2RhPVP	100	100	44	56	57	43	0	0

[a] Reactions conditions: phenol (75 µmol), solvent n-hexane (3 mL), catalyst (36 mg, 3.7 µmol), and substrate/catalyst = 200, 75 °C, 6 bar H_2. [b] Conversion and selectivity determined by GC.

Considering the whole series of catalysts investigated, Pd catalysts were the most selective for the conversion of phenol to cyclohexanone with the lower production of cyclohexanol. Cyclohexanone is a valuable intermediate in the preparation of ε-caprolactam, which is used in the manufacturing of nylon-6, nylon-6,6 and polyamide resins. Cyclohexanone is industrially produced by the hydrogenation of phenol or oxidation of cyclohexene.[188] In this way, a catalyst with high selectivity to cyclohexanone is very interesting. Moreover, the formation of cyclohexane due to the hydrodeoxygenation of phenol is also very interesting as an alternative route for the production of alkanes. Phenol is a model for lingocelullosic biomass and the preparation of catalysts selective to the hydrodeoxygenation opens the possibility to produce fuels from bio-feedstock.[189] The formation of cyclohexane was observed at mild conditions, but with low selectivity and mainly with the silica support for Pd, Rh and Ru catalyst. Zhao *et al.*[189b] reported the hydrodeoxygenation at 150 ºC, 50 bar H_2, substrate/catalyst ratio 500 in H_3PO_4 aqueous solution (0.5 wt%).

The hydrogenation of phenol using the magnetic support Fe_3O_4@SiO_2TiO_2 resulted in a higher selectivity to cyclohexanol, independently of the metal NPs. This indicates that the support is affecting the catalytic performance of the supported metal NPs. The formation of cyclohexanol during the hydrogenation of phenol is enhanced by the presence of acidic groups on the support surface. This result demonstrates the possibility to tune catalytic properties of supported metal NPs.

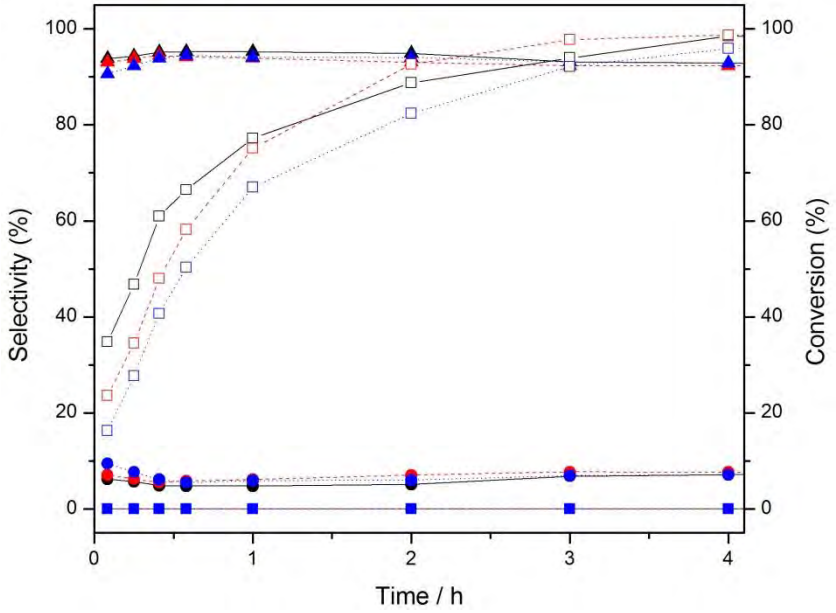

Figure 4.49. Phenol hydrogenation/hydrodeoxygenation using Fe_3O_4@SiO_2CalPdPVP at H_2 pressure of 6 bar (black), 3 (red) and 1 bar (blue). Conversion of phenol (empty squares) and selectivity to cyclohexanol (circles), cyclohexanone (triangles) and cyclohexane (squares).

Typically in the heterogeneous catalysis a calcination procedure is usually applied in order to enhance the catalytic properties of the material, either by improving the metal support interaction or by removing surface contaminants. Consequently, to study the effect of calcination, the Pd catalysts were calcined at 300 ºC for 2 h, to remove the PVP stabilizer. The obtained materials were tested in the hydrogenation of phenol using water and n-hexane as solvent. The reactions were analyzed after 2 h by GC and the results are presented in table 4.18. Independently on the solvent and catalyst, the selectivity to cyclohexanone was very high. In water, the formation of cyclohexanol was not observed and conversions were lower than 80 %, except for titania which presented 100 % conversion to cyclohexanone. The formation of cyclohexane was observed only for the ceria support in water, which is interesting because ceria support showed the lowest conversion both in water and n-hexane. A small enhancement of the catalytic results can be observed comparing the results obtained with the as prepared Pd catalysts in n-hexane (except for ceria support). However, the use of

water as solvent was not a good alternative, because the catalysts could not be totally removed by a magnet. This is sometimes observed for silica particles that stabilize very well in water and, then, are less easily separated magnetically. Thus, for this reason the n-hexane was the selected solvent. The as prepared catalysts were not used in aqueous solution to avoid metal leaching, once PVP is well soluble in water.

Table 4.18. Hydrogenation of phenol with calcined Pd using water and n-hexane as solvent.[a]

Entry	Catalyst	Conv. (%)[b]	Selectivity (%)[b]		
			cyclohexanone	cyclohexanol	cyclohexane
1	Fe_3O_4@SiO_2CalPdPVP[c]	79	100	0	0
2	Fe_3O_4@$SiO_2$$CeO_2$PdPVP[c]	70	93	0	7
3	Fe_3O_4@$SiO_2$$TiO_2$PdPVP[c]	100	100	0	0
4	Fe_3O_4@SiO_2CalPdPVP[d]	98	95	5	0
5	Fe_3O_4@$SiO_2$$CeO_2$PdPVP[d]	25	95	5	0
6	Fe_3O_4@$SiO_2$$TiO_2$PdPVP[d]	99	96	4	0

[a] Reactions conditions: phenol (75 μmol, in 3 mL [c] water or [d] n-hexane), catalyst (36 mg, 3.7 μmol), substrate/catalyst = 20, 75°C, 6 bar H_2. [b] Conversion and selectivity determined by GC.

4.3.2.4. Benzyl alcohol oxidation

A very interesting reaction for the evaluation of support influence in the catalytic activity of supported metal NPs is the oxidation of benzyl alcohol. However, we could not use the supported catalysts due to the high solubility of PVP in polar media and, consequently, leaching of metal@PVP NPs to the solution. Some interesting and worth mention catalytic results were obtained using the supports and colloidal PVP-stabilized NPs of Ru, Rh, Pd and Au (Table 4.19). These reactions were intended as controls for the comparison of support influence.

Table 4.19. Oxidation of Benzyl alcohol

Entry	Catalyst[a]	Time (h)	Conv. (%)	Selectivity to benzaldehyde (%)
1[b]	-	24	4	78
2	Fe_3O_4@SiO_2CeO_2	24	0.3	47
3	Fe_3O_4@SiO_2TiO_2	24	0	--
4	Fe_3O_4@SiO_2Cal	24	0	--
5	Ru@PVP	2	7	98
6	Ru@PVP	24	20	99
7	Au@PVP	2	2.4	100
8	Au@PVP	24	5.7	98
9	Rh@PVP	2	0.9	100
10	Rh@PVP	24	1.5	91
11	Pd@PVP	2	23	86
12	Pd@PVP	24	95	71

[a] Reaction conditions: benzyl alcohol (1 mL, 10 mmol), catalyst (2 mg, 2 μmol), 100 ºC, 3 bar O_2 and substrate/catalyst = 5000. [b] Reaction without catalyst.

A blank reaction with benzyl alcohol only in the reactor resulted after 24 h in the conversion of around 4 % of the substrate (table 4.19 entry 1). The blank reaction with support and substrate resulted in a remarkable reduction of conversion of benzyl alcohol.

In the reactions performed with colloidal NPs some initial conclusions are: (a) gold is very selective, but not very active; (b) ruthenium is selective to benzaldehyde and only moderately active; (c) rhodium is selective, but is poorly active and (d) palladium is very active and not selective. The trend observed for the series of catalysts are in agreement with literature data. The results observed make Au@PVP NPs interesting candidates for further studies in the oxidation of alcohols. In fact, Au NP catalysts have received a lot of attention in the literature given the high selectivity they provide in oxidation reactions.[190] Since, the

preparation of Au@PVP was not straightforward it will be presented later in the section 4.3.3.1.

The colloidal Au@PVP NPs were not stable under reaction conditions and the solution color changed from brown to red, which is an indication of change in particle size or aggregation. The TEM characterization of the sample recovered after the reaction (figure 4.50 A) showed Au NPs with average diameter larger than before catalysis (4.0 ± 1.5 nm). The TEM analysis after reaction of the Rh@PVP NPs and Ru@PVP NPs did not show any NP morphological or size modification. The Rh@PVP NPs size after reaction is 1.9 ± 0.4 nm and Ru@PVP NPs is 1.6 ± 0.2 nm (figure 4.50 B and C).

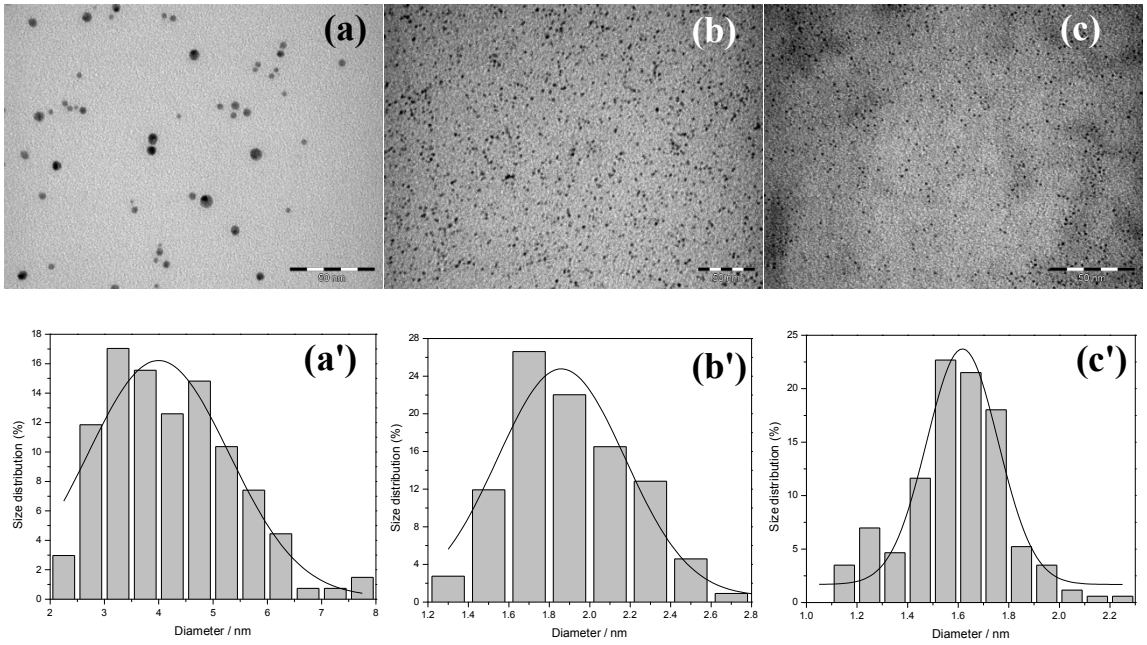

Figure 4.50. Micrograph obtained by TEM of (a) Au@PVP, (b) Rh@PVP and (c)Ru@PVP after benzyl alcohol oxidation and the correspondent size distribution histogram adjusted to a Gaussian function. Scale bar = 50 nm

The Pd@PVP was not analyzed because the NP precipitated after the reaction. The supported Pd NPs employed in the oxidation of benzyl alcohol did not precipitate, but the metal leaching was sufficient to turn the supernatant solution color into black. The NPs did

not precipitate in the presence of the support; however, they did not stay attached to the support either, which means that we could not study the influence of support because, at the end, the NPs are not interacting with the support and are acting free in solution. The samples after 24 h with colloidal Pd@PVP NPs resulted in a solid product meaning a high conversion to benzoic acid. Otherwise, in the presence of support the resulting product after 24 h is liquid. Thus, the lack of precipitation is clearly due to less benzoic acid formation. No further studies were performed.

In an attempt to remove PVP and minimize the metal leaching, the supported Au@PVP NPs catalysts were calcined at 300 ºC for 2 h under air atmosphere. Unfortunately, the resulting materials were not active in the benzyl alcohol or CO oxidation. The lack of activity in both reactions indicated that the thermal treatment resulted in large metal NPs, once that the activity for CO oxidation is size dependent.[22]

4.3.3. Difficulties found in the preparation of preformed metal nanoparticles

4.3.3.1. Gold nanoparticles stabilized with PVP

Gold catalysts and exhibit excellent catalytic properties and high selectivity in various reactions, especially oxidation ones; however, gold has a limited impact on industrial catalysis. For instance, Au NPs are known to be very active catalysts in the oxidation of CO at low temperature. They also received attention as catalysts for the selective oxidation of alcohols to aldehydes.[190]

In nanocatalysis, a challenge still to be overcome is the preparation of catalysts of controlled size that are sufficiently stable, while maintaining an acceptable activity and selectivity under real catalytic conditions. One objective of this thesis was to look for synthesis conditions in solution to obtain size-controlled gold NPs, which is not trivial, in order to prepare Au-supported catalysts and study the influence of the support on the catalytic performance. Literature data already reported that the activity of gold nanoparticles can be affected by the nature of the supports.[191] For example, Au supported on nanoceria was described as active for benzyl alcohol oxidation in absence of added base, usually necessary as co-catalyst.[192]

Our first intent towards the synthesis of size-controlled Au NPs was the preparation of a gold complex and its decomposition into Au@PVP NPs. The selected complex was Chloro(tetrahydrothiophene)gold(I) (AuCl(THT)) (figure 4.51) employed by de Caro *et al.*[154] as precursor for the preparation of Au@PVP NPs.

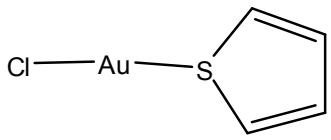

Figure 4.51. Structure of AuCl(THT)

The complex AuCl(THT) was prepared from the reaction of $AuCl_3$ with THT in degassed ethanol. The complex was characterized by elemental analysis (Table 4.20) and FTIR (figure 4.52). The elemental analysis experimental results are in agreement with the theoretical calculation and the vibrational bands in the FTIR spectra are characteristic of AuCl(THT) (ν_{Au-Cl} = 328 cm^{-1} and ν_{Au-S} = 347 cm^{-1}).

Table 4.20. Elemental analysis of AuCl(THT)

Element	Theoretical %	Experimental %
C	14.99	14.77
H	2.52	2.31

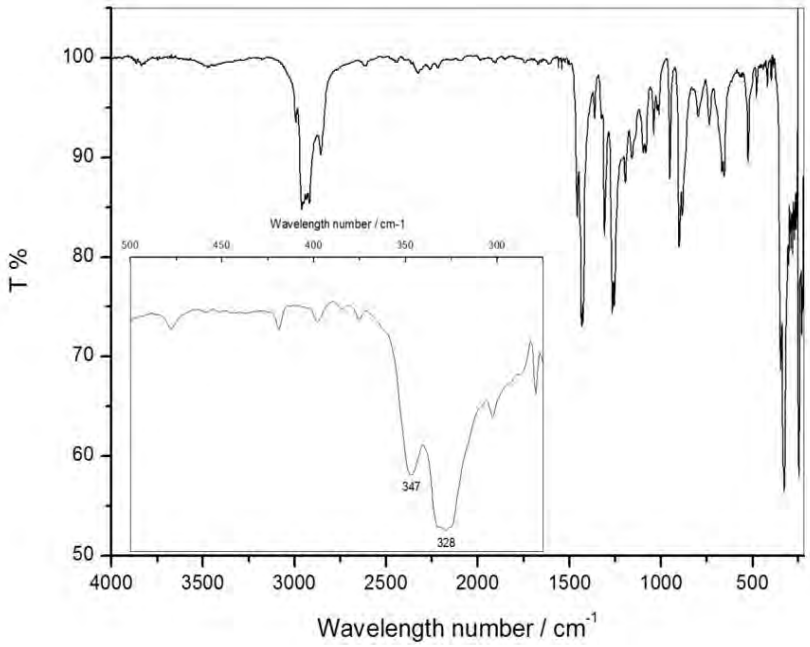

Figure 4.52. Infrared transmission spectrum of AuCl(THT) obtained using CsBr pellets

The procedure to prepare Au@PVP followed the same principle as for Rh, Pd and Ru@PVP NPs and is also very similar to a method reported by de Caro *et al.*[154] who decomposed the complex AuCl(THT) in dichloromethane under CO atmosphere at room temperature. The gold precursor was first dissolved in a THF solution of PVP and submitted to 3 bar hydrogen pressure. After 20 h, the solution did not show any visible sign of change. The first and most clear indication of Au NPs formation is the color. Indeed, Au NPs display plasmon bands and lead to colored colloidal solution where the color is size dependent. The fact that the Au@PVP NPs were not formed could be attributed to a solvent effect given we used THF and not dichloromethane as reported. In another reaction we reproduced the

reaction conditions of de Caro *et al.* that are dichloromethane as solvent and atmosphere of 1 bar CO, but it was also unsuccessful. In order to remove light influence, the reactor was covered with aluminum foil. However, this covering did not afford any improvement. Consequently, a series of reactions with variation of parameters like temperature, atmosphere, pressure and light exposure were performed to try to obtain optimized conditions to prepared Au@PVP by the previously reported method. Independently of the conditions, at room temperature no sign of reaction was observed. At 70 ºC, both under argon or CO atmosphere, the reaction resulted in the formation of a brown precipitate, which demonstrated that the temperature was responsible for the decomposition of the metal precursor. The materials obtained with this method were comprised of gold particles of uncontrolled size and morphology with a diameter higher that 200 nm. The light exposure did not affect the reaction, except for a reactor left opened to air that resulted in bulk gold. As a second attempt to promote the reduction of the gold precursor at room temperature (mild conditions) $NaBH_4$ was added as reducing agent instead of CO or H_2, resulting in a dark blue solution. The TEM analysis revealed a poor control in morphology and size (figure 4.53a).

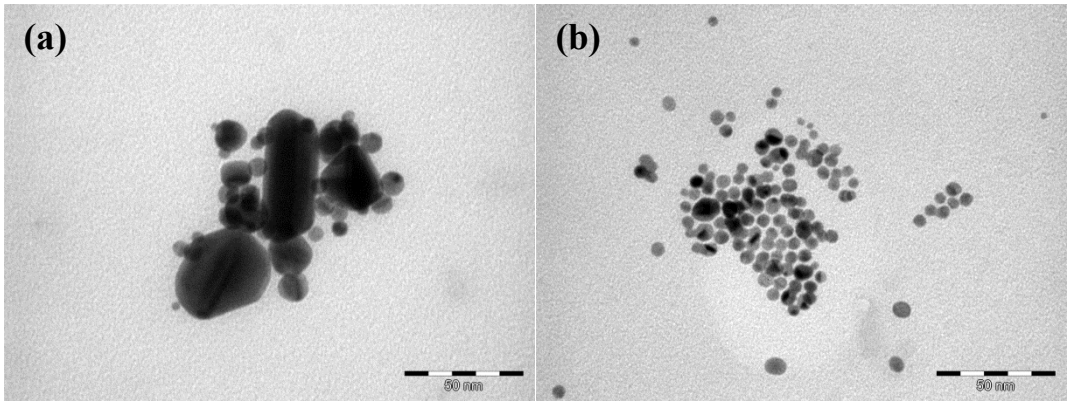

Figure 4.53. Micrograph obtained by TEM of gold particles prepared by reduction of AuCl(THT) with (a) $NaBH_4$ and PVP and (a) H_2 and hexadecylamine.

Gomez *et al.*[193] discussed the preparation of Au NPs using the AuCl(THT) as precursor and hexadecylamine (HDA) as stabilizer. The presence of HAD induces formation of an intermediate gold amino complex that can be reduced by H_2. Figure 4.53b shows the TEM micrograph of the Au NPs obtained after addition of small amount of HDA in the reaction medium. The resulting material is morphologically controlled, but the particle diameter is larger than we expected (10-15 nm). Although, this method appeared interesting in terms of size-control we moved back to the search of a synthetic method for smaller gold nanoparticles stabilized by PVP.

To prepare small Au@PVP NPs, we followed a method reported by Tsunoyama *et al.*[155] that consists in the addition of $NaBH_4$ in an aqueous solution of $HAuCl_4$ and PVP at low temperature. The characterization by TEM showed an agglomerated material before purification (figure 4.54b), but nicely dispersed and small Au@PVP NPs (1.1 ± 0.2 nm) were observed after dialysis against water (figure 4.54a). The dialysis does not select the particles or separate the agglomerates, but is most likely that the removal of the dissolved salts, that induce the agglomeration, provide a clear solution.

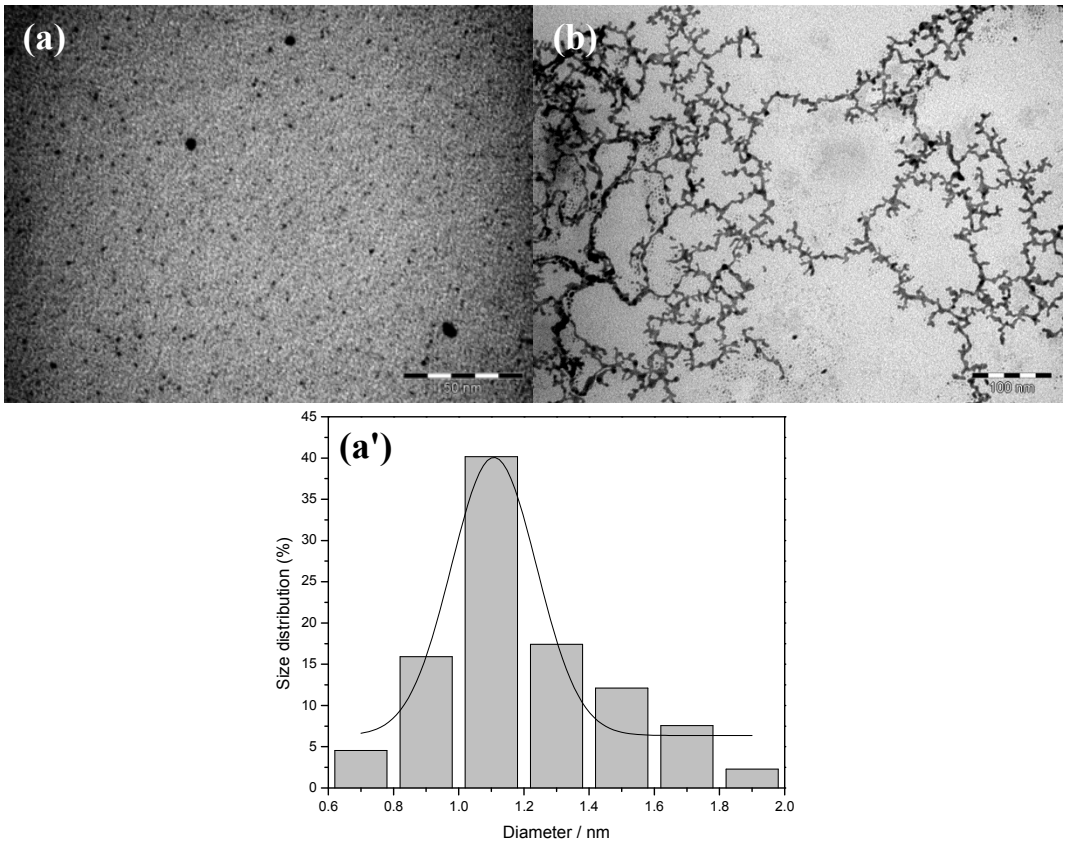

Figure 4.54. Micrograph obtained by TEM of Au@PVP (a) after and (b) before dialysis and (a') the size distribution histogram adjusted to a Gaussian function of the Au@PVP after dialysis.

4.3.3.2. Rhodium nanoparticles with PVA and organometallic approach

The preformed Rh NPs used in this thesis were prepared using $RhCl_3.xH_2O$ and PVA as stabilizer (metal reduction method) or $Rh(C_3H_5)_3$ and PVP as stabilizer (organometallic decomposition method). In order to justify the selection of different stabilizer agents, we should mention that we have tried the preparation of Rh@PVA using the organometallic approach, in order to compare with previous results; however, the PVA is not soluble in THF and, then addition of water was necessary. The addition of water in the reaction media allowed the solubilization of PVA and the presence of THF the solubilization of the Rh precursor. The reactor was pressurized with 3 bar H_2 under magnetic stirring and kept under

stirring and pressure for 20 h. The resulting solution was a colloidal suspension of Rh@PVA that was characterized by TEM (figure 4.55a). However, after a few days the metal particles precipitated. This precipitation is attributed to the presence of THF, because it can be prevented if the material is dried and redispersed in water after preparation. The Rh@PVA material prepared by this method is comprised of individual particles and large aggregates (also comprised of small particles). This is probably a solvent effect due to the presence of THF in solution, which should interfere in the solubilization of PVA.

Rh@PVA prepared by using the same conditions (THF/Water) and $RhCl_3.xH_2O$ as precursor exhibited very similar aggregates, as observed by TEM analysis (figure 4.55b).

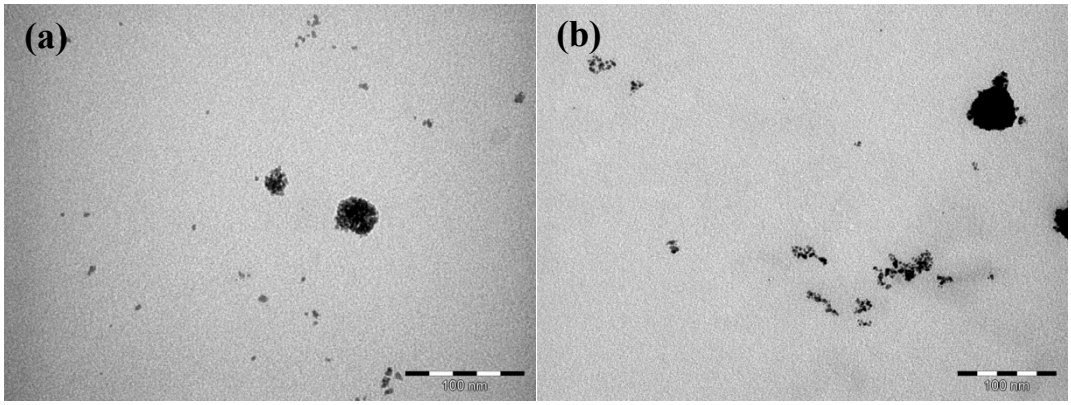

Figure 4.55. Micrograph obtained by TEM of Rh@PVA prepared using as precursor (a) $Rh(C_3H_5)_3$ and (b) $RhCl_3.xH_2O$. Scale bar = 100 nm.

Independently of the presence of aggregates, the Rh@PVA aqueous suspension prepared by the organometallic decomposition method was employed in the hydrogenation of cyclohexene at room temperature, 3 bar H_2 and substrate-to-catalyst molar ratio of 35600. The reaction was followed for 1 h and the conversion determined by GC was 58 %.After the hydrogenation reaction the catalyst phase was visually similar to the fresh suspension, so the solution was recycled to a second reaction. After 1 h the GC analysis showed a conversion of 11 % of cyclohexene to cyclohexane. The TEM analysis of the Rh@PVA after catalysis

showed an increase in the aggregation of small particles (figure 4.56). Thus, despite the catalyst deactivation the use of organometallic precursor was and enhancement in the stability of colloidal Rh@PVA NPs solution.

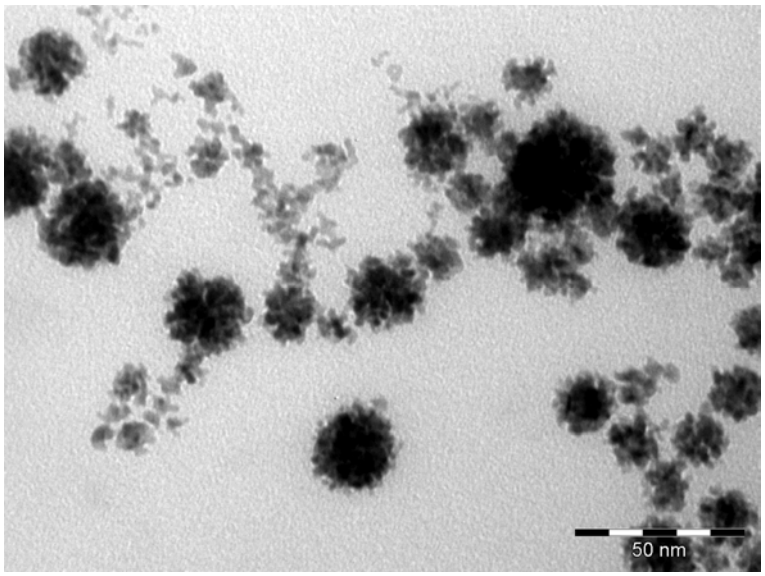

Figure 4.56. Micrograph obtained by TEM of Rh@PVA prepared by organometallic approach after hydrogenation of cyclohexene.

5. CONCLUSION

Magnetic separation is present in numerous material treatment operations due to their inherent magnetic properties, but only in the last decade it received attention as a very promising method to recover catalysts from product solutions. Several strategies for the immobilization of non-magnetic catalysts on magnetic supports have been developed. The immobilization of catalysts on iron oxides, e.g. magnetite, is possible, and coating of the magnetic material with a protective layer improves the stability and facilitates the immobilization process. However, the magnetic supports available are still mostly limited to silica, polymer and carbon-coated magnetic materials. The preparation of magnetic supports containing different oxides can thus expand the applicability of magnetic separation in catalysis. In the context frame of this PhD work, we could demonstrate that a support material comprised of silica-coated magnetite ($Fe_3O_4@SiO_2$) can be calcined, preserving the morphology and magnetic properties. The silica shell provides protection to the magnetic core against oxidation. This protection should be related to the hindrance of oxygen diffusion to the magnetic cores and to the formation of Fe-O-Si bonds inherent to the silica coating mechanism. The calcination increased the surface area and allowed the development of a post-coating process for the deposition of titania and ceria onto the silica surface. Thus, $Fe_3O_4@SiO_2TiO_2$ and $Fe_3O_4@SiO_2CeO_2$ support materials comprised of particles of titania or ceria onto the silica shell were successfully prepared. The new developed support materials were used for the preparation of magnetically recoverable catalysts containing Rh, Pd and Ru nanoparticles.

A first set of rhodium catalysts supported on silica-coated magnetite were prepared by IMP of rhodium(III) chloride. The impregnation step was possible after functionalization of

the support with amine groups, as demonstrated previously by our research group. The reduction of Rh^{3+} ions was performed using $NaBH_4$ or hydrazine as reducing agents to surpass the reproducibility issues during the reduction with H_2. The Rh catalysts prepared by reduction with $NaBH_4$ were very active in the hydrogenation of cyclohexene. Despite the similar metal NPs size, the catalyst reduced by hydrazine showed lower activity. In fact, the catalytic activity of hydrazine reduced Rh catalysts were similar to previous reported H_2 reduce Rh catalyst. In order to gain a better control on the metal NPs characteristics (size and composition), colloidal Rh@PVA NPs were prepared by reduction of rhodium(III) chloride by $NaBH_4$ in an aqueous solution containing 1 wt% PVA. The Rh@PVA NPs of 4.2 ± 1.2 nm form a very stable aqueous colloidal solution that can be used directly for biphasic reaction with the catalyst being in the aqueous phase and the substrate, i.e. cyclohexene, being the organic phase. However, the colloidal solution is not stable under reaction conditions and the NPs precipitated even at 25 ºC and could not be reused. The immobilization of Rh@PVA on $Fe_3O_4@SiO_2NH_2$ resulted in a more stable catalyst and also eliminated the mass transfer limitation due to the presence of aqueous phase. The TOF in the hydrogenation of cyclohexene reached values of 135,000 h^{-1} with a TON of 35600 $mol_{substrate}$ $mol^{-1}_{catalyst}$, while at the same conditions the unsupported Rh NPs showed a TOF of 31000 h^{-1}. The catalyst was also active for benzene hydrogenation, but the catalyst deactivates upon recycling. The determined by the quantification of Rh content in the products of cyclohexene and benzene hydrogenation was below the detection limit for Rh by ICP OES, which exclude metal leaching. The characterization by TEM demonstrated that the NPs morphology and size were not changed after catalytic reactions. Thus, the Rh catalyst was very stable under reaction conditions.

Palladium catalysts supported on silica-coated magnetite were also prepared by the IMP of palladium(II) chloride using H_2 as reducing agent. The calcined support

Fe_3O_4@SiO_2Cal was not capable to adsorb Pd^{2+} ions, but the non-calcined support adsorbs Pd^{2+} ions even without functionalizing its surface. The Fe_3O_4@SiO_2Pd catalyst showed the higher catalytic activity in hydrogenation of cyclohexene, but also a strong deactivation upon recycling. The functionalization of the silica surface with amine groups allowed us to prepare a more stable but less active catalyst. Colloidal Pd@PVP-1 NPs prepared using palladium(II) chloride were immobilized on the same solids, but in this case only amine functionalized solids were able to uptake the metal nanoparticles from the impregnation solution. The catalyst prepared with calcined support, which contains higher surface area and higher amount of amine groups, was less active than the catalyst prepared with non-calcined support. Thus, it suggests a deleterious effect on the catalytic activity by amine groups. The poisoning effect to amine groups has precedents in the literature, but has to be studied in more detail.

Rhodium, ruthenium and palladium colloidal NPs of controlled size and composition were prepared by the decomposition of organometallic compounds in the presence of PVP and hydrogen. These M@PVP NPs were immobilized on Fe_3O_4@SiO_2Cal, Fe_3O_4@SiO_2CeO_2 and Fe_3O_4@SiO_2TiO_2. The Rh and Pd catalysts were employed in the cyclohexene hydrogenation. The Fe_3O_4@SiO_2CeO_2RhPVP was the most active catalyst reaching a TOF of ca. 125,000 h^{-1}, while Fe_3O_4@SiO_2TiO_2RhPVP reached the same activity after recycling and Fe_3O_4@SiO_2CalRhPVP was always less active than the other catalysts reaching a TOF of 75,000 h^{-1}. Considering that all catalysts were prepared with similar NPs, this behavior might be related to differences in the elimination of PVP stabilizer. Preliminary result obtained during temperature programmed oxidation of CO showed that the conversion of CO was dependent on the elimination of PVP. On the other hand, the silica supported Fe_3O_4@SiO_2CalPdPVP was the most active among the palladium catalysts in liquid phase reaction. However, the temperature for maximum conversion of cyclohexene was the same for all the Pd catalysts, which demonstrated the absence of support influence. In the case of

Rh catalysts, the temperature was different (T_{max} Ce < T_{max} Ti < T_{max} Si) and is in agreement with the order of activity showed in liquid phase hydrogenation during recycling. These catalysts were also employed in the hydrogenation of phenol. The Pd catalysts were able to selectively convert phenol in cyclohexanone, no matter the support and the reaction conditions used. Rhodium and ruthenium catalysts were not able to stop the reaction and cyclohexanone was further hydrogenated to cyclohexanol. The formation of cyclohexanol is more effective in the case of the support with titania, the most acid of the series. The hydrodeoxygenation of phenol to produce cyclohexane, which is also a very interesting product if one consider the conversion of phenol derived from biomass into alkanes, occurred mainly in the support with silica.

In this way, the major contribution of this thesis is related to the demonstration that the preparation of supported metal nanocatalysts is not a trivial procedure. The IMP method, which in principle can be considered a simple way to obtain supported metal nanoparticles, is not so straightforward and the reproducibility of catalytic properties can be a problem. Depending on the metal and support, the impregnation procedure can be less effective, while the functionalization of the support is an alternative to improve metal-support interaction. The reduction with hydrogen is the cleaner option, but $NaBH_4$ was shown to provide higher activity. The main concern about the use of $NaBH_4$ or hydrazine is the unknown species adsorbed on the metal surface after reduction. For the comparison of different supports, the size and size distribution of the supported metal nanoparticles prepared by IMP method will be affected by the support, which is a limitation for comparison between catalysts. The immobilization of colloidal metal NPs (SI method) is an excellent alternative to prepared catalysts in different supports with metal NPs of similar size. The main drawback is the presence of a chosen stabilizing agent. It was shown that it can lead to more active catalysts, but the catalytic activity can still be affected by the support. The type of support and the

presence and nature of ligands are very important during the preparation of supported catalysts and can affect the catalytic activity, even in support unrelated reactions. The metal – support interaction can affect the chemistry on the surface of pre-formed NPs and the way the stabilizers will be removed after the immobilization process. Also, the preparation of magnetic nanocomposites containing titania and ceria with high morphological control is not easy, but deposition of metal oxides on silica-coated magnetite can be easily performed through different methods. This observation demonstrates how a widely known catalyst support can be very versatile and modified to further improve catalyst performances.

6. PERSPECTIVES

The development of ceria and titania deposition methods into silica-coated magnetite is a very interesting contribution to the catalysis field. The observation of the thermal stability of the silica coated magnetite allows the deposition of a large variety of oxides and the application of these new supports in support sensitive reactions is very interesting. The deposition of MgO and Al_2O_3 on silica-coated magnetite was also performed, but they are still being characterized.

One important contribution of this thesis is in the preparation of catalysts. We demonstrated that there are several variables that can affect the catalytic activity of a supported NP. This demonstrated that the control of the preparation procedure is very important and that depending on the study intention this control is even more important. Thus, the SI method using either NPs from salts or organometallics precursors is very reproducible and very important for support effect studies.

This thesis work will continue with the further characterization of silica-protection of magnetic cores against oxidation, phenol hydrogenation will be more explore and new magnetic supports will be prepared and used as catalyst support for hydrogenation reactions.

7. REFERENCES

1. Sheldon, R. A., E factors, green chemistry and catalysis: an odyssey. *Chem. Commun.* **2008,** (29), 3352-3365.
2. Anastas, P. T.; Warner, J. C., Green chemistry: Theory and pratice. Oxford University Press: New York, 1998; p 30.
3. (a) Kalidindi, S. B.; Jagirdar, B. R., Nanocatalysis and Prospects of Green Chemistry. *Chemsuschem* **2012,** *5* (1), 65-75; (b) Polshettiwar, V.; Tewodros, A., *Nanocatalysis: Synthesis and Applications*. John Wiley & Sons: Hoboken, New Jersey, 2013.
4. (a) Daniel, M. C.; Astruc, D., Gold nanoparticles: Assembly, supramolecular chemistry, quantum-size-related properties, and applications toward biology, catalysis, and nanotechnology. *Chem. Rev.* **2004,** *104* (1), 293-346; (b) Stratakis, M.; Garcia, H., Catalysis by Supported Gold Nanoparticles: Beyond Aerobic Oxidative Processes. *Chem. Rev.* **2012,** *112* (8), 4469-4506; (c) Corma, A.; Garcia, H., Supported gold nanoparticles as catalysts for organic reactions. *Chem. Soc. Rev.* **2008,** *37* (9), 2096-2126.
5. Haruta, M.; Kobayashi, T.; Sano, H.; Yamada, N., Novel Gold Catalysts for the Oxidation of Carbon-Monoxide at a Temperature Far Below 0-Degrees-C. *Chem. Lett.* **1987,** (2), 405-408.
6. Cuenya, B. R.; Behafarid, F., Nanocatalysis: size- and shape-dependent chemisorption and catalytic reactivity. *Surf. Sci. Rep.* **2015,** *70* (2), 135-187.
7. Henry, C. R., Catalysis by nanoparticles. In *Nanocatalysis*, 2 ed.; Heiz, U.; Landman, U., Eds. Springer Verlag: Berlin, 2006; p 245.
8. Zaera, F., New Challenges in Heterogeneous Catalysis for the 21st Century. *Catal. Lett.* **2012,** *142* (5), 501-516.
9. Philippot, K.; Serp, P., Concepts in Nanocatalysis. In *Nanomaterials in Catalysis*, Wiley-VCH Verlag GmbH & Co. KGaA: 2013; pp 1-54.
10. Van Santen, R. A., Complementary Structure Sensitive and Insensitive Catalytic Relationships. *Acc. Chem. Res.* **2009,** *42* (1), 57-66.
11. Toshima, N., Metal nanoparticles used as catalysts. In *Dekker encyclopedia of nanoscience and nanotechnology*, Schwarz, J. A.; Contescu, C. I.; Putyera, K., Eds. Marcel Dekker: New York, 2004; Vol. 3, p 1869.
12. (a) Jia, C.-J.; Schuth, F., Colloidal metal nanoparticles as a component of designed catalyst. *Phys. Chem. Chem. Phys.* **2011,** *13* (7), 2457-2487; (b) Astruc, D.; Lu, F.; Aranzaes, J. R., Nanoparticles as recyclable catalysts: The frontier between homogeneous and heterogeneous catalysis. *Angew. Chem. Int. Ed.* **2005,** *44* (48), 7852-7872; (c) Wilcoxon, J. P.; Abrams, B. L., Synthesis, structure and properties of metal nanoclusters. *Chem. Soc. Rev.* **2006,** *35* (11), 1162-1194.
13. Chaudret, B., Organometallic approach to nanoparticles synthesis and self-organization. *Comptes Rendus Physique* **2005,** *6* (1), 117-131.
14. Narayanan, R.; El-Sayed, M. A., Catalysis with Transition Metal Nanoparticles in Colloidal Solution: Nanoparticle Shape Dependence and Stability. *The Journal of Physical Chemistry B* **2005,** *109* (26), 12663-12676.
15. Rossi, L. M.; Vono, L. L. R.; Garcia, M. A. S.; Faria, T. L. T.; Lopez-Sanchez, J. A., Screening of Soluble Rhodium Nanoparticles as Precursor for Highly Active Hydrogenation Catalysts: The Effect of the Stabilizing Agents. *Top. Catal.* **2013,** *56* (13-14), 1228-1238.
16. Libuda, J.; Schalow, T.; Brandt, B.; Laurin, M.; Schauermann, S., Model studies in heterogeneous catalysis at the microscopic level: from the structure and composition of surfaces to reaction kinetics. *Microchimica Acta* **2006,** *156* (1-2), 9-20.
17. Schauermann, S.; Nilius, N.; Shaikhutdinov, S.; Freund, H.-J., Nanoparticles for Heterogeneous Catalysis: New Mechanistic Insights. *Acc. Chem. Res.* **2013,** *46* (8), 1673-1681.

18. Campbell, C. T., The Energetics of Supported Metal Nanoparticles: Relationships to Sintering Rates and Catalytic Activity. *Acc. Chem. Res.* **2013,** *46* (8), 1712-1719.
19. Wender, H.; Migowski, P.; Feil, A. F.; Teixeira, S. R.; Dupont, J., Sputtering deposition of nanoparticles onto liquid substrates: Recent advances and future trends. *Coord. Chem. Rev.* **2013,** *257* (17–18), 2468-2483.
20. Henry, C. R., Growth, Structure and Morphology of Supported Metal Clusters Studied by Surface Science Techniques. *Cryst. Res. Technol.* **1998,** *33* (7-8), 1119-1140.
21. (a) Campelo, J. M.; Luna, D.; Luque, R.; Marinas, J. M.; Romero, A. A., Sustainable Preparation of Supported Metal Nanoparticles and Their Applications in Catalysis. *Chemsuschem* **2009,** *2* (1), 18-45; (b) Mori, K.; Yamashita, H., Design of Colloidal and Supported Metal Nanoparticles: Their Synthesis, Characterization, and Catalytic Application. *J. Jpn. Petrol. Inst.* **2011,** *54* (1), 1-14.
22. Okumura, M.; Fujitani, T.; Huang, J.; Ishida, T., A Career in Catalysis: Masatake Haruta. *ACS Catal.* **2015,** *5* (8), 4699-4707.
23. Costa, N. J. S.; Rossi, L. M., Synthesis of supported metal nanoparticle catalysts using ligand assisted methods. *Nanoscale* **2012,** *4* (19), 5826-5834.
24. De Rogatis, L.; Cargnello, M.; Gombac, V.; Lorenzut, B.; Montini, T.; Fornasiero, P., Embedded Phases: A Way to Active and Stable Catalysts. *Chemsuschem* **2010,** *3* (1), 24-42.
25. Haruta, M.; Tsubota, S.; Kobayashi, T.; Kageyama, H.; Genet, M. J.; Delmon, B., Low-Temperature Oxidation of CO over Gold Supported on TiO2, α-Fe2O3, and Co3O4. *J. Catal.* **1993,** *144* (1), 175-192.
26. Kuroda, K.; Ishida, T.; Haruta, M., Reduction of 4-nitrophenol to 4-aminophenol over Au nanoparticles deposited on PMMA. *J. Mol. Catal. A: Chem.* **2009,** *298* (1-2), 7-11.
27. Guerrero, M.; Costa, N. J. S.; Vono, L. L. R.; Rossi, L. M.; Gusevskaya, E. V.; Philippot, K., Taking advantage of a terpyridine ligand for the deposition of Pd nanoparticles onto a magnetic material for selective hydrogenation reactions. *Journal of Materials Chemistry A* **2013,** *1* (4), 1441-1449.
28. Wojcieszak, R.; Gaigneaux, E. M.; Ruiz, P., Direct Methyl Formate Formation from Methanol over Supported Palladium Nanoparticles at Low Temperature. *Chemcatchem* **2013,** *5* (1), 339-348.
29. Colmenares Q, J. C., Ultrasound and Photochemical Procedures for Nanocatalysts Preparation: Application in Photocatalytic Biomass Valorization. *J. Nanosci. Nanotechnol.* **2013,** *13* (7), 4787-4798.
30. Rashid, H. U.; Yu, K.; Umar, M. N.; Anjum, M. N.; Khan, K.; Ahmad, N.; Jans, M. T., Catalyst role in chemical vapor deposition (CVD) process: A review. *Rev. Adv. Mater. Sci.* **2015,** *40* (3), 235-248.
31. Villa, A.; Wang, D.; Veith, G. M.; Vindigni, F.; Prati, L., Sol immobilization technique: a delicate balance between activity, selectivity and stability of gold catalysts. *Catal. Sci. Technol.* **2013,** *3* (11), 3036-3041.
32. Lopez-Sanchez, J. A.; Dimitratos, N.; Hammond, C.; Brett, G. L.; Kesavan, L.; White, S.; Miedziak, P.; Tiruvalam, R.; Jenkins, R. L.; Carley, A. F.; Knight, D.; Kiely, C. J.; Hutchings, G. J., Facile removal of stabilizer-ligands from supported gold nanoparticles. *Nature Chemistry* **2011,** *3* (7), 551-556.
33. Amiens, C.; Chaudret, B.; Ciuculescu-Pradines, D.; Colliere, V.; Fajerwerg, K.; Fau, P.; Kahn, M.; Maisonnat, A.; Soulantica, K.; Philippot, K., Organometallic approach for the synthesis of nanostructures. *New J. Chem.* **2013,** *37* (11), 3374-3401.
34. (a) Costa, N. J. S.; Jardim, R. F.; Masunaga, S. H.; Zanchet, D.; Landers, R.; Rossi, L. M., Direct Access to Oxidation-Resistant Nickel Catalysts through an Organometallic Precursor. *ACS Catal.* **2012,** *2* (6), 925-929; (b) Costa, N. J. S.; Guerrero, M.; Collière, V.; Teixeira-Neto, É.; Landers, R.; Philippot, K.; Rossi, L. M., Organometallic Preparation of Ni, Pd, and NiPd Nanoparticles for the Design of Supported Nanocatalysts. *ACS Catal.* **2014,** *4* (6), 1735-1742.
35. Chorkendorff, I.; Niemantsverdriet, J. W., *Concepts os modern catalysis and kinetics*. WILEY-VCH Verlag GmbH & Co.KGaA: Weinheim, 2003; p 189-194.
36. Melo, M. d. O.; Silva, L. A., Photocatalytic production of hydrogen: an innovative use for biomass derivatives. *J. Braz. Chem. Soc.* **2011,** *22*, 1399-1406.

37. Choudhary, V. R.; Dhar, A.; Jana, P.; Jha, R.; Uphade, B. S., A green process for chlorine-free benzaldehyde from the solvent-free oxidation of benzyl alcohol with molecular oxygen over a supported nano-size gold catalyst. *Green Chem.* **2005,** *7* (11), 768-770.
38. Moulijn, J. A.; Ponec, V., Heterogeneous catalysis. In *Catalysis: An integrated approach to homogeneous, heterogeneous and industrial catalysis*, Moulijn, J. A.; Van Leeuwen, P. W. N. M.; Van Santen, R. A., Eds. Elsevier Science Publishers B.V: Netherlands, 1993; pp 176-184.
39. Doyle, A. M.; Shaikhutdinov, S. K.; Jackson, S. D.; Freund, H. J., Hydrogenation on metal surfaces: Why are nanoparticles more active than single crystals? *Angew. Chem. Int. Ed.* **2003,** *42* (42), 5240-5243.
40. Domínguez-Quintero, O.; Martínez, S.; Henríquez, Y.; D'Ornelas, L.; Krentzien, H.; Osuna, J., Silica-supported palladium nanoparticles show remarkable hydrogenation catalytic activity. *J. Mol. Catal. A: Chem.* **2003,** *197* (1–2), 185-191.
41. Li, S.; Chen, G.; Sun, L., Selective hydrogenation of 3,3-dimethylbutanoyl chloride to 3,3-dimethylbutyraldehyde with silica supported Pd nanoparticle catalyst. *Catal. Commun.* **2011,** *12* (9), 813-816.
42. Lim, M.; De Castro, K. A.; Oh, S.; Lee, K.; Chang, Y.-W.; Kim, H.; Rhee, H., Pd nanoparticles dispersed on solid supports: synthesis, characterization and catalytic activity on selective hydrogenation of olefins in aqueous media. *Appl. Organomet. Chem.* **2011,** *25* (1), 1-8.
43. Rossi, L. M.; Vono, L. L. R.; Silva, F. P.; Kiyohara, P. K.; Duarte, E. L.; Matos, J. R., Magnetically recoverable scavenger for palladium based on thiol-modified magnetite nanoparticles. *Appl. Catal., A* **2007,** *330*, 139-144.
44. Rossi, L. M.; Nangoi, I. M.; Costa, N. J. S., Ligand-Assisted Preparation of Palladium Supported Nanoparticles: a Step toward Size Control. *Inorg. Chem.* **2009,** *48* (11), 4640-4642.
45. Rossi, L. M.; Silva, F. P.; Vono, L. L. R.; Kiyohara, P. K.; Duarte, E. L.; Itri, R.; Landers, R.; Machado, G., Superparamagnetic nanoparticle-supported palladium: a highly stable magnetically recoverable and reusable catalyst for hydrogenation reactions. *Green Chem.* **2007,** *9* (4), 379-385.
46. Zhao, Y., Facile synthesis of Pd nanoparticles on SiO2 for hydrogenation of biomass-derived furfural. *Environ Chem Lett* **2014,** *12* (1), 185-190.
47. Chatterjee, M.; Ishizaka, T.; Suzuki, T.; Suzuki, A.; Kawanami, H., In situ synthesized Pd nanoparticles supported on B-MCM-41: an efficient catalyst for hydrogenation of nitroaromatics in supercritical carbon dioxide. *Green Chem.* **2012,** *14* (12), 3415-3422.
48. Mastalir, Á.; Rác, B.; Király, Z.; Molnár, Á., In situ generation of Pd nanoparticles in MCM-41 and catalytic applications in liquid-phase alkyne hydrogenations. *J. Mol. Catal. A: Chem.* **2007,** *264* (1–2), 170-178.
49. Na-Chiangmai, C.; Tiengchad, N.; Kittisakmontree, P.; Mekasuwandumrong, O.; Powell, J.; Panpranot, J., Characteristics and Catalytic Properties of Mesocellular Foam Silica Supported Pd Nanoparticles in the Liquid-Phase Selective Hydrogenation of Phenylacetylene. *Catal. Lett.* **2011,** *141* (8), 1149-1155.
50. Lin, C.-J.; Huang, S.-H.; Lai, N.-C.; Yang, C.-M., Efficient Room-Temperature Aqueous-Phase Hydrogenation of Phenol to Cyclohexanone Catalyzed by Pd Nanoparticles Supported on Mesoporous MMT-1 Silica with Unevenly Distributed Functionalities. *ACS Catal.* **2015,** *5* (7), 4121-4129.
51. Lee, S.-S.; Park, B.-K.; Byeon, S.-H.; Chang, F.; Kim, H., Mesoporous Silica-Supported Pd Nanoparticles; Highly Selective Catalyst for Hydrogenation of Olefins in Supercritical Carbon Dioxide. *Chem. Mater.* **2006,** *18* (24), 5631-5633.
52. Liu, Y.; Dong, Z.; Li, X.; Le, X.; Zhang, W.; Ma, J., Aqueous-phase hydrodechlorination and further hydrogenation of chlorophenols to cyclohexanone in water over palladium nanoparticles modified dendritic mesoporous silica nanospheres catalyst. *RSC Advances* **2015,** *5* (27), 20716-20723.
53. Zhang, F.; Yang, H., Multifunctional mesoporous silica-supported palladium nanoparticles for selective phenol hydrogenation in the aqueous phase. *Catal. Sci. Technol.* **2015,** *5* (1), 572-577.
54. Martins, J.; Batail, N.; Silva, S.; Rafik-Clement, S.; Karelovic, A.; Debecker, D. P.; Chaumonnot, A.; Uzio, D., CO2 hydrogenation with shape-controlled Pd nanoparticles embedded in mesoporous silica: Elucidating stability and selectivity issues. *Catal. Commun.* **2015,** *58*, 11-15.

55. Li, K.-T.; Hsu, M.-H.; Wang, I., Palladium core–porous silica shell-nanoparticles for catalyzing the hydrogenation of 4-carboxybenzaldehyde. *Catal. Commun.* **2008,** *9* (13), 2257-2260.
56. Zhang, H.; Yang, Y.; Dai, W.; Lu, S.; Yu, H.; Ji, Y., Size-controlled Pd Nanoparticles Supported on α-Al2O3 as Heterogeneous Catalyst for Selective Hydrogenation of Acetylene. *Chin. J. Chem. Eng.* **2014,** *22* (5), 516-521.
57. Liu, J.; Liao, X.; Shi, B., Pd nanoparticles immobilized on boehmite by using tannic acid as structure-directing agent and stabilizer: a high performance catalyst for hydrogenation of olefins. *Res. Chem. Intermed.* **2014,** *40* (1), 249-258.
58. Zhang, F.; Chen, J.; Chen, P.; Sun, Z.; Xu, S., Pd nanoparticles supported on hydrotalcite-modified porous alumina spheres as selective hydrogenation catalyst. *AlChE J.* **2012,** *58* (6), 1853-1861.
59. Pinilla, J. L.; García, A. B.; Philippot, K.; Lara, P.; García-Suárez, E. J.; Millan, M., Carbon-supported Pd nanoparticles as catalysts for anthracene hydrogenation. *Fuel* **2014,** *116*, 729-735.
60. Li, Z.; Liu, J.; Xia, C.; Li, F., Nitrogen-Functionalized Ordered Mesoporous Carbons as Multifunctional Supports of Ultrasmall Pd Nanoparticles for Hydrogenation of Phenol. *ACS Catal.* **2013,** *3* (11), 2440-2448.
61. Han, K.-Y.; Zuo, H.-R.; Zhu, Z.-W.; Cao, G.-P.; Lu, C.; Wang, Y.-H., High Performance of Palladium Nanoparticles Supported on Carbon Nanotubes for the Hydrogenation of Commercial Polystyrene. *Ind. Eng. Chem. Res.* **2013,** *52* (50), 17750-17759.
62. Wang, Z.; Liu, H.; Chen, L.; Chou, L.; Wang, X., Green and facile synthesis of carbon nanotube supported Pd nanoparticle catalysts and their application in the hydrogenation of nitrobenzene. *J. Mater. Res.* **2013,** *28* (10), 1326-1333.
63. Yan, K.; Lafleur, T.; Liao, J., Facile synthesis of palladium nanoparticles supported on multi-walled carbon nanotube for efficient hydrogenation of biomass-derived levulinic acid. *J. Nanopart. Res.* **2013,** *15* (9), 1-7.
64. Cano, M.; Benito, A. M.; Maser, W. K.; Urriolabeitia, E. P., High catalytic performance of palladium nanoparticles supported on multiwalled carbon nanotubes in alkene hydrogenation reactions. *New J. Chem.* **2013,** *37* (7), 1968-1972.
65. Chen, P.; Chew, L. M.; Kostka, A.; Muhler, M.; Xia, W., The structural and electronic promoting effect of nitrogen-doped carbon nanotubes on supported Pd nanoparticles for selective olefin hydrogenation. *Catal. Sci. Technol.* **2013,** *3* (8), 1964-1971.
66. Nasir Baig, R. B.; Varma, R. S., Magnetic Carbon-Supported Palladium Nanoparticles: An Efficient and Sustainable Catalyst for Hydrogenation Reactions. *ACS Sustainable Chemistry & Engineering* **2014,** *2* (9), 2155-2158.
67. Kainz, Q. M.; Linhardt, R.; Grass, R. N.; Vilé, G.; Pérez-Ramírez, J.; Stark, W. J.; Reiser, O., Palladium Nanoparticles Supported on Magnetic Carbon-Coated Cobalt Nanobeads: Highly Active and Recyclable Catalysts for Alkene Hydrogenation. *Adv. Funct. Mater.* **2014,** *24* (14), 2020-2027.
68. Dell'Anna, M. M.; Capodiferro, V. F.; Mali, M.; Manno, D.; Cotugno, P.; Monopoli, A.; Mastrorilli, P., Highly selective hydrogenation of quinolines promoted by recyclable polymer supported palladium nanoparticles under mild conditions in aqueous medium. *Applied Catalysis A: General* **2014,** *481*, 89-95.
69. Ishida, T.; Onuma, Y.; Kinjo, K.; Hamasaki, A.; Ohashi, H.; Honma, T.; Akita, T.; Yokoyama, T.; Tokunaga, M.; Haruta, M., Preparation of microporous polymer-encapsulated Pd nanoparticles and their catalytic performance for hydrogenation and oxidation. *Tetrahedron* **2014,** *70* (36), 6150-6155.
70. Zhang, D.; Ye, F.; Guan, Y.; Wang, Y.; Hensen, E. J. M., Hydrogenation of [gamma]-valerolactone in ethanol over Pd nanoparticles supported on sulfonic acid functionalized MIL-101. *RSC Advances* **2014,** *4* (74), 39558-39564.
71. Zhao, X.; Jin, Y.; Zhang, F.; Zhong, Y.; Zhu, W., Catalytic hydrogenation of 2,3,5-trimethylbenzoquinone over Pd nanoparticles confined in the cages of MIL-101(Cr). *Chem. Eng. J.* **2014,** *239*, 33-41.
72. (a) Jiang, T.; Du, S.; Jafari, T.; Zhong, W.; Sun, Y.; Song, W.; Luo, Z.; Hines, W. A.; Suib, S. L., Synthesis of mesoporous γ-Fe2O3 supported palladium nanoparticles and investigation of their roles as magnetically recyclable catalysts for nitrobenzene hydrogenation. *Applied Catalysis A: General* **2015,** *502*, 105-113; (b) Wang, H.-B.; Zhang, Y.-H.; Zhang, Y.-B.; Zhang, F.-W.; Niu, J.-R.;

Yang, H.-L.; Li, R.; Ma, J.-T., Pd immobilized on thiol-modified magnetic nanoparticles: A complete magnetically recoverable and highly active catalyst for hydrogenation reactions. *Solid State Sciences* **2012,** *14* (9), 1256-1262; (c) Zhang, F.; Jin, J.; Zhong, X.; Li, S.; Niu, J.; Li, R.; Ma, J., Pd immobilized on amine-functionalized magnetite nanoparticles: a novel and highly active catalyst for hydrogenation and Heck reactions. *Green Chem.* **2011,** *13* (5), 1238-1243.

73. Mandal, S.; Roy, D.; Chaudhari, R. V.; Sastry, M., Pt and Pd Nanoparticles Immobilized on Amine-Functionalized Zeolite: Excellent Catalysts for Hydrogenation and Heck Reactions. *Chem. Mater.* **2004,** *16* (19), 3714-3724.

74. (a) Liu, P.; Li, G.; Chang, W.-T.; Wu, M.-Y.; Li, Y.-X.; Wang, J., Highly dispersed Pd nanoparticles supported on nitrogen-doped graphene with enhanced hydrogenation activity. *RSC Advances* **2015,** *5* (89), 72785-72792; (b) Cano, M.; Benito, A. M.; Urriolabeitia, E. P.; Arenal, R.; Maser, W. K., Reduced graphene oxide: firm support for catalytically active palladium nanoparticles and game changer in selective hydrogenation reactions. *Nanoscale* **2013,** *5* (21), 10189-10193.

75. Yang, J.-H.; Ma, D., Graphene-supported Pd nanoparticles: microwave-assisted synthesis and as microwave-active selective hydrogenation catalysts. *RSC Advances* **2013,** *3* (26), 10131-10134.

76. Szőri, K.; Puskás, R.; Szőllősi, G.; Bertóti, I.; Szépvölgyi, J.; Bartók, M., Palladium Nanoparticle–Graphene Catalysts for Asymmetric Hydrogenation. *Catal. Lett.* **2013,** *143* (6), 539-546.

77. Zhao, Y.; Zhang, H.; Huang, C.; Chen, S.; Yu, B.; Xu, J.; Liu, Z., Pd nanoparticles immobilized on graphite oxide modified with a base: Highly efficient catalysts for selective hydrogenation of citral. *Sci. China Chem.* **2013,** *56* (2), 203-209.

78. Rahi, R.; Fang, M.; Ahmed, A.; Sanchez-Delgado, R. A., Hydrogenation of quinolines, alkenes, and biodiesel by palladium nanoparticles supported on magnesium oxide. *Dalton Transactions* **2012,** *41* (48), 14490-14497.

79. Mehri, A.; Kochkar, H.; Daniele, S.; Mendez, V.; Ghorbel, A.; Berhault, G., One-pot deposition of palladium on hybrid TiO2 nanoparticles and catalytic applications in hydrogenation. *J. Colloid Interface Sci.* **2012,** *369* (1), 309-316.

80. Kulagina, M. A.; Gerasimov, E. Y.; Kardash, T. Y.; Simonov, P. A.; Romanenko, A. V., A universal method to form Pd nanoparticles on low-surface-area inorganic powders and their support-dependent catalytic activity in hydrogenation of maleic acid. *Catal. Today* **2015,** *246*, 72-80.

81. Dal Santo, V.; Gallo, A.; Naldoni, A.; Sordelli, L., Selective butadiene hydrogenation by Pd nanoparticles deposed onto nano-sized oxide supports by CVD of Pd-hexafluoroacetylacetonate. *Inorg. Chim. Acta* **2012,** *380*, 216-222.

82. Nadgeri, J. M.; Telkar, M. M.; Rode, C. V., Hydrogenation activity and selectivity behavior of supported palladium nanoparticles. *Catal. Commun.* **2008,** *9* (3), 441-446.

83. Domínguez-Domínguez, S.; Berenguer-Murcia, Á.; Linares-Solano, Á.; Cazorla-Amorós, D., Inorganic materials as supports for palladium nanoparticles: Application in the semi-hydrogenation of phenylacetylene. *J. Catal.* **2008,** *257* (1), 87-95.

84. (a) Mevellec, V.; Nowicki, A.; Roucoux, A.; Dujardin, C.; Granger, P.; Payen, E.; Philippot, K., A simple and reproducible method for the synthesis of silica-supported rhodium nanoparticles and their investigation in the hydrogenation of aromatic compounds. *New J. Chem.* **2006,** *30* (8), 1214-1219; (b) Bhorali, N.; Ganguli, J., Hydrogenation of Alkenes with Rhodium Nanoparticles Supported on SBA-15. *Catal. Lett.* **2013,** *143* (3), 276-281; (c) Cao, P.; Ni, Y.; Zou, R.; Zhang, L.; Yue, D., Enhanced catalytic properties of rhodium nanoparticles deposited on chemically modified SiO2 for hydrogenation of nitrile butadiene rubber. *RSC Advances* **2015,** *5* (5), 3417-3424.

85. Baghbanian, S. M.; Farhang, M.; Vahdat, S. M.; Tajbakhsh, M., Hydrogenation of arenes, nitroarenes, and alkenes catalyzed by rhodium nanoparticles supported on natural nanozeolite clinoptilolite. *J. Mol. Catal. A: Chem.* **2015,** *407*, 128-136.

86. Agarwal, S.; Ganguli, J. N., Selective hydrogenation of monoterpenes on Rhodium (0) nanoparticles stabilized in Montmorillonite K-10 clay. *J. Mol. Catal. A: Chem.* **2013,** *372*, 44-50.

87. Park, K. H.; Jang, K.; Kim, H. J.; Son, S. U., Near-Monodisperse Tetrahedral Rhodium Nanoparticles on Charcoal: The Shape-Dependent Catalytic Hydrogenation of Arenes. *Angewandte Chemie International Edition* **2007,** *46* (7), 1152-1155.

88. (a) Pan, H.-B.; Wai, C. M., Sonochemical One-Pot Synthesis of Carbon Nanotube-Supported Rhodium Nanoparticles for Room-Temperature Hydrogenation of Arenes. *J. Phys. Chem. C* **2009,** *113*

(46), 19782-19788; (b) Kakade, B. A.; Sahoo, S.; Halligudi, S. B.; Pillai, V. K., Highly Selective Catalytic Hydrogenation of Arenes using Rhodium Nanoparticles Supported on Multiwalled Carbon Nanotubes. *J. Phys. Chem. C* **2008,** *112* (35), 13317-13319; (c) Pan, H.-B.; Wai, C. M., One-Step Synthesis of Size-Tunable Rhodium Nanoparticles on Carbon Nanotubes: A Study of Particle Size Effect on Hydrogenation of Xylene. *J. Phys. Chem. C* **2010,** *114* (26), 11364-11369.

89. (a) Park, I. S.; Kwon, M. S.; Kang, K. Y.; Lee, J. S.; Park, J., Rhodium and Iridium Nanoparticles Entrapped in Aluminum Oxyhydroxide Nanofibers: Catalysts for Hydrogenations of Arenes and Ketones at Room Temperature with Hydrogen Balloon. *Adv. Synth. Catal.* **2007,** *349* (11-12), 2039-2047; (b) Fan, G.-Y.; Wu, J., Mild hydrogenation of quinoline to decahydroquinoline over rhodium nanoparticles entrapped in aluminum oxy-hydroxide. *Catal. Commun.* **2013,** *31*, 81-85.

90. Park, I. S.; Kwon, M. S.; Kim, N.; Lee, J. S.; Kang, K. Y.; Park, J., Rhodium nanoparticles entrapped in boehmite nanofibers: recyclable catalyst for arene hydrogenation under mild conditions. *Chem. Commun.* **2005,** (45), 5667-5669.

91. (a) Zahmakıran, M.; Román-Leshkov, Y.; Zhang, Y., Rhodium(0) Nanoparticles Supported on Nanocrystalline Hydroxyapatite: Highly Effective Catalytic System for the Solvent-Free Hydrogenation of Aromatics at Room Temperature. *Langmuir* **2012,** *28* (1), 60-64; (b) Huang, L.; Luo, P.; Pei, W.; Liu, X.; Wang, Y.; Wang, J.; Xing, W.; Huang, J., Selective Hydrogenation of Nitroarenes and Olefins over Rhodium Nanoparticles on Hydroxyapatite. *Adv. Synth. Catal.* **2012,** *354* (14-15), 2689-2694.

92. Jacinto, M. J.; Kiyohara, P. K.; Masunaga, S. H.; Jardim, R. F.; Rossi, L. M., Recoverable rhodium nanoparticles: Synthesis, characterization and catalytic performance in hydrogenation reactions. *Appl. Catal., A* **2008,** *338* (1-2), 52-57.

93. Sánchez, A.; Fang, M.; Ahmed, A.; Sánchez-Delgado, R. A., Hydrogenation of arenes, N-heteroaromatic compounds, and alkenes catalyzed by rhodium nanoparticles supported on magnesium oxide. *Applied Catalysis A: General* **2014,** *477*, 117-124.

94. Barthe, L.; Denicourt-Nowicki, A.; Roucoux, A.; Philippot, K.; Chaudret, B.; Hemati, M., Model arenes hydrogenation with silica-supported rhodium nanoparticles: The role of the silica grains and of the solvent on catalytic activities. *Catal. Commun.* **2009,** *10* (8), 1235-1239.

95. Hubert, C.; Denicourt-Nowicki, A.; Beaunier, P.; Roucoux, A., TiO2-supported Rh nanoparticles: From green catalyst preparation to application in arene hydrogenation in neat water. *Green Chem.* **2010,** *12* (7), 1167-1170.

96. Sarmah, P. P.; Dutta, D. K., Chemoselective reduction of a nitro group through transfer hydrogenation catalysed by Ru0-nanoparticles stabilized on modified Montmorillonite clay. *Green Chem.* **2012,** *14* (4), 1086-1093.

97. (a) Süss-Fink, G.; Khan, F.-A.; Boudon, J.; Spassov, V., Shape- and Size-Selective Preparation of Hectorite-Supported Ruthenium Nanoparticles for the Catalytic Hydrogenation of Benzene. *J. Cluster Sci.* **2009,** *20* (2), 341-353; (b) Süss-Fink, G.; Mollwitz, B.; Therrien, B.; Dadras, M.; Laurenczy, G.; Meister, A.; Meister, G., Ruthenium Nanoparticles Intercalated in Hectorite: A Reusable Hydrogenation Catalyst for Benzene and Toluene. *J. Cluster Sci.* **2007,** *18* (1), 87-95.

98. Khan, F.-A.; Vallat, A.; Süss-Fink, G., Highly selective CC bond hydrogenation in α,β-unsaturated ketones catalyzed by hectorite-supported ruthenium nanoparticles. *J. Mol. Catal. A: Chem.* **2012,** *355*, 168-173.

99. (a) Wang, Y.; Rong, Z.; Wang, Y.; Zhang, P.; Wang, Y.; Qu, J., Ruthenium nanoparticles loaded on multiwalled carbon nanotubes for liquid-phase hydrogenation of fine chemicals: An exploration of confinement effect. *J. Catal.* **2015,** *329*, 95-106; (b) Takasaki, M.; Motoyama, Y.; Higashi, K.; Yoon, S.-H.; Mochida, I.; Nagashima, H., Ruthenium Nanoparticles on Nano-Level-Controlled Carbon Supports as Highly Effective Catalysts for Arene Hydrogenation. *Chemistry – An Asian Journal* **2007,** *2* (12), 1524-1533.

100. Antonetti, C.; Oubenali, M.; Raspolli Galletti, A. M.; Serp, P.; Vannucci, G., Novel microwave synthesis of ruthenium nanoparticles supported on carbon nanotubes active in the selective hydrogenation of p-chloronitrobenzene to p-chloroaniline. *Applied Catalysis A: General* **2012,** *421–422*, 99-107.

101. Ni, X.; Zhang, B.; Li, C.; Pang, M.; Su, D.; Williams, C. T.; Liang, C., Microwave-assisted green synthesis of uniform Ru nanoparticles supported on non-functional carbon nanotubes for cinnamaldehyde hydrogenation. *Catal. Commun.* **2012,** *24*, 65-69.
102. Iqbal, S.; Kondrat, S. A.; Jones, D. R.; Schoenmakers, D. C.; Edwards, J. K.; Lu, L.; Yeo, B. R.; Wells, P. P.; Gibson, E. K.; Morgan, D. J.; Kiely, C. J.; Hutchings, G. J., Ruthenium Nanoparticles Supported on Carbon: An Active Catalyst for the Hydrogenation of Lactic Acid to 1,2-Propanediol. *ACS Catal.* **2015,** *5* (9), 5047-5059.
103. Guo, S.; Liew, K.; Li, J., Catalytic Activity of Ruthenium Nanoparticles Supported on Carbon Nanotubes for Hydrogenation of Soybean Oil. *J Am Oil Chem Soc* **2009,** *86* (12), 1141-1147.
104. (a) Huang, J.; Jiang, T.; Han, B.; Wu, W.; Liu, Z.; Xie, Z.; Zhang, J., A Novel Method to Immobilize Ru Nanoparticles on SBA-15 Firmly by Ionic Liquid and Hydrogenation of Arene. *Catal. Lett.* **2005,** *103* (1-2), 59-62; (b) Bianchini, C.; Dal Santo, V.; Meli, A.; Moneti, S.; Moreno, M.; Oberhauser, W.; Psaro, R.; Sordelli, L.; Vizza, F., A comparison between silica-immobilized ruthenium(II) single sites and silica-supported ruthenium nanoparticles in the catalytic hydrogenation of model hetero- and polyaromatics contained in raw oil materials. *J. Catal.* **2003,** *213* (1), 47-62.
105. Fang, M.; Sánchez-Delgado, R. A., Ruthenium nanoparticles supported on magnesium oxide: A versatile and recyclable dual-site catalyst for hydrogenation of mono- and poly-cyclic arenes, N-heteroaromatics, and S-heteroaromatics. *J. Catal.* **2014,** *311*, 357-368.
106. Zuo, B.; Wang, Y.; Wang, Q.; Zhang, J.; Wu, N.; Peng, L.; Gui, L.; Wang, X.; Wang, R.; Yu, D., An efficient ruthenium catalyst for selective hydrogenation of ortho-chloronitrobenzene prepared via assembling ruthenium and tin oxide nanoparticles. *J. Catal.* **2004,** *222* (2), 493-498.
107. Khan, F.-A.; Süss-Fink, G., Superparamagnetic Core-Shell-Type Fe3O4/Ru Nanoparticles as Catalysts for the Selective Hydrogenation of an Unconstrained α,β-Unsaturated Ketone. *Eur. J. Inorg. Chem.* **2012,** *2012* (4), 727-732.
108. Cao, S.; Monnier, J. R.; Williams, C. T.; Diao, W.; Regalbuto, J. R., Rational nanoparticle synthesis to determine the effects of size, support, and K dopant on Ru activity for levulinic acid hydrogenation to γ-valerolactone. *J. Catal.* **2015,** *326*, 69-81.
109. Liu, J.; Bai, P.; Zhao, X. S., Ruthenium nanoparticles embedded in mesoporous carbon microfibers: preparation, characterization and catalytic properties in the hydrogenation of d-glucose. *Phys. Chem. Chem. Phys.* **2011,** *13* (9), 3758-3763.
110. Lin, Q.; Liu, X. Y.; Jiang, Y.; Wang, Y.; Huang, Y.; Zhang, T., Crystal phase effects on the structure and performance of ruthenium nanoparticles for CO2 hydrogenation. *Catal. Sci. Technol.* **2014,** *4* (7), 2058-2063.
111. Jahjah, M.; Kihn, Y.; Teuma, E.; Gómez, M., Ruthenium nanoparticles supported on multi-walled carbon nanotubes: Highly effective catalytic system for hydrogenation processes. *J. Mol. Catal. A: Chem.* **2010,** *332* (1–2), 106-112.
112. Hansen, T. W.; DeLaRiva, A. T.; Challa, S. R.; Datye, A. K., Sintering of Catalytic Nanoparticles: Particle Migration or Ostwald Ripening? *Acc. Chem. Res.* **2013,** *46* (8), 1720-1730.
113. Cao, A.; Lu, R.; Veser, G., Stabilizing metal nanoparticles for heterogeneous catalysis. *Phys. Chem. Chem. Phys.* **2010,** *12* (41), 13499-13510.
114. Liu, S.; Bai, S.-Q.; Zheng, Y.; Shah, K. W.; Han, M.-Y., Composite Metal–Oxide Nanocatalysts. *Chemcatchem* **2012,** *4* (10), 1462-1484.
115. Deutschmann , O.; Knözingerh, H.; Kochloefl, K.; Turek, T., In *Heterogeneous catalysis and solid catalysts*, Wiley-VCH Verlag GmbH & Co. KGaA: Weinheim, 2009; pp 80-82.
116. Rossi, L. M.; Garcia, M. A. S.; Vono, L. L. R., Recent Advances in the Development of Magnetically Recoverable Metal Nanoparticle Catalysts. *J. Braz. Chem. Soc.* **2012,** *23* (11), 1959.
117. (a) Shylesh, S.; Schunemann, V.; Thiel, W. R., Magnetically Separable Nanocatalysts: Bridges between Homogeneous and Heterogeneous Catalysis. *Angew. Chem. Int. Ed.* **2010,** *49* (20), 3428-3459; (b) Govan, J.; Gun'ko, Y. K., Recent Advances in the Application of Magnetic Nanoparticles as a Support for Homogeneous Catalysts. *Nanomaterials* **2014,** *4* (2), 222-241.
118. Rossi, L. M.; Costa, N. J. S.; Silva, F. P.; Goncalves, R. V., Magnetic nanocatalysts: supported metal nanoparticles for catalytic applications. *Nanotechnology Reviews* **2013,** *2* (5), 597-614.
119. (a) Gupta, A. K.; Gupta, M., Synthesis and surface engineering of iron oxide nanoparticles for biomedical applications. *Biomaterials* **2005,** *26* (18), 3995-4021; (b) Taupitz, M.; Schnorr, J.;

Abramjuk, C.; Wagner, S.; Pilgrimm, H.; Hunigen, H.; Hamm, B., New generation of monomer-stabilized very small superparamagnetic iron oxide particles (VSOP) as contrast medium for MR angiography: Preclinical results in rats and rabbits. *J. Magn. Reson. Imag.* **2000,** *12* (6), 905-911.
120. (a) Rossi, L. M.; Quach, A. D.; Rosenzweig, Z., Glucose oxidase-magnetite nanoparticle bioconjugate for glucose sensing. *Anal. Bioanal. Chem.* **2004,** *380* (4), 606-613; (b) Huang, S. H.; Liao, M. H.; Chen, D. H., Direct binding and characterization of lipase onto magnetic nanoparticles. *Biotechnol. Progr.* **2003,** *19* (3), 1095-1100; (c) Chen, D. H.; Liao, M. H., Preparation and characterization of YADH-bound magnetic nanoparticles. *J. Mol. Catal. B: Enzym.* **2002,** *16* (5-6), 283-291.
121. (a) Hancock, J. P.; Kemshead, J. T., A rapid and highly selective approach to cell separations using an immunomagnetic colloid. *J. Immunol. Methods* **1993,** *164* (1), 51-60; (b) Dyal, A.; Loos, K.; Noto, M.; Chang, S. W.; Spagnoli, C.; Shafi, K.; Ulman, A.; Cowman, M.; Gross, R. A., Activity of Candida rugosa lipase immobilized on gamma-Fe2O3 magnetic nanoparticles. *J. Am. Chem. Soc.* **2003,** *125* (7), 1684-1685.
122. (a) Lubbe, A. S.; Bergemann, C.; Riess, H.; Schriever, F.; Reichardt, P.; Possinger, K.; Matthias, M.; Dorken, B.; Herrmann, F.; Gurtler, R.; Hohenberger, P.; Haas, N.; Sohr, R.; Sander, B.; Lemke, A. J.; Ohlendorf, D.; Huhnt, W.; Huhn, D., Clinical experiences with magnetic drug targeting: A phase I study with 4'-epidoxorubicin in 14 patients with advanced solid tumors. *Cancer Res.* **1996,** *56* (20), 4686-4693; (b) Pankhurst, Q. A.; Connolly, J.; Jones, S. K.; Dobson, J., Applications of magnetic nanoparticles in biomedicine. *J. Phys. D: Appl. Phys.* **2003,** *36* (13), R167-R181.
123. Schwertmann, U.; Cornell, R. M., *The Iron Oxides: Structure, Properties, Reactions, Occurrence and Uses*. 1 ed.; Wiley-VHC Gmbh & Co KGaA: 1996.
124. Lu, A. H.; Salabas, E. L.; Schuth, F., Magnetic nanoparticles: Synthesis, protection, functionalization, and application. *Angew. Chem. Int. Ed.* **2007,** *46* (8), 1222-1244.
125. Rossi, L. M.; Costa, N. J. S.; Silva, F. P.; Wojcieszak, R., Magnetic nanomaterials in catalysis: advanced catalysts for magnetic separation and beyond. *Green Chem.* **2014,** *16* (6), 2906-2933.
126. Gawande, M. B.; Monga, Y.; Zboril, R.; Sharma, R. K., Silica-decorated magnetic nanocomposites for catalytic applications. *Coord. Chem. Rev.* **2015,** *288*, 118-143.
127. Zhu, M.; Diao, G., Review on the progress in synthesis and application of magnetic carbon nanocomposites. *Nanoscale* **2011,** *3* (7), 2748-2767.
128. Philipse, A. P.; Vanbruggen, M. P. B.; Pathmamanoharan, C., Magnetic Silica Dispersions - Preparation and Stability of Surface-Modified Silica Particles with a Magnetic Core. *Langmuir* **1994,** *10* (1), 92-99.
129. Tartaj, P.; Morales, M. D.; Veintemillas-Verdaguer, S.; Gonzalez-Carreno, T.; Serna, C. J., The preparation of magnetic nanoparticles for applications in biomedicine. *J. Phys. D: Appl. Phys.* **2003,** *36* (13), R182-R197.
130. Yi, D. K.; Lee, S. S.; Ying, J. Y., Synthesis and applications of magnetic nanocomposite catalysts. *Chem. Mater.* **2006,** *18* (10), 2459-2461.
131. Ehrman, S. H.; Friedlander, S. K.; Zachariah, M. R., Phase segregation in binary SiO2/TiO2 and SiO2/Fe2O3 nanoparticle aerosols formed in a premixed flame. *J. Mater. Res.* **1999,** *14* (12), 4551-4561.
132. Zhang, X. F.; Dong, X. L.; Huang, H.; Lv, B.; Zhu, X. G.; Lei, J. P.; Ma, S.; Liu, W.; Zhang, Z. D., Synthesis, structure and magnetic properties of SiO2-coated Fe nanocapsules. *Materials Science and Engineering a-Structural Materials Properties Microstructure and Processing* **2007,** *454*, 211-215.
133. Tada, D. B.; Vono, L. L. R.; Duarte, E. L.; Itri, R.; Kiyohara, P. K.; Baptista, M. S.; Rossi, L. M., Methylene blue-containing silica-coated magnetic particles: A potential magnetic carrier for photodynamic therapy. *Langmuir* **2007,** *23* (15), 8194-8199.
134. Vogt, C.; Toprak, M. S.; Muhammed, M.; Laurent, S.; Bridot, J. L.; Muller, R. N., High quality and tuneable silica shell-magnetic core nanoparticles. *J. Nanopart. Res.* **2010,** *12* (4), 1137-1147.
135. Dong, X.; Chen, H.; Zhao, W.; Li, X.; Shi, J., Synthesis and magnetic properties of mesostructured gamma-Fe2O3/carbon composites by a Co-casting method. *Chem. Mater.* **2007,** *19* (14), 3484-3490.

136. Wang, Z. H.; Choi, C. J.; Kim, B. K.; Kim, J. C.; Zhang, Z. D., Characterization and magnetic properties of carbon-coated cobalt nanocapsules synthesized by the chemical vapor-condensation process. *Carbon* **2003,** *41* (9), 1751-1758.
137. Wang, Z.; Mao, P.; He, N., Synthesis and characteristics of carbon encapsulated magnetic nanoparticles produced by a hydrothermal reaction. *Carbon* **2006,** *44* (15), 3277-3284.
138. Alvarez, P. M.; Jaramillo, J.; Lopez-Pinero, F.; Plucinski, P. K., Preparation and characterization of magnetic TiO2 nanoparticles and their utilization for the degradation of emerging pollutants in water. *Appl. Catal., B* **2010,** *100* (1-2), 338-345.
139. Ye, M. M.; Zorba, S.; He, L.; Hu, Y. X.; Maxwell, R. T.; Farah, C.; Zhang, Q. A.; Yin, Y. D., Self-assembly of superparamagnetic magnetite particles into peapod-like structures and their application in optical modulation. *J. Mater. Chem.* **2010,** *20* (37), 7965-7969.
140. He, Q.; Zhang, Z.; Xiong, J.; Xiong, Y.; Xiao, H., A novel biomaterial - Fe_3O_4:TiO_2 core-shell nano particle with magnetic performance and high visible light photocatalytic activity. *Opt. Mater.* **2008,** *31* (2), 380-384.
141. Beydoun, D.; Amal, R.; Low, G. K. C.; McEvoy, S., Novel photocatalyst: Titania-coated magnetite. Activity and photodissolution. *J. Phys. Chem. B* **2000,** *104* (18), 4387-4396.
142. Liu, H.; Jia, Z.; Ji, S.; Zheng, Y.; Li, M.; Yang, H., Synthesis of TiO_2/SiO_2@Fe_3O_4 magnetic microspheres and their properties of photocatalytic degradation dyestuff. *Catal. Today* **2011,** *175* (1), 293-298.
143. Sun, L.; Zhang, C. Z.; Chen, L. G.; Liu, J.; Jin, H. Y.; Xu, H. Y.; Ding, L., Preparation of alumina-coated magnetite nanoparticle for extraction of trimethoprim from environmental water samples based on mixed hemimicelles solid-phase extraction. *Anal. Chim. Acta* **2009,** *638* (2), 162-168.
144. Chaudhuri, R. G.; Paria, S., Core/Shell Nanoparticles: Classes, Properties, Synthesis Mechanisms, Characterization, and Applications. *Chem. Rev.* **2012,** *112* (4), 2373-2433.
145. Vono, L. L. R. Estudo da imobilização de fotossensibilizadores em nanomateriais magnéticos. Dissertação, Universidade de São Paulo, São Paulo, 2010.
146. Shen, L. F.; Laibinis, P. E.; Hatton, T. A., Bilayer surfactant stabilized magnetic fluids: Synthesis and interactions at interfaces. *Langmuir* **1999,** *15* (2), 447-453.
147. Yi, D. K.; Lee, S. S.; Papaefthymiou, G. C.; Ying, J. Y., Nanoparticle architectures templated by SiO_2/Fe_2O_3 nanocomposites. *Chem. Mater.* **2006,** *18* (3), 614-619.
148. Taylor, I.; Howard, A. G., Measurement of primary amine groups on surface-modified silica and their role in metal binding. *Anal. Chim. Acta* **1993,** *271* (1), 77-82.
149. Güttel, R.; Paul, M.; Schuth, F., Activity improvement of gold yolk–shell catalysts for CO oxidation by doping with TiO_2. *Catal. Sci. Technol.* **2011,** *1*, 65-68.
150. Powell, J.; Shaw, B. L., Transition metal-carbon bonds. Part XIV. Allylic complexes of rhodium. *Journal of the Chemical Society A: Inorganic, Physical, Theoretical* **1968,** (0), 583-596.
151. Uson, R.; Laguna, A.; Laguna, M.; Briggs, D. A.; Murray, H. H.; Fackler, J. P., (Tetrahydrothiophene)Gold(I) or Gold(III) Complexes. In *Inorg. Synth.*, John Wiley & Sons, Inc.: 2007; pp 85-91.
152. Teranishi, T.; Miyake, M., Size control of palladium nanoparticles and their crystal structures. *Chem. Mater.* **1998,** *10* (2), 594-600.
153. Pan, C.; Pelzer, K.; Philippot, K.; Chaudret, B.; Dassenoy, F.; Lecante, P.; Casanove, M.-J., Ligand-Stabilized Ruthenium Nanoparticles: Synthesis, Organization, and Dynamics. *J. Am. Chem. Soc.* **2001,** *123* (31), 7584-7593.
154. deCaro, D.; Agelou, V.; Duteil, A.; Chaudret, B.; Mazel, R.; Roucau, C.; Bradley, J. S., Preparation from organometallic precursors, characterization and some reactivity of copper and gold colloids sterically protected by nitrocellulose, polyvinylpyrrolidone or polydimethyl phenylene oxide. *New J. Chem.* **1995,** *19* (12), 1265-1274.
155. Tsunoyama, H.; Sakurai, H.; Ichikuni, N.; Negishi, Y.; Tsukuda, T., Colloidal Gold Nanoparticles as Catalyst for Carbon-Carbon Bond Formation: Application to Aerobic Homocoupling of Phenylboronic Acid in Water. *Langmuir* **2004,** *20* (26), 11293-11296.
156. Umpierre, A. P.; de Jesús, E.; Dupont, J., Turnover Numbers and Soluble Metal Nanoparticles. *Chemcatchem* **2011,** *3* (9), 1413-1418.

157. Margelefsky, E. L.; Zeidan, R. K.; Davis, M. E., Cooperative catalysis by silica-supported organic functional groups. *Chem. Soc. Rev.* **2008,** *37* (6), 1118-1126.
158. Sharma, R. K.; Sharma, S.; Dutta, S.; Zboril, R.; Gawande, M. B., Silica-nanosphere-based organic-inorganic hybrid nanomaterials: synthesis, functionalization and applications in catalysis. *Green Chem.* **2015,** *17* (6), 3207-3230.
159. Wang, J.; White, W. B.; Adair, J. H., Evaluation of Dispersion Methods for Silica-Based Composite Nanoparticles. *J. Am. Ceram. Soc.* **2006,** *89* (7), 2359-2363.
160. Cornell, R. M.; Schwertmann; U, *The Iron Oxides: Structure, Properties, Reactions, Occurrence and Uses*. 1 ed.; Wiley-VHC Gmbh & Co KGaA: 1996.
161. Barbeta, V. B.; Jardim, R. F.; Kiyohara, P. K.; Effenberger, F. B.; Rossi, L. M., Magnetic properties of Fe3O4 nanoparticles coated with oleic and dodecanoic acids. *J. Appl. Phys.* **2010,** *107* (7).
162. Tada, D. B. Desenvolvimento de nanopartículas fotossenssibilizadoras. Universidade de São Paulo, São Paulo, 2007.
163. McCafferty, E.; Wightman, J. P., Determination of the concentration of surface hydroxyl groups on metal oxide films by a quantitative XPS method. *Surf. Interface Anal.* **1998,** *26* (8), 549-564.
164. Brundle, C. R.; Chuang, T. J.; Wandelt, K., Core and valence level photoemission studies of iron oxide surfaces and the oxidation of iron. *Surf. Sci.* **1977,** *68*, 459-468.
165. Hamwi, A.; Latouche, C.; Marchand, V.; Dupuis, J.; Benoit, R., Perfluorofullerenes: Characterization and structural aspects. *J. Phys. Chem. Solids* **1996,** *57* (6–8), 991-998.
166. Kwon, H.-W.; Lim, Y.-M.; Tripathy, S. K.; Kim, B.-G.; Lee, M.-S.; Yu, Y.-T., Synthesis of Au/TiO2 core-shell nanoparticles from titanium isopropoxide and thermal resistance effect of TiO2 shell. *Japanese Journal of Applied Physics* **2007,** *46* (4B), 2567-2570.
167. (a) Ao, Y. H.; Xu, J. J.; Fu, D. G.; Ba, L.; Yuan, C. W., Deposition of anatase titania onto carbon encapsulated magnetite nanoparticles. *Nanotechnology* **2008,** *19* (40); (b) Xu, J.; Ao, Y.; Fu, D.; Yuan, C., Low-temperature preparation of anatase titania-coated magnetite. *J. Phys. Chem. Solids* **2008,** *69* (8), 1980-1984.
168. Usha, K.; Mondal, B.; Sengupta, D.; Kumbhakar, P., Photo-conversion efficiency measurement of dye-sensitized solar cell using nanocrystalline TiO2 thin film as photo-anodes. *Measurement* **2015,** *61*, 21-26.
169. Lin, Y.-L.; Wang, T.-J.; Jin, Y., Surface characteristics of hydrous silica-coated TiO2 particles. *Powder Technol.* **2002,** *123* (2–3), 194-198.
170. Liu, C.; Yang, D.; Jiao, Y.; Tian, Y.; Wang, Y.; Jiang, Z., Biomimetic Synthesis of TiO2–SiO2–Ag Nanocomposites with Enhanced Visible-Light Photocatalytic Activity. *ACS Applied Materials & Interfaces* **2013,** *5* (9), 3824-3832.
171. Bensalem, A.; Bozon-Verduraz, F.; Delamar, M.; Bugli, G., Preparation and characterization of highly dispersed silica-supported ceria. *Applied Catalysis A: General* **1995,** *121* (1), 81-93.
172. Concepción, P.; Corma, A.; Silvestre-Albero, J.; Franco, V.; Chane-Ching, J. Y., Chemoselective Hydrogenation Catalysts: Pt on Mesostructured CeO2 Nanoparticles Embedded within Ultrathin Layers of SiO2 Binder. *J. Am. Chem. Soc.* **2004,** *126* (17), 5523-5532.
173. (a) Gutiérrez, L.-F.; Hamoudi, S.; Belkacemi, K., Effective gold catalyst supported on mesoporous silica decorated by ceria for the synthesis of high value lactobionic acid. *Applied Catalysis A: General* **2012,** *425–426*, 213-223; (b) Burroughs, P.; Hamnett, A.; Orchard, A. F.; Thornton, G., Satellite structure in the X-ray photoelectron spectra of some binary and mixed oxides of lanthanum and cerium. *J. Chem. Soc., Dalton Trans.* **1976,** (17), 1686-1698.
174. El Fallah, J.; Hilaire, L.; Roméo, M.; Le Normand, F., Effect of surface treatments, photon and electron impacts on the ceria 3d core level. *J. Electron. Spectrosc. Relat. Phenom.* **1995,** *73* (1), 89-103.
175. Jacinto, M. J.; Silva, F. P.; Kiyohara, P. K.; Landers, R.; Rossi, L. M., Catalyst Recovery and Recycling Facilitated by Magnetic Separation: Iridium and Other Metal Nanoparticles. *Chemcatchem* **2012,** *4* (5), 698-703.
176. Pélisson, C.-H.; Vono, L. L. R.; Hubert, C.; Denicourt-Nowicki, A.; Rossi, L. M.; Roucoux, A., Moving from surfactant-stabilized aqueous rhodium (0) colloidal suspension to heterogeneous

magnetite-supported rhodium nanocatalysts: Synthesis, characterization and catalytic performance in hydrogenation reactions. *Catal. Today* **2012,** *183* (1), 124-129.
177. Silva, T. A. G.; Landers, R.; Rossi, L. M., Magnetically recoverable AuPd nanoparticles prepared by a coordination capture method as a reusable catalyst for green oxidation of benzyl alcohol. *Catal. Sci. Technol.* **2013,** *3* (11), 2993-2999.
178. Larpent, C.; Menn, F. B.-L.; Patin, H., New highly water-soluble surfactants stabilize colloidal rhodium(O) suspensions useful in biphasic catalysis. *J. Mol. Catal.* **1991,** *65*, L35-L40.
179. Stowell, C. A.; Korgel, B. A., Iridium nanocrystal synthesis and surface coating-dependent catalytic activity. *Nano Lett.* **2005,** *5* (7), 1203-1207.
180. Sermon, P. A.; Georgiades, G.; Vong, M. S. W.; Martin-Luengo, M. A.; Reyes, P. N., Evidence of Surface-Reaction Segregation in Cyclohexene Hydrogenation and Dehydrogenation Over Supported Platinum. *Proc. R. Soc. Lond. A* **1987,** *410* (1839), 353-372.
181. Rioux, R. M.; Hsu, B. B.; Grass, M. E.; Song, H.; Somorjai, G. A., Influence of Particle Size on Reaction Selectivity in Cyclohexene Hydrogenation and Dehydrogenation over Silica-Supported Monodisperse Pt Particles. *Catal. Lett.* **2008,** *126* (1-2), 10-19.
182. Molnár, E. v.; Tasi, G.; Kónya, Z.; Kiricsi, I., Infrared spectroscopy studies of cyclohexene hydrogenation and dehydrogenation catalyzed by platinum nanoparticles supported on mesoporous silicate (SBA-15). Part 1: The role of particle size of Pt nanocrystals supported on SBA-15 silicate. *Catal. Lett.* **2005,** *101* (3-4), 159-167.
183. Somorjai, G. A.; Rioux, R. M., High technology catalysts towards 100% selectivity fabrication, characterization and reaction studies. *Catal. Today* **2005,** *100* (3-4), 201-215.
184. Escobar, J.; Reyes, J. A. D. L.; Viveros, T.; Barrera, M. C., Cyclohexane dehydrogenation over wet-impregnated Ni on Al2O3-TiO2 sol-gel oxides. *Ind. Eng. Chem. Res.* **2006,** *45* (16), 5693-5700.
185. Dummer, N. F.; Bawaked, S.; Hayward, J.; Jenkins, R.; Hutchings, G. J., Oxidative dehydrogenation of cyclohexane and cyclohexene over supported gold, palladium and gold-palladium catalysts. *Catal. Today* **2010,** *154* (1-2), 2-6.
186. (a) Panizza, M.; Resini, C.; Busca, G.; Fernández López, E.; Sánchez Escribano, V., A Study of the Oxidative Dehydrogenation of Cyclohexane Over Oxide Catalysts. *Catal. Lett.* **2003,** *89* (3-4), 199-205; (b) Lee, S.; Vece, M. D.; Lee, B.; Seifert, S.; Winans, R. E.; Vajda, S., Oxidative dehydrogenation of cyclohexene on size selected subnanometer cobalt clusters: improved catalytic performance via evolution of cluster-assembled nanostructures. *Phys. Chem. Chem. Phys.* **2012,** *14* (26), 9336-9342.
187. Cheng, L.; Dai, Q.; Li, H.; Wang, X., Highly selective hydrogenation of phenol and derivatives over Pd catalysts supported on SiO2 and γ-Al2O3 in aqueous media. *Catal. Commun.* **2014,** *57*, 23-28.
188. Zou, G.; Zhong, W.; Mao, L.; Xu, Q.; Xiao, J.; Yin, D.; Xiao, Z.; Kirk, S. R.; Shu, T., A non-nitric acid method of adipic acid synthesis: organic solvent- and promoter-free oxidation of cyclohexanone with oxygen over hollow-structured Mn/TS-1 catalysts. *Green Chem.* **2015,** *17* (3), 1884-1892.
189. (a) Mortensen, P. M.; Grunwaldt, J. D.; Jensen, P. A.; Knudsen, K. G.; Jensen, A. D., A review of catalytic upgrading of bio-oil to engine fuels. *Applied Catalysis A: General* **2011,** *407* (1–2), 1-19; (b) Zhao, C.; Kou, Y.; Lemonidou, A. A.; Li, X.; Lercher, J. A., Highly Selective Catalytic Conversion of Phenolic Bio-Oil to Alkanes. *Angew. Chem. Int. Ed.* **2009,** *48* (22), 3987-3990.
190. Meenakshisundaram, S.; Nowicka, E.; Miedziak, P. J.; Brett, G. L.; Jenkins, R. L.; Dimitratos, N.; Taylor, S. H.; Knight, D. W.; Bethell, D.; Hutchings, G. J., Oxidation of alcohols using supported gold and gold-palladium nanoparticles. *Faraday Discuss.* **2010,** *145* (0), 341-356.
191. Enache, D. I.; Knight, D. W.; Hutchings, G. J., Solvent-free oxidation of primary alcohols to aldehydes using supported gold catalysts. *Catal. Lett.* **2005,** *103* (1-2), 43-52.
192. Abad, A.; Concepcion, P.; Corma, A.; Garcia, H., A collaborative effect between gold and a support induces the selective oxidation of alcohols. *Angew. Chem. Int. Ed.* **2005,** *44* (26), 4066-4069.
193. Gomez, S.; Philippot, K.; Colliere, V.; Chaudret, B.; Senocq, F.; Lecante, P., Gold nanoparticles from self-assembled gold(I) amine precursors. *Chem. Commun.* **2000,** (19), 1945-1946.